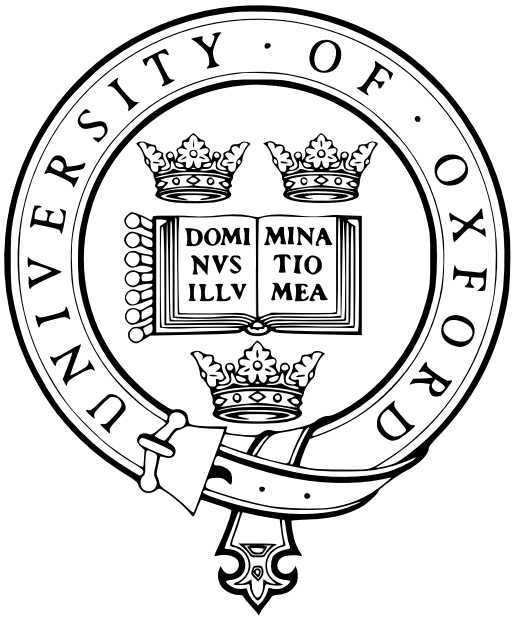


Colloidal liquid crystals: phase behavior, dynamics and confinement

Louis B. G. Cortes

Christ Church
University of Oxford

Supervisor: Prof. Dirk G. A. L. Aarts

A thesis submitted for the degree of
Doctor of Philosophy

Trinity 2019

Abstract

In this thesis, we report on the phase behaviour, dynamics and confinement of micron-sized colloidal silica rods with small gravitational length. In sedimentation-diffusion equilibrium, distinct isotropic, nematic, smectic and crystal phases are found to coexist within tens of micrometers. By combining confocal microscopy and tracer particles, the rods' phase behavior and dynamics are characterized across the whole phase diagram in a single sedimentation-diffusion experiment.

Our experimental approach allows to quantitatively compare the sedimentation-diffusion equilibrium of charged rods with theoretical predictions. All predicted phases are observed. However, the thickness of the upper sediment – counting the isotropic, nematic and smectic regions – is found to be inflated with respect to the hard rod prediction, up to a factor 2. We consider the possible effect of polydispersity, electrostatic repulsion and the entropy of counterions (Donnan effect). We conclude that only the Donnan effect can explain the observed inflation. To support the hypothesis, we independently determine the surface charge of silica rods and discuss the results.

Subsequently, we measure the self-diffusion of rod-like particles in sedimentation-diffusion equilibrium. Firstly, a molecular dynamic simulation is used to test the method. The self-diffusion coefficients are measured across the whole phase diagram and compared to bulk simulations – without gravity. We then present experimental results for an aspect ratio of 10, which has not been yet reported upon in literature. We reproduce most trends predicted by simulations. In particular, we find evidence of strong correlation between rotational and translational diffusion approaching the nematic phase, and a crossover between diffusion parallel and perpendicular to the nematic director in the smectic phase. However, we measure smaller diffusion coefficients than predicted by simulation, which is consistent with work on viral colloidal liquid crystals with larger aspect ratio.

Finally, we study sedimentation-diffusion equilibrium in confinement, with a focus on the smectic phase, and consider three geometries: the square, the lozenge and the annulus. The interplay between boundary conditions, elasticities and defects lead to a host of different structures.

In squares and disks, we mostly observe the smectic bridge state. However, by transforming the shapes into annuli and lozenges, we force new configurations. The transitions are characterized in light of phenomenological models to extract the ratios between: the energy of an edge dislocation, the energy of a disclination line and the bending energy of smectic layers.

Declaration

This thesis is submitted for the degree of Doctor of Philosophy in Physical and Theoretical Chemistry at the University of Oxford. No part of this thesis has been accepted or is currently being submitted for any degree, diploma, certificate or other qualification in this University or elsewhere. This thesis is wholly my own work, except where indicated.

Contents

Abstract **i**

Declaration **iii**

1 Introduction **1**

1.1 Structured fluids 1

1.2 Colloidal liquid crystals 3

1.3 Scope of the thesis 4

2 Theoretical background and experimental methods **7**

2.1 Physics of colloidal liquid crystals 8

2.1.1 Diffusion of colloids, the role of thermal energy 8

2.1.2 Entropy driven phase transitions 17

2.1.3 Colloid interactions 26

2.1.4 Elasticities of mesophases 28

2.1.5 Defects in mesophases 30

2.2 Experimental methods 31

2.2.1 Colloidal rods 32

2.2.2 Sample preparation 37

2.2.3 Video-microscopy 39

2.2.4 Image analysis 40

3 Phase behavior of colloidal rods in sedimentation-diffusion equilibrium 47

3.1 Introduction . . . 48

3.2 Sedimentation-diffusion equilibrium of hard spherocylinders . . . 48

3.2.1 Theoretical background . . . 49

3.2.2 Method . . . 51

3.2.3 Results and discussion . . . 53

3.3 Simulation . . . 54

3.3.1 Method . . . 54

3.3.2 Analysis . . . 55

3.3.3 Results . . . 56

3.3.4 Discussion . . . 60

3.4 Simulation vs theory . . . 61

3.5 Experiments . . . 64

3.5.1 Method . . . 64

3.5.2 Analysis . . . 66

3.5.3 Results . . . 67

3.6 Experiments vs theory and simulation . . . 71

3.6.1 Inflated upper sediments . . . 71

3.6.2 Nematic order parameter . . . 76

3.7 Conclusion and outlook . . . 77

4 The Donnan effect on the sedimentation-diffusion equilibrium of silica rods 81

4.1 Introduction . . . 83

4.2 Sedimentation-diffusion equilibrium of charged rods . . . 84

4.2.1 Mapping of charged rods on the phase behavior of hard rods . . . 84

4.2.2 Donnan equilibrium . . . 86

4.2.3 Density profile of charged rods . . . 89

4.2.4 Initial conditions and effective diameter . . . 91
4.2.5 Linearities of the density profiles . . . 93
4.2.6 Donnan effect in the semi-dilute isotropic . . . 95
4.3 Surface charge of silica rods in water . . . 96
4.3.1 Introduction . . . 96
4.3.2 Theoretical estimate . . . 97
4.3.3 Experimental estimate . . . 99
4.3.4 Counterion condensation . . . 101
4.4 Discussion . . . 103
4.5 Conclusion and outlook . . . 105

5 Self-diffusion of colloidal rods in sedimentation-diffusion equilibrium 107

5.1 Introduction . . . 108
5.2 Theoretical background . . . 111
5.3 Simulation . . . 113
5.3.1 Simulation method . . . 113
5.3.2 Analysis of self-diffusion in sedimentation-diffusion equilibrium . . . 114
5.3.3 Results . . . 119
5.4 Experiments . . . 125
5.4.1 Experimental methods . . . 125
5.4.2 How to measure 3D rotation with 2D snapshots . . . 127
5.4.3 Experimental Results . . . 131
5.5 Conclusion . . . 142

6 Confinement of liquid crystals 145

6.1 Introduction . . . 146
6.2 Experimental technique . . . 148
6.3 Applicability of the method . . . 150

6.3.1 Sedimentation-diffusion equilibrium in confinement 150
6.3.2 Dynamics and stability 152
6.4 Squares and rectangles 153
6.4.1 Qualitative observations 154
6.4.2 Statistical analysis into squares 158
6.5 Lozenges 160
6.5.1 Model 160
6.5.2 Method 162
6.5.3 Results 163
6.6 Annuli 166
6.6.1 Method 167
6.6.2 Results 168
6.6.3 A phenomenological model for the smectic states 171
6.6.4 Coexisting nematic structures 174
6.7 Conclusion 176

Summary **179**

Bibliography **183**

List of Publications **199**

Acknowledgement of Funding **201**

Acknowledgements **203**

Chapter 1

Introduction

1.1 Structured fluids

Everyone is familiar with paint, soap or egg white. These structured liquids are sometimes referred to as soft matter or complex fluids because of their structure's fragility and complex response to external stress. Indeed, they can be deformed by stresses of same magnitude as thermal energy. Furthermore, these deformations induce non-linear responses to external stresses making these materials non-Newtonian. The link between structural and rheological properties is not trival and, for example, leads to opposing behaviours for a mixture of corn starch with water and for quicksand. The shear thickening cornstarch mixture can be pored in a swimming pool like a liquid but will react like a solid when faced with a person running. In contrast, shear thinning quicksand can fix a still object, but will sink a moving one. These phenomena are exploited for industrial purposes. For instance ketchup, mayonnaise and toothpaste are designed to be shear thinning [1]. On the other hand, shear thickening is used to make flexible but shock resilient materials [2, 3].

Soft matter's impact on industry goes beyond these few examples. Indeed, structured fluids containing polymer, surfactants or colloidal particles are found in many sectors. In food, cosmetic and agrochemical industries, formulation and stabilization of colloidal suspensions (i.e. creams, milks, gels, concentrates) is an everyday challenge. This is equally true in the construction industry with processing of paint and cement. The extraordinary properties of surfactants and polymers are essential in the research and development of glue, printing, drug delivery [4], oil

extraction, etc. Last but not least liquid crystals find applications on domains ranging from specialized imaging technologies [5] to consumer goods such as liquid crystal displays (LCDs) [6] and smart windows [7]).

On the academic side, soft matter greatly benefits from collaborations between physicists, chemists and biologists with complementary backgrounds and knowledge. The sub-field of active matter is a good example where multiple talents are combined to address typical soft matter problems [8]. However, it can also go the other way around, as soft matter systems have been use to solve physical problems. A great example is the contribution of Jean Baptiste Perrin (Nobel Prize 1926) to molecular theories. He used a simple suspension of gambodge particles, a yellow pigment produced from tree resin, to prove the existence of molecules and thereby enable determination of their mass (see section 2.1.1).

Perrin's method was not an isolated case, there are many instances where biological materials are used as model systems. For example another Nobel prize laureate, Lars Onsager (Nobel prize 1968), in the mid 20th century was inspired by the self assembly of purified long and thin viruses to develop his theory on an entropy driven phase transition [9], introducing the earliest version of density functional theory (DFT).

Despite previous brilliant contributions, structured liquids are considered to have become a coherent research field in the past thirty to fifty years by developing a tool-kit of predictive and comprehensive theories and methods. This is considered to have been driven by a third Nobel prize laureate, Pierre-Gille de Gennes (Nobel Prize 1991) with his work on polymers [10], wetting [11] and liquid crystals [12].

The ultimate understanding of a material can only be obtained by linking the macroscopic properties to the microscopic components. The work of Onsager is an example of this. He related the phase behaviour of a suspension of hard rods to their aspect ratio [9] by maximizing their entropy. His ingenious approach is treated in section 2.1.2. The main limitation of Onsager theory is that it breaks down at high concentration. When this kind of bottom-up approach is too complex due to high concentration, not well defined sub-units, etc., another strategy is followed. Systems are looked at as whole and their properties, described by theories, are measured macroscopically. This approach has been followed to look at properties of thermotropic liquid crystals [12], and is driven by experimental work.

In this thesis we present experiments on colloidal liquid crystals. The beauty of this system relies on the fact that it can be described by both microscopic and macroscopic theories, which means that we contribute to bridging these two descriptions. Before providing further motivations (section 1.3) we will first give a short definition for colloidal liquid crystals (CLCs).

1.2 Colloidal liquid crystals

Liquid Crystals form a well defined category of structured liquids, which can form liquid crystal phases, also referred to as mesophases. These are intermediate states, between the liquid and the crystal phases, where the sample remains liquid but presents some kind of order. On one hand, the soft liquid phase can be controlled with weak electric or magnetic fields. On the another hand, the structured nature of the substance can interact with light. This is how liquid crystal displays (LCDs) operate in smart phones, computers and TV screens.

A *colloidal* dispersion is a suspension of an element A into medium B stable against sedimentation or creaming. This includes emulsions, foams, etc. For example milk is a colloidal suspension of fat droplets in an aqueous medium. One would expect that fat droplets cream at the surface of the milk as fat is lighter than water. However, this is prevented by thermally agitated water molecules bumping into the droplets. The thermal energy does not depend on the size of the droplets, unlike gravity. This effect limits the size of a colloidal particle to a maximum of 1 to 10μm, whereas the smallest colloids would be a couple of orders of magnitude bigger than the solvent, i.e. a few tens of nanometres.

CLCs are formed by a suspension of particles with anisotropic interactions. This anisotropy most often arises from their shape: a dispersion of rods or platelets can form liquid crystal phases. Within this work we will refer often to an ideal type of CLCs: hard spherocylinders. The adjective *hard* is used to qualify particles that do not interact apart from the fact they cannot overlap. The phase behaviour of such particles has been studied in detail [13]. Upon an increase of concentration, spherocylinders go through the sequence of phases illustrated in figure 1.1: first the isotropic phase without order, then the nematic phase with long range orientational order but no positional order, then the smectic phase with an additional semi-long range positional order (characterized by the formation of layers) and finally the crystalline phase. These liquid crystal phases are described in greater details in section 2.1.2.

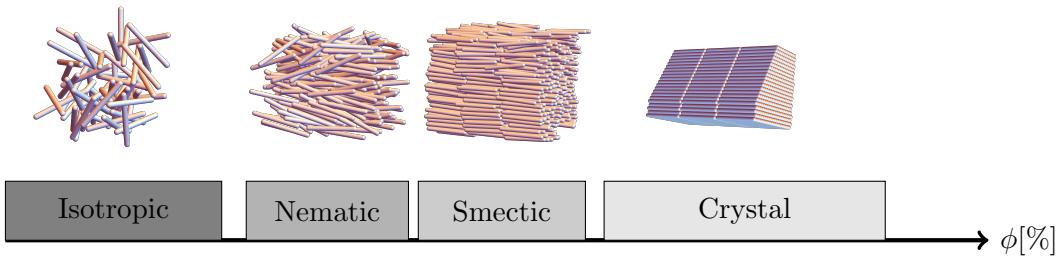


Figure 1.1: Typical phase behaviour of hard spherocylinders, with ϕ the volume fraction of rods.

On the top of the rich phase behaviour CLCs also form an equally interesting system to study interfaces. Indeed, most of the phase transitions are first order, CLCs therefore present thermodynamically stable phase coexistences.

Examples of CLCs are: biological (deoxyribonucleic acid (DNA) origami [14], some viruses [15], actin bundels [16], collagen systems [17], nanocellulose [18]) but also industrial. For example the company Teijin Aramid produces polyaramids fibers reinforced by liquid crystalline order [19], a method shared by spiders producing their silk [20]. The particles' alignment is a key factor in the fibers' quality [21] and partly depends on confinement and flow before coagulation. The food industry is also interested in CLCs. A contemporary problem is to replace fat with a natural low energy counterpart, for example long and thin cellulose fibers, in order to either improve the texture or stability of the products [22]. There are also natural occurrences of inorganic particles such as clay, or synthetic ones, a review on mineral CLCs can be found here [23].

1.3 Scope of the thesis

The rising interest in colloidal liquid crystals is partly motivated by its potential relevance for industrial applications and modeling of biological systems. In addition to the fabrication of fibers and the formulation of food products, the design of composite material is an industrial problem that stimulates fundamental work on liquid crystals. In particular, an option to make conductive and transparent thin films is to dope a non-conductive matrix with carbon nanotubes [24], if long enough the tubes percolate at a low concentration [25], this provides a conductive and transparent film. Understanding how flow or confinement affects the percolation threshold is an example of a fundamental problem [26].

Colloidal liquid crystals are relevant for biology in the respect that many biological elements are anisotropic and dispersed in aqueous media. Sometimes they even form liquid crystal phases,

for example actin filaments can form a nematic phase, and cell membranes are made of a smectic lipid bi-layer. Understanding the phase behaviour and dynamic of ideal liquid crystals in a controlled environment is a first step toward understanding systems as complex as actin filaments [27], packing of DNA into virus heads [28] or cytoskeleton self-organization [29].

Within this thesis we study the phase behaviour and diffusion of colloidal liquid crystals: we experimentally observe isotropic, nematic and smectic phases as well as their interfaces. Furthermore we address the problem of confinement with a focus on the smectic phase. Our global approach aims to experimentally test and inspire theoretical and computational works on liquid crystals, especially CLCs. To do so we need an experimental system as ideal as possible. We then characterize our system in the light of existing simulations and theories on hard rods. The system is observed in direct space and at the single particle level for various reasons. Firstly, it provides direct evidence in the form of visual material that is easy to share with the community and more likely to be widely understood. In some instances this direct evidence cannot be obtained in any other way. For example, the tube theory [30] postulates that long and thin rods in the dense isotropic phase will reptate through the network formed by the other particles. For rods this will lead to a strong coupling between translation and rotation [30, 31]. This theory is complemented by scattering experiments showing that rotational diffusion scales with concentration as predicted [32]. However, this remarkable work only gives indirect evidence and rotation-translation coupling can only be observed at the single particle level. This shows how direct visualization can be a powerful tool to try and develop theories. This is equally true when confronting experiments with molecular simulations, as these are also based on single particle information.

Direct visualization requires particles around the micrometer size which is the top end of the colloidal scale. Luckily this length scale comes together with a time scale around the second which is ideal for video-microscopy. Another advantage of such a large system resides in its interfacial properties. Hard rods have predicted phase coexistences, which means that interface are naturally formed within a range of concentrations. These interfaces are characterized by ultra low surface tensions as $\gamma \propto \frac{k_B T}{\sigma^2}$, where σ the particle diameter. Colloids with a diameter of one micron ($10^{-6}m$) are expected to generate an interfaces 10^8 time softer than water molecules of a few angstrom ($10^{-10}m$). This has led to direct observation of thermally induced capillary waves in colloid polymer mixture [33]. The interplay between thermal fluctuations and liquid crystals

anisotropic properties opens many fundamental questions [34, 35].

The thesis is organized as follows.

In chapter 2, we present theoretical background and experimental methods.

In chapter 3, we study the phase behaviour of colloidal rods in sedimentation-diffusion equilibrium by means of theory, simulation and experiments. Whereas good agreement is found between theory and simulations of hard rods, the experimental sediments of charged silica rods are found to be largely inflated.

In chapter 4, we make a case for a credible explanation of the inflated sediments: the Donnan effect [36]. We first generalize our theoretical model to include both electrostatic repulsion and the entropy of counterions. The model is found to be in good agreement with experiments for rod surface charge 'A'. The particle surface charge is then estimated separately and compared to 'A'.

In chapter 5, we exploit the sedimentation-diffusion equilibrium to investigate the rod self-diffusion across the whole phase diagram. The results are laid out in light of existing work.

In chapter 6, the sedimentation-diffusion is established in confining chambers. We first introduce the method and its potential. Then, we focus on the confinement of the smectic phase. We consider squares, found in good agreement with preceding simulations, and exploratory shapes of lozenges and annuli. In particular, by introducing phenomenological models to characterize the discovered states, we extract energy ratios between: layer bending, edge dislocations and line disclinations.

Chapter 2

Theoretical background and experimental methods

Abstract

In this chapter, we first present important notions on which subsequent chapters are largely based. In particular, we introduce the gravitational length $l_g = \frac{k_B T}{m_b\, g}$ that rules the sedimentation-diffusion density profile. We also describe essential aspects of the phase behavior of hard rods, the interaction potential between charged rods and the self-diffusion of a cylinder. We finally provide background information on the elasticities and defects in liquid crystal phases which is particularly relevant for chapter 6.

We then lay out our experimental methods. We start with the method employed to synthesize the colloidal rod systems studied across the entire thesis. There are essentially two silica rod [37] systems which are characterized by their mean length L, diameter σ, aspect ratio $p = L/\sigma$ and gravitational length l_g:

- the rods LC012: $L = 2.7\,\mu\text{m}$, $\sigma = 0.28\,\mu\text{m}$, $p = 8.5$, $l_g = 3.3\,\mu\text{m}$.
- the rods LC017: $L = 5.26\,\mu\text{m}$, $\sigma = 0.39\,\mu\text{m}$, $p = 12.6$, $l_g = 0.8\,\mu\text{m}$.

We then detail the core of experimental techniques, composed of: cell fabrication, video microscopy and image analysis.

This chapter is divided into two independents parts. Section 2.1 provides a theoretical background on the physics of CLCs and section 2.2 details experimental methods.

2.1 Physics of colloidal liquid crystals

In this section, we first present theoretical concepts with a particle based approach:

- Section 2.1.1 starts with historical facts about Brownian motion followed by mathematical and physical descriptions. In particular, it is shown that the particle motion is directly related to its geometry, the solvent viscosity and thermal energy. The sedimentation-diffusion equilibrium of colloids is briefly introduced.
- Section 2.1.2 continues with the phase behavior of hard rods and treats its dependency on aspect ratio and concentration.
- Section 2.1.3 introduces the DLVO potential which is usually used to describe the interaction between charged colloids.

The two remaining parts of the section are dedicated to: continuum theories describing the elasticities of liquid crystal phases and a review of topological defects expected in the nematic and smectic phases.

2.1.1 Diffusion of colloids, the role of thermal energy

The diffusion of colloids has been used in the beginning of the XX's century to prove the existence of atoms and molecules [38]. In this section, we first return to this historical event to introduce the analogy between colloids and molecules. We then derive the mathematical link between stochastic displacements and the diffusion coefficient. We subsequently show that the diffusion coefficient of a colloid is equal to the product of the thermal energy and its mobility. Finally, we describe motion of a cylinder and provide its self-diffusion coefficients calculated at infinite dilution.

Brownian motion, the visible impact of invisible molecules

Brownian motion is named after the botanist Robert Brown ($1773 - 1858$) who reported of the stochastic displacements of small particles escaped from pollen grains suspended into water. This behavior was then confirmed by a handful of physicists, who suggested the molecular origin of Brownian motion: Wiener (1863), Delsaulx and Carbonnelle (1877) [39, 40]. However, their work received little attention and did not provide enough experimental evidence to refute other explanations. With the work of Gouy (1888) it became clear that convection was not responsible for Brownian motion [41–43]. A mathematical description came through Albert Einstein's kinetic theory of the Brownian movement. It predicted that molecular density fluctuations will induce particle displacements, and related this thermal motion to the solvent viscosity, the Avogadro constant and the particle size. [44]. Brownian motion then formed a strong case against the flickering scientific agreement on the continuous nature of matter. A couple of years later, Einstein theory was followed by a series of experiments by Jean Baptiste Perrin on Brownian motion (translation and rotation) and on the barometric distribution of colloids [38]. These quantitative studies proved in two independent ways the existence of molecules. One way was to experimentally confirm Einstein theory and the second was to use colloids as model of gas molecules. Indeed, Perrin found that the density profile of colloids, at low volume fractions, follows the same barometric distribution as a perfect gas. In that respect, he showed that colloids could be used as a model of molecules. These two methods led to a strikingly precise measurement of the Avogadro number. Perrin therefore not only proved molecules' existence but also was able to determine their weight and kinetic energy. For this, he received a Nobel Prize in 1926.

In the next two sections, we will first describe mathematically Brownian motion following Einstein's path. In order to relate this motion to physical parameters we will not reproduce Einstein work. We will instead consider that a colloidal gas behaves like a perfect gas and make use of Fick's law.

Mathematics of stochastic motion

The aim of this section is to find the evolution of the probability $P(x,t)$ to find a particle at a certain time t and position x, given initial conditions. The particle displacements Δ follow a

given symmetric probability density function $\phi(\Delta) = \phi(-\Delta)$, independent of time or space. This function ϕ will generate random displacements. We address the problem in 1D for simplicity. The density ρ is the product of $P(x,t)$ and the number of particles N:

$$\rho(x,t) = NP(x,t). \tag{2.1}$$

Before starting, note that the variation of density with time and space can be expanded as follow:

$$\rho(x+\Delta,t) = \rho(x,t) + \Delta\frac{\partial\rho}{\partial x} + \frac{\Delta^2}{2}\frac{\partial^2\rho}{\partial x^2} + ... \ , \tag{2.2}$$

$$\rho(x,t+\tau) = \rho(x,t) + \tau\frac{\partial\rho}{\partial t} + \frac{\tau^2}{2}\frac{\partial^2\rho}{\partial t^2} + ... \ . \tag{2.3}$$

Knowing the density at time t, we want to determine the density at time $t+\tau$. For a particle at position $x+\Delta$ the probabilty of moving to position x within a delay τ is called $\phi(-\Delta)$. Then

$$\rho(x,t+\tau) = \int_{-\infty}^{\infty} d\Delta[\rho(x+\Delta,t)\phi(-\Delta)] \tag{2.4}$$

and using equation 2.2

$$\rho(x,t+\tau) = \int_{-\infty}^{\infty} d\Delta[(\rho(x,t) + \Delta\frac{\partial\rho}{\partial x} + \frac{\Delta^2}{2}\frac{\partial^2\rho}{\partial x^2} + ...)\phi(-\Delta)] \ . \tag{2.5}$$

Splitting the integrals

$$\rho(x,t+\tau) = \int_{-\infty}^{\infty} d\Delta[\rho(x,t)\phi(-\Delta)] + \int_{-\infty}^{\infty} d\Delta[\Delta\frac{\partial\rho}{\partial x}\phi(-\Delta)] + \int_{-\infty}^{\infty} d\Delta[\frac{\Delta^2}{2}\frac{\partial^2\rho}{\partial x^2}\phi(-\Delta)] + ... \tag{2.6}$$

and taking terms in ρ out of the integrals

$$\rho(x,t+\tau) = \rho(x,t)\int_{-\infty}^{\infty} d\Delta[\phi(-\Delta)] + \frac{\partial\rho}{\partial x}\int_{-\infty}^{\infty} d\Delta[\Delta\phi(-\Delta)] + \frac{\partial^2\rho}{\partial x^2}\int_{-\infty}^{\infty} d\Delta[\frac{\Delta^2}{2}\phi(-\Delta)] + ... \ . \tag{2.7}$$

The first integral is equal to one by normalization of the probability function and the second integral (as all uneven integrals) is equal to zero by symmetry, that leaves

$$\rho(x, t+\tau) = \rho(x,t) + \frac{\partial^2 \rho}{\partial x^2} \int_{-\infty}^{\infty} d\Delta [\frac{\Delta^2}{2} \phi(-\Delta)] + ... \ . \tag{2.8}$$

By definition

$$\frac{\partial \rho}{\partial t} = \frac{\rho(x, t+\tau) - \rho(x,t)}{\tau} \ , \tag{2.9}$$

and introducing the diffusion coefficient constant

$$D = \int_{-\infty}^{\infty} d\Delta [\frac{\Delta^2}{2\tau} \phi(-\Delta)] \tag{2.10}$$

we obtain the diffusion equation

$$\frac{\partial \rho}{\partial t} = \frac{\partial^2 \rho}{\partial x^2} D \ . \tag{2.11}$$

For one particle with initial position $x = 0$ at time $t = 0$, the solution of equation (2.11) is

$$\rho(x,t) = P(x,t) = \frac{1}{\sqrt{4\pi D t}} \exp(-\frac{x^2}{4Dt}) \ . \tag{2.12}$$

This is only valid if D is independent of time and position. From there one can obtain the moments:

$$\langle x \rangle = \frac{\sum_{i=1}^{n} x_i}{n} = 0 \ . \tag{2.13}$$

$$\left\langle x^2 \right\rangle = \frac{\sum_{i=1}^{n} x_i^2}{n} = 2Dt \ . \tag{2.14}$$

A first result here is equation 2.10 that gives the relationship between the diffusion coefficient and the probability density function, which is a useful tool for simulations. The second and main result is equation 2.14; the mean square displacement (MSD) $\left\langle x^2 \right\rangle$ is directly proportional to the diffusion coefficient D and time. In multiple dimensions d, this can be generalized to:

$$\left\langle ||\vec{r}||^2(t) \right\rangle = 2dD_{\mathrm{t}}t \ . \tag{2.15}$$

This establishes the link between the particle trajectory $\vec{r}(t)$ and the diffusion coefficient D. Note that the diffusive regime described by equations 2.14 and 2.15 is the consequence of stochastic displacements. For a colloidal particle these equations are only valid for times larger than the Brownian time τ_D, see chapter 5 for additional information. In the next section, we will relate D to the thermal energy.

Sedimentation diffusion equilibrium of colloids

Perrin showed that the density profile of colloids at sedimentation-diffusion equilibrium follows a barometric distribution similar to a perfect gas:

$$\rho(h) = \rho(0) \exp(-\frac{m_b\, g\, h}{k_B T}) \ , \tag{2.16}$$

with ρ the number density of particles, h the altitude, m_b the particle's buoyant mass[1] and $\vec{g}$ the acceleration of earth. The typical length scale on which the density varies is called gravitational length:

$$l_g = \frac{k_B T}{m_b\, g} \ . \tag{2.17}$$

At sedimentation-diffusion equilibrium, the gravitational forces are compensated by the gradient of osmotic pressure (i.e. concentration). If we only consider gravity the particle should sediment at a speed v_s, whereas, without gravity, the colloid would move up at a speed v_d, to maximize their entropy.

The hypothetical sedimentation speed can be obtained from the total force exerted on a sedimenting sphere $\vec{F_s}$, which is the sum of its weight $\vec{P}$ and friction forces $\vec{f}$:

$$\vec{F_s} = \vec{P} + \vec{f} = m_b\, \vec{g} - \frac{1}{\mu}\vec{v_s} \ , \tag{2.18}$$

with μ the particle's mobility. Using Newton's second law, projecting along $\vec{g}$ and assuming

[1] $m_b = \Delta\rho v_0$, with v_0 the particle specific volume and $\Delta\rho$ the difference of density between the particle and the solvent.

equilibrium, i.e. $\frac{dv}{dt} = 0$ we obtain

$$F_s = m_b \frac{dv_s}{dt} = m_b\, g - \frac{1}{\mu} v_s = 0 \qquad \rightarrow \qquad v_s = \mu\, m_b\, g\ . \tag{2.19}$$

The hypothetical diffusion speed v_d is determined from Fick's first law:

$$J = \rho v_d = -D \frac{\partial \rho}{\partial h} \qquad \rightarrow \qquad v_d = D \frac{m_b\, g}{k_B T}\ , \tag{2.20}$$

where J is the flux of colloid and ρ has been replaced by equation 2.16.

At sedimentation-diffusion equilibrium, there is no net speed, $v_d = v_s$ and

$$\mu\, m_b\, g = D \frac{m_b\, g}{k_B T}. \tag{2.21}$$

We can finally extract the diffusion coefficient, the product of the thermal energy and the particle's mobility

$$D = \mu k_B T\ . \tag{2.22}$$

This result contains a direct link between the macroscopic viscosity of the medium and the microscopic displacements of the particle. Indeed, the mobility of a sphere is $\mu = (6\pi\eta R)^{-1}$. This implies by measuring the mean square displacement of a sphere (or its diffusion coefficient) in a well defined medium allows to determinate its radius. This technique has for example been used to measure hydrodynamic gyration radius of polymer [10].

Diffusion of a rod

The Brownian motion of a rod splits into translational and rotational components. The total translational diffusion coefficient D_{t} is related to the mean square displacement by

$$\left\langle ||\vec{r}||^2(t) \right\rangle = 6 D_{\mathrm{t}} t\ , \tag{2.23}$$

this can be split into one diffusion component parallel to the rod main axis ($2D_t^{\parallel}t$) and two components perpendicular ($2 \times 2D_t^{\perp}t$)

$$\left\langle ||\vec{r}||^2(t) \right\rangle = 2D_{\mathrm{t}}^{\parallel}t + 4D_{\mathrm{t}}^{\perp}t \ . \tag{2.24}$$

For each of these diffusion coefficients D_i, there are associated mobilities μ_i (equation 2.22), explicitly

$$\begin{cases} D_{\mathrm{t}} = \mu_{\mathrm{t}} k_B T \\ D^{\parallel} = \mu^{\parallel} k_B T \\ D^{\perp} = \mu^{\perp} k_B T \end{cases} . \tag{2.25}$$

We can then express the total mobility as

$$\mu_{\mathrm{t}} = \frac{1}{3}\mu^{\parallel} + \frac{2}{3}\mu^{\perp} \ . \tag{2.26}$$

These mobilities have been calculated for cylinders, in the infinite dilution limit, using the bead-shell model treatment [45]:

$$\begin{cases} \mu_0^{\parallel} = \frac{1}{2\pi\eta_0 L}\left(\ln(p) + \gamma_{\parallel}\right) \\ \mu_0^{\perp} = \frac{1}{4\pi\eta_0 L}\left(\ln(p) + \gamma_{\perp}\right) \\ \mu_{\mathrm{t}0} = \frac{1}{3\pi\eta_0 L}\left(\ln(p) + \gamma\right) \end{cases} , \tag{2.27}$$

where the subscript '$_0$' refers to the infinite dilution limit, $p = L/\sigma$ is the aspect ratio and γ_i are end effect terms, which are calculated and interpolated for different aspect ratios to give

$$\begin{cases} \gamma_{\parallel} = -0.207 + 0.980p^{-1} - 0.133p^{-2} \\ \gamma_{\perp} = 0.839 + 0.185p^{-1} + 0.233p^{-2} \\ \gamma = \frac{\gamma_{\parallel}+\gamma_{\perp}}{2} = 0.312 + 0.565p^{-1} + 0.1p^{-2} \end{cases} . \tag{2.28}$$

Let us consider now rotational diffusion. We can discriminate two components one about the short axis and one about the long axis with diffusion coefficients D_r and $D_r^{\parallel}$. They have also

been calculated in the infinite dilution limit [45]

$$\begin{cases} D_{r0} = \frac{3k_BT}{\pi\eta_0 L^3} \ln p + \delta_\perp \\ D_{r0}^{\parallel} = \frac{k_BT}{\pi\eta_0 L^3 A_0} \frac{p^2}{1+\delta_\parallel} \end{cases} , \tag{2.29}$$

where $A_0 = 3.84$ and

$$\begin{cases} \delta_\perp = -0.662 + 0.917p^{-1} - 0.050p^{-2} \\ \delta_\parallel = 0.677p^{-1} - 0.183p^{-2} \end{cases} . \tag{2.30}$$

However, the diffusion about the long axis cannot be measured experimentally, because of the cylindrical symmetry. We will then focus on the diffusion about the short axis. Rotational diffusion can be seen as translational diffusion along the perimeter of a circle in 2D, or on the surface of a sphere in 3D. Because the space is now closed, the mean square angular displacement is not the most convenient tool to measure the rotational diffusion coefficient experimentally. It can only be measured if we know all the infinitesimal angular displacements. We then introduce the auto-correlation function $\Theta(t)$, depending only on particle's orientation $\hat{u}$ at time t and time 0.

$$\Theta(t) = \langle \hat{u}(t).\hat{u}(0) \rangle = \int_{-\infty}^{\infty} [P(\hat{u}, t)\hat{u}(t).\hat{u}(0)] d\hat{u} \ , \tag{2.31}$$

with $P(\hat{u}, t)$ some probability density function. Again, we address the problem in 2D for simplicity.

We then have two-dimensional $\hat{u}(x, y)$, resulting in the dot product $\hat{u}(t).\hat{u}(0) = cos[\theta(t) - \theta(0)]$, with θ the angle with respect to the x axis. Assuming without loss of generality $\theta(0) = 0$ equation 2.31 can be rewritten as

$$\Theta_{2D}(t) = \langle \hat{u}(t).\hat{u}(0) \rangle = \int_{-\infty}^{\infty} [P(\theta) cos(\theta)] d\theta \ . \tag{2.32}$$

Rotational diffusion with one degree of freedom is analogous to Brownian motion along a circular line of radius 1. Therefore, the probability distribution function is the same as 1D translational diffusion. It is the solution of the diffusion equation 2.12, with D_R the rotational diffusion

coefficient:

$$P(\theta) = \frac{1}{\sqrt{4\pi D_R t}} \exp\left(-\frac{\theta^2}{4D_R t}\right) \ . \tag{2.33}$$

Combining 2.32 and 2.33 and integrating gives

$$\Theta_{2D}(t) = \langle \hat{u}(t).\hat{u}(0) \rangle = \exp(-D_R t) \ . \tag{2.34}$$

In 3D, with two degrees of freedom, one obtains

$$\Theta_{3D}(t) = \langle \hat{u}(t).\hat{u}(0) \rangle = \exp(-2D_R t) \ . \tag{2.35}$$

In contrast to the mean square angular displacement, this auto-correlation function does not require the full history of the particle orientations. However, the orientation is defined by a vector. Consequently, an angle θ needs to be discriminated from $\theta + \pi$. Yet for a rod, this cannot be done without the history of displacements. We use the second Legendre polynomial to avoid this issue, which in 3D gives

$$P_2^{3D}(t) = \frac{1}{2} \left\langle 3 \left(\hat{u}(t).\hat{u}(0)\right)^2 - 1 \right\rangle = \exp(-6D_R t) \tag{2.36}$$

and in 2D translates to

$$P^{2D}(t) = \left\langle 2 \left(\hat{u}(t).\hat{u}(0)\right)^2 - 1 \right\rangle = \exp(-4D_R t) \ , \tag{2.37}$$

or

$$P^{2D}(t) = \left\langle 2\cos^2\left(\theta(t) - \theta(0)\right) - 1 \right\rangle = \exp(-4D_R t) \ . \tag{2.38}$$

We can then simply apply the function P_2 to a set of measured orientations ($\theta \in [-\pi/2, \pi/2]$) with a permissive time resolution in order to measure the rotational diffusion coefficient.

In order to compare results from simulations and experiments, the mean square displacement can be scaled by the rod's square diameter σ^2, and the time by the characteristic time $\tau = \frac{\sigma^2}{D_{t0}}$.

2.1.2 Entropy driven phase transitions

In this section, we introduce the phase behavior of colloidal hard rods. We start with the seminal work of Onsager on the *isotropic to nematic* (I-N) phase transition [9]. We then report on simulations establishing the phase behavior of sphero-cylinder on a wide range of concentrations and aspect ratios [46]. We finally familiarize ourselves with the order parameters commonly used to identify and characterize the nematic and smectic phases.

Onsager theory on the isotropic-nematic phase transition

Onsager was inspired by experiments on the Tobacco mosaic virus [15], a long and thin virus affecting tobacco plants [47], to develop his theory on the I-N phase transition [9]. He modeled the viruses as hard rods with infinite aspect ratio ($p = L/\sigma = \infty$). Using this purely repulsive system he found an I-N phase transition driven by entropy, upon an increase of concentration. This finding contrasts with the more intuitive case of molecular liquid crystals, in which the attraction between molecules brings order and the entropy contributes to disorder [48].

The entropy in its simplest form ($S = k_B \ln(\Omega)$) can be seen as proportional to the logarithm of the number of configurations Ω accessible to a system. For hard interactions there is no potential energy $U = 0$, and minimizing the free energy is then equivalent to maximizing the entropy, i.e. the number of configurations.

We propose a study case to understand the effect of hard-core interactions on the entropy, which is illustrated in figure 2.1. We confine two-dimensional rods of size 1x2 into boxes. The box dimensions, of 2x2 and 3x3, aims to depict conditions at high and low concentration. We place two rods and count the number of configurations for non-interacting (ghost) rods, aligned hard rods and disordered hard rods. This cartoon aims to show two things: (1) particle-particle interactions decrease the total number of configurations due to excluded volume effects, and (2) the disordered state, which is entropically favorable at low concentrations, becomes less stable than the aligned (vertical) state at higher densities. This competition between orientational entropy and excluded volume effects is the crux of Onsager theory.

The free energy per particle for an anisotropic liquid can be split into a non-interacting rod free energy F_{id} summed up with two competing components accounting for restricted orientations

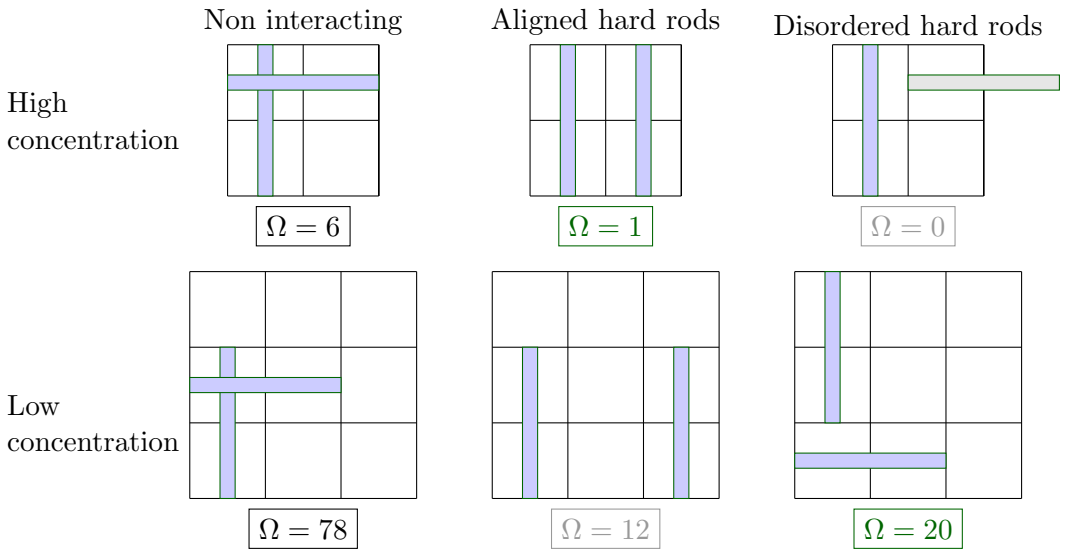


Figure 2.1: Case study of 2D rods of dimensions 1x2 confined in 2x2 (high concentration) and 3x3 (low concentration) boxes. We count the number of configurations accessible for ghost rods (left), aligned hard rods (middle) and disordered hard rods (right). Note that a symmetry argument makes vertical and horizontal states redundant in the case of aligned rods, therefore only vertical states are considered.

F_{or} and excluded volume effects $F_{packing}$:

$$\begin{aligned} F &= F_{id} \\ &+ F_{or} \\ &+ F_{packing} \ . \end{aligned}$$

For infinitely thin hard rods, it may be formulated by the following functional [12]:

$$\begin{aligned} F &= F_0 + k_B T \ln\left(4\pi \frac{N}{V}\right) \\ &+ k_B T \int f_{\vec{u}} \ln\left(f_{\vec{u}}\right) d\Omega \\ &+ \frac{1}{2} k_B T \frac{N}{V} \int\int f_{\vec{u}} f_{\vec{u}'} \beta(\vec{u}\vec{u}') d\Omega d\Omega' + O\left(\left(\frac{N}{V}\right)^2\right) \ , \end{aligned} \tag{2.39}$$

where F_0 is a constant, $\frac{N}{V}$ is the number density of rods and $f_{\vec{u}}$ is the orientation distribution function (ODF). The ODF gives the probability for a rod to point in a small solid angle $d\Omega$ around the vector $\vec{u}$; it is normalized by

$$\int_0^{4\pi} f_{\vec{u}} d\Omega = 1 \qquad \text{or} \qquad 2\pi \int_0^{\pi} f(\theta) \sin(\theta) d\theta = 1 \ , \tag{2.40}$$

given the cylindrical and inversion symmetries, and where θ denotes the angle between a rod and the nematic direction $\vec{n}$. To quantify the alignment of liquid crystals it is common to use the uniaxial nematic order parameter related to the ODF by

$$S_2 = 2\pi \int_0^{\pi} f(\theta) \frac{3\cos^2(\theta) - 1}{2} \sin(\theta) d\theta \ , \tag{2.41}$$

and generally in d dimensions

$$S_2 = \left\langle \frac{d\cos^2(\theta_i) - 1}{d-1} \right\rangle \ , \tag{2.42}$$

where $\langle\rangle$ denotes an average over all orientations θ_i relative to the nematic director. The order parameter can vary between zero in the isotropic phase, and one in a fully aligned state[2].

Coming back to expression 2.39 we want to find the ODF $f_{\vec{u}}$ that minimizes the free energy. Let us consider each term in the extreme cases where the rod orientations are isotropically distributed — $f_{\vec{u}} = \frac{1}{4\pi}$, and where they are fully aligned — $f_{\vec{u}} = \frac{\delta(1-|\cos(\theta)|)}{4\pi}$ (where δ is the Dirac function).

F_{id} does not depend on $f_{\vec{u}}$, therefore it can be ignored.

F_{or} is the free energy per rod due to restricted orientations. In the isotropic case, all orientations are equally probable, so the free energy per rod is at the minimum — $F_{or} = -k_B T \ln(4\pi)$. For a fully aligned system only one orientation is available, so the free energy penalty per rod is at the maximum — $F_{or} = 0$.

$F_{packing}$ is the free energy penalty due to particle hard-core interactions. In the case of pairwise-additive interactions, it may be split into two contributions accounting for two-body and many-body effects ($F_{packing} = F_2 + O\left(\left(\frac{N}{V}\right)^2\right)$). Onsager showed that $O\left(\left(\frac{N}{V}\right)^2\right) \to 0$ when $\frac{L}{\sigma} \to \infty$ [9]. This leaves us with the first term where $\beta(\vec{u}\vec{u}')$ is the volume excluded by a rod with the orientation $\vec{u}$ to a rod with an orientation $\vec{u}'$. The average free energy penalty per rod $F_{packing}$ is then directly proportional to the average mutual excluded volume of two particles.

For infinitely long and thin rods, the end effect can be neglected and β simply calculated (see figure 2.2):

$$\beta(\vec{u}\vec{u}') = 2L^2\sigma \left|\sin(\gamma)\right| \tag{2.43}$$

[2]In principle the S_2 can take negative values up to -0.5 when the rods are all perpendicular to the nematic director. However, the nematic director is generally defined by the rods' local average orientation and therefore $S \geq 0$.

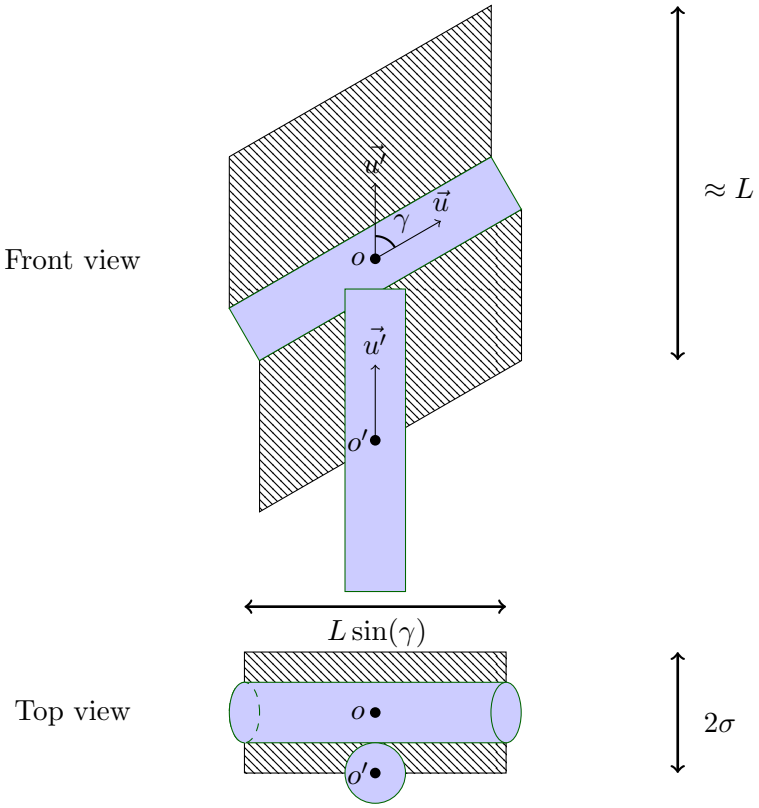


Figure 2.2: Representation of the three-dimensional volume excluded v_{excl} by one cylinder to another in the limit where $L >> \sigma$. L is the length of a cylinders, σ the diameter and γ the angle between the two cylinders' main axis. The excluded volume is $v_{excl} = 2L^2\sigma\,|\sin(\gamma)|$.

with γ the angle between $\vec{u}$ and $\vec{u}'$. In the fully aligned state $F_{packing} = 0$ and in the isotropic case

$$F_{packing} = \frac{1}{2} k_B T \frac{N}{V} \int_0^{2\pi} \int_0^{\pi} \frac{1}{4\pi} 2L^2 \sigma \sin^2(\theta) d\theta d\phi = \frac{\pi}{4} k_B T \frac{N}{V} L^2 \sigma \ .$$

We can qualitatively locate the rod volume fraction at the phase transition ϕ_{IN} by comparing the free energy of the isotropic and fully aligned cases. We expect the phase transition to occur when

$$F^{iso} = F^{aligned} \qquad \text{i.e.} \qquad \frac{\pi}{4} \frac{N}{V} L^2 \sigma - \ln(4\pi) = 0 \ .$$

Introducing the rod volume $v_0 = \pi \frac{\sigma^2}{4} L$ and and volume fraction $\phi = N \frac{v_0}{V}$, we find

$$\phi_{IN} = \ln(4\pi) \frac{\sigma}{L} \qquad \text{i.e.} \qquad \phi_{IN} \approx 2.5 \frac{\sigma}{L} \ .$$

By comparing the fully aligned and fully disordered states, we can then find the dependence of the phase transition volume fraction with the rod aspect ratio to be $\phi_{IN} \propto \frac{1}{p}$. We show below that this result is confirmed when properly solving the problem.

In order to address the problem fully, Onsager suggested a trial function [9]

$$f_o(\cos\theta) = \frac{\alpha \cosh(\alpha \cos\theta)}{4\pi \sinh \alpha}. \tag{2.44}$$

He then minimized the free energy (equation 2.39) with respect to α. Above a given concentration the free energy was found to be at the minimum for a coexistence of isotropic and nematic phases. The phase coexistence concentrations were found by equating the isotropic phase osmotic pressure and chemical potential – Π_I and μ_I, to the nematic phase osmotic pressure and chemical potential – Π_N and μ_N, via

$$\Pi = -\left(\frac{\partial F}{\partial V}\right)_{N,T,\mu_0,\mu_1,\ldots} \qquad \text{and} \qquad \mu = \left(\frac{\partial F}{\partial N}\right)_{V,T,\mu_0,\mu_1,\ldots} \tag{2.45}$$

where N, V, T and μ_i are the number of particles, volume, absolute temperature and chemical potential of the solvent components. Onsager located the volume fractions at which the isotropic phase ends, $\phi_I = 3.340 \frac{\sigma}{L}$, and where the nematic phase begins, $\phi_N = 4.486 \frac{\sigma}{L}$. From ϕ_N he

determined $\alpha = 18.58$ and from α determined $S = 0.848$.
A numerical approach *formally* minimized the free energy F (functional of $f_{\vec{u}}$) leading to a similar but more accurate result [49]:

$$\phi_I = 3.290\frac{\sigma}{L} \qquad \phi_N = 4.191\frac{\sigma}{L} \qquad S = 0.7922\ . \tag{2.46}$$

The I-N phase transition of colloidal rods is then characterized by a small jump in relative concentration $\frac{\phi_N - \phi_I}{\phi_I} \approx 0.35$ but a large jump in the order parameter S_2, from 0 in the isotropic phase to 0.8 in the strongly aligned nematic phase.

Many implementations of Onsager theory have been developed to account for different types of interactions [9, 50], different shapes [51, 52] or polydispersity [49, 53]. Other implementations have been made in order to look at the phase behavior [13], but also mechanical properties [54], interfacial properties [34, 55, 56] and the effects of confinement [57, 58]. An important implementation for us is the so-called Parsons-Lee approximation [59, 60], which adapts Onsager theory to finite aspect ratio. The Parsons-Lee approximation, shows almost perfect agreement with simulations down to an aspect ratio of five [61].

Phase behavior of hard spherocylinders

Early experimental work can be found on the phase behavior of rod-like colloids beyond the nematic phase. The smectic phase, characterized by layer formation, has been observed as early as 1927 – in a colloidal solution of akaganeite (β-FeOOH) [62] (see [63] for a review), and 1949 – in a suspension of biological viruses [64]. Theoretical descriptions first emerged in the 70s [65, 66]. However, unlike its application to the I-N phase transition, Onsager treatment for the nematic-to-smectic phase transition does not provide an exact results. For this reason, results from simulations are usually used as references to look at concentrated liquid crystals. In particular, Bolhuis and Frenkel used computational methods to describe the phase behavior of spherocylinders. The aspect ratio of a sphereocylinder is commonly described by $p = L/D$, where L is the length of the cylinder (excluding the hemispherical caps) and D is the diameter. The phase behavior was studied for aspect ratios varying from 0 (sphere) to infinity (Onsager limit) [46]; Bolhuis and Frenkel established the phase diagram reproduced in figure 2.3.

In figure 2.3, we can read the sequence of phases that spherocylinders self-assemble into,

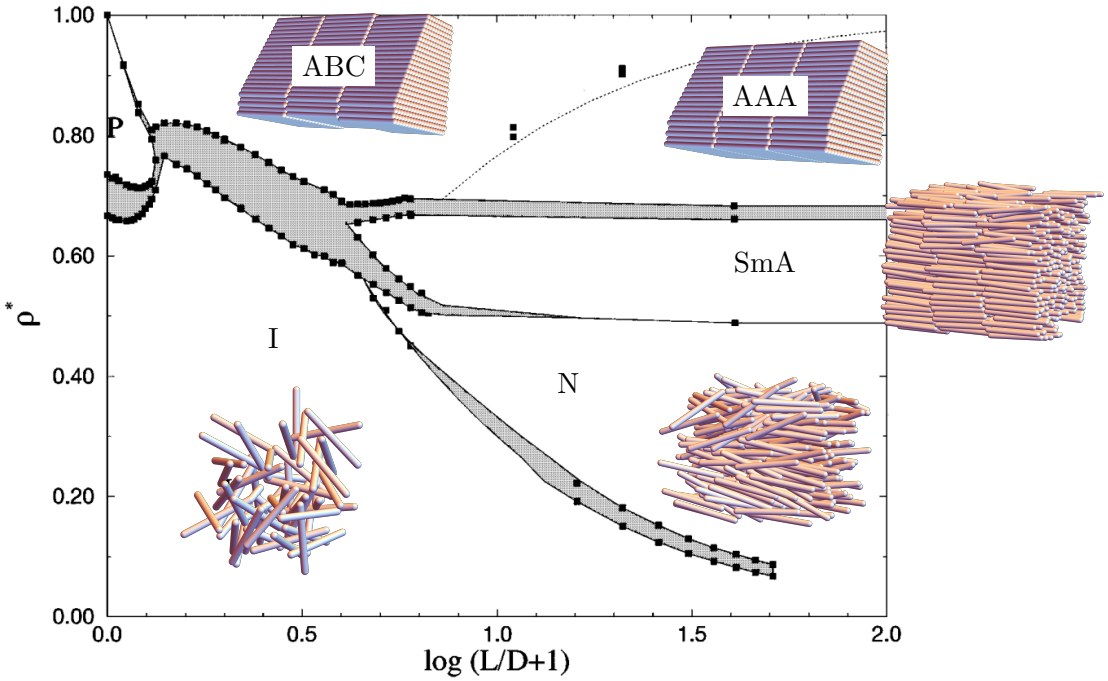


Figure 2.3: Phase behavior of spherocylinders with an aspect ratio ($p = L/\sigma \equiv L/D$) between 0 and 100, reproduced without permission from [46]. $\phi^* \equiv \rho^\star$ is the reduced density. I, N, Sm, AAA and ABC stand for isotropic, nematic, smectic-A, AAA crystal and ABC crystal.

depending on their aspect ratio and concentration. For an aspect ratio $p = 10$ ($\log(11) \approx 1$), from low to high concentrations we read the following sequence of phases: isotropic, nematic, smectic A and crystal (AAA followed by ABC). This sequence of phases is identical for higher aspect ratios. However, for aspect ratios below $p = 3.7$ ($\log(p+1) = 0.67$), no nematic phase can be formed. And similarly, below $p = 3.1$ ($\log(p+1) = 0.61$) no smectic phase can be formed. In order to study all isotropic, nematic and smectic phases, an aspect ratio higher than 5 is recommended.

Another important observation is that above $p \approx 8$ the *nematic to smectic-A* (N-SmA) and *smectic-A to crystal* (SmA-K) phase transitions seem to be independent of the aspect ratio[3]. In contrast, the I-N phase transition concentration decreases for increasing aspect ratio.

Figure 2.3 also tells us about the nature of the phase transitions. The gray areas between phases indicate coexistence regions, which imply first order phase transitions [69]. Therefore, for aspect ratios higher than eight the I-N and SmA-K phase transitions were found to be clearly first order. However, the nature of the N-SmA transition remained unclear; later work determined it as weakly first order in the limit of infinite aspect ratio [68]. The I-N, N-SmA and SmA-K phase

[3]The N-SmA phase transition concentrations have only been determined in literature as: $p \leq 5$ ($0.53 < \phi^*_{NS} < 0.55$) [46, 61, 67], $p = 40$ ($\phi^*_{NS} \approx 0.47$) [46] and $p = \infty$ ($\phi^*_{NS} \approx 0.5$) [68].

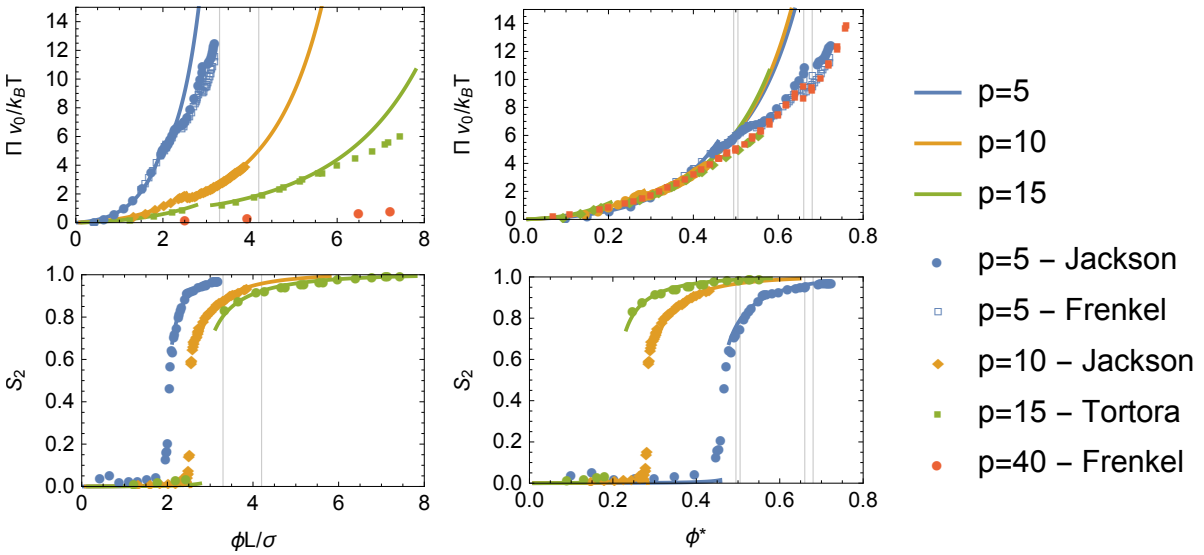


Figure 2.4: The equation of state (top row) and the nematic order parameter (bottom row) as a function of Onsager's concentration $\phi L/\sigma$ (left column) and reduced density $\phi^\star = \phi/\phi_{cp}$ (right column). It compares theoretical predictions [70] using the Parsons-Lee approximation with simulation from Tortora *et al.* [70], Frenkel *et al.* [46] and Jackson *et al.* [61, 67]. The vertical pairs of lines indicate from left to right indicate the I-N, N-SmA and SmA-K phase transitions predicted for infinite aspect ratio [49, 68].

transitions are then characterized by a jump on the corresponding order parameters. Those order parameters will be presented at the end of this section.

Simulations also provide us with the equation of state. In principle, for any aspect ratio p, the osmotic pressure Π can be calculated for all volume fractions smaller than the maximum packing fraction

$$\phi_{cp} = \frac{\pi\,(2+3p)}{6\left(\sqrt{2}+\sqrt{3p}\right)}\ . \tag{2.47}$$

There is a three-way relationship between pressure, the order parameter and volume fraction, which can be fully measured by simulations. Note that this is equally true for theories on the I-N phase transition. It is then possible to compare theories and simulations, in order to check the validity of theoretical approximations. In figure 2.4, we show all results known to us for aspect ratios $p \geq 5$ [46, 61, 67, 70]. We compare Monte-Carlo simulations with Onsager theory incorporating the Parsons-Lee approximation. The order parameter (S_2) and the scaled pressure $\Pi v_0/(k_B T)$ are plotted against concentration. The concentration is expressed in two different ways: Onsager concentration $\phi L/\sigma$ relevant for the I-N transition, and reduced density $\phi^\star = \phi/\phi_{cp}$ relevant for the N-SmA and SmA-K transitions. We observe a good agreement between simulations and theory for all the aspect ratios $p \geq 5$ and $\phi^* < 40\%$.

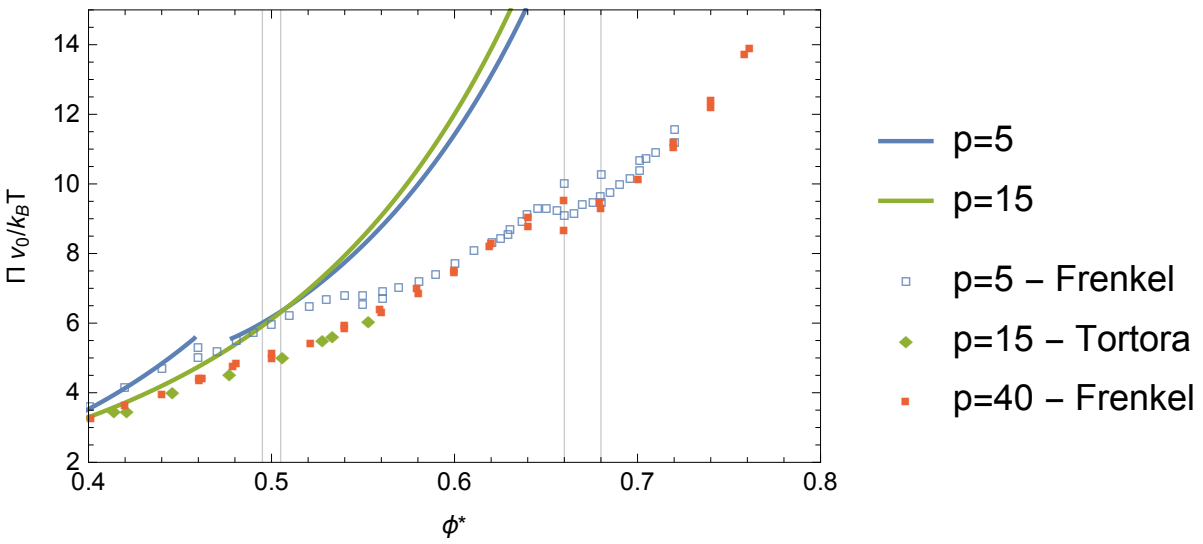


Figure 2.5: Equation of state versus reduced density $\phi^\star = \phi/\phi_{cp}$. Zoom on densities $0.4 < \phi^\star < 0.8$.

Interestingly, the equation of state $\Pi(\phi^\star)$, approaching the SmA-K phase transition (pair of vertical lines around $\phi^* = 0.67$), seems very similar for the aspect ratios $p = 5$ and $p = 40$. This can be observed in figure 2.5. So, at high densities and when the volume fraction is scaled by the maximum packing fraction, not only does the phase behavior seems independent of the aspect ratio, but the equation of state too.

We will now briefly introduce the phase transitions. *The I-N phase transition* is first order. It induces long range orientational order. The transition volume fraction depends on concentration and aspect ratio. In the limit where $p \to \infty$,

$$3.3p^{-1} < \phi_{IN} < 4.2p^{-1} \ . \tag{2.48}$$

The order parameter is the nematic order parameter described previously; in d dimensions

$$S_2 = \left\langle \frac{d\cos^2(\theta_i) - 1}{d-1} \right\rangle \ . \tag{2.49}$$

The N-SmA phase transition is weakly first order [68]. It induces one-dimension positional ordering. The orientational order is maintained and additionally the rods form layers along the nematic director. Within those layers (perpendicular to the nematic director) there is no positional order. The coexistence concentration range has not been clearly determined for aspect ratio p higher than five. However, the transition does not depend much on the aspect ratio,

and even less so if we normalize the volume fraction by volume fraction at close packing ϕ_{cp} (equation 2.47). [46, 68]. For high aspect ratio it is found that

$$\phi^{\star}_{NS} \approx 0.5 \ . \tag{2.50}$$

The smectic order parameter is defined in [68] by the magnitude of the Fourier component of the normalized density along the director $\hat{n} = \hat{x}$:

$$\tau = \frac{1}{N} \left| \sum_{j=1}^{N} \exp\left(i k_{\mathrm{x}}\, x_j\right) \right| \ , \tag{2.51}$$

where x_j is the x coordinate of the center of mass of the jth spherocylinder and $k_{\mathrm{x}} = 2\pi/\lambda_{sm}$ with λ_{sm} being the periodicity of the smectic layers.

The SmA-K phase transition is first order. It induces additional positional ordering within and in between the layers. Again, above an aspect ratio of $p \approx 5$ the transition does not depend much on the aspect ratio [46, 61]. For $p > 10$ it is found that

$$0.66 < \phi^{*}_{SK} < 0.68 \ . \tag{2.52}$$

The hexagonal order within the layer can be estimated using the bond orientational order parameter ψ_6, commonly used to describe 2D crystals of hard disks [71, 72]. The order parameter is given by the absolute value of the sixth Fourier component of the bond angle distribution function

$$\Psi_6 = \left| \frac{1}{N_{bond}} \sum_{j} \sum_{k} \exp\left(i 6 \phi_{jk}\right) \right| \ , \tag{2.53}$$

with ϕ_{jk} the angle between the bond connecting j and k and a fixed reference axis, and where N_{bond} is the number of bonds in the system.

2.1.3 Colloid interactions

In section 2.1.2, we considered hard interactions between particles. Here we introduce a more realistic potential for charged colloids: the Derjarguin-Landau-Verwey-Overbeek (DLVO) potential. We highlight the effect of salt concentration on the stability of colloids.

DLVO potential

Particle-particle interactions are generally described in terms of energy by use of the pair potential U. The pair potential is a function of the relative position $\vec{r}$ of the particles and, in case of rods, their orientations $\vec{u_1}$ and $\vec{u_2}$. The form of the potential will depend of the type on interaction. But for charged colloids it is common to use the DLVO potential [73, 74]. The DLVO potential splits into two parts: the van der Waals potential U_{vdW} and the double layer potential U_{el}.

$$U_{DLVO}(\vec{r}, \vec{u_1}, \vec{u_2}) = U_{vdW}(\vec{r}, \vec{u_1}, \vec{u_2}) + U_{el}(\vec{r}, \vec{u_1}, \vec{u_2}) \tag{2.54}$$

The full expressions of U_{vdW} and U_{el} for rods can be found in [75].
The van der Waals potential U_{vdW} accounts for molecular pairwise $-1/r^6$ potentials. It is consequently long range and, for colloids made of the same material, always attractive. Its strength is given by the Hamaker constant A, which mainly depends on the dielectric constant ϵ and the mismatch between the particle's and medium's visible light refractive indices n_p and n_m. The Hamaker constant reads:

$$A = \frac{3}{4} k_B T \left(\frac{\epsilon_p - \epsilon_m}{\epsilon_p + \epsilon_m} \right)^2 + \frac{3h \langle \nu_e \rangle}{16\sqrt{2}} \frac{\left(n_p^2 - n_m^2\right)^2}{\left(n_p^2 + n_m^2\right)^{3/2}} \tag{2.55}$$

with k_B Boltzmann constant, h the Plank constant and $\langle \nu_e \rangle$ the mean electronic vibration frequency of the particle and the medium.
The double layer potential follows from Debye-Hückel theory. For two isolated point charges of charge q into a medium the electrostatic potential reads:

$$U(r) = \frac{q^2}{4\pi\epsilon_0\epsilon_m r} \quad , \tag{2.56}$$

where ϵ_0 is the vaccum dielectric permittivity. However, for a charged colloidal particle the problem becomes more difficult. • Colloids get charged by dissociation of terminal group which releases counter ions in the solvent. These charges along with other charges already present in the solvent will form a screening cloud. This many body problem can be addressed using the mean field Poisson-Boltzmann theory. The particular case of spherical colloids is treated by

Debye-Hückel theory and leads to a potential decaying exponentially [74, 76]:

$$U_{el} \propto Z^2 \exp\left(-\frac{r}{\lambda_D}\right) \quad . \tag{2.57}$$

The range of the interaction is set by the Debye length λ_D, which increases with the dielectric constant of the medium ϵ_m and decreases with concentration of ions n_j of charge q_j:

$$\lambda_D = \kappa^{-1} = \left(\frac{\epsilon_0 \epsilon_m k_B T}{\Sigma_{j=1}^{N} n_j q_j^2}\right)^{\frac{1}{2}} \tag{2.58}$$

The inverse Debye screening length is sometimes given as

$$\kappa = (8\pi\lambda_B I)^{-\frac{1}{2}} \; ; \; \lambda_B = \frac{e^2}{4\pi\epsilon_0\epsilon_m k_B T}, \; I = \frac{1}{2}\Sigma_{j=1}^{N} n_j q_j^2, \tag{2.59}$$

where λ_B is the Bjerrum length and I the ionic strength. In water, at ambient temperature, $\lambda_B \approx 0.7\,\mathrm{nm}$.

The stability against aggregation is then a balance between the van der Waals attraction and double layer repulsion. The presence of salt will favor aggregation whereas refractive index matching will increase stability. An appearance of this is found at river deltas, when clear water meets salty water, colloidal suspensions are destabilized by the increase of salt, so they sediment, clog the river and spread across the riverbed forming the well known deltas.

Solvation

In some cases, further interactions have to be considered in order to accurately characterize particle interactions. Such an example is solvation, which is due to a strong attraction between solvent molecules and a colloidal surface. It induces a molecular ranged repulsive potential between colloids competing against the van der Waals attraction.

2.1.4 Elasticities of mesophases

The crystalline nature of mesophases can be described through elasticities. Each mesophase will match to a given ground state, where the energy is minimal. Continuous deviations from this

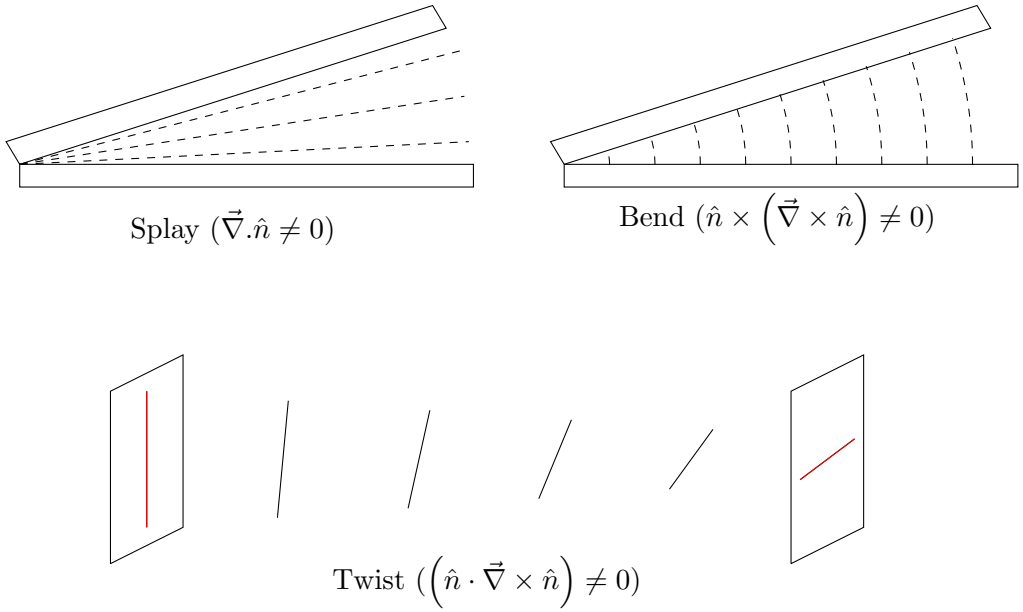


Figure 2.6: Three types of nematic deformations. Rectangles represent container walls and lines the nematic director $\hat{n}$.

ground state due to thermal fluctuations or external fields will lead to an increase of the free energy proportional to elastic constants. We will first consider the nematic phase, followed by the smectic phase.

Nematic phase

In a nematic single crystal in the ground state, particles share a common average orientation called the nematic director $\hat{n}$. Weak deformations will lead to distortion of the vector field $\hat{n}(\vec{r})$ at a much larger scale than the individual particle. In this context, continuum theory that only considers the vector field can be used [12].

The Frank-Oseen formulation of the distortion free energy of a nematic phase reads:

$$F_d = \frac{1}{2}K_1\left(\vec{\nabla}\cdot\hat{n}\right)^2 + \frac{1}{2}K_2\left(\hat{n}\cdot\vec{\nabla}\times\hat{n}\right)^2 + \frac{1}{2}K_3\left(\hat{n}\times\left(\vec{\nabla}\times\hat{n}\right)\right)^2, \tag{2.60}$$

where $K1$, $K2$ and $K3$ are the splay, twist and bend elastic constants corresponding to the three deformations illustrated in figure 2.6. In general $K_3 > K1 \approx K_2$. For example, hard rods with $p = \frac{L}{\sigma} = 10$ and $\phi = 35\%$ have elastics constants estimated to be $K1 \approx 1.2\frac{k_BT}{\sigma}$, $K_2 = 0.5\frac{k_BT}{\sigma}$ and $K_3 = 15\frac{k_BT}{\sigma}$ [77].

Despite these differences, the one constant approximation $K_1 = K_2 = K_3 \equiv K$ is a convenient

approximation to solve problems as the free energy reduces to:

$$F_{d0} = \frac{1}{2}K\left(\left(\vec{\nabla}\cdot\hat{n}\right)^2 + \left(\vec{\nabla}\times\hat{n}\right)^2\right). \tag{2.61}$$

Smectic A phase

The "poor man's" elasticity model sees the smectic ground state as a lattice. The layers are laying in the (x, y) plane and the particles align along the z-axis. Again, the liquid crystal is modeled as being continuous. Displacements from this lattice at each point (x, y, z) are given by the one-dimensional displacement field u. The free energy of the smectic is then expressed as:

$$F_s = \frac{C}{2}\int d^2x\left[\left(\vec{\nabla}_z u\right)^2 + \lambda_p^2\left(\vec{\nabla}_\perp^2 u\right)^2\right], \tag{2.62}$$

where C is an elastic modulus, $\vec{\nabla}_z = \left(0, 0, \frac{\partial}{\partial z}\right)$ and $\vec{\nabla}_\perp^2 = \left(\frac{\partial^2}{\partial x^2}, \frac{\partial^2}{\partial y^2}, 0\right)$. The first and second terms of the expression account for the layer's dilation and curvature; λ_p is the penetration length, the length scale over which curvature is comparable to compression.

2.1.5 Defects in mesophases

Defects are observed in all crystalline structures. They correspond to a discontinuous change in the positional or orientational order.

Disclination

All defects characterized by discontinuity in orientation are refered to as disclinations. Therefore, all defects in nematics are disclinations. They can appear as a point, a line or a sheet, where the nematic director $\vec{n}$ varies abruptly or is undefined. Note that sheets will be unstable [12].

By observing the nematic director around a defect core, the defect's type can be identified. In figure 2.7 we show how to measure the sign and strength of a defect.

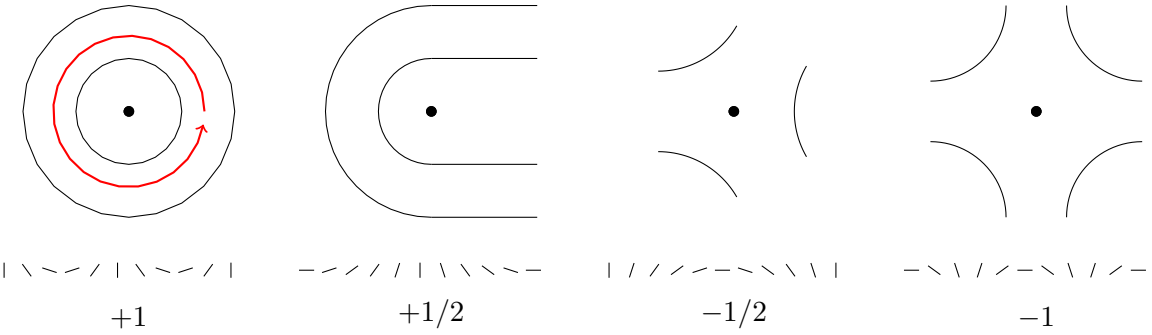


Figure 2.7: Core structures in nematic LCs, determination of sign and strength of 4 types of defects. The first row shows defect structures; bullet points indicate disclination cores and lines follow the nematic director $\vec{n}$. The second row shows the evolution of $\vec{n}$ when rotating anticlockwise around the core (red arrow). The final row gives the sign and strength of the defect. The sign is positive if $\vec{n}$ rotates in the same direction as the red arrow. The strength is the director number of full (2π) rotations.

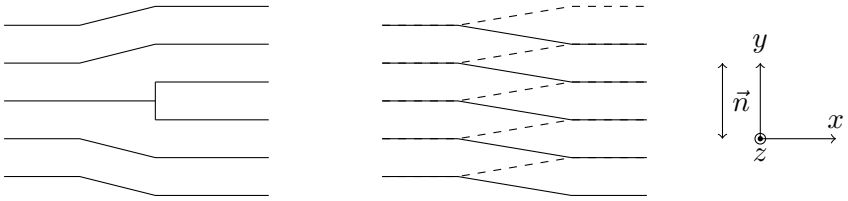


Figure 2.8: Dislocations in the smectic phase. The full and dashed lines indicates the space between two adjacent layers in and out of focus.

Dislocation

Dislocations are discontinuities in positional order. Therefore, they cannot exist in the nematic phase. In the smectic phase, we observe two kinds of dislocations: edge and screw. We represent these two dislocations in figure 2.8. Edge dislocations are two-dimensional; they are characterized by the insertion of one or many layers. Screw dislocations are three-dimensional, they cannot be observed in two dimensions. They are formed when adjacent layers are shifted by one layer spacing in the direction parallel to the nematic director, and thus only on one side of the dislocation core.

2.2 Experimental methods

We combine in this work many ingredients in order to observe rods directly and at the single particle level. The most important of which is the dispersion of rods itself. We will first justify the use of silica rods and detail the synthesis method. We will then explain further experimental

Type	Particle	Length [μm]	Diameter [nm]	Aspect ratio	Phases
Mineral rods	iron (hydr)oxide [83]	0.2-0.7	60-130	4-8	I-S
	Selenium [83]	0.82	230	3.5	I-S
	Nickel [83]	2-6	100-300	10-35	I-N-S
	Silica [37]	0.2-10	200-2000	1-25	I-N-S
Polymeric rods	PMMA Ellipsoids [84, 85]	2-10	≈600	1-12	I-N
	SU8 [86]	1-100	200-1000	1-100	I-N
Viruses	fd [87]	≈ 1	10	100	I-N-S
	TMV [88]	0.28	15	20	I-N-S

Table 2.1: Selection of micrometric rod systems. I, N and S stand for isotropic, nematic and smectic.

methods about the observation cells' fabrication, video-microscopy and image analysis.

2.2.1 Colloidal rods

Our colloidal system need to fulfill the following requirements.

First, the length of the particles needs to reach the micron scale in order to determine its position and orientation by microscopy techniques. However, this is only enough to detect tracer particles. To have a chance to observe every single particle their diameters need to exceed 400 nm [78].

We also have prerequisites about the aspect ratio and polydispersity of the particles, in order to form nematic and smectic phases. Polydispersity suppresses the smectic phase [79–82] and low aspect ratios suppress the nematic phase [46]. We then need a standard deviation of the length distribution $s_L < 30\% \langle L \rangle$ (see footnote[4]) and an aspect ratio $p > 5$ [46], preferably $p > 10$ to have a comfortably large nematic region.

A third important parameter is the difference of refractive index between solvent and particles Δn. Three-dimensional confocal microscopy imaging can only be achieved in good conditions if $\Delta n = 0$.

In table 2.1, we give the main characteristics of a selection of rods that have been observed by optical microscopy. We report three types of rods. The polymeric rods are very good systems for confocal microscopy. However, such systems have not yet been able to form all isotropic, nematic and smectic phases, presumably due to polydispersity or shape. Moreover the PMMA ellipsoid fabrication process requires special tools and the SU8 system [86] was not known at the beginning of my PhD.

The viral rods are a very good match for our experiment: they form a good system of hard

[4] Approximation for parallel infinitely thin rods from [79]

rods, self-assemble into all desired phases and are ideal for confocal microscopy. However, their diameter is very small; consequently, only tracer particles can be observed.
Among the mineral rods, the nickel and silica cover the right range of aspect ratios. Their diameter is large enough so that all single particles can be observed (at least in 2D). However, the nickel rods do not fit requirements to be observed by confocal microscopy, contrary to silica, making silica rods our system of choice.

Silica rod synthesis

The silica rod system has been developed by the Utrecht soft condensed matter group. They have studied in detail the synthesis [37], characterization & labelling [89] as well as the phase behavior [90].
The simple one pot synthesis is performed in two steps. The first step aims to form an emulsion of a water rich phase in pentanol. This is achieved by adding the right proportions of reagents to the pentanol. These are polyvinylpyrrolidone, water, sodium citrate, ammonia and ethanol. After this step, tetraethylorthosilicate (TEOS) is added to the mixture. After migration through the pentanol, TEOS hydrolyses and condenses into silica when it reaches the water rich droplet. The silica then grows into a hemisphere pushing the water away, which then forms a mirror hemisphere. At this point, the anisotropic supply of hydrolyzed TEOS leads to a unidirectional growth transforming the hemispheric silica structure into bullet shaped particles.

The rod diameter of the particle is largely set by the initial droplet size and varies from around 200 to 300 nm. However, the length can be tuned from one diameter to a few micrometers. The density has been found to be around $\rho = 1900\,\mathrm{kg\,m^{-3}}$ and the refractive index $n \approx 1.45$ [89].
Rods can be labeled immediately with fluorescence by adding fluorescent molecules to the mixture. Note that this method results in a non-uniform fluorescence signal across the rod. Alternatively, extra layers of silica can be added with or without florescence. This powerful core-shell synthesis has been employed in [91]. The authors could detect, via 3D confocal microscopy, every single rod's position and orientation. The drawback of coating extra layers is that it decreases the extent of the nematic phase. This happens in two ways: first by reducing the aspect ratio there is a reduction in the nematic concentration region (see section 2.1.2 or [46]); second

Name	Pentanol [mL]	PVP [g]	Water [mL]	Sodium Citrate[1] [mL]	Ethanol [mL]	Ammonia[1] [mL]	TEOS [mL]	RITC[1] [mL]
LC010	100	*5*	*3*	0.6	9	*2.200*	0.9	*0.8345*
LC011	100	10	*2.9*	*0.4*	9	2.025	0.9	*0.8345*
LC012	100	10	2.7	0.6	9	2.025	0.9	0
LC017	1200	120	32.4	7.2	*128*	24.3	10.8+*5.4*	0

Table 2.2: Amount of chemical used for each synthesis. Element annotated 1 are solutions, for example 'sodium citrate solution' (see text for details). Emphasis is used to indicate when the proportion of one component differs from the synthesis LC012. The symbol + indicates addition in an extra step (see text).

by increasing the particle's volume the gravitational length is reduced [92]. We will show in chapter 3 that gravity has a strong effect on the behavior of silica rods. As a result, the nematic phase formed by core shell particles with short aspect ratio (p=5) and small gravitational length ($l_g = 550\,\text{nm}$) is hardly observable [93].

In order to observe a nematic phase we want the rods as thin as possible. Consequently, we do not proceed to additional growth steps. All rods are synthesized in one step. We produced four batches of particles. Two batches of fluorescent (LC010 and LC011) and non-fluorescent (LC012 and LC017) rods attempting to match the sizes. This method is generally robust; however, addition of dye or up scaling the synthesis can slightly affect the rods dimensions. We describe below the methods used to synthesize the batch LC017.
In a two liter container, full dissolution of 120 g of polyvinylpyrrolidone (PVP40 Sigma-Aldrich) into 1.2 L of 1-pentanol (138975 Sigma-Aldrich) was obtained after 3 h in a sonication bath. As a next step, 32.4 mL of deionized water (Milli-Q), 7.2 mL of sodium citrate at 0.18 M in water (S4641 Sigma-Aldrich) and 128 mL of ethanol (32221 Sigma-Aldrich) were added to the solution. This was then shaken in a steady circular motion for 100 s. A final addition of 24.3 mL of ammonium hydroxide solution (09861 Fluka Sigma-Aldrich) and 10.8 mL of tetraethyleorthosilicate (157811000 Fisher Scientific) was performed. The solution was shaken again for 40 s, and left for 4 h. Following this, 5.4 mL of tetraethyleorthosilicate were added; the solution was shaken for 10 s and left for 15 h.

The fluorescent rods LC010 were synthesized by using the same protocol with a slightly different recipe. The amount of chemicals was the following: PVP 5 g, pentanol 113 g, water 3 mL, sodium citrate 0.6 mL, ethanol 9 mL, ammonia 2.2 mL, TEOS 0.9 mL. In addition, as an extra-step, 834 µL of dying agent solution was added, and the mixture shaken for 15 s. The dying solution was made up of 5 mL of ethanol (32221 Sigma-Aldrich), 35.5 mg of rhodamine b

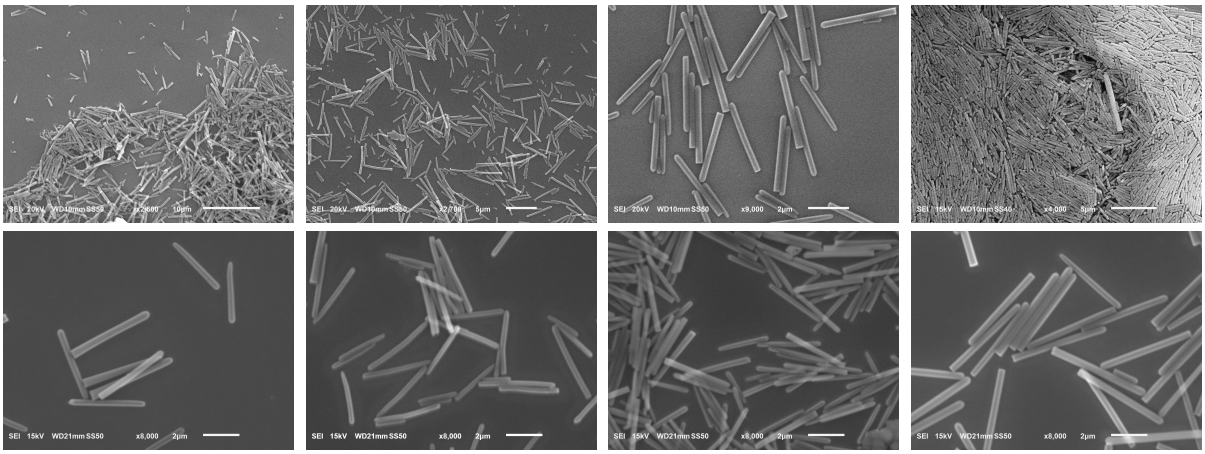
		Ab.	LC017	LC010	LC012	LC011
Length	[µm]	L	$5.26 \pm 8\%$	$4.1 \pm 15\%$	$2.7 \pm 28\%$	$2.7 \pm 35\%$
Diameter	[µm]	σ	$0.39 \pm 14\%$	$0.38 \pm 14\%$	$0.28 \pm 9\%$	$0.25 \pm 14\%$
Aspect ratio		p	$12.6 \pm 8\%$	$9.8 \pm 10\%$	$8.5 \pm 25\%$	$9.6 \pm 28\%$
l_g in water	[µm]	l_g	$0.80 \pm 30\%$	$1.19 \pm 80\%$	$3.3 \pm 57\%$	$4.7 \pm 60\%$
Number of particle		N	145	117	284	132
Surface	[µm^2]	S	$6.53 \pm 20\%$	$5.0 \pm 28\%$	$2.48 \pm 36\%$	$2.13 \pm 50\%$
Volume	[µm^3]	v_0	$0.66 \pm 40\%$	$0.49 \pm 42\%$	$0.18 \pm 44\%$	0.14 ± 73

Table 2.3: Silica rods properties after the sorting step. Measurements have been performed on scanning electron microscope images (see section 2.2.4). The signs ± indicate polydispersity as the standard deviation divided by the mean value.

isothiocyanate (283924 Aldrich) and 35 µL of (3-aminopropyl)triethoxysilane (741442 Aldrich). This was stirred overnight.

After the synthesis, the suspensions were cleaned. As a first cleaning step, the rods were centrifuged for 70 min at $2400g$. As a second step, the sediments were collected, dispersed into ethanol and centrifuged again at $2000g$ for 20 min. This second step was repeated 8 times; from the third to the fifth time, particles were dispersed in water instead of ethanol.

In table 2.2, we give the recipe used for each of the batches. Apart from the RITC solution that is optional, all other ingredients are essential to the formation of straight rods. If their amount is excessively reduced or increased, spherical or curly rods will be produced [37]. We use the recipe for LC012 as a reference. Each alteration is based on additional materials in [37]. Most changes have been made in order to produce longer particles. For the rods LC010, the PVP amount has been reduced to obtain longer rods, and at the same time water and ammonia content has been increased to avoid the curly rod region. RITC has been added to produce fluorescent particles. LC011 has a similar strategy to LC010 but the amount of sodium citrate has been reduced instead of PVP and ammonia, which have been kept unchanged. For LC017, the synthesis has been up-scaled to produce more particles and in order to counter balance the up-scaling effect (making rods thicker and shorter) the amount of ethanol has been increased. To make particles longer, additional TEOS has been added.



(LC010) (LC011) (LC012) (LC017)

Figure 2.9: Scanning electron microscopy snapshots of rods after cleaning (first row) and after sorting (second row).

Results

The results of the synthesis are analyzed by Scanning Electron Microscopy (SEM) offering better resolution than optical microscopy[5], which is limited by the wavelength of light. In figure 2.9, we show snapshots from different syntheses after cleaning and sorting. We can appreciate from these snapshots that by trying to increase the particle aspect ratio, we have introduced a lot of polydispersity (synthesis LC010, LC011 and LC017). To remove the largest rods centrifugation at 250g for 5 minutes was performed, keeping the supernatants. Normal sedimentation was then used to isolate the longer rods, and thus reduce the polydispersity. The rods' length and area are measured from SEM images (see section 2.2.4 and figure 2.15). From the end-to-end length L and the area A we obtain: the diameter $\sigma = A/L$, the aspect ratio $p = (L-\sigma)/\sigma$, the surface $S = \pi A$, the volume $v_0 = \frac{\pi}{4}\sigma A$ and the gravitational length in water $l_g = \frac{\Delta\rho v_0 g}{k_B T}$. The final rod properties are listed in table 2.3.

We have not performed further characterization of the rods. However, we know from [89] that the density of silica rods is about $\rho_r \approx 1900\,\mathrm{kg\,m^{-3}}$ and the refractive index $n \approx 1.45$. It is also important to note that our fluorescent labeling method does not spread the dye evenly on the rods. Because the fluorescent signal is stronger on one side the rods, they resemble tadpoles on fluorescent microscopy images (example figure 2.11 (c) and (d)).

[5]Exploiting the duality wave-particle, the (de Broglie) wavelength of an electron can conveniently be expressed as $\lambda = \frac{hc}{pc}$, with $hc \approx 1.2\,\mathrm{keV\,nm}$ and pc is an energy in (keV). Typically electrons with a kinetic energy of 10 keV have a wavelength of 0.1 nm well below the optical wavelength ($\lambda \approx 500\,\mathrm{nm}$).

2.2.2 Sample preparation

In order to be observed, rods are suspended in a solvent and confined into a glass cell. The types of cells used are presented in this section. We will start with the most sophisticated ones made using soft lithography techniques.

Soft lithography

Soft photolithography is a technique that combines use of a photo-polymer and a silicone elastomer in order to produce micrometric structures. Any two-dimensional pattern printed on a mask can then be translated into a three-dimensional structure with tunable thickness, typically from one to one hundred of micrometers. Replication of the structure can be then molded at a cheap cost using PDMS.
This technique is commonly used to fabricate microfluidic devices that control flow at the micron scale. Advantages include ability to: (1) probe systems over four orders of magnitude with channel sizes ranging from a micron to a centimeter, (2) integrate complex chemical physical and biological functions, and (3) parallelize experiments, opening the doors on better statistical analysis. Within this work, we do not use flow or complex functions: soft lithography is simply used to fabricate confinement chambers with sizes comparable to the particle's length. The versatility of the method allows us to study a wide range of sizes and provide us with more statistical evidence. In particular, this is a way to probe the behavior of complex fluids below the mesoscopic scale [94].

We use a three step protocol to fabricate our cells. A primary structure is made of SU8 following manufacturer directives [95]. From this, a negative PDMS stamp is molded. Finally, this stamp is used to mold a UV-glue channel on a coverslip. Fabrication steps and parameters depend on the desired features thickness. An example for 10 µm thick structures is detailed figure 2.10.
Note that it is also possible to make a cell directly out of SU-8 or PDMS [96]. We also would like to emphasize a few points. First, the fabrication process was carried on in a *clean room* to avoid presence of dust. Second, silicon wafers were heated up before spin coating to eliminate potential moisture. Third, we used a *chrome mask* with high printing resolution and a UV filter in order to make a structure of a few microns. Finally, adhesion between the coverslip and

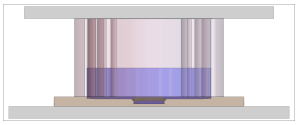
Step one: SU-8 structure	
	5 mL of SU-8 2015 is pored at the center of a 10 cm silicon wafer and **spin coated** at 500 rpm for 15 s and 1500 rpm for 30 s. The wafer is then pre-**baked** at 95 °C for 2 min 30 s.
	SU-8 not covered by the photomask is **exposed** to UV-light ($\approx 120\,\mathrm{mJ\,cm^{-2}}$) and the wafer is **baked again.**
	Unexposed SU-8 is **disolved** by dipping the wafer into propylene glycol monoethyl ether acetate for 2 min 30 s.
Step two: PDMS stamp	
	The silicon wafer with SU-8 structures is covered with a 1:10 reticulant-elastomer sylgar 184 mixture using tape to prevent spillage. Air bubbles are removed under vacuum and the PDMS is solidified overnight in an oven at 75 °C.
Step three: UV-glue cells	
	The PDMS stamp is detached and cut to select desired features. NOA81 fast curing UV-glue is dropped on the PDMS stamp.
	Air bubbles are vacuumed out, the glue is covered by an hydrophobic coverslip and exposed to UV light ($\approx 50\,\mathrm{mJ\,cm^{-2}}$) (so that it becomes solid-like but remains sticky).
	The UV-glue patterned surface is now bonded to the coverglass and free from the PDMS.
	A Teflon tube is glued (NOA-81, exposure $\approx 280\,\mathrm{mJ\,cm^{-2}}$) around the UV-glue structure to form a reservoir.
	The reservoir can finally be filled with a suspension of particles and closed with a second coverslip to prevent evaporation.

Figure 2.10: Fabrication of UV-glue reservoir cells.

UV-glue was improved by silanizing coverslips with hexamethyldisilazane.

Types of cells

Three types of cell are used in this thesis: the reservoir cell presented in figure 2.10, capillaries and home made channel also made by soft lithography techniques.

2.2.3 Video-microscopy

We use three microscopy techniques to observe our colloidal liquid crystals: bright field (BF), epi-fluorescence and confocal microscopy. We choose one technique over the other depending on the sample nature and required resolutions.

In bright field microscopy, collimated light is focused onto the sample's region of interest. This region is then imaged with an objective and captured on camera. Micrometric colloids are observable by BF microscopy as long as they diffract light, i.e. as long as their refractive index differs from the solvent's. The contrast of the method mainly depends on this refractive index mismatch. The optimum optical spatial resolutions in the x-, y- and z-dimension can be approximated by

$$R_{x,y} = \frac{1.22\lambda}{NA(\text{obj}) + NA(\text{cond})} \qquad \text{and} \qquad R_z = \frac{2\lambda}{NA(\text{obj})^2} \text{ [97].} \tag{2.63}$$

They depend on the objective and condenser numerical apertures (NA(obj) and NA(cond)) and the light wavelength λ. Note that the resolution of the image P_r in 'μm pixel^{-1}' need to be smaller (i.e. better) than the optical resolution, this can be written $P_r < 1R_{x,y}$ pixel^{-1}.
In our experiments, we use an Olympus IX73 microscope with a 1.42 NA 60x oil immersion objective. Images are captured by a Ximea CMOS xiQ with a resolution of 2048$\times$2048 pixels^2. The minimum time resolution is about 10ms.

In epi-fluorescence microscopy, the objective also plays the role of condenser: it is used to excite sample's fluorescent molecules and collect their fluorescence, which is filtered and recorded on camera. This technique can only image fluorescent particles. However, it does not need refractive index mismatch, it is even encouraged to index match the particles with the solvent. Index matching allows a reduction of scattering effects, which improves the contrast, in particular when looking deep (>10 µm) into a dense sample ($\phi > 10\%$).
We use the same microscope, objective and camera for BF and fluorescence microscopy. The lighting is performed by a *coolLED pE-300* system from Olympus with a wavelength of excitation: $\lambda_{exc} \approx$270 nm.

Confocal microscopy also requires fluorescent particles and uses a single objective for excitation and collection purposes. A confocal microscope differs from a fluorescence microscope

Technique	Objectve magnification	Objectve NA	Condenser NA	Mean excitation wavelength [nm]	$R_{x,y}$ [nm]	R_z [nm]	P_r [nm/pixel]
Bright Field	10x	0.25	0.55	≈550	900	17000	546
Bright Field	60x	1.42	0.55	≈550	340	545	91
Fluorescence	60x	1.42	1.42	≈ 570	245	545	91
Thorlab confocal	60x	1.42	1.42	532	150	370	∅
Zeiss confocal	60x	1.4	1.4	532	150	370	∅

Table 2.4: Resolutions provided by our microscopy techniques in ideal conditions.

by its pinhole, which is placed at the back focal place of the objective. This pinhole blocks any light that is not going to or coming from the focal point. In other words, the sample is only illuminated at one spot and the light is only collected from that same spot. In order to form an image, a confocal microscope needs to measure intensity point by point and reconstructs a pseudo-image from the points. For laser scanning confocal microscopes (LSCM), this is achieved using two fast moving mirrors. This technique is slower than fluorescence but it offers a slightly better resolution [78]:

$$R_{x,y} = \frac{0.8\lambda}{2NA(\text{obj})} \tag{2.64}$$

$$R_z = \frac{1.4\lambda}{NA(\text{obj})^2} \tag{2.65}$$

Nevertheless, more so than the resolution, the ability to section the sample in the z-direction results in a better contrast and the possibility to form three-dimensional images. The typical time resolution for recent LSCM and for a 2048×2048 pixel^2 image is 300 ms. However, a 512×512 image can be scanned in 17 ms. We use two LSCMs: an Olympus microscope upgraded with Thorlab confocal system and a Zeiss confocal microscope that can be rotated by 90° in order to observe samples from the side.

We sum up the main characteristics of each technique in table 2.4.

2.2.4 Image analysis

Prior to analysis some images are filtered and often binarized. We will first explain our filtering and binarization methods giving concrete examples. We will then present our particle and layer detection methods.

All image analysis and treatments are either performed with the program ImageJ or Wol-

fram Mathematica. We will refer in this section to functions that are embedded in Mathematica.

Filtering

Filtering is used to bring out desirable features of an image by reducing what is considered as noise. A common one is the *Gaussian* filter that averages the intensity of neighboring pixels, an efficient way to reduce noise. However, it tends to reduces the aspect ratio of elongated objects. This problem can be overcome by using the so-called *FourierDCTFilter* (integrated in Mathematica). This high-pass filter 'locally thresholds the discrete cosine transform (DCT) of overlapping sub-images'.

We employ these two filters on a series of snapshots in figure 2.11 so they can be compared to raw images. The rows (a) and (b) are BF snapshots of LC017 rods in a smectic phase. The rectangle in (b) has dimensions $15\times25\,\mu m^2$, and is observed with a 60x magnification objective that can resolve single rods. The square in (a) ($100\times100\,\mu m^2$) is observed with a 10x objective that can only resolve the smectic layers. Rows (c) and (d) show 60x confocal microscopy images of LC010 fluorescent rods in a background of LC017. The signal-noise ratio difference is due to different aperture time about 2 s for (c) and 0.02 s for (d).

The use of a filter is not always relevant. For example in (b) and (c), little improvement is observed. However, for the very noisy image (d) both filters seem to improve the contrast. As mentioned before, among this two we prefer the DCT filter as it better preserves the rod-like shape.

Binarization

Binarization is used to isolate components that will later be measured. We compare two binarization methods a standard method that applies a unique intensity threshold and a more elaborate method that locally adapts it. This second method is an integrated function in Mathematica called 'LocalAdaptativeBinarize' (LAB).

These two methods are applied to the collection of images introduced in the previous section. The results are displayed in figure 2.12. From the rows (a) and (b) we can clearly see the benefits of using LAB over its simpler counterpart. By locally adjusting the binarization

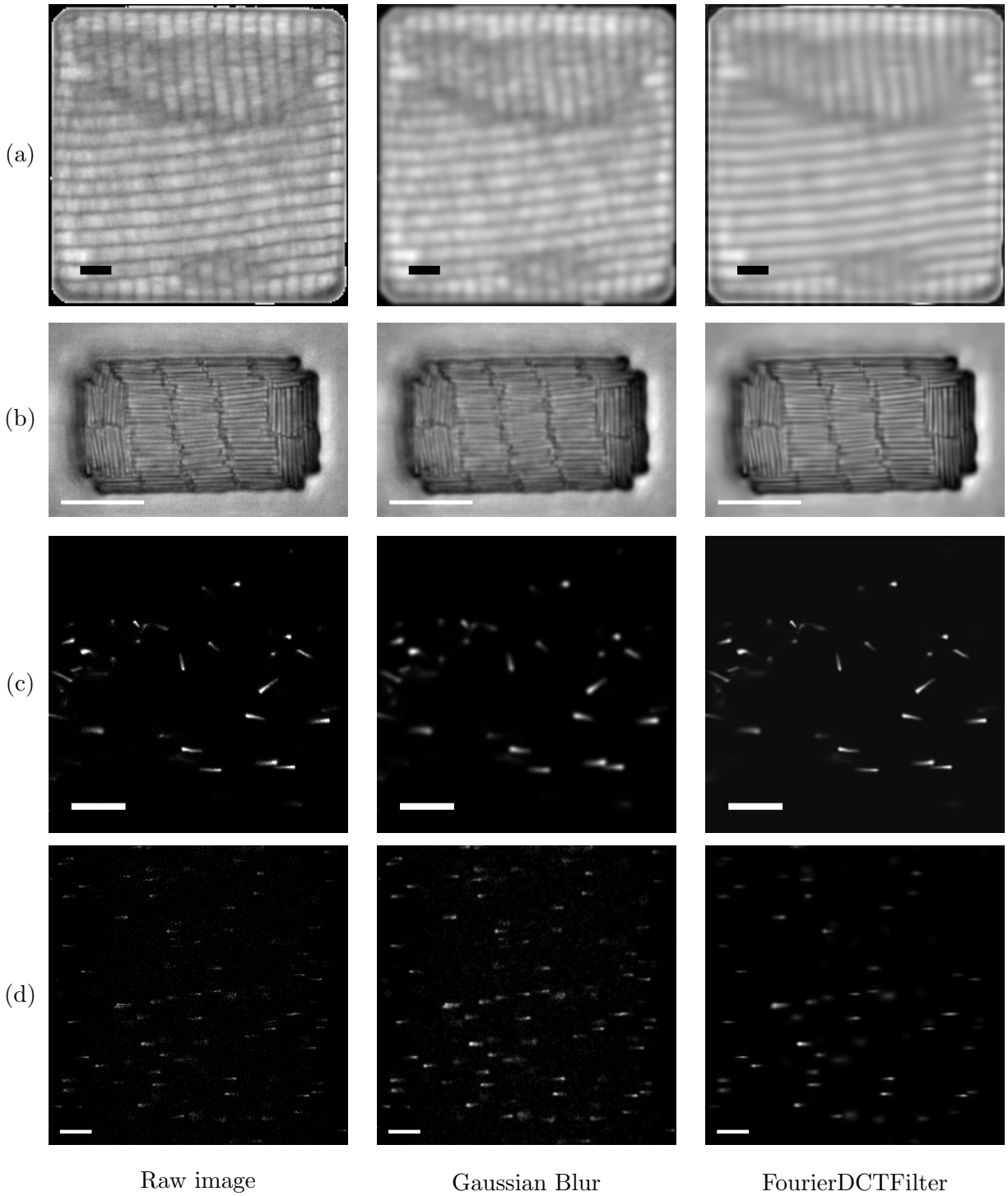


Figure 2.11: The effect of Gaussian and discrete cosine transform filter on images from BF microscopy ((a),(b)) and LSCM ((c),(d)). Scale bars are 10 µm long and 5 pixel wide.

thresholds it ignores large scale variations of intensity. It then better detects the elements on bright field images. For the confocal images, this is less obvious. The density of objects being lower, most objects can be identified either way. However, it seems that LAB better preserves the rods' aspect ratio.

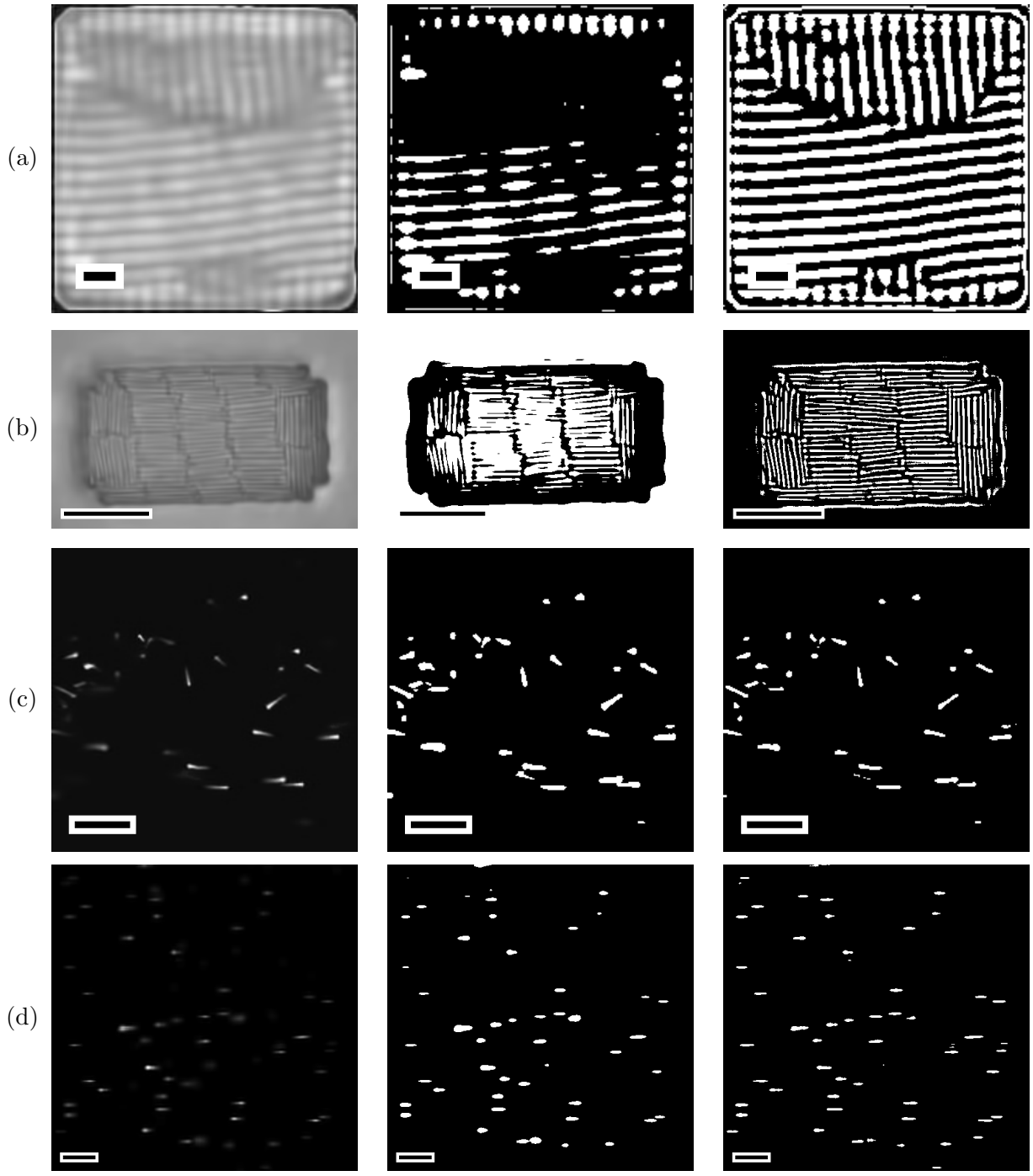
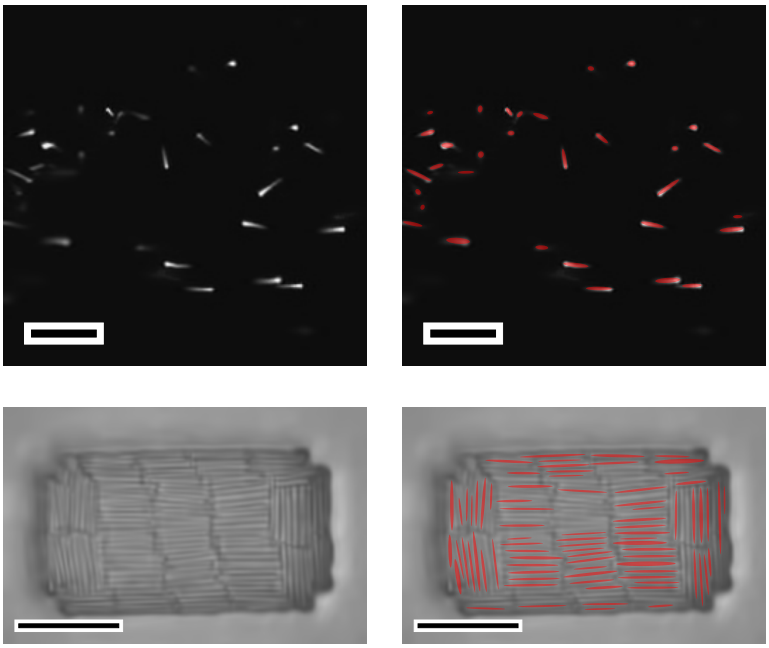


Figure 2.12: The effect of standard and 'locally adapted' binarization on filtered images from figure 2.11. (a) and (b) are bright field images of LC017 rods in the smectic phase (magnification 10x and 60x). (c) and (d) are confocal images of LC010 fluorescent particles.

Particle measurement

Once the image is binarized, components can be easily measured using the Mathematica function 'ComponentMeasurement'. The rod position, orientation, length and diameter can be directly



Filtered image Detected particles

Figure 2.13: Processed confocal miscroscopy pseudo-images of tracer particles (LC010) into a invisible background of rods (LC017) and solvent. The top row is a side view of coexisting isotropic, nematic and smectic phases and the bottom row is a birds eye view of the smectic phase. Red ellipses show components that match the (tuned) selection criteria.

measured by fitting elements with ellipses. Components with unrealistic dimensions can be discarded by tuning the selection criteria. An example of this method is shown in figure 2.13 for a BF image, resolving almost every single rod, and for a confocal image of tracer particles.

We would like to highlight that the orientation measured using the 'ComponentMeasurement' function is given between $-\pi$ and π. However, ellipsoids have an inversion symmetry, an arbitrary orientation θ_i is equivalent to $\theta_i + \pi$. To illustrate the problem we create an artificial image (figure 2.14 (a)) where short segment have an orientation close to $-\pi/2$ and longer ones that gradually reach $\pi/2$. The measured orientation is plotted against the segment length; we expect a straight line but for the above reason, we obtain a discontinuous graph (figure 2.14 (b)). In order to put the orientations back in a convenient form we sequentially apply the following modifications to all orientations θ_i:

$$\text{(1) If } \theta_i < 0 \text{ then } \theta_i = \theta_i + \pi \tag{2.66}$$

$$\text{(2) If } \theta_i > \pi/2 \text{ then } \theta_i = \theta_i - \pi \tag{2.67}$$

The corrected angles are plotted in figure 2.14 (c).

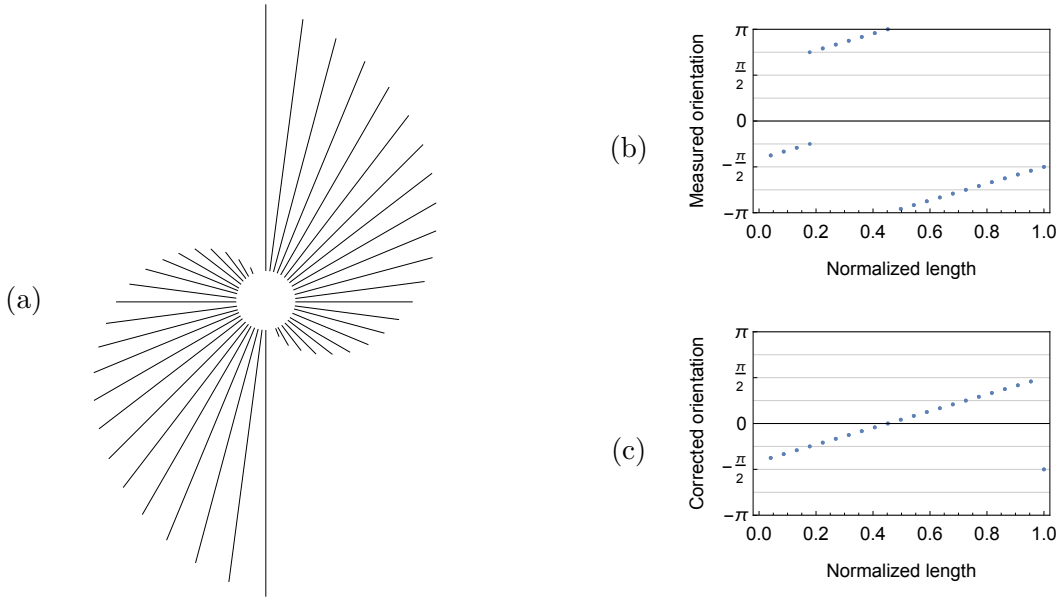


Figure 2.14: The correction of orientation measurement highlights. (a) is the artificial test-image. (b) plots the measured orientation of the black segments represented in (a) as function of their length. And (c) plots the corrected orientations of the segments.

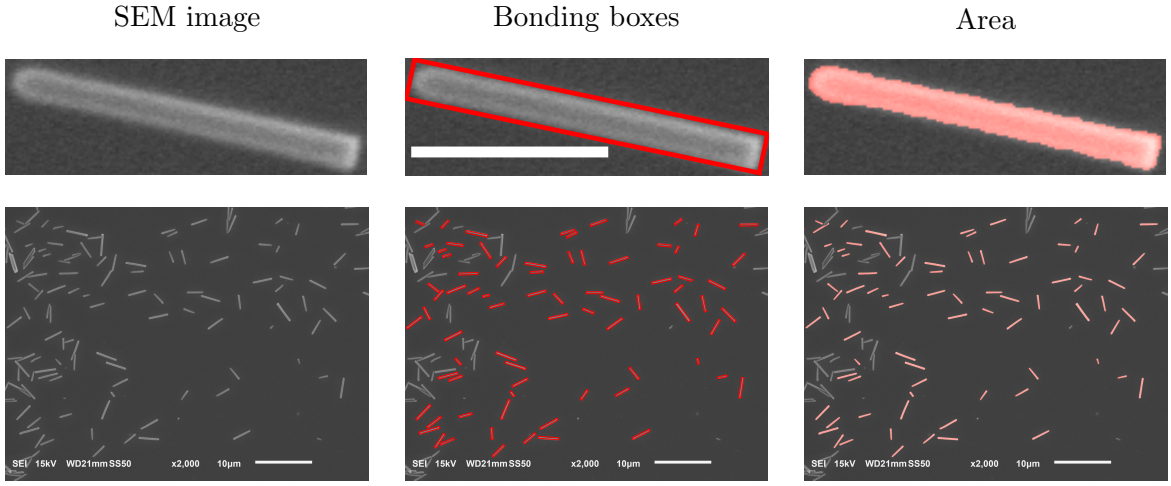


Figure 2.15: Measurement of rods lengths and diameters from SEM images. Minimum oriented bounding boxes are shown as well as the detected area. The scale bar (top row) is 2 µm.

To measure the rod dimensions from SEM images, we find the minimum orientated bounding box that encloses a particle (part of ComponentMeasurement function); this more accurately determines the particle length compared to fitting with an ellipse. However, because our rods are bullet shaped and some happen to be slightly bent, the bounding box tends to overestimate the diameter. Nevertheless, the area of the component (number of pixels) can be precisely measured. The diameter is calculated from the length L and area A: $\sigma = A/L$. Typical analysis snapshots are shown in figure 2.15.

Chapter 3

Phase behavior of colloidal rods in sedimentation-diffusion equilibrium

Abstract

We study the sedimentation-diffusion equilibrium of colloidal rods with length/breadth ratio $5 < p < 20$ by means of theory, simulation ($p = 10$) and experiments ($p = 8.5$ and 12.6). The simulation and the experiments are performed in the regime of small gravitational length. In this regime, the thermal energy is comparable to the potential energy of the rods, and therefore important variations of concentration occur at the particle's length scale. This induces coexistence of liquid crystal phases within a few particle lengths.

The local density approximation is used and coupled to the *equation of state* (EOS) of hard spherocylinders to determine the density profile of hard rods. We consider aspect ratios ranging from 5 to 20 and find that the thickness of the sediment is largely independent of the rod's aspect ratio. Furthermore, we predict that this sediment, if measured between the dense smectic ($\phi = 60\%$) and the dilute isotropic ($\phi = 1\%$), is approximately equal to $32 l_g$.

This prediction is mostly confirmed by a molecular dynamics simulation of rods made of 21 fused spheres and with an aspect ratio of 10. However, in experiments we observe density profiles inflated by up to a factor of 2. We further characterize the different liquid crystal phases by measuring the nematic and smectic order parameters. We find good agreement between simulation and theory. However, the nematic order parameter in our experiments increases more steeply close to the isotropic-nematic phase transition.

3.1 Introduction

In the previous chapters, we have related how Perrin [38] used the analogy between a colloidal and a molecular gas in sedimentation-diffusion equilibrium to prove, in one way, the existence of molecules. Perrin's experiments were performed at low concentrations of colloids, in a regime where particles' interactions have small relevance. However, sedimentation-diffusion equilibrium is not limited to this regime. For example, experimental work, using a monolayer of hard spheres on a tilted stage, made use of gravity in order to study the phase behavior of hard disks [98]. They located the first order liquid-to-hexatic and second order hexatic-to-crystal phase transitions in very good agreement with simulation [99]. The concentration gradient induced by gravity allowed them to find the EOSs and study the capillary waves at the liquid-hexatic interface in a single experiment. This is precisely the strength of the methods, being able to study the whole phase diagram of colloidal particles in a single experiment. Furthermore, it induces phase coexistence, which can be difficult to obtain otherwise.

The aim of this chapter is to compare the phase behavior of our experimental system with theoretical and computational predictions of hard rods in sedimentation-diffusion equilibrium.

The chapter is structured as follow. In section 3.2, we theoretically predict the density profile of hard spherocylinders in sedimentation-diffusion equilibrium for aspect ratios $5 < p < 20$. In section 3.3, we present the result from a molecular dynamic simulation of rods at sedimentation-diffusion equilibrium, where the rods are made of fused spheres and have an aspect ratio $p = 10$. The simulated density profile is compared to the theoretical prediction is section 3.4. In section 3.5 and 3.6, we present experimental results and compare them with simulation and theory. Conclusions are finally drawn in section 3.7.

3.2 Sedimentation-diffusion equilibrium of hard spherocylinders

In this section, we first introduce the background relationship between the density profile of colloids in sedimentation-diffusion equilibrium and their EOS. As a second part, we present the method used to determine the EOS of hard spherocylinders with aspect ratios $5 < p < 20$. Finally, we use these EOSs to predict the rods' density profiles and discuss the results.

3.2.1 Theoretical background

Sedimentation-diffusion equilibrium is reached when the sedimentation flux is balanced by the opposite diffusion flux, which is driven by concentration gradients. Consequently, there is no net flow in the system. The density profile at equilibrium can be determined as a function of the suspension EOS $\Pi(\phi)$ and gravitational length l_g [92, 100].
Considering gravity acting along the z-axis. The variation of osmotic pressure $d\Pi$, exerted on a surface S, going up by dz can be written as

$$d\Pi = \frac{dF}{S} = -\frac{M\,g}{S} = -\phi(z)\,\Delta\rho\,dz\,g\ , \tag{3.1}$$

where dF is the variation of force exerted on S, $M = \phi(z)\,\Delta\rho\,dz\,S$ the excess of mass due to the colloids present in the volume $S\,dz$, $\phi(z)$ the volume fraction of colloids at position z, $\Delta\rho$ the difference of density between the particle and the solvent, and g earth's acceleration. Differentiating $\frac{d\Pi}{dz} = \frac{d\Pi}{d\phi}\frac{d\phi}{dz}$, we can rewrite equation 3.1 as

$$\frac{d\phi}{dz} = -\Delta\rho\,\phi(z)\,g\,\left(\frac{d\Pi}{d\phi}\right)^{-1}\ . \tag{3.2}$$

We next introduce the scaled pressure $\Pi^\star$ and the gravitational length l_g

$$\Pi^\star = \Pi\,(k_B\,T)^{-1}\,v_0 \qquad \text{and} \qquad l_g = \frac{k_B\,T}{\Delta\rho\,v_0\,g}\ , \tag{3.3}$$

to finally obtain

$$\frac{d\phi}{dz} = -l_g^{-1}\,\phi(z)\,\left(\frac{d\Pi^\star}{d\phi}\right)^{-1}\ . \tag{3.4}$$

Assuming a maximum height H, the initial condition can be fulfilled by:

$$\frac{1}{H}\int_0^H \phi(z)dz = \phi_0\ , \tag{3.5}$$

where ϕ_0 is the initial volume fraction, prior sedimentation. This can more conveniently be written as

$$-\int_0^H d\Pi = \Pi(0) - \Pi(H) = \int_0^H \phi(z)\,g\,\Delta\rho dz = \phi_0\,H\,g\,\Delta\rho\ . \tag{3.6}$$

In our work, the container will always be considered infinitely high, $H >> l_g$, so that $\Pi(H) = 0$. The initial condition then reads

$$\Pi(z = 0) = \phi_0 \, H \, g \, \Delta\rho \ , \tag{3.7}$$

which leads to

$$\Pi^\star(z = 0) = \phi_0 \, H \, l_g^{-1}. \tag{3.8}$$

Equation 3.4 can be solved numerically to obtain the density profile $\phi(z)$ as long as the EOS $\Pi^\star(z)$ and the gravitational length are known.

Local density approximation and other concerns

Before we look at the sedimentation-diffusion equilibrium of hard spherocylinders, we would like to highlight some possible issues.

The method described above makes use of the local density approximation. The effect of large pressure gradients has not been the object of a devoted study. However, a simulation of hard rods, with an aspect ratio $p = 5$ and strong gravitational field $l_g \approx D$, found an EOS in very good agreement with simulation [92].

One can equally wonder about the impact of interfaces. The intrinsic width of the I-N interface, for example, usually reaches a particle length [34]. What happens when the extent of the nematic phase is comparable to the width of the interface? Furthermore, theory predicts an isotropic-nematic coexistence with equal pressure of both phases. However, due to gravity the pressure is constantly varying with height. This causes a problem in solving equation 3.4 as $\frac{d\Pi^\star}{d\phi} = 0$. Note that this can be overcome by assuming a jump in concentration at the height z, where the phase transition pressure is reached. However, this discontinuous jump is not physical, as thermal fluctuations would smear it out. These problems related to the treatment of the interfaces can hardly be taken into account. However, in [92] the presence of interfaces did not visibly affect the EOS at sedimentation-diffusion equilibrium.

For charged colloids in a solvent hosting a small number of charges, the Donnan effect [36]

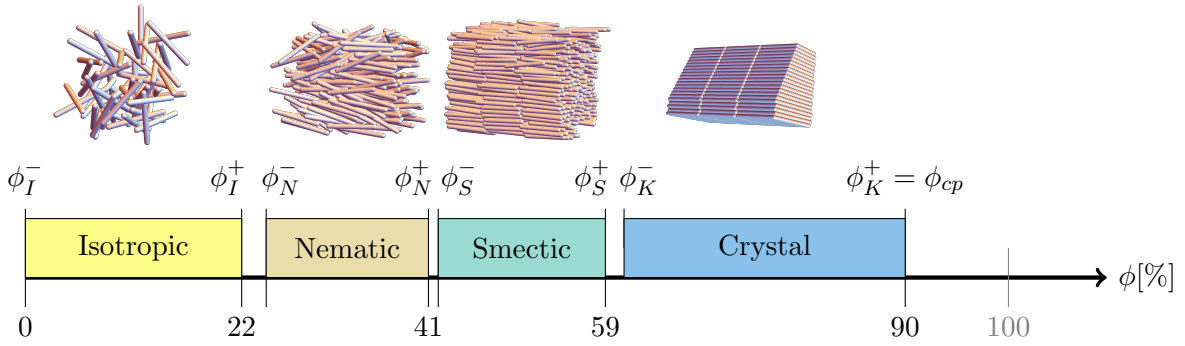


Figure 3.1: Phase behavior of hard spherocylinders with aspect ration $L/D = 12$. The close packing (or maximum volume) fraction is $\phi_{cp} = 0.895$.

can dramatically affect the density profile [100]. However, this effect can be neglected if the number density of colloids $n(z)$ is small compared to the number density of ions $2n_s$: $n(z) < 2n_s/Z^2$, where Z is the number of electric charges per colloid [101]. The Donnan effect will be addressed in more detail in chapter 4.

3.2.2 Method

The *full* EOS for spherocylinders with *arbitrary* aspect ratios cannot be found in literature. In this section, we make approximations in order to obtain them. The EOSs are determined from the infinite dilution to the crystal phase by stitching results from simulations [46, 68] and density functional theory [70]. They are then used to predict the density profile of hard rods, with different aspect ratios, in a semi-infinite space, by solving equation 3.4.

The EOS of hard spherocylinders $\Pi^\star(\phi)$ depends on the rod's aspect ratio. For any aspect ratio $p > 5$, the EOS has multiple domains (isotropic, nematic, smectic A and crystalline) bridged together by coexistence regions. We will determine the EOS, for different aspect ratios, based on results from simulation and theory and making three approximations: (1) the EOS predicted by DFT is valid on the whole isotropic and nematic regions, (2) the EOS beyond the N-S coexistence is independent of the aspect ratio[1] and (3) the scaled packing fraction marking the nematic-smectic coexistence can be interpolated from table 3.1.

The EOS is built up by joining a part from theoretical prediction $\Pi^\star_{th}$ (I-N regions) to another part from simulation results $\Pi^\star_{sim}$ (S-K regions). $\Pi^\star_{th}$ has been determined by DFT [70] and $\Pi^\star_{sim}$ is interpolated from simulation results where $p = 40$ [46]. The theoretical EOS is

[1] For scaled packing fraction $\phi^\star = \frac{\phi}{\phi_{cp}}$.

p	3	4	5	10	∞
$\phi^\star_{N+}$	0.587 [46]	0.545 [46]	0.513 [46]	*0.46*	0.46 [68]
$\phi^\star_{S-}$	0.663 [46]	0.590 [46]	0.546 [46]	*0.47*	0.47 [68]

Table 3.1: Scaled densities of coexisting nematic ($\phi^\star_{N+}$) and smectic ($\phi^\star_{S-}$) phases for different aspect ratios p. The values emphasized for $p = 10$ are assumed to be equal to $p = \infty$.

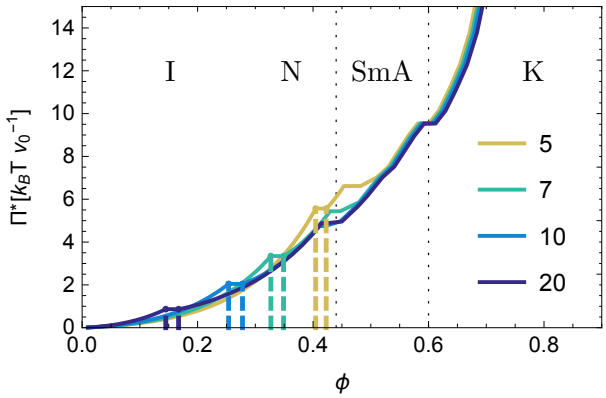


Figure 3.2: Equation of state of hard spherocylinders with various aspect ratios. The pairs of thick dashed lines indicate the I-N phase transitions and the thin dotted line approximate the N-SmA and SmA-K phase transition.

used below the N-S coexistence: $\phi^\star < \phi^\star_{N+}$. It is also used to determine the phase coexistence pressure: $\Pi_{NS} = \Pi^\star_{th}\left(\phi^\star_{N+}\right)$. Then, the EOS from simulation is used above the N-S coexistence, i.e. for $\phi^\star > \phi^\star_{S-} + \delta$, where δ ensures that the pressure in the smectic phase is higher than at coexistence. Example of EOS for aspect ratios of 5, 7, 10 and 20 are plotted in figure 3.2, the I-N coexistences are indicated by pairs of dashed lines.

Let us come back on the three approximations by comparing the EOS from theory and bulk simulations plotted in figure 2.4 and 2.5 (page 24). We notice a good agreement in the I-N regions. However, the end of the nematic phase $0.4 < \phi^\star < 0.5$, we observe (figure 2.4, $p = 15$) that the simulations start to deviate from theory. We believe that the theory is to blame here, as in principle, the theory is not valid at high concentrations. This is going against approximation (1), which will then overestimate the pressure of the N-S transition. In practice, it artificially increases the extent of the nematic phase at the expense of the smectic phase. In approximation (2), we considered the EOS independent of the aspect ratio above the N-S phase transition. Looking at figure 2.4, we can say that this is true for $\phi^\star > 0.6$, as the EOSs of $p = 5$ and $p = 40$ overlap. Nevertheless, between $\phi^\star = 0.5$ and $\phi^\star = 0.6$, only $p = 15$ and $p = 40$ are matching. This indicates that approximation (2) may not hold for $p = 5$, and remain a concern up to $p = 15$. The validity of the third approximation is difficult to pin down because of the lack of data; we can only assume the behavior is similar to approximation (2). On the top of

these approximations, we note that the EOS determined by simulation [46] was biased, near the crystal phase, by the box size [68].

3.2.3 Results and discussion

In the left panel of figure 3.3, we show the density profile calculated for an aspect ratio $p = 10$ and a pressure at the bottom wall $\Pi^\star(z = 0) = 15$. At the bottom ($z = 0$), in the crystal phase, the concentration is maximum. Going up in z, the concentration continuously decreases until it reaches the upper SmA-K coexistence density; at the phase transition, a jump in concentration is observed and the smectic phase starts. The process is repeated at the following N-SmA and I-N phase transitions. The 'end' of the isotropic phase is defined at the height where $\phi = 1\%$, this working definition will be used to compare the thickness isotropic part pf the sediment phase to the nematic and smectic parts. From the left panel of figure 3.3, we can extract the heights z_i, at which the phases transitions occur. It is important to note that these heights: (1) will only be shifted by a constant if the number of particles (i.e. $\Pi^\star(z = 0)$) increases, and (2) are proportional to the gravitational length.

The dependency of the phase transition heights with the aspect ratio is plotted in the right panel of figure 3.3. For $p = 10$, we recover the phase transition heights from the left panel: $z_{SmA-K} = 8.5 l_g$, $z_{N-SmA} = 17.8 l_g$, $z_{I-N} = 25.5 l_g$ and the volume fraction 1% is reached at $z_{\phi=1\%} = 40.4 l_g$. This plot shows that the proportion of crystalline phase (■) is mostly independent of the aspect ratio. Furthermore, the accumulated width of the isotropic (■), nematic (■) and smectic (■) phases (W_{I+N+S}) is also independent of the aspect ratio; only their relative proportions vary. This part of the sediment, including the I, N and SmA phases will be referred to as the *upper sediment*.

In sum, for any aspect ratio $5 < p < 20$, the top of the isotropic phase ($\phi = 1\%$) will be separated from the SmA-K interface, by approximately $32\, l_g$. And this statement should hold for short ranged repulsive rod-rod interactions. Indeed, the only effect would be to, effectively, increase the particle diameter [9, 102], which would reduce the aspect ratio and increase $\Pi^\star(z = 0)$, shifting up the three phases. This will be further discussed in chapter 4.

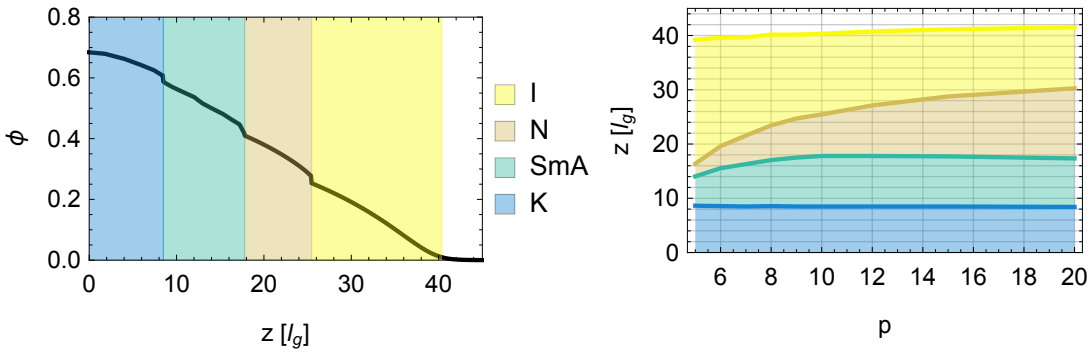


Figure 3.3: Theoretical results for arbitrary gravitational length l_g and a pressure at the bottom wall $\Pi^\star(z=0)=15$. We plot the volume fraction of hard rods as a function of the height for $p=10$ (left), and the heights of the phase transitions as a function of the aspect ratio (right).

3.3 Simulation

3.3.1 Method

The simulation was performed by my colleague Maxime Tortora using the HOOMD-Blue simulation toolkit [103]. This molecular dynamic code has been optimized for GPU [104] and allows the simulation of complex shapes through rigid body constraints [105].

The rods were made of 21 fused spheres of diameter σ separated by a distance $\sigma/2$. The resulting aspect ratio and volume were $p=10$ and $v_0 \approx 7.72\sigma^3$. The volume of a bounding spherocylinder is about 10% larger than the volume of the rod $v_{sp} \approx 8.38\sigma^3$.

Rod interactions were mediated by the individual spheres. The spheres from different rods interacted through a Lennard-Jones potential that reproduces the phase behavior of hard spheres.

Gravitational forces were exerted on the center of each individual spheres and were equal to $\frac{k_BT}{40\sigma}$, which correspond to a rod gravitational length of $l_g=\frac{40}{21}\sigma$.

The simulation box consisted of a 112σ sided square, where the origin was chosen at its center. The box was filled with 51200 rods to reach an initial volume fraction of 30%. Hard-walls were used at the bottom and at the top of the box, in order to obtain a sedimentation-diffusion equilibrium. On the four remaining sides, periodic boundary conditions were applied.

The system was prepared as a crystal of perfectly aligned rods (along the x-axis) that

occupy the entire simulation box. It was then left to equilibrate for $\Delta t = 10000\tau$, where $\tau = \sigma^2/D_{t0}$ (= 1 in simulation unit) is the characteristic time required for an isolated rod to diffuse twice its diameter. At $t^\star = 0$ the system was assumed to be at equilibrium. Illustrations of the simulation box at $t^\star = 0$ are shown in figure 3.4.

No special care was taken to account for hydrodynamic interactions ($D_{t0} = D_0^{\parallel} = D_0^{\perp} = D_{r0}$). The transition between the ballistic and diffusive regimes was set at a time $\tau_B = \mu_{t0} m$ (= 1 in simulation unit). Note that in this simulation $\tau_B = \tau$, whereas for colloids we expect $\tau_B << \tau$, see chapter 6 for details on the dynamics.

3.3.2 Analysis

Order parameters characteristic to the nematic, smectic and crystal phases[2], were measured at different heights z of the simulation box and averaged over 43 times sampled from $t^\star = 0$ and $t^\star = 1050\tau_B$. Due to deformations and defects in the smectic and crystal phases the order parameters (τ and ψ_6) were measured locally. In order to measure the smectic order parameter, for each z-bin, the box was divided into y-slices of width 9σ; the order parameter was then measured for each slice and averaged over all slices. In order to measure the order parameter in the crystal phase, ψ_6 was measured for each rod and averaged over all rods at a given height. The cut-off threshold, used in ψ_6, to find nearest neighbors was set to 1.5σ between two rods' center of mass, additionally only the bond angle component orthogonal to the rod's main axis was considered to measure ψ_6.

The volume fraction $\phi(z)$ was measured by counting the number of rods' center of mass n in a volume v around the height z,

$$\phi(z) = \frac{n}{v} v_0 \ , \tag{3.9}$$

with v_0 the rod volume. It was averaged over time.

The pressure $\Pi^\star(z)$ was obtained by counting the number of rods (n_a) higher than z. Similarly to equation 3.1 and using equation 3.3 we obtain

$$\Pi^\star(z) = \Pi(z)\frac{v_0}{kT} = \frac{n_a\, v_0}{S\, l_g} \ , \tag{3.10}$$

[2]The order parameters were introduced in section 2.1.2

where the surface of the box is $S = (112\sigma)^2$.

3.3.3 Results

The results presented are limited to the phase behavior of rods at times $t > t^\star = 10000\tau_B$, when the sedimentation-diffusion equilibrium was close to being reached.

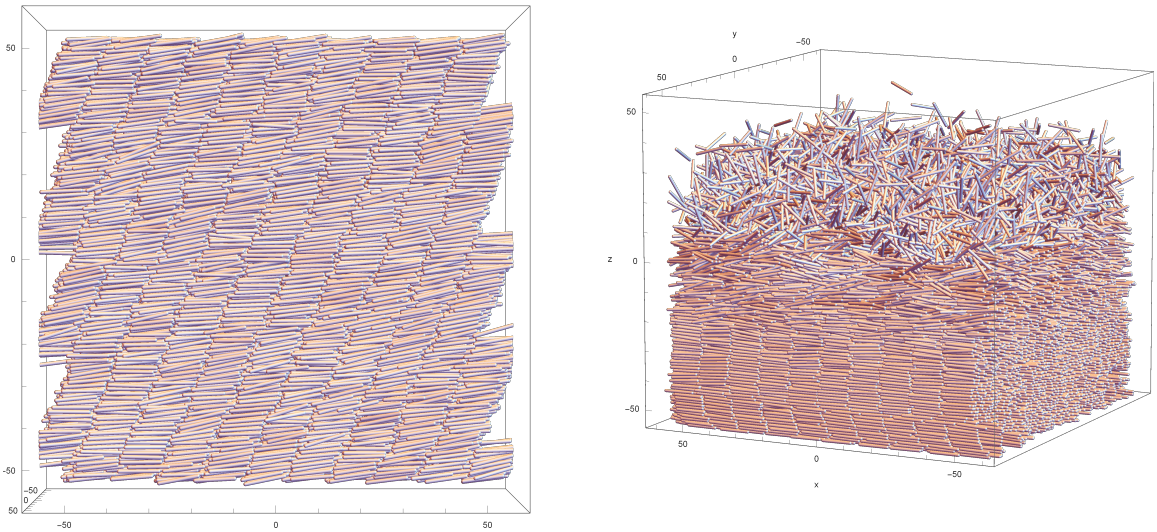
A snapshot of the simulation box is presented in figure 3.4, with different views. The front view clearly shows coexistence of a layered smectic phase (at the bottom), an orientated nematic phase (in the middle) and a disordered isotropic phase (vanishing at the top). The structure was found to be stable over the simulation time $(1050\tau_B)$[3]. However, a number of defects can be observed. For example, the smectic layers are not orthogonal to the nematic director (top view). We also observe what seems to be an edge dislocation in figure 3.4 (front view). Further distortions and defects can be observed in figure 3.5: in the crystal phase (left graph), a clear screw dislocation is observed around $y = 20\sigma$; in the smectic phase (right), an edge dislocation is located around $(x, y) = (10\sigma, 10\sigma)$ and an undefined defect spreads around $y = -20\sigma$.

The time dependence of the density profile is shown in figure 3.6, in order to check that the system has reached equilibrium. In the left panel, no noticeable difference can be observed between the density profiles at the beginning (●) and at the end (●) of the simulation. Nevertheless, sedimentation is unveiled in the right panel, showing that the rods' averaged height decreases slowly over time. Even though it is clear that the system has not reached complete equilibrium, the sedimentation seems extremely slow. Therefore, in order to save calculation time, we will consider the system in this regime.

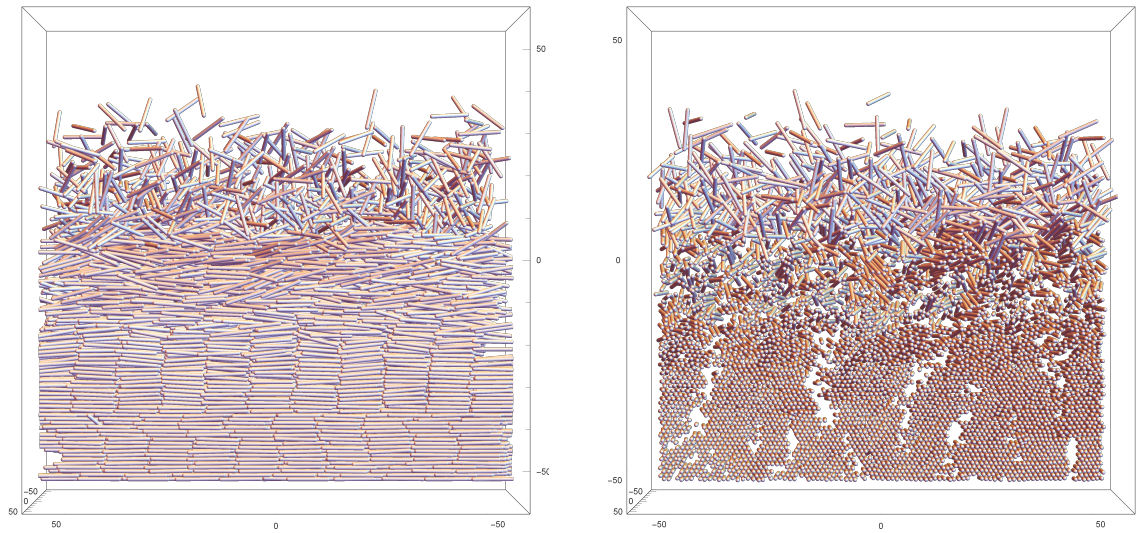
The order parameters S_2, τ and ψ_6 are plotted in figure 3.7, as a function of the height z. The different phases were located based on the order parameters: the isotropic phase location was determined by $S_2 < 0.2$ and $\phi > 1\%$, the nematic phase by $S_2 > 0.73$[4] and $\tau < 0.2$, the smectic phase by $\tau > 0.4$ [106] and $\psi_6 < 0.65$, finally the crystal phase by $\psi_6 > 0.7$ [106]. Note that $\phi > 1\%$, $S_2 < 0.2$, $\tau < 0.2$ and $\psi_6 < 0.65$ have been chosen based on a working definition following the experiments. The region corresponding to each phase is colored with a separate color. The error bars, quantifying the standard deviation of order parameter values with time,

[3] In this simulation $\tau_B = \tau = \sigma^2/D_{t0}$ is equal to the characteristic time required for an isolated rod to diffuse twice its diameter.

[4] 0.73 is the order parameter of the nematic phase at the I-N coexistence for the simulated system, as calculated per DFT [70]



Top view Perspective view



Front view Side view

Figure 3.4: Illustration of the simulation box at $t^\star = 0$. On the projected views, only a fraction of the rods, which positions in the third dimension are in between -30σ and -20σ, is represented.

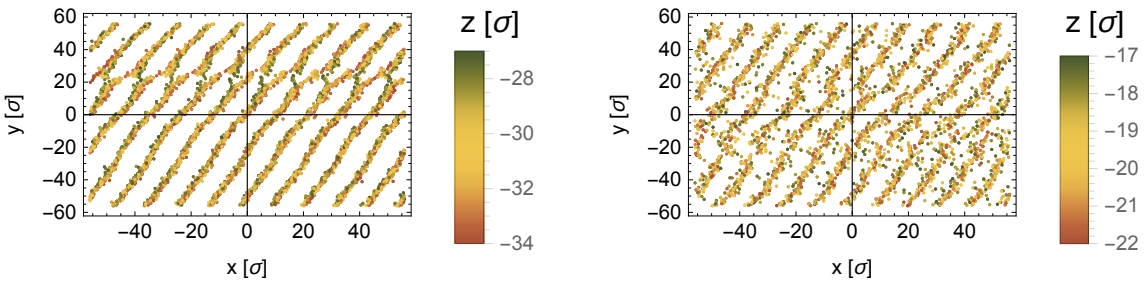


Figure 3.5: Distribution of rods' center of mass projected in the x,y plane for two different z-slices. The heights correspond to the beginning of the crystal and smectic phases (left and right).

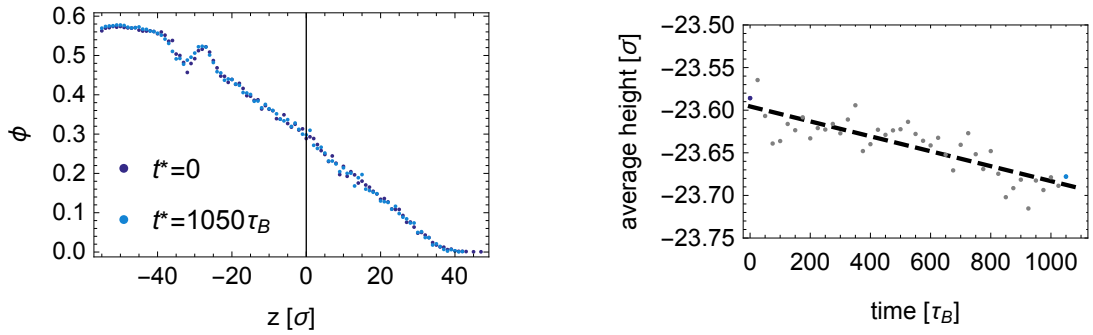


Figure 3.6: On the left panel, the rod volume fraction is plotted as a function of the height, at the beginning (●) and the end (●) of the simulation. On the right panel, the averaged height of the rods is plotted as a function of time.

reflect that the order parameters were stable over time.

The rods' osmotic pressure and volume fraction are determined at all heights in figure 3.8. We note that the density profile is highly non-exponential, and it even looks linear for $5\% < \phi < 50\%$. However, at low density $\phi < 0.5\%$ the exponential decrease in volume fraction $\phi \propto e^{-z/l_g^{\text{s-d}}}$ is recovered, giving $l_g^{\text{s-d}} = 2.08\sigma$. This is overestimating the actual gravitational length, $l_g = 1.9\sigma$, by about ten percent. This overestimate is due to the fact that hard rods do not behave like a perfect gas at $\phi = 0.01$. Within the Onsager limit, $\Pi^\star(\phi) = \phi\left(1 + \phi\frac{L}{\sigma}\right)$ and then for an aspect ratio of 10 at one percent volume fraction $\frac{d\Pi^\star}{d\phi}(0.01) = 1+10*0.01 = 1.1$. This is ten percent higher than a perfect gas. The perfect gas behavior is only recover for $\frac{L}{\sigma}\phi << 1$.

The EOS $\Pi^\star(\phi)$ corresponding to the simulated sedimentation-diffusion equilibrium is extracted from figure 3.8 and plotted in figure 3.9 (•). The background colors correspond to different phases as determined by the order parameters in figure 3.7. This simulated EOS is compared to the EOS predicted by DFT calculations [70] (—). We focus our attention in the I-N regions, where the DFT is valid. We then observe a good agreement up to $\phi = 10\%$. At higher concentration our measurement seems a bit off. And when the nematic phase is reached, at $\phi = 25\%$, we note a clear deviation. To put this deviation in perspective, we plot the bulk EOS of hard spherocylinders determined by theory (—) and bulk simulation (○), keeping the same aspect ratio $p = 10$. We make two observations. Firstly, the DFT calculation (—) matches very well the bulk simulations (○). Secondly, the difference between the EOS of spherocylinders (—) and fused spheres (—) predicted by DFT is reasonably small. The deviation of the EOS we simulated at sedimentation-diffusion equilibrium (•) to the DFT prediction (—) is then non negligible. It may be due to the fact complete equilibrium has not been each or other effects.

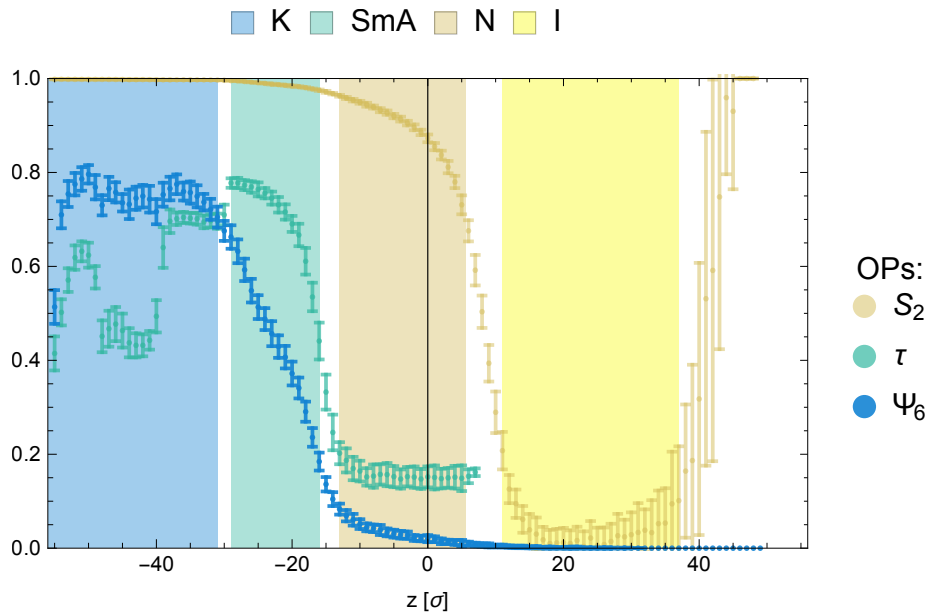


Figure 3.7: Time average of the bond orientational order parameter ψ_6 (●), smectic order parameter τ (●), and uniaxial nematic order parameter S_2 (●) against the height z. The filled areas correspond from left to right to the crystal ($\psi_6 > 0.7$), smectic A ($\tau > 0.4$ and $\psi_6 < 0.65$), nematic ($S_2 > 0.7$ and $\tau < 0.2$) and isotropic (I) phases ($S_2 < 0.2$ and $\phi > 1\%$). The error bars represent the standard deviation.

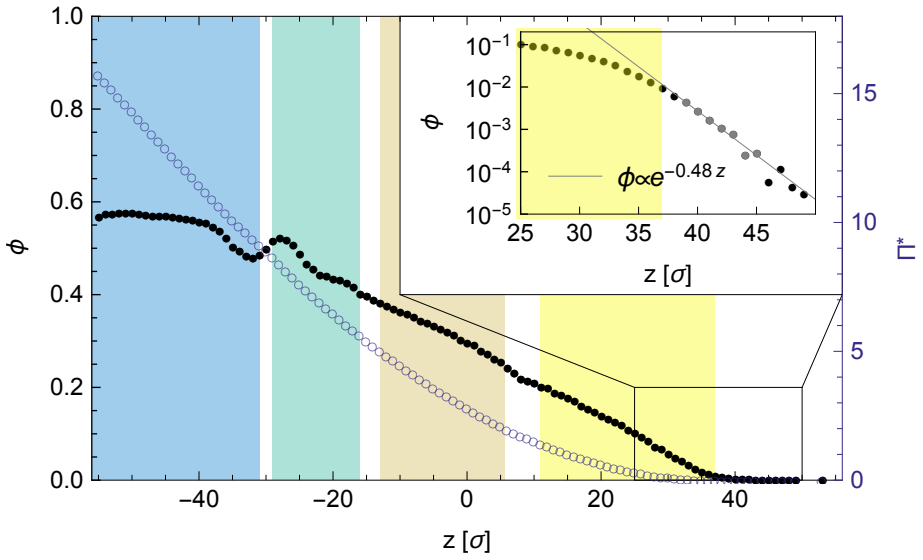


Figure 3.8: Volume fraction ϕ (left axis, •) and scaled pressure $\Pi^\star$ (right axis, ∘) plotted against the height z. The inset shows a fit of the exponential decay of $\phi(z)$ for $45 < z < 50$ (i.e. $\phi < 0.5\%$).

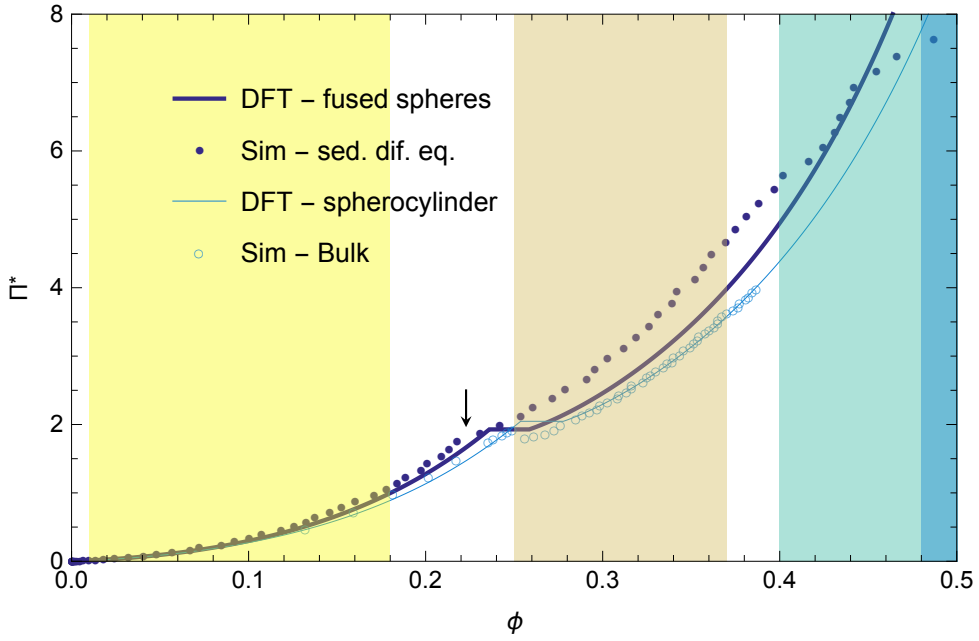


Figure 3.9: Equation of state measured from simulations (markers) are compared to DFT calculations [70] (lines), for $p = 10$. We compare our simulation results (●) to bulk simulations of hard spherocylinders (○) [67].

One can also use figure 3.9 to locate the I-N transition. In theory (—), it is given by the plateau around $\phi = 24.5\%$ and $\Pi^\star = 1.9$. In our simulation (●), according to the nematic order parameter, it is somewhere in the white area spreading from $\phi = 18\%$ to $\phi = 25\%$. However, we can find a pseudo plateau, indicated by the arrow at $\phi = 22.5\%$ and $\Pi^\star = 1.9$. We conclude from this that the I-N phase transition might occur, in our simulations, at the predicted pressure but at a slightly lower volume fraction. It seems that the proximity of the nematic phase is increasing the pressure in the isotropic phase.

3.3.4 Discussion

In principle, simulating sedimentation-diffusion equilibrium of colloids is a convenient way to obtain its EOS. This method has led to an accurate determination of the EOS, in a Monte Carlo simulation, using spherocylinders with an aspect ratio $p = 5$ and a gravitational length comparable to our own [92]. The discrepancy observed in our work might to be due to the fact that equilibrium has not been reached. It is therefore difficult to comment on other effects, such as the box size, the bottom wall or most interestingly the interplay between coexisting phases. Nevertheless, we note that it is odd that in the isotropic and nematic phases, where the dynamics are the fastest, we still observe discrepancy with theory (see figure 3.9). And it

seems unlikely that equilibrium is the only reason to this. The slow dynamics in this system are related to the diffusion of colloidal rods, which will be addressed in chapter 5.

In this MD simulation, reaching equilibrium was problematic. However, it showed how fast sedimentation generates deformations and defects in the smectic and crystalline phases, which remain stable on the simulation timescale. This might actually be an interesting approach to study defects in LCs. Furthermore, it provides us with a reference framework that will be confronted to our experiments.
In the next section, we will compare the density profile obtained in simulation with the theoretical prediction.

3.4 Simulation vs theory

In figure 3.10, we compare the density profile obtained from simulation(····) with the theoretical one(——). This last one is obtained for parameters matching the simulation: the rod aspect ratio is $p = 10$, the pressure at the bottom is $\Pi^\star(z = 0) = 16.55$ and the gravitational length is $lg = \frac{40}{21}\sigma$. The only difference is the detailed shape of the rod, which is in simulation a chain of fused spheres and in theory represented by spherocylinders.

Theoretically(——), the phase transitions are infinitely thin. They are indicated by vertical lines matching the density jumps in concentration. However, in our simulation(▪▪▪▪) the phase transition have a finite thickness, that relates to the interfaces. These wide interfaces are not included in the theoretical treatment but have a physical origin [34].

Another striking point is that the simulated density profile is 11.5σ wider than the theoretical one, which corresponds to a spread of about ten percent. This can be partly explained by a 5.5σ thicker crystalline phase. The dilation of the crystalline phase can be understood as a way to compensate for the low volume fraction in the crystalline phase. Indeed, in the simulation the rods have not found the most efficient packing and could not reach the predicted volume fraction. Reasons might include: inappropriate ratio between the box size and the smectic layer spacing, rod detailed shape and/or equilibration time.

The 6.5σ remaining are mostly located in the nematic phase. In the simulation the nematic phase, excluding interfaces, has a width of 16σ, which is already a bit larger than the predicted

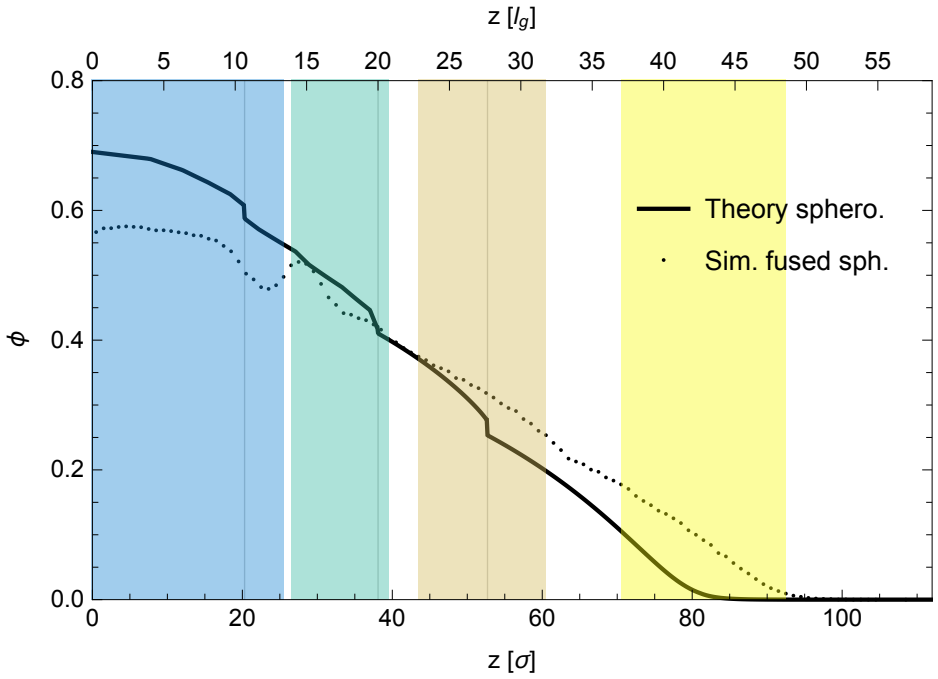


Figure 3.10: Theoretical density profile of hard spherocylinder (——) and measured density profile in our simulation of fused spheres (····), for $p = 10$ and $lg \approx 1.9\sigma$.

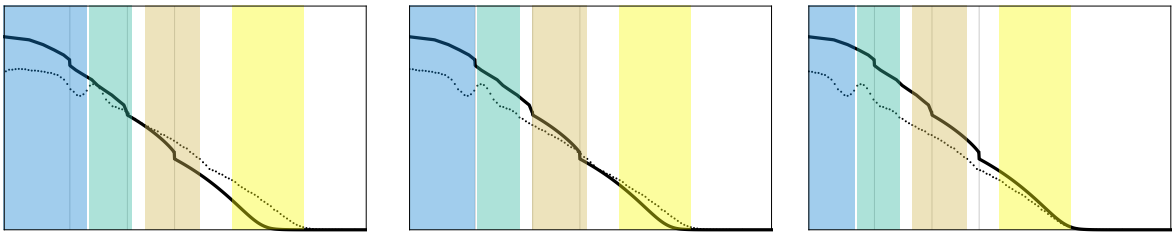


Figure 3.11: Reproduction of figure 3.10, where the theoretical prediction (——) has been shifted by 0 (left), 5.5σ (middle), and 11.5σ (right).

value of 14.7σ. If we add to this half of the I-N and N-SmA interfaces, we obtain a thickness of about 21σ. In figure 3.11, we shift the theoretical prediction by 0σ, 5.5σ and 11.5σ to allow easier comparison, of the extent of the phases, between simulation and theory. From the three panels of figure 3.11, we see that the crystal, nematic and isotropic phases are larger than predicted, but the smectic phase is smaller than predicted.

The mismatch of the density profiles in the isotropic and nematic regions derives from the one observed in the EOS, figure 3.9. Therefore, only a minor fraction of it is due to the difference of rod shape between simulation and theory. This means that the widening of the nematic phase is mostly unexplained.

The theoretical density profile is directly produced from the EOS. We then compare, in figure 3.12, the EOSs from simulation and theory. We note that the phase transitions happen

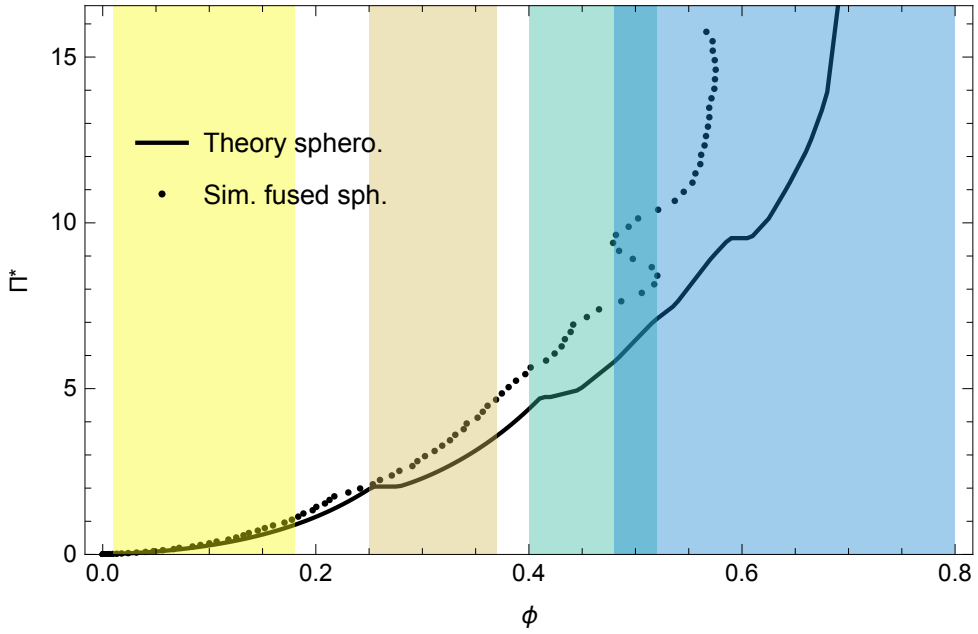


Figure 3.12: Equation of state of spherocylinders (theory) and fused sphere rods (simulation), for $p = 10$.

roughly at the same pressures in theory and simulation. However, if we look more into details, a considerable shift can be seen at the N-SmA phase transition. Assuming that the theoretical EOS is correct, the smectic phase would be expected to form at smaller pressure. This would imply that something is preventing the formation of layers. The origin of this phenomenon is unclear; it might be related to defects in the smectic phase, the box size or simply an inaccurate theoretical EOS. Nevertheless, this contributes to explain why the smectic sediment is slightly smaller than predicted.

In conclusion, the whole EOS and density profile show small discrepancies. This can be partly explained by the inadequate choice of EOS that considers spherocylinders rather than fused spheres. However, as shown in figure 3.9, this is not the main issue in the isotropic and nematic phases. The fact that rods have not achieved complete sedimentation-diffusion equilibrium is a concern, but it cannot be established whether it is the cause of discrepancies is the isotropic and nematic phases. On one hand, rods are sedimenting at what seems to be a constant speed (see figure 3.6). But on the other hand, if the sedimentation is slow enough, we could expect at least a partial-equilibrium in the isotropic and nematic phases where the concentrations are smaller, but we still observe discrepancies in these regions.

More generally, if we look back, the theoretical prediction offers a reasonable agreement with the simulation. Furthermore, the overall shape of the density profile is very similar in

simulation and experiment: from the top of the container to the bottom, we have first an exponential increase of the concentration for $\phi < 0.5\%$ (figure 3.8), then a quasi-linear increase of the concentration on most of the density profile and finally we slowly reach a plateau in the crystal phase. In the next section, we will present experimental results.

3.5 Experiments

3.5.1 Method

The aim of this section is to explain the influence and choice of key experimental parameters. In table 3.2, we summarise these parameters for each experiment. They are divided into four groups.

We use two different types of cell: UV-glue cells made using soft lithography techniques and capillaries. The UV-glue cells have the best optical properties (coverslip #1) and tunable size. However, they cannot be used with DMF, which accounts for capillaries are used as an alternative. We use *CM Scientific* capillaries, with dimensions $300\times300\,\mu m^2$ and wall thickness $150\,\mu m$.

No convection was observed in the experiments, the dense isotropic, nematic and smectic phases were clearly unaffected. Therefore, no special care was taken to prevent convection effect.

The rods were imaged using confocal microscopy. In order to observe them at different heights, two techniques were employed. The first technique made use of a tilted Zeiss LSCM in order to observe, from the side (x-z plane), coexisting phases in a single snapshot. And thus, at a fixed distance from the wall δz. The second technique, employed a faster Thorlab LSCM in order to scan, from the bottom (x-y plane), the sample at various heights. This last technique required close refractive index matching $\Delta n \approx 0$. We call δz the range of distances from the coverslip explored during an experiment, a fixed value corresponds to the Zeiss microscope and a range of values to the Thorlab system. LSCM is always a trade-off between image quality and imaging speed. Parameters such as frame rate, resolutions (res.) and image dimensions were tuned to obtain exploitable images.

The samples studied are mixtures of three components: rods, solvent and salt. The role

Tag	Cell	Imaging					Running			
		Frame rate [s^{-1}]	Image Size [σ^2]	xy res. [$\frac{\sigma}{\text{pixel}}$]	z res. [$\frac{\sigma}{\text{pixel}}$]	δz [σ]	t_{eq} [h]	t_{exp} [h]	$1/v_d$ [s L^{-1}]	τ_L [s]
Exp0003	UV-Glue	0.48	347×132	0.56	2.4	20	12	2.9	10400	16.4
Exp0405	Capillary	0.33	310×188	0.48	2.1	60	12	12.8	60000	17
Exp0441	Capillary	0.56	243×128	0.48	1.	0-54	12	0.5	-	17
Exp0600	Capillary	0.57	243×130	0.48	1.	0-55	12	0.5	-	17
Exp0601	Capillary	0.57	243×130	0.48	1.	0-55	12	0.5	-	17
Exp0602	Capillary	0.57	243×130	0.48	1.	0-55	12	0.5	-	17
Exp1000	Capillary	0.25	586×586	0.57	3.4	60	12	1.09	3930	2.6

Tag	Sample									
	Rods	Solvent	Salt (conc.) [mM]	σ [µm]	L/σ [σ]	lg [µm]	λ_D [nm]	Δn	*f.dyed* [%]	ϕ_0 [%]
Exp0003	LC010-17	Water	NaCl (1)	0.39	12.6	0.8	9.7	0.1	0.2	7.7
Exp0405	LC010-17	DMF	None	0.39	12.6	0.74	-	0.02	0.2	11.8
Exp0441	LC010-17	DMF	None	0.39	12.6	0.74	-	0.02	0.2	11.8
Exp0600	LC010-17	DMF	LiCl (0.5)	0.39	12.6	0.74	9.2	0.02	0.2	5.9
Exp0601	LC010-17	DMF	LiCl (0.5)	0.39	12.6	0.74	9.2	0.02	0.2	5.9
Exp0602	LC010-17	DMF	LiCl (0.5)	0.39	12.6	0.74	9.2	0.02	0.2	5.9
Exp1000	LC011-12	DMF	None	0.28	8.5	3.1	-	0.02	1.0	4.85

Table 3.2: Experimental parameters. The expression LiCl (0.5) means that 0.5mM of LiCl has been added to the dispersion.

of the salt was to reduce the range of the double layer repulsion, which can be estimated by the Debye length λ_D (equation 2.58, page 28). The solvent used was either milli-Q water, used for convenience, or DMF, used for index matching. DMSO was not used as it was inducing sticking of particles to the walls. Finally, the rods were themselves a mixture. A mixture composed of a fraction *f.dyed* of dyed particles, used as tracers, and a background of unlabelled particles. The mixtures were either LC011-12 or LC010-17, whose properties were given in table 2.3, page 35.

An experiment was run as follows. First, the cell was filled with a suspension of rods of concentration ϕ_0. After, approximately 20 minutes most of the sedimentation was achieved and smectic layers had already appeared at the bottom. Nevertheless, the sample was left to equilibrate for a longer time t_{eq}, typically overnight. In most instances, a small drift could still be observed after this time, most likely due to cell extremely slow leakage. The average drift v_d is given, as the time required to drift by one rod length L/v_d, in table 3.2. This can be directly compared to the the time required to diffuse by one rod length τ_L. We finally give the total image capturing time t_{exp}.

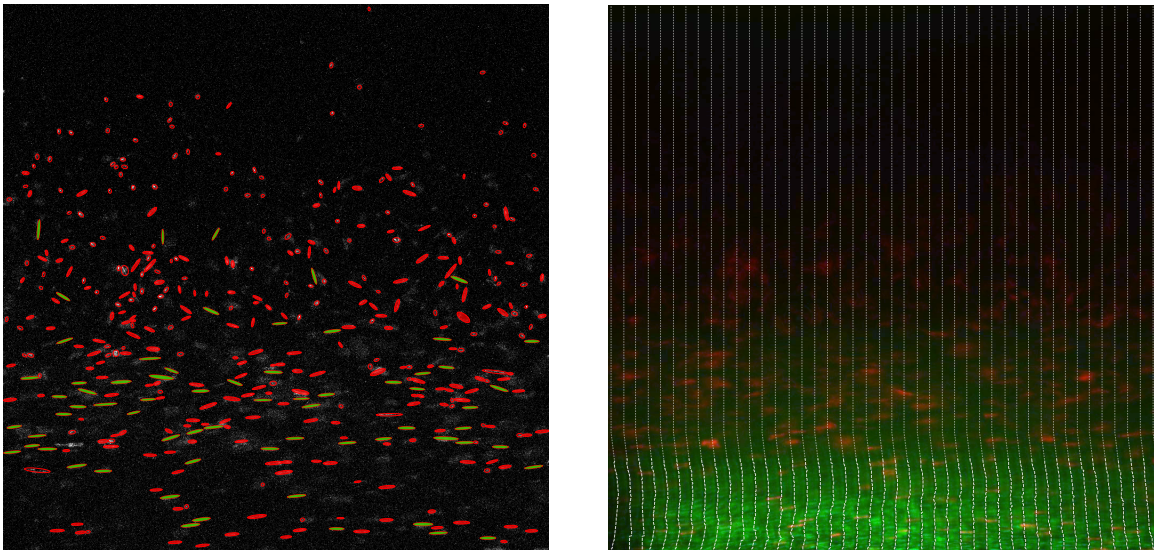


Figure 3.13: Detection of particles (left) and layer (right) from experiment 'Exp1000'. Detected particles are shown by red ellipse contours; red and green filling are applied for particle with aspect ratios greater than 2 and 6. Layers are tracked at the bottom (dashed line) and extrapolated (dotted lines).

3.5.2 Analysis

Pseudo images were captured with LSCM into two channels. One channel was gathering the fluorescent light from tracer particles, and the second channel was collecting the scattered light allowing to detect smectic layers. We chose the arbitrary colors green and red to display the scattered and fluorescence light in all figures. Tracer particles can be detected easily as they are rarely close to each other. Fluorescence images are first filtered, if necessary, then binarized and finally the elements corresponding to the fluorescent rods are fitted with an ellipse in order to measure: aspect ratio, position and orientation. We show in figure 3.13 two processed images. On the left the detected rods are fitted with ellipses and on the right the dark spaces between layers have been detected and highlighted with dashed white lines. These lines have been extrapolated with dotted lines into the nematic and isotropic phases.

From the single particle information we measure as a function of the height z: the number of dyed particles $N^\star$ together with the nematic and smectic order parameters. To measure $N^\star$ we use all detected elements, shown by red ellipse contour in figure 3.13. However, to measure the nematic order parameter, we select aspect ratios greater than two. This value has been chosen to eliminate most of the elements that correspond to particles out of focus, or in contact with other particles. Similarly, to measure τ we select aspect ratios greater than 6, in order to exclude the most of particle out of focus. Indeed, a rod out of focus appears darker, and because

the fluorescent molecules are gradually distributed along the particles' long-axes, when a rod is out of focus only its brighter side is detected. Consequently, the center of this detected element is shifted with respect to the actual center of the rod and therefore, reduces the smectic order parameter τ.

The measured elements were distributed into z-bins to measure $N^\star$, S_2 and τ as a function of z.
The mean orientation $\langle\alpha\rangle$ is measured in each bin in order to calculate S_2 using equation 2.41, where $d = 2$ and $\theta_i = \alpha_i - \langle\alpha\rangle$.
To measure the smectic order parameter, due to defects or distortions in the smectic layers, we measure the particles' position relative to the closest layer center instead of their absolute position. Then, we use equation 2.51, where x_j is the position relative to the layer center and N the number of elements in the bin.

The position of the denser phase is estimated at the height where the dyed particles are immobile. The nature of the phase has not been clearly identified in this work. We will call it the crystal phase as we expect a crystal phase for hard rods. However, note that polydispersity is likely to prevent the formation of a crystal (only a smectic B phase was identified in [90]). The smectic, nematic and isotropic phases are found using the order parameters (same criteria as in section 3.3.3). We expect the concentration of hard rods with an aspect ratio $p \approx 12$ to be of about twenty percent exiting the I-N interface towards the isotropic phase (see figure 3.8). Therefore, we decided to normalized $N^\star$ in order to have $N^\star(z_{I^+}) = 20\%$ when the isotropic phase meet the nematic phase. The 'end' of the isotropic phase was defined in section 3.3.3 estimated at $N^\star(z_{I^-}) = 1\% = N^\star(z_{I^+})/20$.

3.5.3 Results

We compare two experimental systems based on the rods 'LC012' and 'LC017'. The rods 'LC017', with the largest number (17), are longer, wider and more elongated. As a consequence, they are heavier and their mean gravitational length is smaller than the rods 'LC012'. In DMF, for the rods 'LC017' $l_g = 0.74\,\mu\text{m} \approx 2\sigma$, which is 4 times smaller than the rods 'LC012', where $l_g = 3.1\,\mu\text{m} \approx 10\sigma$. The aspect ratio of 'LC017' is 12.6 instead of 8.5 for 'LC012'. Note that the rods 'LC017' are also less polydisperse. In figure 3.14, we plot histograms of gravitational lengths for the two rod systems. These gravitational lengths are calculated based on SEM images, i.e.

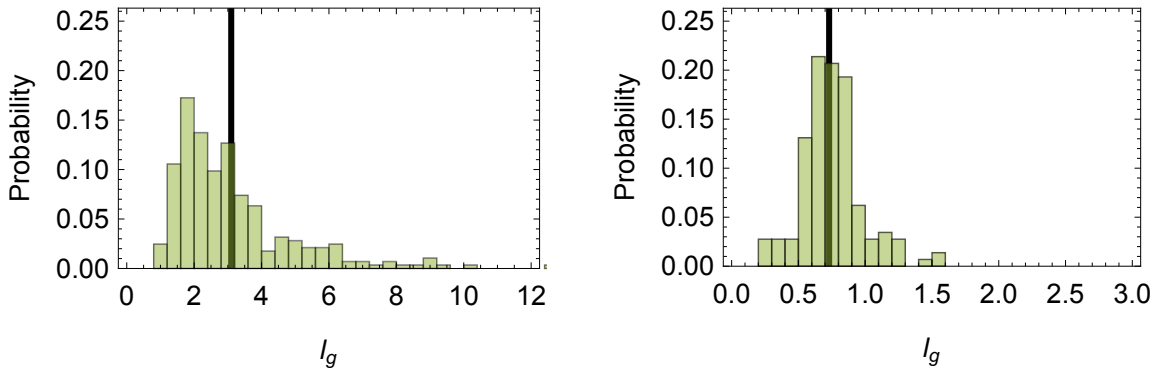
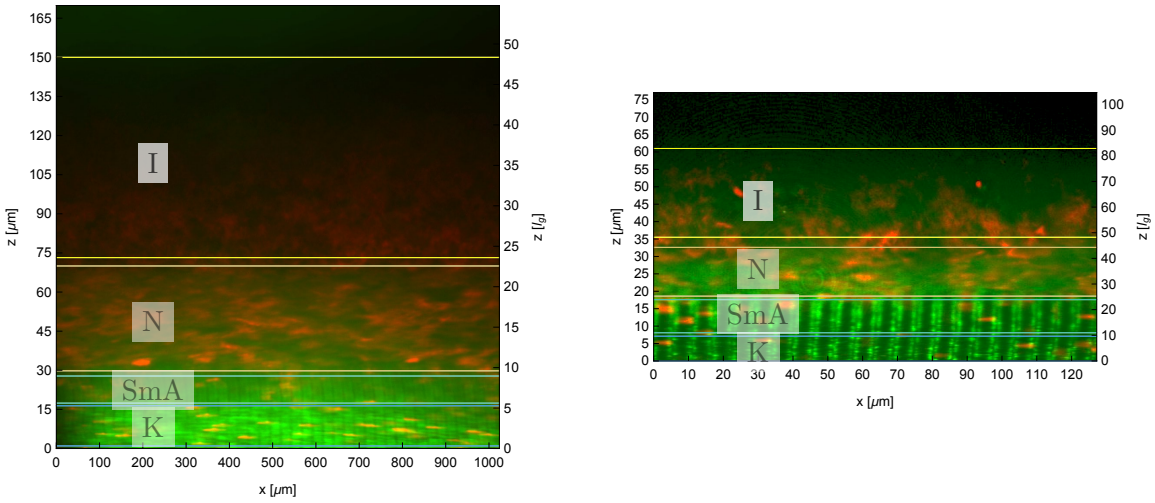


Figure 3.14: Histograms of the gravitational lengths, in DMF, for particles 'LC012' (left) and 'LC017' (right). The vertical black lines show the mean values.



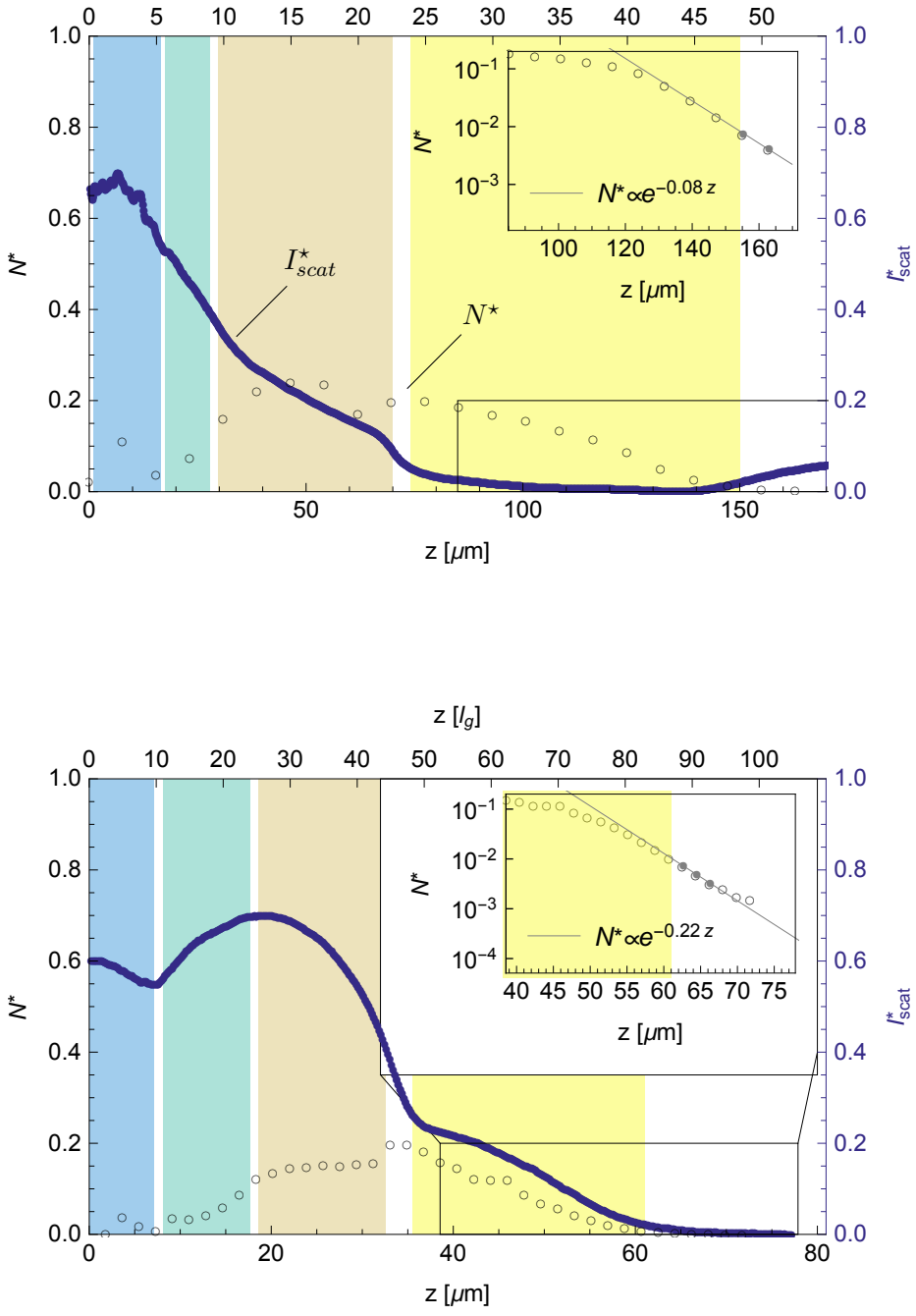
'Exp1000'/ 'LC011-12'/ light particles

'Exp0405'/ 'LC010-17'/ heavy particles

Figure 3.15: Average of 100 LSCM images of silica rods at sedimentation-diffusion equilibrium. We indicates the location of the isotropic (I, —), nematic (N —), smectic (SmA —) and crystal (K —) phases.

on the particles' size.

In figure 3.15, we show side-by-side representations of experiments 'Exp1000' and 'Exp0405', where mixtures of rods LC011-12 and LC010-17 were dispersed into pure DMF and observed from the side. For clarity, we will largely refer to these experiments as 'LC012' and 'LC017'. The images shown are averages over 100 snapshots, the green channel shows the back-scattered light and the red the fluorescent tracer particles. From top to bottom we delimit using horizontal lines the isotropic (I, —), nematic (N —), smectic (SmA —) and crystal (K —) phases. Because the gravitational length is larger for the rods 'LC012' than 'LC017', the field of view had to be increased in order to fit all 4 phases.



'Exp1000'
'LC011-12'
light particles

'Exp0405'
'LC010-17'
heavy particles

Figure 3.16: Back scaterred light intensity $I^{\star}$ (●) and scaled number of dyed rods $N^{\star}$ (○) plotted as a function of the height z. The inset shows a fit of the exponential decays of $N\star$, in the region $0.01 < N^{\star} < 0.001$.

In figure 3.16, we attempt to access the density profile of rods $\phi(z)$ in two ways: by measuring the number of dyed rods $N^\star$ (○) and the intensity of the back scattered light averaged over all frames $I^\star$ (●). The first signal is normalized to be equal to 20% on the isotropic side of the I-N interface, and the second to be equal to 70% at the maximum. It appears obvious that neither of them is proportional to the bulk rod concentration.
The scattered light (●) depends on many experimental details such as: imaging depth, the rod's organization, the field of view, etc. In particular, when the refractive index of rods and solvent is closely matched, as it is here, the back-scattered light from the rods is hard to predict. And indeed, we observe different scattered light signal in these two experiments.
The number of fluorescent rods $N^\star$ (○) is low in the smectic and crystal phases. Approaching the nematic phase, the number of dyed particles increases and a plateau is reached. This plateau lasts across the whole nematic phase and fairly deep into the isotropic phase. This density profile of dyed rods contrasts with the bulk volume fraction that should be going down almost linearly in this region. The dyed rods are not evenly distributed within the bulk due to a phenomenon called fractionation, also referred to as partitioning or segregation.

Partitioning in polydisperse LCs has been studied theoretically [79,80,107–111] and experimentally [112–114]. The difficulty here resides not only on polydispersity in both lengths *and* diameters, but also in the polydispersity in masses. This coupling between gravity and polydispersity has received less attention [115]. However, in an experiment similar to ours, a very polydisperse ($L = 216\,\mathrm{nm}\ \pm 55\%$) suspension of *goethite nanorods* was used, and particles were also stabilized by electrostatic double layer [113]. Although their gravitational length was one hundred times larger, their cell was 100 times higher too, and coexistence of isotropic, nematic, smectic and columnar phases was achieved. Whereas the smectic phase should be suppressed by a length polydispersity above 20% [111, 116], they observed smectic domains, concluding that fractionation was reducing polydispersity locally. Furthermore, they found that, on average, rods were longer in the nematic phases than in the isotropic. That is precisely what we expect in our system, not only the dyed but also the bulk particles should be subjected to partitioning.

Coming back to our experiments, in figure 3.16, we observe in both cases under-representation of dyed particles (○) in the smectic and nematic phases compared to the isotropic. This partitioning effect can be partly explained by the smaller mass of the dyed particles. We also suspect length-segregation in the smectic phase reducing further the amount of dyed rods. It is interest-

ing to note that the concentration of dyed rods increases again in the crystal phase, suggesting that rods have been kinetically trapped.

In the simulation, we observed for volume fractions between 0.01 and 0.001 an exponential decay of the density profile $\phi(z) \propto \exp(-z/l_g^{\text{s-d}})$. The extracted gravitational length $l_g^{\text{s-d}}$ formed a reasonable estimate of the actual gravitational length: we found $l_g^{\text{s-d}} \approx 1.1 l_g$. We explained that the discrepancy was related to the second viral coefficient and would disappear for $\phi\frac{L}{\sigma} << 1$. We propose to measure $l_g^{\text{s-d}}$ experimentally, for the rods 'LC012' ($\frac{L}{\sigma} = 8.5$, $l_g = 3.1\,\mu\text{m}$) and 'LC017' ($\frac{L}{\sigma} = 12.6$, $l_g = 0.74\,\mu\text{m}$). We use the normalized number of dyed particles $N^\star$ to approximate the rod volume fraction. The volume fractions $\phi < 1\%$ are fitted by an exponential profile (see insets of figure 3.16). We extract the gravitational lengths, $l_g^{\text{s-d}}(\text{LC012}) = 12\,\mu\text{m} \approx 4 l_g$ and $l_g^{\text{s-d}}(\text{LC017}) = 4.5\,\mu\text{m} \approx 6 l_g$. These measurements of the gravitational length are therefore 4-6 times larger than expected. We will come back on this in the next chapter. However, we would like to highlight that $l_g^{\text{s-d}}$ is measured at volume fraction $\phi < 1\%$. Therefore, there is a relatively small number of particles in this area of the sample. As a result the statistic is poor. Moreover, as less than 1:10000 rods contribute to this part of the density profile, we can then suspect partitioning to have an important effect. In consequence, the measurements of $l_g^{\text{s-d}}$ could be biased by a small fraction of the lightest dyed particles.

The different phases are identified by measuring the nematic and smectic order parameters plotted in figure 3.17. These order parameters were introduced on page 25. We locate the I-N interface when $0.2 < S_2 < 0.7$, the N-S when $0.2 < \tau < 0.4$ and the Sm-K where the rods are unable to move. We then measure the thickness of the phases, scale them by the gravitational length and compare them to our simulation and theoretical predictions in figure 3.18.

3.6 Experiments vs theory and simulation

3.6.1 Inflated upper sediments

We will first focus on the upper sediment, which we define from the dense smectic phase ($\phi = 60\%$) to the low density isotropic ($\phi = 1\%$). The width of the upper sediment W_{I+N+S} is indicated by the top of each column in figure 3.18. In theory, W_{I+N+S} is predicted to be practically the same for an aspect ratio of 10 (The. 10) or 13 (The. 13): $W_{I+N+S} \approx 32 l_g$.

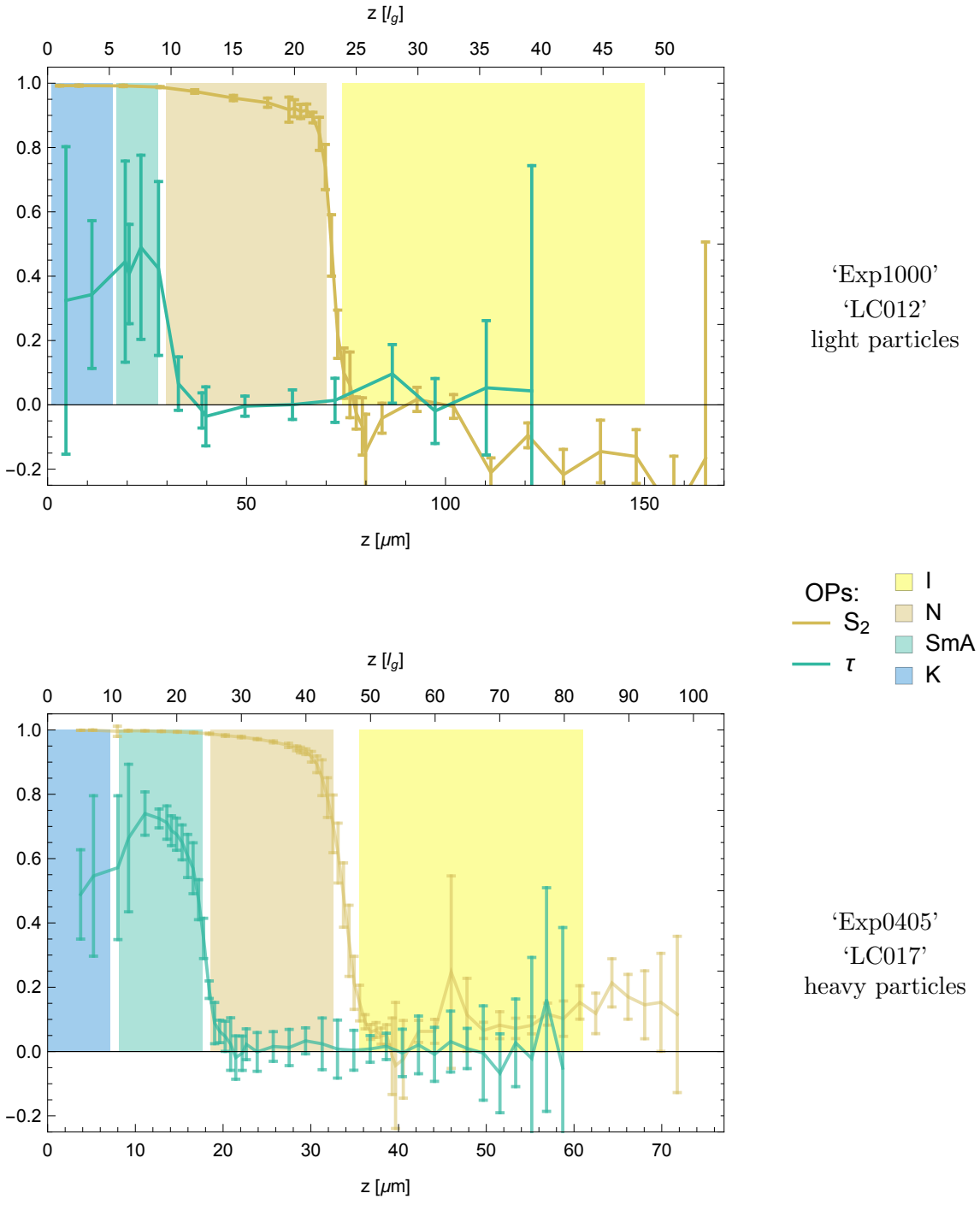


Figure 3.17: Smectic order parameter τ (—), and uniaxial nematic order parameter S_2 (—) against the height z. The error bars indicate standard deviation.

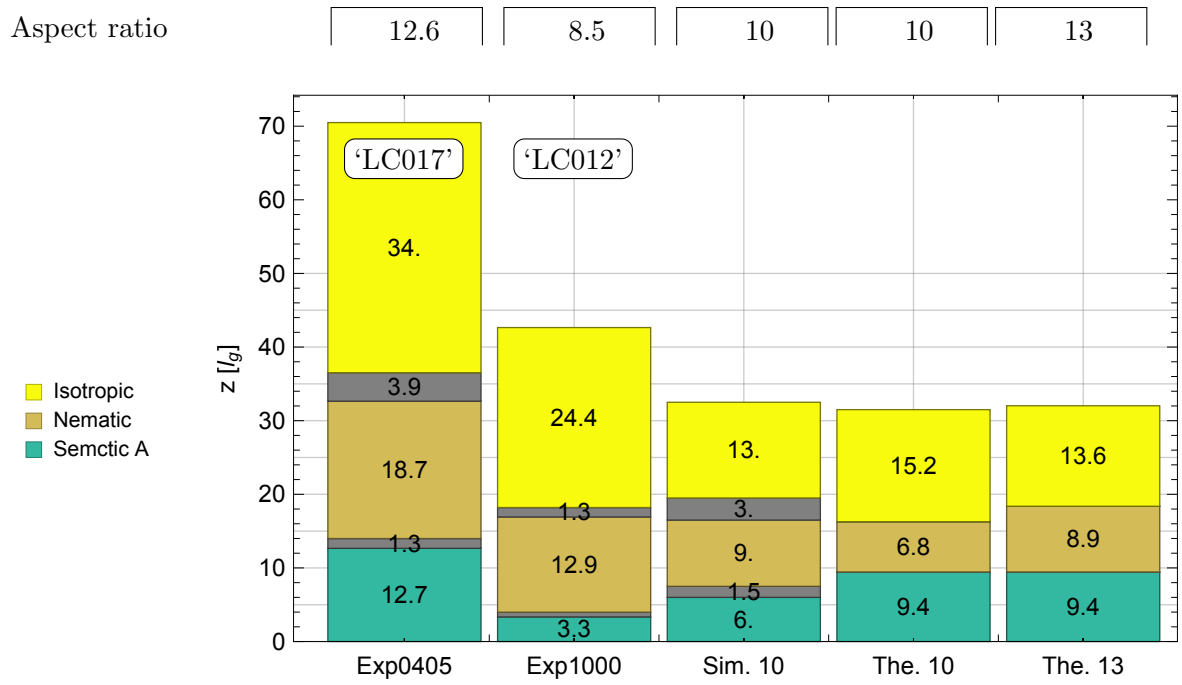


Figure 3.18: Width of the isotropic (■), nematic (■) and smectic (■) sediments for experiments (Exp), theory (The) and simulation (Sim). Results from Exp0405 and Exp1000, corresponding to silica rods 'LC017'($p = 12.6$) and 'LC012'($p = 8.5$) dispersed in pure DMF, are compared with the simulation of fused sphere with aspect ratio $p = 10$ and theoretical predictions of hard rods with $p = 10$ and 13.

However, it is striking that, in both experiments, W_{I+N+S} is larger than $32l_g$. Which means that the density profile is inflated. To quantify this inflation, we introduce an effective gravitational length such that $W_{I+N+S} = 32l_g^{eff}$. We find $l_g^{eff} = 1.33l_g$ for the rods 'LC012' and $l_g^{eff} = 2l_g$ for the rods 'LC017'.

We note that, the most extended density profile corresponds to the less polydisperse rods ('LC017'). This is an indication that polydispersity is not playing a major role in the inflation of the density profile. We do not expect double layer repulsion or the aspect ratio to play a role either in this part of the density profile (see chapter 4). In principle, only the gravitational length should matter. The rods' gravitational length was calculated using a density of $\rho_{rod} = 1900\,\mathrm{kg\,m^{-3}}$ [89] and by measuring their volume from SEM images (with a resolution of $25\,\mathrm{nm\ pixel^{-1}}$). In figure 3.14, we plot the histogram of gravitational lengths for both rod systems. One could imagine that only the smallest rods contribute to the I-N-SmA phases when the biggest, sedimenting faster, are mostly present in the crystal phase. Such an effect has been observed in simulations of polydisperse spheres [117], and would effectively increase the gravitational length, supporting our findings. However, this effect should be stronger for the most polydisperse rods, but that is not what we observe. Furthermore, it does not seem realistic that

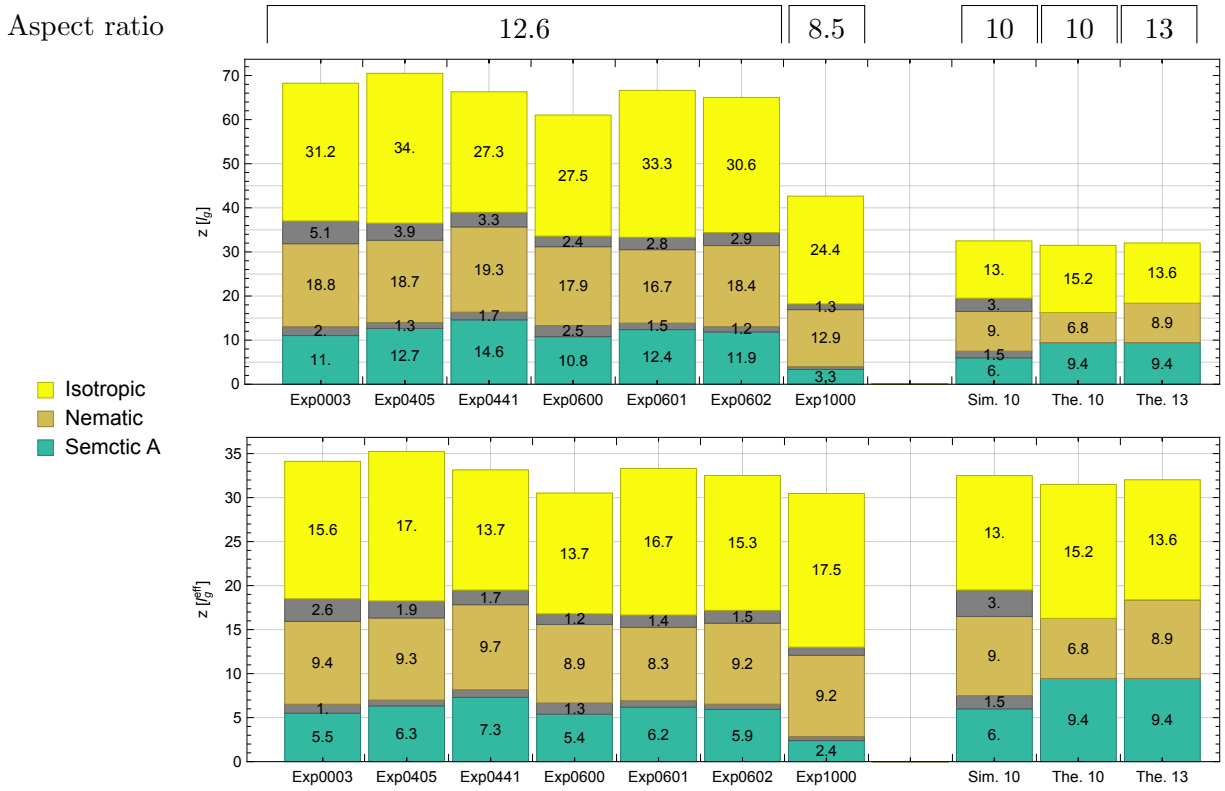


Figure 3.19: Width of the isotropic (■), nematic (■) and smectic (■) sediments for experiments(Exp), simulation (Sim) and theory (The). In the top and bottom graphs the widths are scaled by l_g and l_g^{eff}, respectively, where $l_g^{eff} = 1.33 l_g$ for 'Exp1000' (rods 'LC012'), $l_g^{eff} = 2l_g$ for other experiments (rods 'LC017') and $l_g^{eff} = l_g$ for simulation and theory.

this effect would increase the gravitational length, up to twice its original value, as observed for the rods 'LC017' ('Exp0405'). We then conclude that the inflation of the density profiles is not due to polydispersity.

An inflated apparent gravitational length has been observed [118–121] and theorized [101, 122–125] in the context of charged spheres. The phenomenon was attributed to the Donnan effect that takes into account the osmotic pressure of ions and counterions [36]. The most extreme behaviors were observed for dilute samples, at very low salt concentrations. In order to check for the effect of salt, experiments with rods 'LC017' were repeated in different solvents and at different salt concentrations. In figure 3.19 (top), we show the results obtained for experiments: in water with 1 mM NaCl, in pure DMF and in DMF with 0.5 mM LiCl. We can then for each experiment determine l_g^{eff}, such that the total width of the isotropic, nematic and smectic phases $W_{I+N+S} = 32 l_g^{eff}$. We report in table 3.3 the effective gravitational length for each experiment. For all experiments with rods 'LC017', regardless of the solvent or salt concentration, we find $l_g^{eff} \approx 2l_g$. Therefore, within experimental error, the addition of salt did

Tag	Bulk rod	Experiment	Salt	p	Solvent	l_g [µm]	l_g^{eff}/l_g	$l_g^{\text{s-d}}/l_g$
Exp0003	LC017	Side	NaCl (1 mM)	12.6	Water	0.8	2.1	4.8
Exp0405	LC017	Side	None	12.6	DMF	0.74	2.3	6.4
Exp0441	LC017	Bottom	None	12.6	DMF	0.74	2.1	4.1
Exp0600	LC017	Bottom	LiCl (0.5 mM)	12.6	DMF	0.74	1.9	6.5
Exp0601	LC017	Bottom	LiCl (0.5 mM)	12.6	DMF	0.74	2.1	7.4
Exp0602	LC017	Bottom	LiCl (0.5 mM)	12.6	DMF	0.74	2.	6.1
Exp1000	LC012	Side	None	8.5	DMF	3.1	1.33	3.6

Table 3.3: Gravitational length for each experiment calculated from SEM images (l_g), by scaling of the accumulated $I + N + SmA$ phases (l_g^{eff}) and by fitting $N^\star(z)$ for $\phi < 1\%$ ($l_g^{\text{s-d}}$).

not affect the thicknesses of the upper sediment. However, we will show chapter 4 why we think the Donnan effect could still explain our inflated density profiles.

For each experiment we equally provide $l_g^{\text{s-d}}$ in table 3.3. We have a general trend where $l_g^{\text{s-d}} > l_g^{eff} > l_g$. However, as discussed before, the measurement of the gravitational length in the semi-dilute regime $l_g^{\text{s-d}}$ should be considered with particular caution, as we suspect partitioning to strongly affect it.

We would like to asses whether or not the density profiles are inflated in a linear fashion. It is clear that, for the rods 'LC017' ('Exp0003' to 'Exp0602'), all phases are inflated. However, they do not seem equally inflated. To ease the comparison, we plot in figure 3.19 (bottom) the thickness of the phases scaled by l_g^{eff}. Let us now compare the relative thicknesses of the different phases, keeping in mind that, independently of this inflation, we expect some discrepancy between experiment and theory, mostly due to polydispersity.

For all experiments we observe a smaller smectic phase than predicted by theory, which is compensated by larger isotropic and nematic phases. We argue that this is mostly due to polydispersity. Indeed, polydispersity is known to destabilize the smectic phase into a nematic phase [111, 116]. Then, we expect to find a smaller smectic and a larger nematic phase in experiments. This is further supported by the fact that we observe the smallest smectic phase for the most polydisperse rods ('LC012', 'Exp1000'). Additionally, we note that an increased nematic/decreased smectic phase was also found in our simulation, which indicates that other effects than polydispersity can contribute to reduce the extent of the smectic phase. Finally, the slightly larger isotropic phase observed in experiments could be explained by a small effect of partitioning in the low density isotropic phase [117], or equally by an effective lowering of the aspect ratio due to double layer interactions [9, 102]. The effect of double layer interaction will be further discussed in the next chapter.

In sum, we observed a global inflation of the upper sediment ($0.01 < \phi < 0.6$), which is not due to polydispersity. This inflation concerns all three isotropic, nematic and smectic phases. However, we argued that polydispersity is affecting the relative thicknesses of the isotropic, nematic and smectic phases. We then believe that it is fair to approximate a linear inflation of the density profile within $1\% < \phi < 60\%$.

From a theoretical perspective the aspect ratio mainly affects the isotropic and nematic phases: the larger is the aspect ratio, the larger is the nematic phase relative to the isotropic. This is confirmed in our experiments: for the rods 'LC012' with $p = 8.5$ we find a larger isotropic phase than the other experiments where $p = 12.6$. This will be further discussed in the next section dedicated to the nematic order parameter.

3.6.2 Nematic order parameter

We propose now to compare the nematic order parameter with predictions from DFT calculations [70]. To realize this we need to determine the nematic order parameter, not as a function of z but as a function of ϕ. We will approximate that the volume fraction is decreasing linearly from the beginning of the smectic phase ($\phi = 51\%$) to the end of the isotropic $\phi = 1\%$. This approximation is made based on the results from simulation and the educated assumption that the density profile is inflated linearly. Note that bulk simulation found the smectic to crystal transition at $\phi \approx 60\%$. In the left panel of figure 3.20, we show that a straight line gives a good estimate of the density profile found in simulation. In right panel of figure 3.20, we plot the nematic order parameter, from the simulation as a function of the volume fraction. The volume fraction is measured (○) or approximated by a linear profile (□). We observe that the nematic order parameter measured in simulation shows a very good agreement with the one predicted by DFT for fused spheres. However, the nematic order parameter from experiment shown in the left panel of figure 3.21 show some discrepancies with DFT calculations. As expected, the I-N transition occurs at higher volume fraction for the smaller aspect ratio (□, 'Exp1000', rods 'LC012'). However, we note that all experimental curves are shifted toward lower aspect ratios, in particular for the rods 'LC017' (○). Given our crude estimate of the volume fraction this is not very surprising. Nevertheless, it might have a physical origin as double layer repulsion is expected to effectively decrease the rod's aspect ratio [9, 102].

Surprisingly the nematic order parameter is higher in experiments than in simulation or

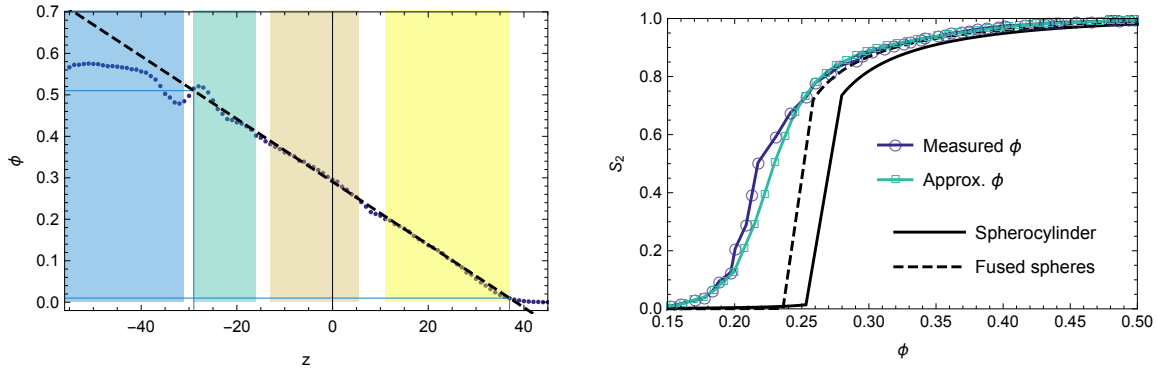


Figure 3.20: (Left) Quasi-linear density profile from simulation of fused sphere with $p = 10$. (Right) The nematic order parameter S_2 measured in simulation is compared to theoretical prediction for fused spheres (▪ ▪ ▪) and spherocylinder (▬) of aspect ratio p=10.

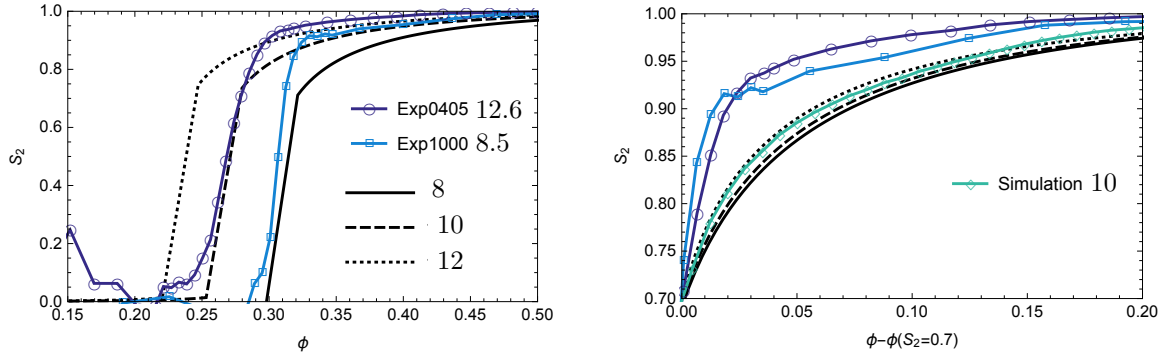


Figure 3.21: (Left) The nematic order parameter S_2 measured in experiments 0405 ($p = 12.6$) and 1000 ($p = 8.5$) is compared to theoretical prediction for spherocylinder with aspect ratios of 8, 10 and 12. (Right) All curve are shifted to cross each other at $S_2 = 0.7$.

theory. In figure 3.21 (right), we shift all the curves $S_2(\phi)$ such that $S(0) = 0.7$. We can then more easily compare the orientational order parameter close to the I-N phase transition, i.e. close to the new origin. The experimental values (▬, ▬) rise faster and higher than predicted by theory(▬), or found in the simulation (▬). This might be related to double layer interactions between rods [126]. However, we believe this is part of a different story, and should be the subject of a devoted study.

3.7 Conclusion and outlook

In this chapter, we have studied the sedimentation-diffusion equilibrium of colloidal rods by means of theory, simulation and experiments. On the theoretical side, we have determined the density profile for hard rods with an aspect ratio ranging from 5 to 20 using a method that can be generalized to any aspect ratio. We have shown that the width of the upper sediment,

defined as the accumulated thickness of the isotropic, nematic and smectic phases, primarily depends on the gravitational length of the rod and is about $32l_g$. We demonstrated that this value should, within 10%, remain constant for any aspect ratio considered.

The molecular dynamics simulation of fused spheres with an aspect ration of 10 showed a good agreement with the theoretical prediction. The thickness of the sediment was found to be only 10% wider than predicted. We showed that concentration of rods in the crystalline phase was relatively low, presumably due to the observed deformations and defects. Putting aside the crystalline phase, we reached even better agreement on the size of the sediment. This result validates the approximations made in our theoretical treatment within a satisfactory 5 to 10% error margin. It also confirms previous results showing that the local density approximation can still be used at low gravitational length [92, 117].

In both theory and simulation, the density profile was found to be decreasing mostly linearly with z. In experiments, the density profile was measured indirectly. The phases were located by measuring the nematic and smectic order parameters based on real-space measurements of the position and orientation of tracer particles. Then, comforted by results from simulation and theory, a linear decrease of the density profile was assumed from the dense smectic phase to the semi-dilute isotropic phase ($\phi = 1\%$). This allowed us to compare the nematic order parameter as a function of the volume fraction between theory, simulation and experiments. We found good agreement between simulation and theory, but interestingly, we measured surprisingly high nematic order parameters in the experiments, which will be considered in a separate study.

We would like to stress the fact that equilibrium is rarely achieved in sedimentation-diffusion experiments of colloids, mainly due to large gravitational length. Indeed, the gravitational length is setting the size of the sediment. And large sediments take longer to equilibrate. Our system is in that sense exceptional. Having a small gravitational length had two advantages: first, we obtained equilibrium within a few hours, and second, the phase behavior could be directly measured as a function of the height z. Having the ability to do so allowed us to confront directly experiments to simulation and theory, revealing inflated density profiles. Indeed, we measured experimentally the thickness of the upper sediment, and found it to be 1.33 to 2 times wider than predicted ($32l_g$). In the next chapter, we will show how accounting for the Donnan effect can qualitatively reproduce this result.

Sedimentation-diffusion equilibrium equally enables formation of dense liquid crystal phases

that can be tricky to obtain experimentally. In chapter 6, we will exploit this phenomenon to study to behavior of dense phases in confinement.

We will finish with an outlook. An important improvement of the technique would be to have the same particles used as tracer and bulk. It would then be possible to measure the volume fraction directly.

A more accurate determination of the density profile of rods in the semi-dilute region could be achieved by labeling all rods and preventing convection effects. Because of partitioning effect, we believe this kind of experiment could only be conclusive for extremely mono-disperse rods or with a technique allowing to measure the rods' size in the semi-dilute isotropic phase.

Our results on the nematic order parameter are rather surprising and worth investigating. As a matter of fact, our rod system is the only one that allows direct and precise enough measurement of the nematic order parameter so it can be compared with simulation and theory. However, by focusing our attention on the whole phase behavior, we had to make sacrifices in time and space resolution. We think that measurement dedicated to the nematic phase would be a better start to look at the possible effect of charges or other phenomena on the nematic order parameters of colloidal rods.

One of the most interesting and straightforward outlooks of this work would be to look at the dynamics of the sediment formation. If the concentration of rods can actually be measured rather than inferred, the sedimentation dynamics will be easily captured. Indeed, our present system matches experimental requirements in terms of time scale and system size.

Finally, this work stirs questions about partitioning. Mixing rods with different sizes but similar gravitational length, for example silica rods($\rho = 1900$) and SU8 rods($\rho = 1200$) could bring interesting insight.

Acknowledgments

I would like to express my deep and sincere gratitude to my colleague Maxime Tortora supervised by Pr. Jonathan Doye. Both parts on theory and simulation of this chapter were based on Maxime's data. In particular, he provided me: the EOS and nematic order parameter for hard rods and fused spheres, and the sedimentation-diffusion simulation of fused sphere. He also was a very helpful resource to discuss with.

I am grateful to Clément Robert for collecting the data of the experiment 'Exp0003' during his summer project.

I also would like to acknowledge Eric Grelet, Pavlik Lettinga and Mariana Menegon for insightful discussions.

Chapter 4

The Donnan effect on the sedimentation-diffusion equilibrium of silica rods

Abstract

In this chapter, we first predict the density profile of charged rods and compare it with experimental results. The density profile is obtained by introducing effective rod dimensions, that account for double layer repulsion, and modifying the EOS to include the contribution of ions and counterions. We show that experimental observations can be qualitatively reproduced by accounting for the osmotic pressure of ions within the Donnan zero-field limit. A match is obtained in the regime where the concentration of counterions is small compared to the concentration of salt. We further show that, in that regime our theoretical treatment predicts a linear inflation of the density profile.

The method allows us to determine an effective surface charge of the rods as well as the range of the double layer repulsion $\alpha\kappa^{-1}$, where α is a constant and κ the inverse Debye length. In particular, at $I = 1$ mM, experimental results are matched for a rod surface charge $\sigma_{Don} = -1260\, e\,\mu\text{m}^{-2}$ and for a range of the double layer repulsion $\alpha\kappa^{-1} \approx 8\kappa^{-1} = 80$ nm.

The surface charge of a silica rod is estimated separately by considering the dissociation constant of silica in water and by measuring the rod zeta potential leading to a self-consistent estimate of $|\sigma_-| > 82500\, e\ \mu\text{m}^{-2}$.

We finally discuss the discrepancy between the two surface charges and limitations of the method.

NB: In this chapter, the particle diameter will be refereed to as D, instead of σ to avoid confusion with the surface charge.

4.1 Introduction

In chapter 3, we studied the sedimentation-diffusion equilibrium of colloidal rods. We first predicted that the width of the sediment formed by hard rods, excluding the crystalline phase, does not depend on the aspect ratio[1]. The accumulated width of the isotropic, nematic and smectic phases was found to be $W_{I+N+S} \approx 32 l_g$, in agreement with the simulation presented in the subsequent section. However, we experimentally measured density profiles up to twice as wide as predicted. We established that polydispersity was not responsible for the dilation of the density profiles and suggested that the Donnan effect[2] might be. We would like to highlight that similarly inflated density profiles have been observed in preliminary experimental results on SU8 rods, recently developed in our lab [86], but also in an independent study on silica rods [93,127]. The authors of [93,127] studied the sedimentation-diffusion equilibrium of silica rods with aspect ratio $p \approx 5$. Combining 3D confocal microscopy and core-shell particles they were able to detect every single particle and measure the density profile of rods. In particular, they showed that an effective diameter had to be introduced to account for the excess of excluded volume due to double layer repulsion [93].

In this chapter, we aim to predict how an effective diameter and the Donnan effect would impact the density profile of silica rods at varying salt concentrations, and confront the prediction to experimental results. To this end, we will focus on physical conditions matching our experiments. In particular, we will consider relatively small Debye lengths κ^{-1} relative to the particle radius a, such that $\kappa a \geq 1$. The chapter will be structured as follows. In section 4.2, we will first explain how double layer repulsion can be accounted for by introducing an effective diameter. We will then provide a general background on the Donnan effect and include both the osmotic pressure of ions (within the Donnan approximation) and the effective diameter to our theoretical treatment. Finally, we will show that, for any experimentally relevant salt concentration and effective diameter, we can find an effective particle surface charge that qualitatively reproduces our experimental observations. In section 4.3, we will independently estimate the surface charge of silica rods. First theoretically, by considering the dissociation constant of silanol groups in water and then experimentally by measuring the zeta-potential of the silica rods. We will further consider the effect of ion condensation. The surface charges

[1] for the range of aspect ratio studied $5 < p < 20$

[2] Within this thesis we use 'Donnan effect' to refer to the effect of ions of the sedimentation-diffusion equilibrium of colloids.

found in sections 4.2 and 4.3 will be compared in section 4.4.

4.2 Sedimentation-diffusion equilibrium of charged rods

In the previous chapter, we introduced the differential equation and initial conditions governing the density profile of colloids in sedimentation-diffusion equilibrium. The differential equations can be generalized to charged colloids

$$\frac{d\phi}{dz} = -l_g^{-1}\,\phi(z)\left(\frac{d\Pi_c^\star}{d\phi} + \frac{d\Pi_i^\star}{d\phi}\right)^{-1} , \tag{4.1}$$

where $\Pi_c(\phi)$ is the equation of state of the charged colloids and $\Pi_i(\phi)$ the equation of state of the ions (added salt plus counterions). The initial condition remains

$$\Pi^\star(z=0) = \phi_0\, H\, l_g^{-1}. \tag{4.2}$$

In section 4.2.1 and 4.2.2, we will determine $\Pi_c(\phi)$ and $\Pi_i(\phi)$. Then, in section 4.2.3, we will solve the differential equation for various salt concentrations and show that density profiles are consistent with experimental results, in the relevant range of effective diameters and salt concentrations. In section 4.2.4, we will determine for $I = 1$ mM, what surface charge and range of the double layer repulsion reproduces our experimental results. Finally, in sections 4.2.5 and 4.2.6 we will discussed the origin of linearities in the density profiles and what inflation we predict in the semi-dilute regime.

4.2.1 Mapping of charged rods on the phase behavior of hard rods

In this section, we aim to determine the equation of state of charged rods in the regime where $\kappa a \geq 1$.

Double layer repulsion between rods will affect the equation of state in two ways: (1) the screened electrostatic repulsion will increase the excluded volume between particles, and (2) a twisting effect (the alignment of charged particles is energetically unfavorable) will slightly shift the I-N phase transition to higher concentration [126]. Twisting is mostly affecting thin and weakly charged rods, i.e. when $\kappa a < 1$. For this reason and for simplicity twisting effects will fall out

of the scope of this work.

The double layer repulsion can be accounted for by attributing effective length and diameter to the rods [9, 102, 126, 128]:

$$L_{eff} = L + \alpha\kappa^{-1} \text{ and } D_{eff} = D + \alpha\kappa^{-1} \ . \tag{4.3}$$

This was first suggested in Onsager's seminal paper [9]: "the effective range of the double layer repulsion will be a modest multiple of the screening distance $1/\kappa$", and confirmed by experimental work [102, 128].

The idea is that the excluded volume between charged rods can be approximated by the excluded volume between hard rods with slightly larger dimensions. The equation of state for charged rods with an aspect ratio $p = L/D$ can then be approximated to the one of hard rods with an aspect ratio $p_{eff} = L_{eff}/D_{eff}$. As discussed before, the density profile of hard rods can be obtained solving equation

$$\frac{d\phi^{eff}}{dz} = -l_g^{-1}\,\phi^{eff}(z)\left(\frac{d\Pi^{\star}}{d\phi^{eff}}\right)^{-1} \ , \tag{4.4}$$

with initial condition

$$\Pi^{\star}(z=0) = \phi_0^{eff}\,H\,l_g^{-1}. \tag{4.5}$$

Then the density profile of charged rods is

$$\phi(z) = \phi^{eff}(z)\frac{v_0}{v_0^{eff}}, \tag{4.6}$$

which means that

$$\Pi^{\star}(z=0) = \frac{v_0^{eff}}{v_0}\phi_0\,H\,l_g^{-1}. \tag{4.7}$$

In sum, within this model, the double layer repulsion has two consequences: (1) to effectively lower the aspect ratio of the particles and (2) to effectively increase the pressure at the bottom. This will translate into the density profile as (1) a wider isotropic region compensated for by a thinner nematic one and (2) a larger crystalline region. Therefore, this will not affect the accumulated width of the isotropic, nematic and smectic phases W_{I+N+S}, and cannot explain

experimental observations of inflated density profiles. Nevertheless, double layer repulsion will be accounted for, in our theoretical treatment.
In the next section, we will introduce the Donnan effect and show how it can affect sediments of rods.

4.2.2 Donnan equilibrium

We just showed that double layer repulsion between rods will inflate the crystalline part of the density profile but will not change the thickness of the upper sediment. However, inflation can be generated by an inhomogeneous distribution of salt. Indeed, when the variation of osmotic pressure of colloids and salt become comparable $\frac{d\Pi_c^\star}{d\phi} \approx \frac{d\Pi_i^\star}{d\phi}$, we expect from equation 4.1, to observe an inflation of the density profile. Inhomogeneous concentration of salt due to the presence of colloids is characterized by the Donnan equilibrium, this phenomenon has been observed for dispersions of charged spheres [118–121].
Imagine a semi-infinite space. The colloids sediment at the bottom of the cell bringing with them their monovalent counterions. The top of the cell acts as a reservoir for the salt concentration. We call n_s the number density of added salt molecules in the reservoir (before dissociation) and $n_c(z)$ the number density of colloids at a height z. The concentration of added salt is related to the ionic strength of the dispersing medium by $n_s = IN_A$. We assume that each colloid releases a number Z_c of counterions that are free to move and contribute to the ions' osmotic pressure. In the zero-field limit, the total osmotic pressure becomes $\Pi(z) = \Pi_c(z) + \Pi_i(z)$, where Π_c and Π_i are the partial pressures of colloids and ions. Note that the partial pressure of ions is contributed by the added salt *and* the counterions.
Considering ions as a perfect gas, the pressure and concentration of ions are directly proportional. The osmotic pressure of salt will affect the density profile if $\frac{d\Pi_i(z)}{dz} \neq 0$, or equivalently if $\frac{d\Pi_i}{d\phi} \neq 0$, where $\phi = \frac{n_c v_0}{V}$ is the volume fraction of colloids. Then, the density profile will not be affected if the concentration of ions is homogeneous. When colloids release counterions, it locally increases the concentration of salt. If this increase of salt is not compensated for, it will induce an excess of osmotic pressure and inflate the density profile. Note that the released counterions have all the same charge. Due to electroneutrality, the counterions cannot escape from their colloids by themselves. They have to 'pair' with an oppositely charged ions that were initially present in solution. We consider two limiting cases.

In the high salt concentration limit, the counterions released by the colloids can 'pair' with widely available oppositely charged ions and diffuse towards the top of the cell, where there are no colloids. In order to completely compensate for the counterions, $\frac{1}{2}Z_c$ charges will be expelled from the proximity of each colloid. Half of them will be positive and half negative. This process will ensure that the concentration of salt is homogeneous. The counterions will not affect the density profile.

$$\frac{d\Pi_i}{d\phi} = 0 \ . \tag{4.8}$$

In the limit of no added salt, the concentration of ions is fully contributed by counterions. Because there are no oppositely charged ions in solution, the counterions cannot migrate in the bulk. Therefore, their concentration is proportional to the concentration of colloids $n_c = \frac{\phi}{v0}$, by extension

$$\frac{d\Pi_i}{d\phi} = \frac{1}{v_0} Z_c k_b T \ . \tag{4.9}$$

This should be compared to the contribution of the colloids. Which, for low concentration of colloid, is of the order of magnitude of a perfect gas of colloids $\frac{d\Pi_c}{d\phi} = \frac{1}{v_0} k_b T$. This shows that, in the limit where $Z_c >> 1$, the osmotic pressure of the counterions dominates the density profile.

The difference of total osmotic pressure Π, between an osmotic cell containing a number density of colloids $n_c = \frac{\phi}{v0}$, and its reservoir with a fixed number density of monovalent salt molecules n_s, has been determined for arbitrarily shaped colloids [123]. The authors assumed an ideal gas of ions diffusing in zero-electric field (i.e. constant Donnan potential) and a relatively small volume fraction of colloids ($\phi_c << 1$). They found that the difference of pressure between the osmotic cell and the reservoir, $\Delta\Pi = \Pi(cell) - \Pi(res)$, followed

$$\frac{\Delta\Pi(n_c)}{k_B T} = \frac{\Delta\Pi_c(n_c, y=0)}{k_B T} + \frac{\Delta\Pi_i(n_c)}{k_B T} = \frac{\Delta\Pi_c(n_c, y=0)}{k_B T} + 2n_s \left(\sqrt{1+y^2} - 1\right) \text{ with } y = \frac{Z_c n_c}{2n_s} \ , \tag{4.10}$$

and where Z_c is the number of released counterions per particle.

In order to find the sedimentation-diffusion equilibrium density profile, we determine the

variation of osmotic pressure with the volume fraction

$$\frac{d\Pi^\star}{d\phi} = \frac{v0}{k_BT}\frac{d\Pi}{d\phi} = \frac{1}{k_BT}\frac{d\Pi}{dn_c} = \frac{1}{k_BT}\left(\frac{d\Pi_i}{dn_c} + \frac{d\Pi_c}{dn_c}\right). \tag{4.11}$$

The equation of state of the colloid Π_c is known. To determine Π_i the equation 4.10 can be generalized to the case the case of sedimentation-diffusion equilibrium [101]. At sedimentation-diffusion equilibrium the number density of colloids n_c becomes a function of the height z: $\Pi = \Pi(n_c(z))$. Assuming that at any height z the counterions are in equilibrium with the reservoir, $\Delta\Pi$ from equation 4.10 becomes the difference between the pressure at a given position $\Pi(n_c(z))$ and the pressure in the reservoir, i.e. at the top of the cell $\Pi(n_c(H) = 0)$. This applies to the partial pressure of ions

$$\Delta\Pi_i = \Pi_i(z) - \Pi_i(H). \tag{4.12}$$

We then obtain from equation 4.10 the ion partial pressure

$$\Pi_i(z) = \Pi_i(H) + 2n_s(\sqrt{1+y^2} - 1)k_BT, \tag{4.13}$$

and its derivative as a function of n_c

$$\frac{d\Pi_i}{dn_c} = \frac{d}{dn_c}\left(2n_s(\sqrt{1+y^2} - 1)k_BT\right), \tag{4.14}$$

as at equilibrium $\Pi_i(H)$ is constant. In terms of volume fraction, this is equivalent to

$$\frac{d\Pi_i^\star}{d\phi} = v_0\frac{d}{d\phi}\left(2n_s(\sqrt{1+y(\phi)^2} - 1)\right) \text{ with } y(\phi) = \frac{Z_c\phi}{2v_0n_s}. \tag{4.15}$$

For a charged rod with effective volume and volume fraction v_0^{eff} and ϕ^{eff}

$$\frac{d\Pi_i^\star}{d\phi^{eff}} = v_0^{eff}\frac{d}{d\phi^{eff}}\left(2n_s(\sqrt{1+y(\phi)^2} - 1)\right) \text{ with } y(\phi) = \frac{Z_c\phi^{eff}}{2v_0^{eff}n_s}. \tag{4.16}$$

When accounting for ions' osmotic pressure and double layer repulsion, the differential equation 4.10, that governs the density profile of colloids, takes the form

$$\frac{d\phi^{eff}}{dz} = -l_g^{-1}\,\phi(z)\left(\frac{d\Pi_c^\star}{d\phi^{eff}} + \frac{d\Pi_i^\star}{d\phi^{eff}}\right)^{-1}. \tag{4.17}$$

Then the effective density profile can be found using the initial condition 4.7, to solve equation 4.17, where $d\Pi_c^\star(\phi^{eff})$ is the equation of state of a hard rod with aspect ration $p^{eff} = L^{eff}/D^{eff}$ and $d\Pi_i^\star(\phi^{eff})$ is given by equation 4.16. The real volume fraction can be simply recovered with equation 4.6.

We note that there is an intrinsic inconsistency in equation 4.16 and 4.17, as the expression of the osmotic pressure of ions is derived in the zero-field limit, which assumes no screening between the colloids $\kappa D < 1$, whereas the introduction of the effective diameter relies on the assumption that $\kappa D > 1$. In our experiments $\kappa D > 1$, which means we have screening and therefore a part of the counterions will not be free and will not be able to contribute to the inflation of the density profile.

In the next section, we will use equation 4.17 to determine the density profile of silica rods, from the isotropic to the crystal phase. This violates the assumption of low colloids concentration. Accounting for large colloid volume fraction would probably entail a factor $1/(1-\phi_c)$, this approximation will be further discussed in section 4.4.

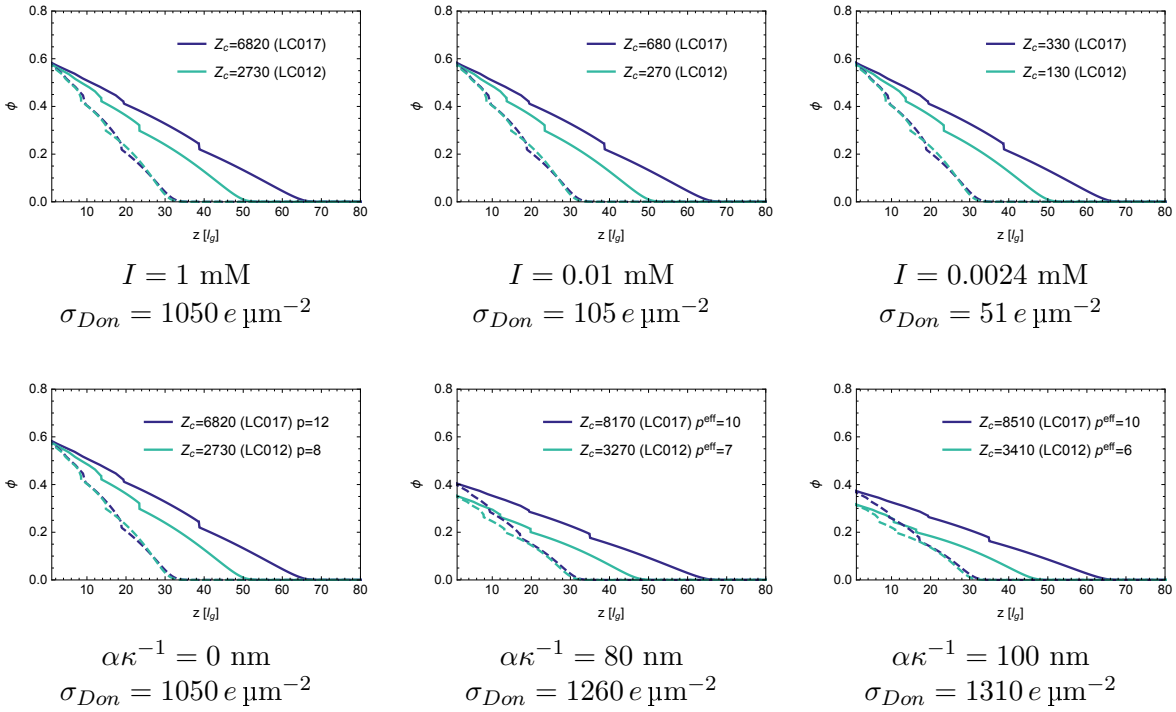
4.2.3 Density profile of charged rods

In sections 3.5 and 3.6, we experimentally measured the thickness of the isotropic, nematic and smectic phases. The accumulated thickness W_{I+N+S} of these three phases, was refereed to as 'the upper sediment'. These upper sediments were found to be wider than $32l_g$, which was the value predicted by theory. Without added salt, we experimentally observed density profiles inflated by 100% in the case of silica rods 'LC017' and by 33% for the particles 'LC012'. Experiments were repeated on silica rods 'LC017' dispersed in a water-based 1 mM NaCl solution and a DMF-based 0.5 mM LiCl solution. These two experiments also resulted on a density profile inflated by 100%. This is surprising as, in principle, the Donnan effect depends on the concentration of salt.

By essence, within the Donnan approximation, the osmotic pressure of ions can inflate any density profile as long as the particles' charge is high enough. In order to assess if the Donnan effect is the cause of our inflated density profiles, we will primarily rely on one experimental observation: the upper sediment of the rods 'LC012' was found to be less inflated than the rods 'LC017'. And importantly, both rod systems should have the same surface charge.

We will first neglect the effect of double layer repulsion $\alpha = 0$ and proceed as follows: equation 4.17 will be solved for the two rod systems, at different salt concentrations imposing a volume fraction $\phi = 59\%$ at the bottom ($\phi(z = 0) = \phi_{SmA-K} = 0.59$). A unique surface charge will be used for both rod systems. This surface charge will be used as a fitting parameter to obtain the upper sediment of the silica rods 'LC017' matching experimental results, i.e. $W_{I+N+S}(\text{LC017}) = 64l_g$. If the Donnan effect is responsible for the inflated density profiles, for a fixed surface charge, we should obtain for the rods 'LC012' $W_{I+N+S}(\text{LC012}) < 64l_g$; a perfect agreement would be obtained for $W_{I+N+S}(\text{LC012}) = 42l_g$, i.e. an inflation by a factor 1.33. The results are presented in the top row of figure 4.1. For $I = 1$ mM, we obtain $W_{I+N+S}(\text{LC017}) = 64l_g$ for a surface charge $\sigma_{Don} = 1050\, e\,\mu\text{m}^{-2}$, which correspond to a colloid charge $Z_c(LC017) = 6820$. The rod LC012, smaller, have fewer charges $Z_c(LC012) = 2730$. Consequently, their density profile is less inflated: we find $W_{I+N+S}(\text{LC012}) = 50l_g$, which is in qualitative agreement with experiments. For smaller ionic strength, the surface charge required to inflate the density profile of the rod LC017 by a factor of 2 is reduced. However, the shape of the density profile and the value of $W_{I+N+S}(\text{LC012})$ are unaffected. Therefore, for any ionic strength we expect the Donnan effect to inflate less the upper sediment of the rod LC012 than the rod LC017, which is in agreement with experimental results.
We also note that σ_{Don} is found to be largely proportional to $\sqrt{I}$. We then observe that the density profiles are independent of the ratio $\frac{\sigma_{Don}^2}{I} \propto \frac{Z_c^2}{n_s}$. We will come back to this in section 4.2.5.

We now consider the effect of double layer repulsion, that can be reduced to the parameter α, which quantifies the range of the interaction ($\alpha\kappa^{-1}$). We fix the ionic strength $I = 1$ mM corresponding to a Debye length $\kappa^{-1} = 10$ nm in water, and vary the parameter α. As done before, for different values of α we tune σ_{Don} to obtain $W_{I+N+S}(\text{LC017}) = 64l_g$. The density profiles are calculated for the initial condition $\phi^{eff}(z = 0) = \phi_{SmA-K} = 0.59$ and plotted in figure 4.1 (bottom row). Qualitatively, we still have $W_{I+N+S}(\text{LC012}) < W_{I+N+S}(\text{LC017})$, as observed in experiment. However, as mentioned before, including double layer repulsion has two effects: (1) it effectively reduces the rods' aspect ratio and so the extent of the nematic phase, (2) it reduces the actual concentration of rods in the different phases. This second point affects the Donnan equilibrium. It can be compensated for, by increasing the surface charge. However, it does not equally impact the rods 'LC012' and 'LC017' as, when α is increased, $W_{I+N+S}(\text{LC012})$ is slightly reduced from $50l_g$ to $46l_g$, which only brings us a closer to the experimental value of



$I = 1$ mM
$\sigma_{Don} = 1050\, e\,\mu\text{m}^{-2}$

$I = 0.01$ mM
$\sigma_{Don} = 105\, e\,\mu\text{m}^{-2}$

$I = 0.0024$ mM
$\sigma_{Don} = 51\, e\,\mu\text{m}^{-2}$

$\alpha\kappa^{-1} = 0$ nm
$\sigma_{Don} = 1050\, e\,\mu\text{m}^{-2}$

$\alpha\kappa^{-1} = 80$ nm
$\sigma_{Don} = 1260\, e\,\mu\text{m}^{-2}$

$\alpha\kappa^{-1} = 100$ nm
$\sigma_{Don} = 1310\, e\,\mu\text{m}^{-2}$

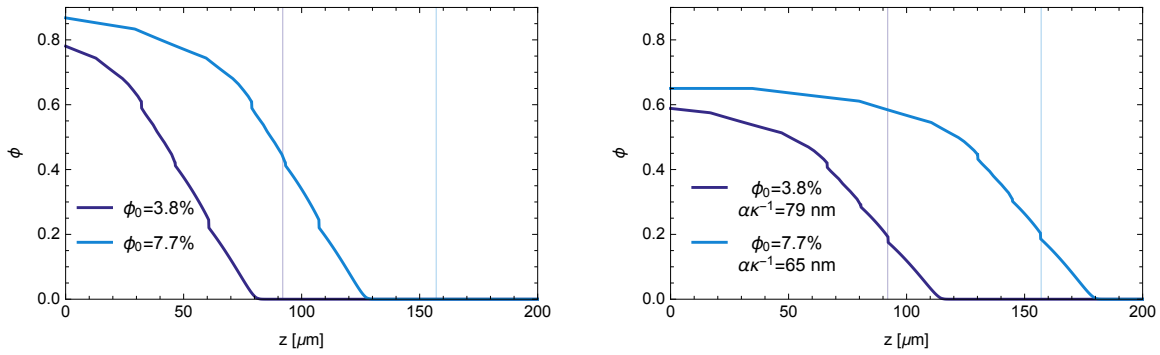
Figure 4.1: Donnan equilibrium for the silica rods 'LC012' and 'LC017', varying the ionic strength with $\alpha = 0$ (top row) and the range of double layer repulsion $\alpha\kappa^{-1}$ with $I = 1$ mM, i.e. $\kappa^{-1} = 10$ nm (bottom row). The dashed lines correspond to the case of hard rods: $Z_c = 0$ and $\alpha = 0$. The surface charge of the rods σ_{Don} was adjusted to obtain $W_{I+N+S}(\text{LC017}) = 64 l_g$ (see text).

$42 l_g$.

In sum, for any salt concentration or effective diameter the Donnan effect can reproduce qualitative our experimental results. It appears curious that the Donnan effect is keeping the relative thickness of the different phases constant (figure 4.1, top row). In other words, the density profile seems globally inflated in a linear fashion. This will be explained in section 4.2.5. In the next section, we will determine the effective diameter of the silica rods dispersed in 1 mM NaCl solution.

4.2.4 Initial conditions and effective diameter

In the previous sections, we focused on the upper part of the sediment. This was motivated by experimental and theoretical difficulties concerning the crystalline phase. Indeed, we do not know the equation of state in the dense crystalline phase ($\Pi > 15 k_B T$). Moreover, rods' polydispersity is likely to affect the maximum packing fraction and the ability to form crystalline phase. Another concern is about the modeling of charged rods as hard rods with an effective diameter $D_{eff} = D + \alpha\kappa$. At very high pressure, we expect the value of α to go down, which is



$\alpha\kappa^{-1} = 0$ $(Z_c = 6820)$ $\alpha\kappa^{-1} \neq 0$ $(Z_c = 8190)$

Figure 4.2: Density profile predicted for the rods 'LC017' dispersed in 1 mM NaCl solution in water and for an initial volume fraction ϕ_0. The vertical lines indicate the height of the I-N interface found in experiments.

not accounted for by our theoretical treatment.

Despite the limitations about the crystalline phase, considering initial conditions is, for us, the most accurate way to quantify the range of the double layer repulsion between the rods. Indeed, the double layer repulsion effectively increases the volume of the rods. Therefore, the actual volume fraction is lowered and we expect the *total* thickness of the sediment to be increased. We are unfortunately not able to measure directly the volume fraction of the rods. However, we can measure the size of the sediment.

Experimentally, the thickness of the sediment was measured for rods 'LC017' with initial volume fraction $\phi = 3.8\%$ and 7.7% dispersed in 1 mM NaCl-water solution. The experiment were performed by Clément Robert as part of his master project. The thickness of the upper sediment was found to be independent of the initial volume fraction of the rods: in both cases $W_{I+N+S} \approx 64 l_g$. However, the thickness of the sediment from the bottom to the isotropic-nematic interface, was found to be respectively $92 \pm 10\,\mu\text{m} = 124 \pm 13 l_g$ and $157 \pm 10\,\mu\text{m} = 212 \pm 13 l_g$. In figure 4.2 (left), we plot the predicted density profile for negligible double layer interaction $\alpha = 0$ but accounting for the Donnan effect ($l_g^{eff} = 2l_g$, $Z_c = 6820$). Without double layer repulsion, the I-N interfaces are predicted to be located at $z \approx 90 l_g$ and $z \approx 160 l_g$, which is about 30% lower than observed in experiments (indicated by vertical lines). This can be corrected for by accounting for double layer repulsion. For each initial condition, we tune the range of the double layer repulsion $\alpha\kappa^{-1}$ to reproduce experimental results. The best matches are plotted in figure 4.2 (right), note that Z_c was slightly increased to keep l_g^{eff} equal to $2l_g$.

We then deduce the range of the double layer interaction to be a "modest multiple" of

the Debye length $\alpha\kappa^{-1} \approx 70 - 80$ nm, i.e. $\alpha \approx 7 - 8$. This result is in good agreement with previous work on shorter silica rods dispersed in a water-DMSO mixture of Debye length $\kappa^{-1} \approx 10$ nm [93]. The authors of found a value $\alpha = 8$. It is equally comparable to values of 3 to 4 found for fd-virus [102].

In conclusion, we have determined, for $I = 1$ mM, the surface charge of silica rods

$$\sigma_{Don} = 1260\, e\, \mu\text{m}^{-2} \ , \tag{4.18}$$

and the range of the double layer interaction

$$\alpha\kappa^{-1} \approx 75 \text{ nm} \ . \tag{4.19}$$

4.2.5 Linearities of the density profiles

We find quasi-linear density profiles, in the range of concentrations $0.01 < \phi < 0.6$, because both colloids and ions have an EOS *globally* quadratic in ϕ. Concerning the colloids, we show in figure 4.3 that the EOS can be approximated by a quadratic function[3]. And for the ions, this is because we are in the particular regime of the Donnan equilibrium where $y < 1$ [121]. The parameter y, introduced in equation 4.15, governs the Donnan equilibrium

$$y(\phi) = \frac{Z_c\phi}{2v_0 n_s} = \frac{S\sigma_{Don}\phi}{2v_0 N_A I}, \tag{4.20}$$

where S is the particle surface. For example, we can calculate y corresponding to the density profiled of figure 4.1: for $0.0024\ mM < I < 1$ mM we have $0.1 > y > 0.005$. For small values of y we can take the Taylor expansion of equation 4.15, going up to the second order we obtain

$$\frac{d\Pi_i^\star}{d\phi} = \frac{Z_c^2\phi}{2n_s v_0} \equiv \beta\phi \ . \tag{4.21}$$

We can then see that the equation of state of the ions is quadratic in ϕ. This also shows that for a ratio $\frac{Z_c^2}{n_s}$ constant the density profile is left unchanged. Then any decrease of salt concentration can be completely canceled by a decrease of the colloid charge, as we saw in figure 4.1 (top row). Within this approximation, we can see how the rod dimensions affect the Donnan effect by

[3] We have no physical argument to explain it. But it would not work without phase transitions. Independently the EOSs are not quadratic in ϕ, for example in the isotropic phase $\Pi^\star \approx \phi + \frac{D}{L}\phi^2$.

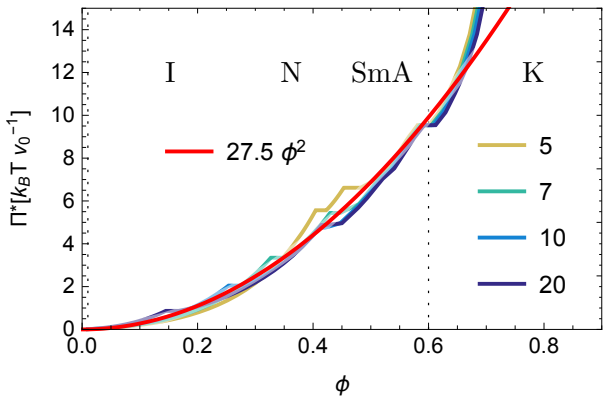


Figure 4.3: Equation of state of hard spherocylinders with various aspect ratios. The red line shows the quadratic-like behavior between $\phi = 1\%$ and $\phi = 60\%$.

comparing β for different rod sizes, for simplicity we neglect the double layer repulsion:

$$\frac{\beta_1}{\beta_2} = \frac{\sigma_{Don}^2 S_1^2 \phi}{2 n_s v_{01}} \frac{2 n_s v_{02}}{\sigma_{Don}^2 S_2^2 \phi} = L_1 / L_2 \ , \tag{4.22}$$

where S is the rod surface area.

For rods with identical surface charge, the longer rods will be more affected by the Donnan effect.

As witnessed in figure 4.3, the equation of state of hard rods can be roughly approximated by a quadratic function and then

$$\frac{d\Pi_c^\star}{d\phi} \approx 55\phi \equiv \gamma\phi \ . \tag{4.23}$$

Substituting expressions 4.21 and 4.23 in the differential equation 4.1 we obtain

$$\frac{d\phi}{dz} = -l_g^{-1} \ (\gamma + \beta)^{-1} \equiv -(\gamma \, l_g^{eff})^{-1} \ , \tag{4.24}$$

which offers a mathematical description to the effective gravitational length:

$$l_g^{eff} = l_g \left(1 + \frac{\beta}{\gamma}\right) . \tag{4.25}$$

For charged rods, the Donnan effect can then be qualitatively captured, in the concentration region $1\% < \phi < 60\%$, by introducing an effective gravitational l_g^{eff} that linearly inflates the density profile.

	Prediction						Experiment		
	$Z_c = 0$			$Z_c \neq 0$					
	l_g^{eff}	l_g^{s-d}	l_g^{dilute}	l_g^{eff}	l_g^{s-d}	l_g^{dilute}	l_g^{eff}	l_g^{s-d}	l_g^{dilute}
LC012	l_g	$1.12l_g$	l_g	$1.6l_g$	$1.24l_g$	l_g	$1.33l_g$	$3.6l_g$	–
LC017	l_g	$1.14l_g$	l_g	$2.0l_g$	$1.39l_g$	l_g	$1.9 - 2.3l_g$	$4 - 7l_g$	–

Table 4.1: Estimates of the gravitational length in the dense ($0.01 < \phi < 0.6$), semi-dilute ($0.001 < \phi < 0.01$) and dilute regimes, from theory and experiments. Prediction including the Donnan effect ($Z_c \neq 0$) considers a surface charge $\sigma_{Don} = 1260\, e\, \mu m^{-2}$, an ionic strength $I = 1$ mM and $\alpha = 8$ such that $l_{g-LC017}^{eff} = 2l_g$.

If we impose for the rods 'LC017' $l_g^{eff}/l_g = 2$, then $\beta_{17} = \gamma$ and so for the rods 'LC012'

$$\frac{l_g^{eff}}{l_g} = \left(1 + \frac{\beta_{12}}{\gamma}\right) = \left(1 + \frac{L_{12}}{L_{17}}\right) \approx 1.5. \tag{4.26}$$

Solving properly the differential equation led in the previous section to a value of 1.6. This confirms that we are able to qualitatively capture the Donnan effect, on the upper sediment, by approximating a quadratic form of the EOS of hard rods.

4.2.6 Donnan effect in the semi-dilute isotropic

At low volume fraction, the variation of osmotic pressure of the colloids with ϕ can be approximated by Onsager's expression

$$\frac{d\Pi_c^\star}{d\phi} \approx 1 + \phi\frac{L}{D} \approx 1 + 10\,\phi. \tag{4.27}$$

Both equations 4.21 and 4.27 are exact in the limit where $\phi \to 0$. It appears then clearly that, in that limit, $\frac{d\Pi^\star}{d\phi}$ will be dominated by the colloid's contribution. And then, the Donnan effect can be neglected, so the tail of the density profile will follow $\phi(z) \propto \exp(-z/l_g^{dilute})$ with $l_g^{dilute} = l_g$. For an intermediate volume fraction of $\phi = 1\%$ we can calculate $\frac{d\Pi_i^\star}{d\phi} = \phi\,\beta \approx \phi\,\gamma \approx 0.5$ when $\frac{d\Pi_c^\star}{d\phi} \approx 1 + 10 * 0.01 = 1.1$. Neither the rods' interaction nor the Donnan effect can be neglected. However, the dominant term is the perfect gas, which explains why the density profile may seem exponential in a small range of concentration. In order to compare with experiment, we fit the theoretical density profile tails between $0.01 < \phi < 0.001$, with and without Donnan effect, for the rods 'LC012' and 'LC017' and extract l_g^{s-d}. The values are provided in table 4.1 where we equally remind the effective gravitational length l_g^{eff} estimated for $1\% < \phi < 60\%$.

Without Donnan effect ($Z_c = 0$), by definition $l_g^{dilute} = l_g$ and by construction $l_g^{eff} = l_g$.

As discussed previously, $l_g^{s-d} > l_g$ due to the non-zero second virial coefficient. We include the Donnan effect and double layer repulsion by considering a ionic strength $I = 1$ mM, $\alpha\kappa^{-1} = 80$ nm and a surface charge $\sigma_{Don} = 1260\, e\,\mu\text{m}^{-2}$. These values are chosen to reproduce the behavior of the rods 'LC017' in the dense part: $l_{g-LC017}^{eff} = 2l_g$. For the two rod systems we find that the Donnan effect is increasing l_g^{s-d} by about $10-15\%$. In the same table, we equally provide the values found in experiments. The semi-dilute gravitational length was found to be four to seven times larger. However, this part of the density profile may not be at equilibrium due to experimental limitations. Indeed, no special care was taken in order to prevent convection effects, which are expected to disturb the sedimentation-diffusion equilibrium at low densities [117,119]. Also, note that the measurement is based on the dyed particles, which have a slightly higher gravitational length, are more polydisperse and are only present in tracer amount. As a result, in the semi-dilute part of the sediment, the measured gravitational length is likely to be biased and the statistics are poor.

4.3 Surface charge of silica rods in water

In this section, we first estimate the surface charge of silica rods based on the rods and solvent properties. We also estimate the surface charge by zeta-potential measurements and consider hypothetical counterion condensation.

4.3.1 Introduction

When dispersed into water, colloids usually acquire charges by releasing counterions in the solvent. The electric potential between the colloid surface and the bulk is commonly described by two regions: the Stern layer and the diffuse layer. In figure 4.4, we overlay a plot of this potential and a cartoon of a colloid with surrounding ions/counterions. We draw a spherical colloid with radius $a = 1$. Close to the colloid surface $r \approx 1$ we represent high density of condensed counterions within the Stern layer, which is indicated by vertical dashed lines. In this region, the potential drops linearly. Further away from the colloid, the potential drops exponentially following Debye-Hückel theory (equation (2.57)).

We aim here to estimate the number of counterions per colloid that contribute to the Donnan effect. However, we are unaware how to measure it directly. We will instead first determine

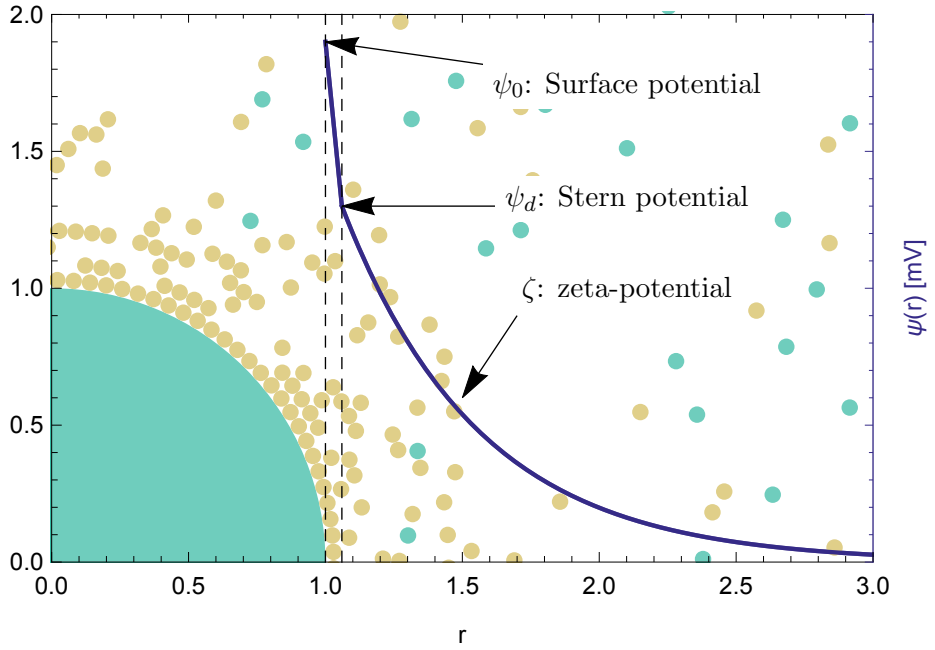


Figure 4.4: Representation of the double layer potential, generated by a charged colloid of radius $a = 1$, as a function of the distance to the colloid center r.

the surface potential of silica surfaces based on the silanol groups' dissociation constant. We will then measure the 'surface charge' at the slipping plane by electrophoretic measurement. The slipping plane is the location, in the diffuse layer, where the ζ-potential is measured. Finally, we discuss counterion condensation following Manning's paper [129], and conclude. The aim of this section is to estimate, the number of charges that contribute to the Donnan effect, and thus for different salt concentrations. Numerical results are applied to silica rods 'LC017' dispersed into MilliQ water (pH = 5.6) and we use NaCl as electrolyte. We address four points: (1) we estimate the absolute surface charge of silica rods dispersed into water; (2) we measure silica rods' electrophoretic mobility to deduce their ζ-potential; (3) we discuss counterion condensation following Manning's paper [129]; and (4) we sum up results and conclude.

4.3.2 Theoretical estimate

Colloids commonly possess electric charges. These charges are acquired through dissociation of terminal groups. In the case of silica, these groups are mainly silanol groups SiOH,

$$\mathrm{SiOH} \rightleftharpoons \mathrm{SiO^-} + \mathrm{H^+} \ . \tag{4.28}$$

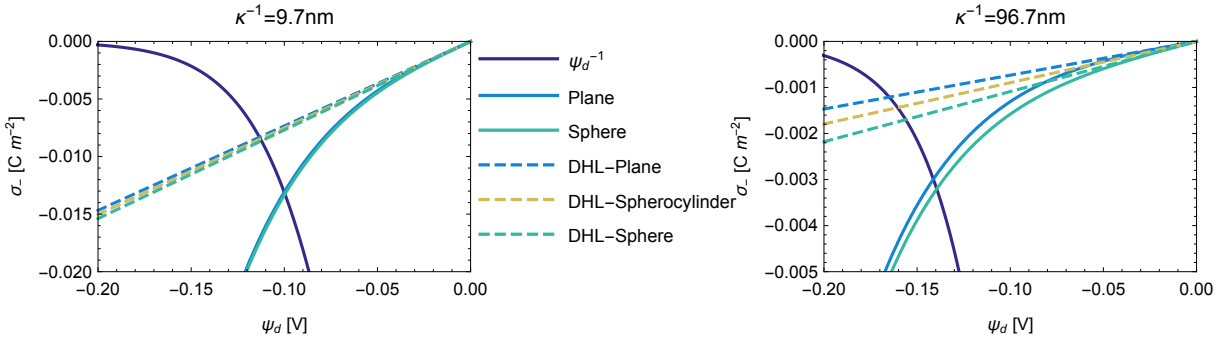


Figure 4.5: Surface charge of a silica σ_- as a function of the Stern potential Ψ_d, for pH = 5.6 and pK = 5.8. The dark blue line is the inverse of equation (4.29), the light blue and green full lines are equation (4.30) and (4.31). The dashed lines are approximations of σ_- valid at low Ψ_d.

Behrens *et al.* proposed a method [130] to determine both the Stern potential ψ_d and the absolute surface charge σ_- for spheres and planes. It consists of solving two self-consistent equations $\psi_d(\sigma_-)$ and $\sigma_-(\psi_d)$. The diffuse layer potential is given by

$$\psi_d(\sigma_-) = \frac{1}{\beta e} \ln \frac{-\sigma_-}{e\Gamma + \sigma_-} - (\mathrm{pH} - \mathrm{pK}) \frac{\ln 10}{\beta e} - \frac{\sigma_-}{C} \ , \tag{4.29}$$

where $\beta = (k_B T)^{-1}$, e is the elementary charge, $\Gamma = 8\,\mathrm{nm}^{-2}$ estimates the density of SiOH sites, pK is the silanol dissociation constant and $C = 2.9\,\mathrm{F\,m}^{-2}$ is the Stern layer phenomenological capacity. The surface charge depends on the surface geometry, for a plane

$$\sigma_-(\psi_d) = \frac{2\epsilon_0\epsilon_m\kappa}{\beta e} \sinh\left(\frac{\beta e \psi_d}{2}\right) \ , \tag{4.30}$$

and for a sphere

$$\sigma_-(\psi_d) = \frac{2\epsilon_0\epsilon_m\kappa}{\beta e} \left(\sinh\left(\frac{\beta e \psi_d}{2}\right) + \frac{2}{\kappa a} \tanh\left(\frac{\beta e \psi_d}{4}\right)\right) \ , \tag{4.31}$$

with $\epsilon_0\epsilon_m$ the permitivity of the medium and κ the inverse Debye length. For a spherocylinder the surface charged can be found elsewhere [131]:

$$\sigma_-(\psi_d) = \psi_d \epsilon_0\epsilon_m\kappa \left(\frac{\mathrm{K}_1(\kappa a)}{\mathrm{K}_0(\kappa a)}\right) \ , \tag{4.32}$$

where K_1 and K_2 are modified Bessel function of the second kind, and the radius $a = D/2$. Note this is only valid for small ψ_d, as it relies on the Debye-Hückel linearization of the Poisson Boltzmann equation.

	$I = 1$ mM		$I = 0.1$ mM		$I = 0.01$ mM		$I = 0.0025$ mM	
pK = 5.8	-13.2	-82500 e	-6.4	-40000 e	-3.1	-19000 e	-2.0	-12500 e
pK = 7.5	-3.2	-20000 e	-1.7	-10500 e	-0.9	-5500 e	-0.6	-3500 e

Table 4.2: Surface charge of silica cylinder in water for a pH of 5.6 and calculated from the self-consistent equations (4.29) and (4.33). Rounded values are given in $\mathrm{mC\,m^{-2}}$ and $\mu\mathrm{m}^{-2}$ for different ionic strengths I and silanol dissociation constants pK [132, 133].

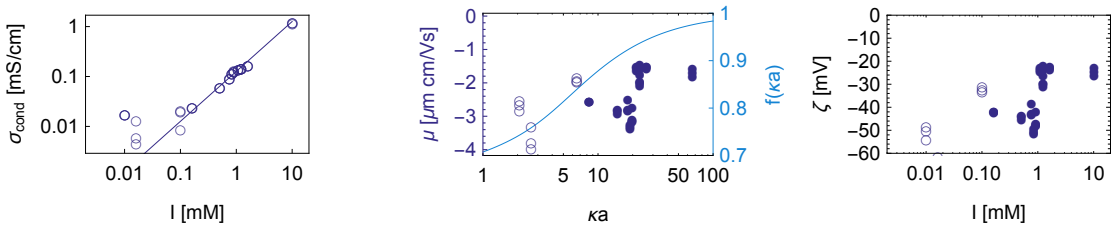
The self-consistent values ψ_d and σ_- can be determined graphically by finding the interception between the inverse of equation (4.29) with the appropriate σ_- function. In figure 4.5, we give an example for a pH of 5.6, a pK of 5.8 and ionic strengths of 1 mM ($\kappa^{-1} = 9.7$ nm) and 0.01 mM ($\kappa^{-1} = 96.7$ nm). We plot with full lines the surface charge σ_- for planar and spherical surfaces within the Poisson-Boltzmann description, and with dashed lines the surface charge following the Debye-Hückel description. We remark that: (1) at higher salt concentration (smaller κ^{-1}) the surfaces are more charged and (2) the Debye-Hückel linearization of the Poisson Boltzmann equation (dashed curves) underestimates the surface charge. In consequence, the surface charge of our rods will be better estimated by equation (4.30) and (4.31) than (4.32). We approximate

$$\sigma_-^{\text{spherocylinder}} \approx \sigma_-^{\text{sphere}}/2 + \sigma_-^{\text{plane}}/2. \tag{4.33}$$

Different values of pK are reported in literature. We find pK = 7.5 in [130, 132] and pK = 5.8 in [133, 134]. We determine the surface charge for these different values in table 4.2. We find that, within our experimental parameters, *the surface charge of silica cylinders increases monotonically with the concentration of salt.*

4.3.3 Experimental estimate

The mobility of silica rods and the conductivity of dispersing medium were measured using Malvern *Zetasizer Nano Z* with disposable cells. The applied effective voltage was 150 V, which corresponded to an electric field $E = 3\,\mathrm{mV\,\mu m^{-1}}$. The volume fraction of rods was $\phi \approx 10^{-6}$. The measurements were performed for ionic strength ranging from $I = 10^{-2}$ mM to $I = 10$ mM. For strong monovalent electrolyte, and sufficiently low concentration, the conductivity is related



(a) (b) (c)

Figure 4.6: Measurements of ζ-potential and conductivity σ_{cond} for silica rods 'LC017' ($L = 5.2\,\mu m$ and $a = D/2 = 200$ nm) dispersed into aqueous sodium chloride electrolyte (pH $\approx 5-6$). The ionic strength I and inverse Debye length κ are calculated from the concentration of added NaCl. The open symbols in (b) and (c) correspond to the region where the conductivity is not proportional to the ionic strength in (a), i.e. $I < 0.16$ mM.

to the ionic strength I by:

$$\sigma_{cond} = I(\Lambda_+ + \Lambda_-), \tag{4.34}$$

where Λ_+ and Λ_- are the limiting molar conductivities of the cations and anions. At 25 °C, $\Lambda_+(Na^+) = 5.01\,mS\,m^2\,mol^{-1}$ and $\Lambda_-(Cl^-) = 7.635\,mS\,m^2\,mol^{-1}$ [135].
In figure 4.6 (a), we plot the measured and predicted (from equation (4.34)) conductivities as a function of the NaCl contribution to the ionic strength I. For $I > 0.16$ mM the conductivity is proportional to the concentration of added salt. However, we observe discrepancies at lower ionic strength.

The ζ-potential of a colloid is related to its electrophoretic mobility μ by Henry equation:

$$\mu = \frac{2\epsilon_m\epsilon_0\zeta f(\kappa a)}{3\eta_m}, \tag{4.35}$$

where η_m is the viscosity of the medium, $f(\kappa a)$ Henry's function and ζ the ζ-potential. Henry's function has been derived by Oshima for infinite and weakly charged spherocylinders [136]:

$$f(\kappa a) = \frac{1}{3}\left(2 + \frac{1}{\left(1 + \frac{2.55}{1+\exp(-\kappa a)}\right)^2}\right). \tag{4.36}$$

Available implementations for higher charges [137] and finite size effect [138] are not reported here for simplicity. However, note that they would only produce a small change.
The measured silica rod mobilities, as a function of the ionic strength, are presented in figure 4.6

(b). We plot them as a function of the product κa, where κ is the inverse Debye length and a the particle radius. The ζ-potential can then be calculated from the mobilities using equation (4.35) and (4.36). In figure 4.6 (c), we plot the calculated ζ-potential as a function of the ionic strength. If we neglect the open circles, we observe $\zeta \approx -45$ mV for $I < 1$ mM and $\zeta = -25$ mV for $I > 1$ mM. The origin of this sudden jump at $I = 1$ mM is unknown to us. It is unlikely to be due to aggregation, as the particles are stable around $I = 1$ mM. Furthermore, the electric field was kept constant, so it is not believed that this is due to flow or field alignment of the rods [138, 139].

The ζ-potential provides us with a lower estimate of the rods surface potential. This can be converted to a lower estimate of the surface charge using equation (4.33). For $I = 1$ mM, taking $\zeta = -40\,\mathrm{mV}$ we read on figure 4.5 (left)

$$\sigma_-(-0.04) = -3.3\,\mathrm{mC\,m^{-2}} = -20700\,e\,\mu\mathrm{m}^{-2}\ , \tag{4.37}$$

taking $\zeta = -20\,\mathrm{mV}$ we read

$$\sigma_-(-0.02) = -1.5\,\mathrm{mC\,m^{-2}} = -9600\,e\,\mu\mathrm{m}^{-2}\ . \tag{4.38}$$

Both values are compatible with an absolute surface charge of $\sigma_- = -82500\,e\,\mu\mathrm{m}^{-2}$ corresponding to a silanol dissociation constant pK = 5.8, at pH = 5.6 and $I = 1$ mM.

4.3.4 Counterion condensation

Counterions released by charged colloids have been predicted to partly condense on the colloid surface resulting in a lower effective charge Z_{eff}. This phenomenon only concerns particles above a threshold surface charge density [140–143]. In [129], Manning determined the fraction of condensed ions for planes, spheres and cylinders. The method is based on the Debye-Hückel linearization of the Poisson-Boltzmann equation and considers a single colloid[4]. For spherocylinders the fraction of free monovalent counterions is found to be

$$Q = -\frac{L}{Z_c \lambda_B} \ln\left(\kappa \frac{L}{Z_c}\right) \kappa a \frac{K_1(\kappa a)}{K_0(\kappa a)}\ , \tag{4.39}$$

[4]Ion condensation has been studied within non-linear Poisson–Boltzmann theory and finite colloid concentration [144–146].

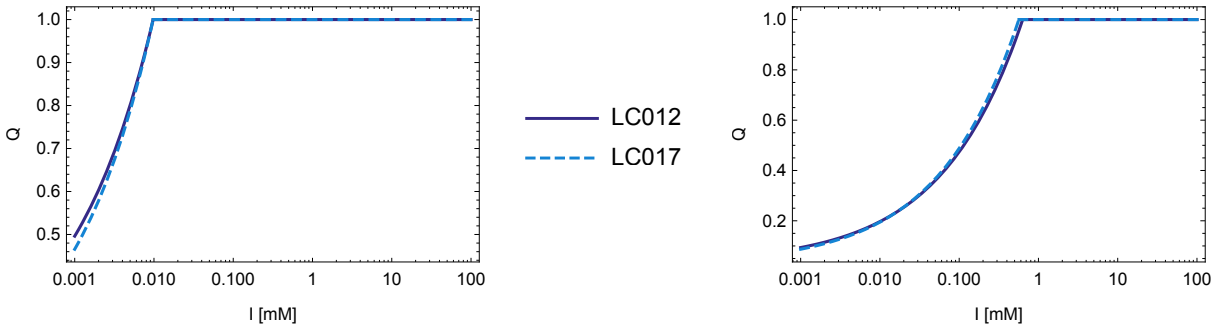


Figure 4.7: Fraction of free ions as a function of the ionic strength I for silica rods 'LC012' and 'LC017' a surface charge $\sigma = -12500\,e\,\mu\text{m}^{-2}$(left) and $\sigma = -82500\,e\,\mu\text{m}^{-2}$ (right).

if $Q < 1$ or 1 otherwise. In the former equation, Z_c is the number of elementary charges per colloid, and λ_B the Bjerrum length. The number of elementary charges per cylinder is related to the rod surface charge by

$$Z_c = \frac{\sigma_-}{S} \approx \frac{\sigma_-}{2\pi a L} \,. \tag{4.40}$$

In figure 4.7, we plot the fraction of free ions (equation (4.39)) as a function of the ionic strength for the rods 'LC012' ($L = 2.7\,\mu\text{m}$, $a = 0.14\,\mu\text{m}$, $S = 2.5\,\mu\text{m}^2$) and 'LC017' ($L = 5.3\,\mu\text{m}$, $a = 0.20\,\mu\text{m}$, $S = 6.5\,\mu\text{m}^2$) assuming surface charges $\sigma = -12500\,e\,\mu\text{m}^{-2}$ (left) and $\sigma = -82500\,e\,\mu\text{m}^{-2}$ (right). These values were predicted, in section 4.3.2, for silica rods dispersed in 0.025 mM and 1 mM solution. We note that: (1) the fraction of free counterions is practically the same for our two rod systems and (2) for $I = 1$ mM we do not expect ions condensation, whereas for $I = 0.025$ mM we find $Q = 0.6$.

In sum, we have first estimated the surface charge of silica cylinders. We have further noticed that the surface charge only slightly depends on the geometry of the surface. Therefore, the same surface charge is expected for all the silica rods used in this thesis. For $I = 1$ mM, we found two candidate surface charges corresponding to dissociation constants of the silanol groups pK = 5.8 and pK = 7.5.

We then measured the ζ-potential of the silica rods 'LC017', leading to a lower estimate to the surface charges at $I = 1$ mM: $|\sigma_-| \geq 20700\,e\ \mu\text{m}^{-2}$. This value was found to be compatible with a pK of 5.8, suggesting a surface charge for the silica rods at 1 mM $\sigma_- = -82500\,e\,\mu\text{m}^{-2}$.

The fraction of condensed counterions, was then determined for our particles following Manning's treatment [129]. For $I = 1$ mM, the theory predicts that all counterions are free for both rod systems ('LC012' and 'LC017'). For $I = 0.025$ mM, we found that 60% of the counterions are

free. We conclude that at $I = 1$ mM, counterion condensation is not occurring, and therefore not attenuating the Donnan effect. However, at lower ionic strength part of the counterions may condense.

4.4 Discussion

In section 3.5, we have studied the sedimentation-diffusion equilibrium of two silica rod systems: the small rods 'LC012' and large rods 'LC017'. Using tracer particles we have measured the thicknesses of the isotropic, nematic and smectic phases. The accumulated thickness of the three phases was found to be 1.33 and 2 times larger than predicted by our theoretical treatment. This inflation of the density profile was found to affect all phases and arguably affect them in a linear fashion. We also showed that addition of salt of 1 mM and 0.5 mM did not considerably affect the phase behavior.

In section 4.2, we have incorporated the osmotic pressure of ions to the equation of state within the Donnan approximation. We considered the case where $I = 1$ mM. We found that for a surface charge $|\sigma_{Don}| = 1260\, e\,\mu\text{m}^{-2}$, and a range of the double layer interaction $\alpha\kappa^{-1} = 80$ nm, the Donnan effect predicts an inflation of the density profile that is: (1) largely proportional to the rod length and (2) linear in the region $1\% < \phi < 60\%$. Which is in agreement with experimental observations. Quantitatively, for these (chosen) conditions, the density profile was found to be inflated, for the rods 'LC012' and 'LC017', by 1.6 times and 2 times. Which is in reasonable agreement with experimental values of 1.33 and 2. To test this finding we independently estimated the absolute surface charge of the rods.

The absolute surface charge of silica rod-shape colloid in 1 mM NaCl water solution (pH = 5.6) was predicted to be $|\sigma_-| = 82500\, e\,\mu\text{m}^{-2}$ (for a silanol dissociation constant of pK = 5.8). We also performed zeta potential measurements suggesting that $|\sigma_-| \geq 20700\, e\,\mu\text{m}^{-2}$. This is significantly larger than the surface charged required to inflate the density profile according to our treatment of the osmotic pressure of ions within the zero-field approximation ($|\sigma_{Don}| = 1260\, e\,\mu\text{m}^{-2}$). However, we expected this approximation to underestimate the real surface charge as it has been derived for unscreened colloids. Therefore, it does not account for condensed ions nor ions contributing to the double layer. Our results suggest that, in 1mM salt solution only $1-5\%$ of the our silica rods counterions contribute to the inflation of the density profile, whereas

the remaining ions are 'trapped' within the double layer.

A more concerning observation is the dependence, or rather independence of the thicknesses of the upper sediment with salt concentration. The rods LC017 were dispersed in water with 1 mM NaCL, in DMF without salt and in DMF with 0.5 mM LiCl. In all cases, a similar density profile was observed. This is surprising as, in principle, the Donnan effect depends on the concentration of salt.
In fact, in the limit where $y << 1$, the Donnan effect is governed by the ratio $n_c Z_c^2/n_s$ (see equation 4.21), where Z_c is the number of charges per colloid contributing to the Donnan effect, n_s and n_c the concentration of salt and colloids. Then, in this regime, if the number of free counterions per colloid depends on the salt concentration, or more precisely if $n_c Z_c \propto \sqrt{n_s}$, then the Donnan effect will be independent of the salt concentration. In our particular case, we showed that both the absolute surface charge of the rod and n_c are expected to decrease with n_s because of: (i) the surface properties of silica (section 4.3.2); (ii) counterion condensation (section 4.3.4); (iii) the effective rod dimensions –

$$\frac{n_c}{n_c^{eff}} \approx \frac{v_0}{v_0^{eff}} \approx \frac{\sigma^2}{(\sigma + \alpha\kappa^{-1})^2}, \tag{4.41}$$

where $\kappa \propto \sqrt{n_s}$ (section 4.2.4).
This qualitatively supports the claim that the Donnan effect does not necessarily depend on the salt concentration. In order to address fully the problem, one would need to make the link between the absolute surface charge of the rod and the number of free ions per colloid.

Finally, we would like to discuss a major approximation concerning the Donnan effect. The pressure of ions is provided assuming that The pressure of ions is provided assuming that the volume fraction of colloid is small ($\phi_c << 1$, $\phi_{water} \approx 1$). However, in principle, the volume fraction of colloids can vary from 0 to about 0.9 for hard rods. For our charged rods, with an effective diameter $D^{eff} \approx 1.2D$, the maximum packing fraction would be $\phi_{cp}(D/D^{eff})^2 \approx 0.6$. Naively we could correct the volume fraction of water by $\phi_W = 1 - \phi$, leading to $y \propto \frac{\phi}{1-\phi}$. The Donnan effect would then be stronger in the dense region. For example, the smectic phase would be 35% more inflated and the isotropic about 10% more. Note that this effect is too small to be detected by our method, which justifies the simplification.

Despite the mentioned approximations, we believe the Donnan effect remains a viable

explanation for our observations. Note that we were, initially, unfamiliar with some important concepts and parts of the literature. For this reason and due to time constraints we have not been able to push the theoretical treatment further.

4.5 Conclusion and outlook

In this chapter, we have first adapted the theoretical treatment of the sedimentation-diffusion equilibrium of hard rods, introduced in chapter 3, to generalize it to charged rods. To do so, we introduced effective rod dimensions that account for the double layer repulsion, and integrated the osmotic pressure of the ions and the counterions to the equation of state within the Donnan approximation.
The double layer repulsion was found to primarily increase the thickness of the crystalline sediment. Conversely, the Donnan effect decreased it but more importantly increased the width of the upper sediment. We showed that this upper sediment density profile could be largely reproduced by the density profile predicted for hard rods, provided that the gravitational length is replaced by an effective gravitational length. We found $l_g^{eff}/l_g = (1 + \beta/\gamma)$, where β and γ are related the EOS of the ions and colloids. We further predicted, assuming that $l_g^{eff} = 2l_g$ for the rods 'LC017', the effective gravitational length of a differently sized silica rod to be $l_g^{eff}/l_g = (1 + L/L_{17})$. Which means for the rods 'LC012' $l_g^{eff} = 1.5l_g$, in qualitative agreement with the experimental value ($l_g^{eff} = 1.33l_g$).

We then considered both double layer repulsion and the Donnan effect. We focused on the rods 'LC017', dispersed in 1 mM water solution, with initial volume fraction $\phi_0 = 3.8\%$ and $\phi_0 = 7.7\%$. The Donnan effect was tuned to obtain $l_g^{eff} = 2l_g$ and the double layer repulsion tuned to accommodate the total height of the sediment. We found agreement with experiment for $|\sigma_{Don}| = 1260\, e\,\mu\text{m}^{-2}$ and $\alpha\kappa^{-1} = 8\kappa = 80$ nm.

The rod surface charge was determined independently to be $|\sigma_-| = 82500\, e\,\mu\text{m}^{-2}$. The difference between the two values could not be explained by counterion condensation as described by Manning [129]. Therefore, our results suggests that, in 1mM solution, most of counterions $(95 - 99\%)$ do not contribute to the Donnan effect because they are trapped within the double layer.

We will finish by delivering an outlook. We hope that this work will trigger more ex-

perimental, computational and theoretical work on the sedimentation-diffusion equilibrium of charged rods. In particular, generalizing the osmotic pressure of ions outside the Donnan approximation and for high colloid concentration would be particularly useful to us. Simulation of the sedimentation-diffusion equilibrium of charged rods would equally be insightful.

Experimentally, it would be interesting to measure the upper sediment of silica rods with other lengths than the one studied. This would allow the dependency of the Donnan effect on the rod length to be confirmed. It would equally be engaging to be able to measure directly the density profile. It would then be easier to observe whether or not the density profile is inflated in a linear fashion.

Acknowledgments

I would like to express my gratitude to Clément Robert that, under our supervision, performed the sedimentation-diffusion experiments on the rods LC017 in water. I would like to acknowledge Eric Grelet, Taiki Yanagishima and Pavlik Lettinga for useful discussions.

Chapter 5

Diffusion of colloidal rods at sedimentation-diffusion equilibrium

Abstract

We study the dynamics of rod-like particles with an aspect ratio $p \approx 10$ in sedimentation-diffusion equilibrium. The method is first tested on a molecular dynamic simulation of chains of beads with an aspect ratio of 10 and a gravitational length $l_g \approx 2\sigma$, where σ is the particle diameter.

We then present experimental results on silica rods with an effective aspect ratio of 10.4 and gravitational length $l_g \approx 2\sigma$. We first introduce an empirical method developed to measure the long-time rotational diffusion coefficient of rods, diffusing in 3D, from 2D snapshots. We then measure the diffusion coefficients in the isotropic, nematic and smectic phases. Our experimental times ranging from 0.1 to about 2000 s allow us to locate a transition between diffusive regimes in all phases. However, only the long-time diffusion coefficients can be properly measured. They are found to be in qualitative agreement with Brownian dynamic simulations [147]. Nevertheless, we found a large quantitative gap between the diffusion coefficients measured in experiments compared to predictions from simulations (typically a factor of 2). This observation echoes to the behavior of viral rods, with larger aspect ratios, that were also found to diffuse more slowly than in simulations [148].

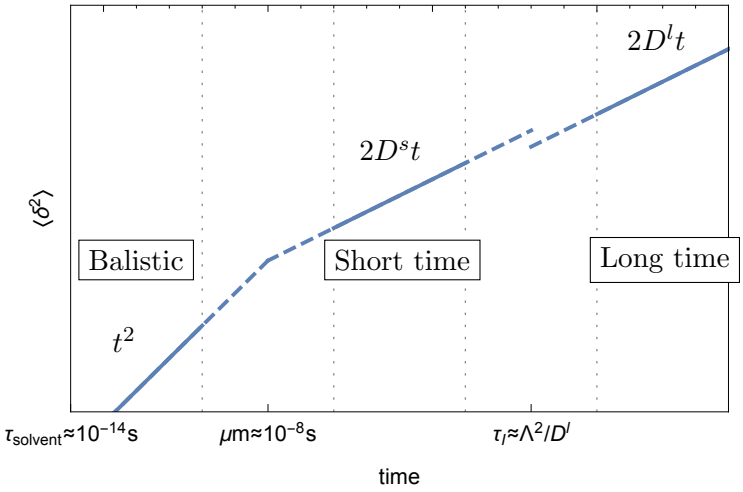


Figure 5.1: Log-log plot of the (1-dimensional) mean square displacement expected for a colloidal particle of mass m and mobility μ in a dense suspension with predominant structural length-scale Λ.

5.1 Introduction

Colloid diffusion in structured environments affects processes in everyday life ranging from the transport of living cells to industrial applications such as the drying of ink and paint. These processes can be studied at different levels. However, the ultimate level of understanding can only be obtained by linking the macroscopic dynamics to the properties of single particles. Substantial amounts of research has been directed to this task and a good understanding has been reached. For an introduction see e.g. reference [149]. However, for most systems, non-ideal particle-particle *direct* and *solvent mediated* interactions remain challenging to capture theoretically, which motivates the drive for well-defined experimental systems [148, 150].

There are two types of diffusion processes: the *collective diffusion* that is induced by density gradients and relates to the motion of many Brownian particles, and the *self-diffusion* that concerns the dynamics of single particles. In this chapter, we are interested in the self-diffusion of rods.

The self-diffusion is usually quantified by the particle mean square displacement $\langle\delta^2\rangle$ (see section 2.1.1). In figure 5.1, we sketch the mean square displacement expected for a colloidal particle. We use a log-log plot to highlight the time-scales involved (largely inspired by [149]). The solvent characteristic time is $\tau_s = 10^{-14}$ s. This is much smaller than the time-scale at which a colloid starts feeling solvent drag $t \approx \mu m \approx 10^{-8}$ s, where m is the mass of the colloid and μ the mobility. For $t << \mu m$, the MSD is ballistic $\langle\delta^2\rangle \propto t^2$, while for $t >> \mu m$ a diffusive

behavior is expected $\langle \delta^2 \rangle \propto t$, in one dimension $\langle \delta^2 \rangle = 2Dt$, where D is the diffusion coefficient.

An additional time-scale τ_I arises in structured environments. The interaction time τ_I is the characteristic time required for a particle to explore the structural free energy landscape resulting from its interactions with the other particles. We discriminate short times, defined by $t << \tau_I$, and long times, where $t >> \tau_I$. At short times, particles mostly diffuse freely in local minimums of the energy landscape. Whereas, at long times they have time to climb many potential barriers. In both cases, diffusive behavior is expected ($\langle \delta^2 \rangle \propto t$). However, the long-time diffusion, hindered by the environment, is slower. In between the two regimes, for $t \approx \tau_I$, the MSD will therefore be sub-diffusive: its derivative will decrease with time. The value of the interaction time τ_I depends on the nature of the energy landscape. In an isotropic dispersion of Brownian particles, this landscape fluctuates dynamically. In this case, τ_I is related to the particles' collective diffusion coefficient which sets the characteristic time of the landscape fluctuations [149]. For a static landscape, such as smectic layers (see e.g. [151]), τ_I can be estimated by Λ^2/D, where Λ is the dominant wave length of the potential and D is the long-time diffusion coefficient. A way to access τ_I, from the particle trajectories, is to measure to the Non-Gaussian Parameter (NGP) α_2, which is expected to peak for $t \approx \tau_I$:

$$\alpha_2(t) = -1 + \frac{\langle \delta^4 \rangle}{3 \langle \delta^2 \rangle^2}. \tag{5.1}$$

The self-diffusion of a colloid can then largely be captured by its short-time and long-time diffusion coefficients. To predict these coefficients one should correctly account for the rods direct *and* solvent mediated interactions, also referred to as hydrodynamic interactions (HI).

Particles' direct interactions are connected to their organization. Despite their apparent simplicity, hard rods present a complex phase behavior as a function of the colloid concentration [46], see section 2.1.2. The structural effects on the dynamics can be largely captured by simulations [147, 152]. However, comparison between experiments [90, 148, 153–156] and simulations [147, 151, 152] are mostly qualitative, with a clearly established, but not well understood role of hydrodynamic interactions [148].

HI materialize as shear and sound waves that are created by particles and propagate through the solvent [149]. The effect of HI on the self-diffusion of colloids is not trivial and may depend on particle shape and size. To illustrate this, we present two examples where experiments

on model particles were compared to simulations to determine the effect of HI.
In the first example, the diffusion of a quasi-two-dimensional colloidal hard sphere fluid was compared to Monte-Carlo simulations of hard disks (neglecting HI) [150]. The long-time diffusion coefficient of this mono-layer of spheres with diameter $\sigma > 1\,\mu\text{m}$ was found to be in very good agreement with simulations, whereas HI were found to lower the short-time diffusion coefficient. In the second example, the diffusion of long and thin viruses ($p \approx 20 - 50$) in the nematic phase was compared to simulations, emphasizing the long-time limit [148]. In this work, the long-time diffusion coefficients were found to be reduced by HI.

Beyond particle interactions, the anisotropy of rods brings additional points of interest. Already in the dilute regime, the diffusion is richer than that of simple spheres. First, the orientational diffusion is easily observable, and second, the translational diffusion becomes direction dependent. Indeed, the motion of a cylinder may be decomposed into two independent rotations and translations (see section 2.1.1). The rotation around the rod long axis will not be considered as it cannot be observed in this work. We will focus on the tumbling rotation D_r and the translations along the rod's long and short axes, $D_\text{t}^\parallel$ and $D_\text{t}^\perp$. The total translational diffusion coefficient is defined as $D_t = \frac{1}{3}D_\text{t}^\parallel + \frac{2}{3}D_\text{t}^\perp$, such that in 3D $\left\langle \delta^2 \right\rangle = 6D_t t$.

In this chapter, we study the diffusion behavior of colloidal rods with an aspect ratio $p \approx 10$. The rods motion is quantified in sedimentation-diffusion equilibrium by means of simulation and experiments. Our aim is twofold: (i) to show that sedimentation-diffusion equilibrium is a convenient way to measure the diffusion coefficients across the whole phase diagram of a colloidal suspension; (ii) to provide experimental data on the dynamics of rods with an aspect ratio that is largely missing in literature. The aspect ratio 10 is particularly interesting, as it is large enough to have a substantial nematic phase [46], but small enough to deviate from the behavior of infinitely long rods.

The chapter is organized as follows. In section 5.2, we review the diffusion behavior of rods as a function of the rod concentration. In section 5.3 and 5.4, we present the simulation and the experimental results. Finally, we draw conclusions in section 5.5.

5.2 Theoretical background

In this section, we introduce the self-diffusion behavior expected for hard rods, from the dilute isotropic to the crystalline phase. We focus on the long-time diffusion coefficient.

In the infinitely dilute regime, there is no difference between long and short times. The translational and rotational diffusion coefficients have been calculated for *cylinders* from the hydrodynamic interactions with the solvent. For an endless rod, one finds

$$\begin{cases} D_{r0} = \frac{3k_BT}{\pi\eta_0 L^3}\ln p \\ D_{\mathrm{t}0} = \frac{k_BT}{2\pi\eta_0 L}\ln p = \frac{1}{3}D_{\mathrm{t}0}^{\parallel} + \frac{2}{3}D_{\mathrm{t}0}^{\perp} \end{cases} . \tag{5.2}$$

For finite rods, well established corrections have been reported [45]. The corrected expressions of D_{r0}, $D_{\mathrm{t}0}$, $D_0^{\parallel}$ and $D_0^{\perp}$, for arbitrary aspect ratios, are given in section 2.1.1. Note that the diffusion parallel to the rod long axis is always larger than the diffusion perpendicular to it $D_0^{\parallel} > D_0^{\perp}$.

These equations have been be used to determine particle dimensions from the dynamical properties [157–159]. We remark that the rotational and translational frictions are higher for a rod than for a sphere of equivalent volume.

In the isotropic phase, the diffusion is commonly divided into three regimes: the dilute regime where $\phi << \frac{v_0}{L^3}$ (i.e. $\phi << 0.4\%$ for our system), the semi-dilute regime where $\frac{v_0}{L^3} < \phi < \frac{v_0}{L^2\sigma} \approx \frac{\sigma}{L}$ (i.e. $0.4\% < \phi < 6\%$) and the concentrated regime $\frac{\sigma}{L} < \phi < \phi_{nem}$ ($6\% < \phi < 20\%$).

A theory is lacking for the dilute regime. However, experimental results [153, 154] suggests that $D_{\mathrm{t}}/D_{\mathrm{t}0} \propto \phi$.

In the semi-dilute regime, the volume per particle is smaller than L^3. Therefore, the rods cannot freely rotate, they are entangled. For large aspect ratios, the tube theory [30,31] describes rods caged by their neighbors. Because of this caging effect, the space available for diffusion is restricted to a tube. This greatly hinders rod rotation and translation perpendicular to its main axis, whereas, to a first order approximation, the translations along the long axis is not affected. By formulating the problem in terms of a mean field Green function, the translation and rotation diffusion coefficient were described by [160, 161]

$$\frac{D_r}{D_{r0}} = (1 + \beta^{-1/2}(4\pi^{-1}\phi\, p^2))^{-2} \text{ and } \frac{D_t}{D_{\mathrm{t}0}} = (1 + \gamma^{-1/2}(4\pi^{-1}\phi\, p^2))^{-2}, \tag{5.3}$$

where β and γ are numerical constants that can be calculated from geometrical considerations ($b \approx 500 - 1000$) [160–162] and p is the aspect ratio. For dense isotropic, reaching the I-N coexistence concentrations, and in the limit of infinite aspect ratio ($p \to \infty$), the relations $\frac{D_r}{D_{r0}} = 30.8/p^2$ and $D_t/D_{\mathrm{t0}} = 1/3$ are predicted [152]. Experimentally, reduced coefficients may be expected due to hydrodynamic interactions.
Note that these expressions were derived for large aspect ratios and failed to describe simulation with aspect ratios $p \leq 6$ [152]. However, for an aspect ratio $p = 10$, reasonable agreement was found at the I-N transition between simulations ($D_r/D_{r0} = 0.19$ and $D_t/D_{\mathrm{t0}} = 0.31$) [152] and theoretical predictions ($D_r/D_{r0} = 0.3$ and $D_t/D_{\mathrm{t0}} = 1/3$).

In the nematic phase, rods align their long axis to the nematic director $\hat{n}$. This structural anisotropy enhances the translational diffusion along $\hat{n}$ ($D_{\mathrm{t}\parallel}$), but hinders the diffusion perpendicular to $\hat{n}$ ($D_{\mathrm{t}\perp}$)[1]. Despite the increase in concentration, the total translational diffusion coefficient $D_t = 1/3D_{\mathrm{t}\parallel} + 2/3D_{\mathrm{t}\perp}$ is often found to increase in the nematic phase relative to the isotropic phase. Qualitative agreement is found between theories [163,164], simulations [147,165] and experiments [148,166]. However, experimental values are typically two to four times smaller than the ones found in simulations [148]. A recent study showed the importance of hydrodynamic interactions [148]. By tuning hydrodynamic interactions in both simulations and experiments, the authors demonstrated that HI were reducing diffusion coefficients by approximately a factor of two. However, the treatment of hydrodynamic interactions was not enough to obtain a quantitative match between simulations and experiments, where particles diffused about half as quickly.

In the smectic phase, the diffusion parallel to the nematic director is strongly hindered by a periodic potential created by the rods themselves, as they self-organize into smectic layers. However, the diffusion perpendicular to the nematic director is mostly unaffected because, within layers, the order remains liquid-like. Opposite observations have been reported between viral particles [155] and silica rods [90]: for the system of elongated viruses, the authors found $D_{\mathrm{t}\parallel} > D_{\mathrm{t}\perp}$, whereas for the silica rods, with an aspect ratio $p \approx 5$, the study measured $D_{\mathrm{t}\parallel} < D_{\mathrm{t}\perp}$. Interestingly, in simulations with an aspect ratio $p = 10$, both regimes were observed: $D_{\mathrm{t}\parallel} > D_{\mathrm{t}\perp}$ close to the nematic phase and $D_{\mathrm{t}\parallel} < D_{\mathrm{t}\perp}$ close to the crystal phase. However, there is no experimental evidence to support this finding.

[1] We make a distinction between the diffusion along the rod main axis $D^{\parallel}$ and along the nematic director $D_{\parallel}$.

In the crystalline phase, in the absence of defects, the rods are not expected to diffuse, but only wiggle around their central position.

5.3 Simulation

The dynamics of rods, with an aspect ratio $p = 10$, is studied in sedimentation-diffusion equilibrium by means of molecular dynamic simulations. The section is divided in three parts: in section 5.3.1, we introduce the simulation method, in section 5.3.2, we present the analysis method, showing that special care should be taken when quantifying self-diffusion in sedimentation-diffusion equilibrium, and finally, results are presented in section 5.3.3.

5.3.1 Simulation method

The molecular dynamic simulation method is introduced in more details in chapter 3.3.1. Maxime Tortora simulated rods with an aspect ratio $p = 10$. They were made of a chain of 21 fused beads with diameter σ. The rod total volume is $v_0 \approx 7.72\sigma^3$, considering a bounding spherocylinders the volume is about 10% larger $v_{sp} \approx 8.38\sigma^3$.

The simulation box consisted of a 112σ sided square, where the origin was chosen at its center. The box was filled with 51200 particles to reach an initial volume fraction of 30%. Hard-walls were used at the bottom and at the top of the box, in order to obtain a sedimentation-diffusion equilibrium. On the four remaining sides, periodic boundary conditions were applied.

The Brownian time marking the transition between ballistic and diffusive regimes was set to $\tau_D = \mu m = D_{\mathrm{t0}}^{-1}\sigma^2$. Note that this is comparable to the typical interaction time $\tau_I = D^{-1}\Lambda^2$, while in experiments several orders of magnitude typically separate τ_I and $\tau_D \approx 10^{-8}s$. This choice of τ_D will largely suppress the short-time diffusion regime, but should not affect the long times. This relatively large value of τ_D allowed Tortora to perform the simulation within a few hours.

The simulation time and space are scaled by the time $\tau = D_{\mathrm{t0}}^{-1}\sigma^2$ and particle diameter σ. The mean square displacement is scaled by σ^2 such that in each dimension:

$$\frac{\left\langle \delta^2 \right\rangle}{\sigma^2} = 2\frac{D_t(\phi)}{D_{\mathrm{t0}}}\frac{t}{\tau} \text{ with } D_{\mathrm{t0}} = \sigma^2\tau^{-1}. \tag{5.4}$$

For $p = 10$, the ratio between rotational and translational diffusion coefficients can be calculated (see section 2.1.1)

$$\frac{D_{r0}}{D_{t0}} = \frac{5.83}{L^2} = \frac{5.83}{(10\sigma)^2} = \frac{0.0583}{\sigma^2}, \text{ which corresponds to } D_{r0} = 0.0583\tau^{-1} \ . \tag{5.5}$$

However, D_{r0} was set in this simulation to be $D_{r0} = 1\tau^{-1}$. The orientational diffusion is therefore set to be faster that what would be expected experimentally. Although this was not initially considered, we will show that it has interesting implications. We equally set the translational diffusion coefficients along the rods' long and short axes equal to the total diffusion coefficient $D_0^{\perp} = D_0^{\parallel} = D_{t0}$, where in principle for a *cylinder* with aspect ratio of 10 $D_{t0} = 1.12D_0^{\perp} = 0.81D_0^{\parallel}$.

Initially, the trajectories are monitored from $t = 0.1\tau$ to $t \approx 1000\tau$. However, most of these trajectories will be cut to avoid diffusion in the z direction (see section 5.3.2). Furthermore, to facilitate calculation of the mean square displacement, the data is divided into a 'short-time' regime $0.5\tau < t < 10\tau$ (based on 56 snapshots) and a 'long-time' regime $25\tau < t < 1000\tau$ (based on 63 snapshots).

The phase behavior was set out in detail in section 3.3. We present the main results in figure 5.2. A snapshot of the x-z plane (a) shows the sedimentation-diffusion equilibrium, where isotropic, nematic, smectic and crystal phases coexist at different z-positions. Each phase was located by measuring the corresponding order parameters (c) and highlighted with colored background. Moreover, a volume fraction ϕ was associated to each z-position (d). In the next section, we will introduce the method used to determine diffusion coefficients.

5.3.2 Analysis of self-diffusion in sedimentation-diffusion equilibrium

Our goal is to use the gradient of concentration imposed by gravity, in the z-direction, to measure the rod's diffusion coefficients across the whole phase diagram. This will be simply achieved by measuring diffusion at different z-positions. However, we need to take one precaution.
The diffusion coefficients are measured from particle trajectories. As soon as a particle diffuses in the z-direction, it starts exploring different concentrations, which affects the accuracy of the method. To limit this effect, the simulation box is divided into 18 bins of width $w_b = 6\sigma$. Each time a trajectory crosses the boundary between two bins, it is split. As a result, we obtain more

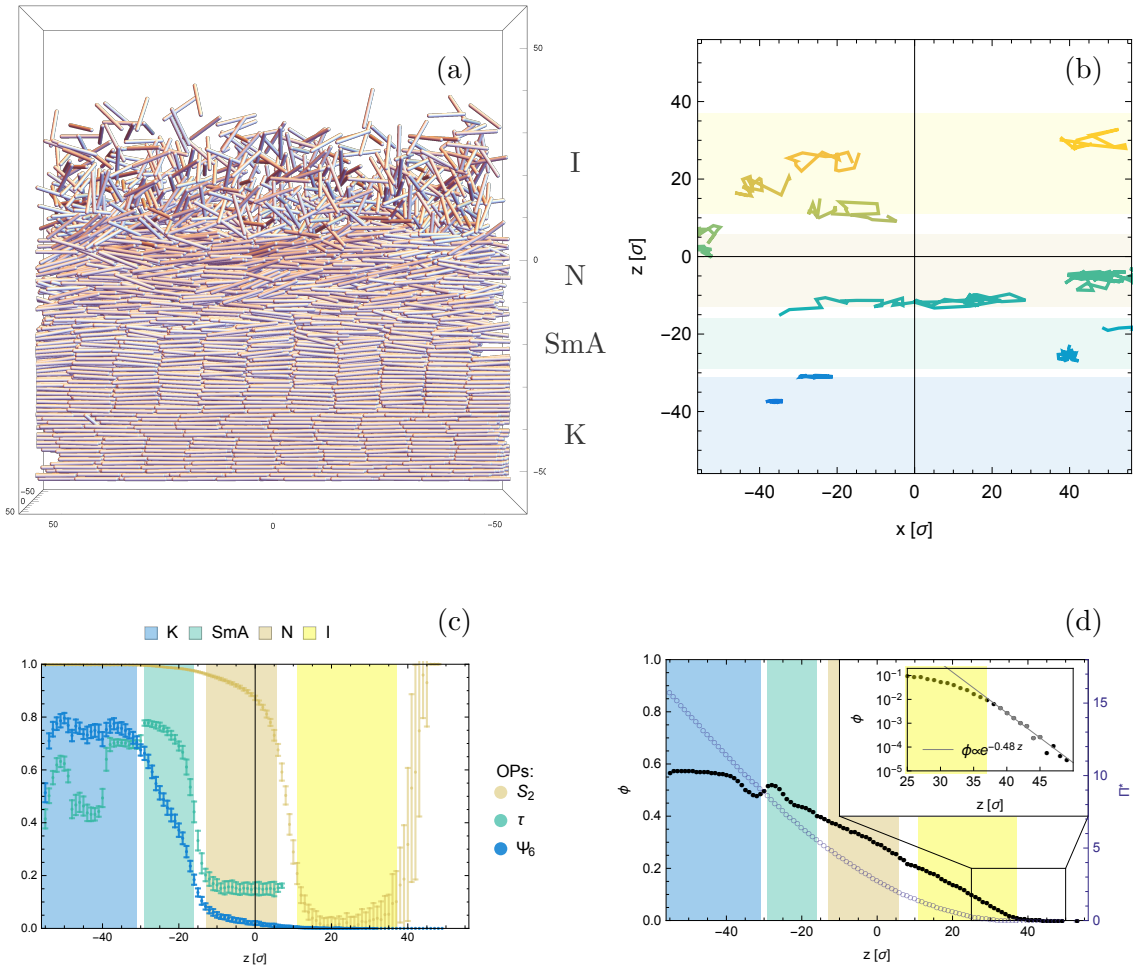


Figure 5.2: (a) x-z snapshot of the simulation box. (b) x-z plot of cut trajectories. (c) Order parameters as a function of z. (d) Volume fraction as a function of z.

trajectories, though cut trajectories have a shorter length, which reduces the statistics at long times. The value of the bin width is a compromise between maximizing the number of bins and maximizing the statistics at long times. We show in figure 5.3 (a-b) a selection of trajectories before and after splitting. They are plotted in the x-z plane, where z is parallel to gravity and x is parallel to the nematic director. The background colors indicate the different phases.

For each bin, we measure the translational and rotational diffusion coefficients by fitting the mean square displacement, figure 5.3 (e), and angular correlation function, figure 5.3 (f). The translational diffusion coefficient is independently measured in the x, y and z directions. For each trajectory, we measure the x-displacements $\delta_x = (x(t+\Delta t) - x(t))$ for Δt varying from 1 to $N-1$ and t varying from 1 to $N-\Delta t$, where N the number of positions per trajectory. The displacements are then grouped by delay time Δt. We show displacement distributions in the isotropic phase ($\bar{z} = 17.8\sigma$) for $\Delta t = 25\tau$, $\Delta t = 50\tau$ and $\Delta t = 75\tau$ in figure 5.3 (c). The statistics are better for short delays because each trajectory contributes $N-\Delta t$ displacements. We choose an arbitrary minimal number of displacements below which the MSD is not calculated; typically $N_{min} = 100 - 1000$. For each delay, we can finally calculate the mean square x-displacement. In figure 5.3 (e), we plot the MSD as a function of delay time and perform a linear regression to obtain the diffusion coefficient in the x-direction

$$\left\langle \delta_x^2 \right\rangle = 2D_{\mathrm{t}x}\Delta t \ ; \ D_{\mathrm{t}x} = 0.27\,\sigma^2\tau^{-1} \ . \tag{5.6}$$

The MSDs can be calculated in similar fashion in y and z directions.

The rotational diffusion coefficient is obtained by fitting the orientation correlation function. If the orientation is perfectly defined in three dimensions we can use the function $\Theta(\Delta t) = \langle \hat{\mathrm{u}}(t).\hat{\mathrm{u}}(t+\Delta t) \rangle$, where $\hat{\mathrm{u}} = (\mathrm{u}_x, \mathrm{u}_y, \mathrm{u}_z)$ is the normalized particle orientation. Instead of the displacements, the dot products are calculated for each trajectory and each delay; we show the distributions of dot products and the correlation function in figure 5.3 (d-f). The rotational diffusion coefficient is obtain by fitting the correlation function to:

$$\Theta(\Delta t) = A \exp\left(-2D_r\Delta t\right) \ ; \ D_r = 0.14\,\mathrm{rad}^2\tau^{-1} \ , \tag{5.7}$$

where $A \approx 1$.

In principle, this method allow us to measure all translational and rotational diffusion

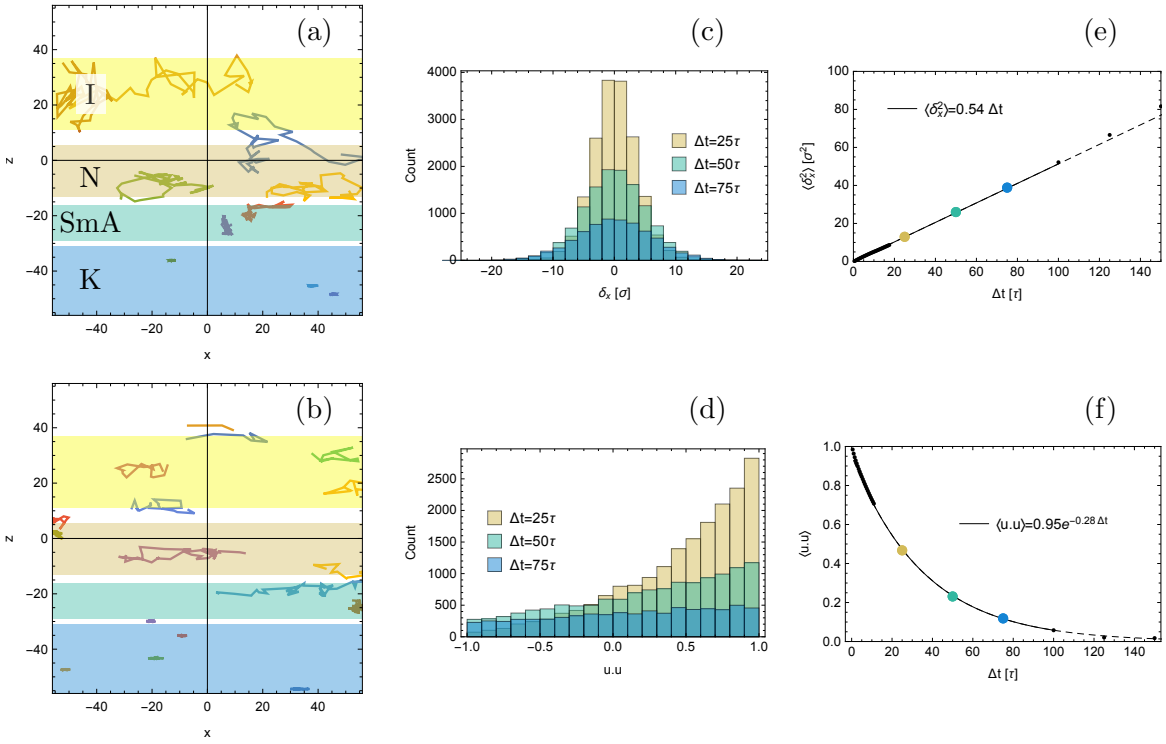


Figure 5.3: (a) Selection of trajectories from MD simulation. (b) Selection of split trajectories. (c) Displacements in x for different delays. (d) Dot products $u(t).u(t+\Delta t)$ for multiple delays. (e) Mean square displacement. (f) Orientation correlation function. Plots (b-f) correspond to data from bin $\bar{z} = 17.8$.

coefficients. However, by cutting trajectories we are introducing a bias on the z-trajectories, which strongly affects the diffusion coefficient in the z-direction. An alternative is to keep the trajectories as a whole. However, they will then explore different phases which will bias the diffusion in all directions. We will come back to this point later.

Note also that, in a confined space, a particle's long-time diffusion coefficient is necessarily equal to 0. In the x- and y-directions, where we use periodic boundary conditions, there is no confinement. However, in the z-direction particles are trapped between two hard walls, so at infinitely long-times, we expect: $\langle \delta_z \rangle = 0$, $\langle \delta_z^2 \rangle = cte$ and $D_{tz} = 0$.

If the long-time diffusion regime is mostly reached before the rod is impacted by confinement, we shall be able to estimate the long-time diffusion coefficient expected in bulk, by fitting the MSD at intermediate times. However, we should expect some bias, due to confinement, that depends non-trivially on the time considered and the distance to the wall. To illustrate the effect of confinement, we plot in figure 5.4 the average particle speed in the z-direction as a function of its average position. We observe that, on average, particles in the isotropic phase have a net speed downwards and particles in the nematic and smectic phases have a net speed upwards. In

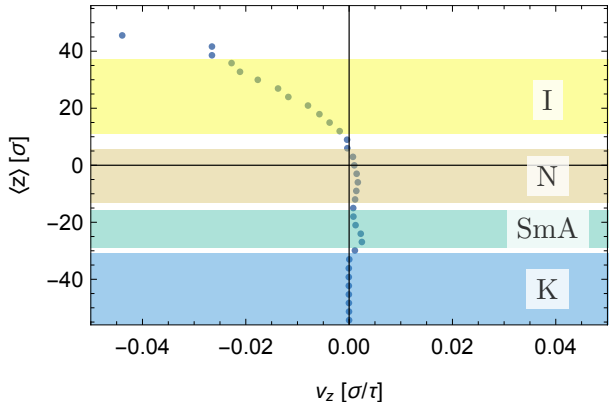


Figure 5.4: Average speed of particle in the z-direction as a function of their average z-position due to confinement.

practice, this confinement effect does not dramatically impact the pseudo 'long-time' diffusion coefficient in the dense phases if measured in the correct time range. However, one should be careful when measuring diffusion coefficient in confinement. Within this thesis, we will focus on the diffusion behavior in the x- and y-directions, where confinement effects are negligible.

Returning on figure 5.4, we observe that the particles in the crystalline phase, $z < 30\sigma$, are largely immobile, and for $z > 40\sigma$, the probability of finding a particle is very small. Interestingly, we locate the crossover between particles moving up and particles moving down around 5σ, which is half-way between the two mentioned positions that could be seen as virtual walls ($z \approx -30\sigma$ and $z = 40\sigma$). A more surprising observation is the dip in the speed at the $N - Sm$ interface, which may suggest that the interface is hindering the rods' passage, from the smectic to the nematic phase. Note that these findings are not relevant for the rest of the chapter and will not be discussed further.

In the next section, we will apply the method presented above to measure the diffusion coefficient as a function of the volume fraction. The attention will be focused on the bins at positions $-40\sigma < z < 40\sigma$. For $z > 40\sigma$, there are not enough particles, and for $z < -40\sigma$, many defects are present. We then have a total of 13 bins. A trajectory corresponding to each bin is plotted in figure 5.2 (b). There is 1 bin in the crystal phase, 1 at the S-K interface, 2 in the smectic phase, 1 at the N-S interface, 2 in the nematic, 1 at the I-N interface and 5 bins in the isotropic phase. For each bin, we will determine the translational and rotational diffusion coefficients.

5.3.3 Results

In figure 5.5, we show typical mean square displacements for the isotropic (a), nematic (b) and smectic (c-d) phases. Our method does not allow us to precisely measure diffusion in the z-direction. However, the bulk behavior is fully characterized by the diffusion parallel and perpendicular to the nematic director, that we can respectively measure along the x- and y-axes. The diffusion along the z-axis is therefore not essential. For each phase, we provide the MSDs parallel and perpendicular to the nematic director $\vec{n} = \vec{x}$. This should not be confused to the direction parallel and perpendicular to the rod main axis $\hat{u}$. For each concentration, we plot the

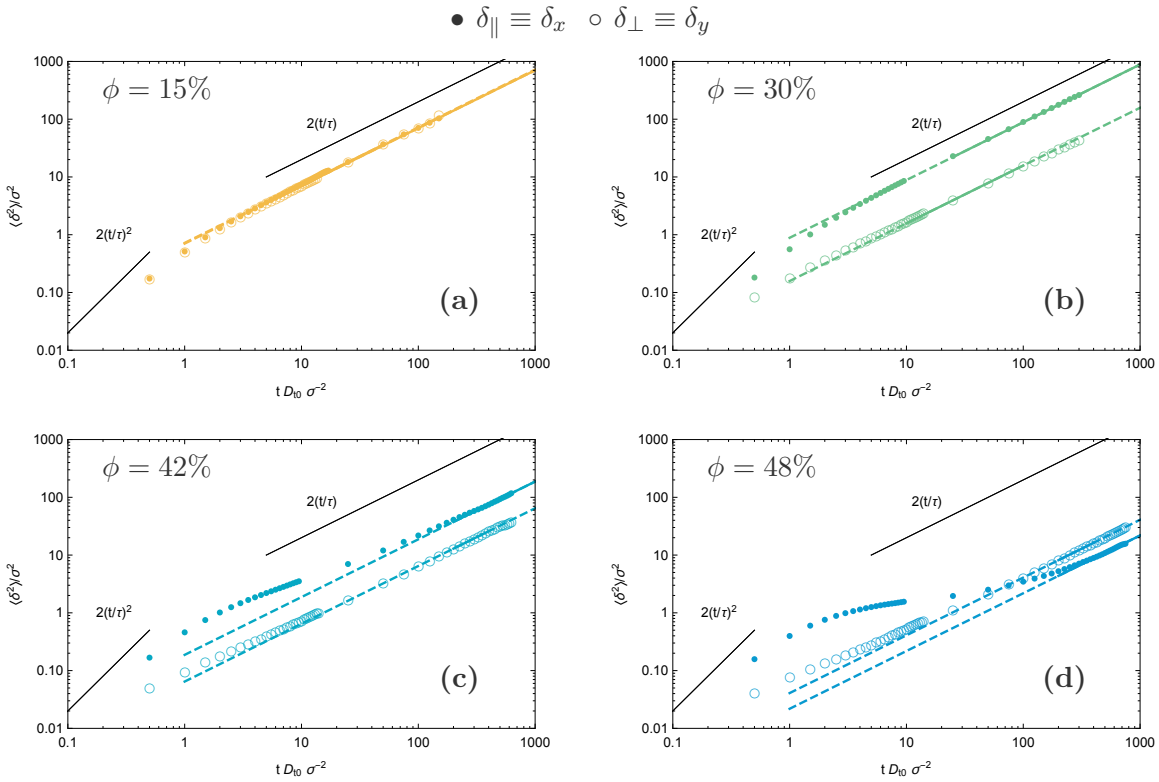


Figure 5.5: Representative examples of MSDs in the isotropic (a), nematic (b) and smectic phase (c-d). The dots (•) and circles (∘) correspond to displacements parallel and perpendicular to the nematic director, i.e. along $\hat{x}$ and $\hat{y}$. With solid black lines we show the MSD expected for a single rod.

scaled MSD $\langle\delta^2\rangle/\sigma^2$ as a function of the scaled time $t/\tau = tD_{t0}\sigma^{-2}$. We use log-log plots to be able to visualize different time-scales. We equally show the trends expected at infinite dilution with black lines: the ballistic regime ($\langle\delta^2\rangle/\sigma^2 \propto (t/\tau)^2$) when $t << \tau_D (= 1\tau)$ and the diffusive regime ($\langle\delta^2\rangle/\sigma^2 = 2t/\tau$) when $t >> \tau_D$. We also indicate the volume fraction (ϕ) at which the MSDs were measured.

In the isotropic phase (a), at $\phi = 15\%$, the behavior is similar to the one expected for

infinite dilution. The diffusion in x- and y-directions match perfectly and a transition from the ballistic to the diffusive regime is observed (roughly around $\tau < t < 5\tau$). However, the slope is shifted down compared to the infinitely dilute case (black line labeled $2t/\tau$), which means that the diffusion coefficient is smaller. The long-time self-diffusion coefficient is obtained by linear regression ($y = ax$) for time $t > 10\tau$.

In the nematic phase (b), at $\phi = 30\%$, we observe anisotropic behavior. The MSD parallel to the nematic director (•) is larger than the MSD perpendicular (∘). In both cases the diffusive regime is mostly reached at $t = 5\tau$.

In the smectic (c-d), we equally observe anisotropic diffusion. At short times, the MSD parallel to the nematic director (•) is higher than the MSD perpendicular (∘), similar to the nematic phase. However, at longer times, when the particles start to interact with the layers, the MSD parallel to the nematic director is strongly sub-diffusive (nonlinear with time), which leads to a reduction of the long-time diffusion coefficient. For $\phi = 42\%$ (c), the MSD parallel to $\vec{n}$ remains larger than the MSD perpendicular to $\vec{n}$, whereas, for $\phi = 48\%$ (d), we observe a crossover between the MSD parallel and perpendicular to $\vec{n}$. In this case, it is unclear whether the diffusive regime is even reached. With increasing concentration, the diffusion becomes slower, which means that the diffusive regime is pushed to longer times, and the fit to the MSD should be adjusted. We fit the MSD for times $200\tau_B < t < 400\tau_B$ and $200\tau_B < t < 1000\tau_B$, in the directions perpendicular and parallel to the nematic director.

In principle, the long-time diffusive regime is expected at times larger than the interaction time $t >> \tau_I$. In practice, it seems to be reached mostly when the mean square displacement reaches the typical caging length-scale [151, 155, 166]. In the smectic phase, the lateral and longitudinal caging length-scales are typically σ and L. We then expect diffusive regimes for $\langle \delta_\perp^2 \rangle \approx \sigma^2$ and $\left\langle \delta_\parallel^2 \right\rangle \approx L^2 = 100\sigma^2$. For $\phi = 42\%$, the diffusive regime seems accessible, the MSD perpendicular and parallel to the nematic director are well described by a linear regressions for times $t > 25\tau_B$ and $t > 600\tau_B$. However, for $\phi = 48\%$, the long-time limit is unlikely to be reached in the direction parallel to the nematic director (•).

The long-time translational and rotational diffusion coefficients are determined by fitting the MSDs and the orientation correlation function for each bin. The data and fits are shown in figure 5.6. Each color corresponds to a unique z-position and concentration indicated in the legend. All MSDs were found to be well described by a linear regression ($y = ax$) apart from two,

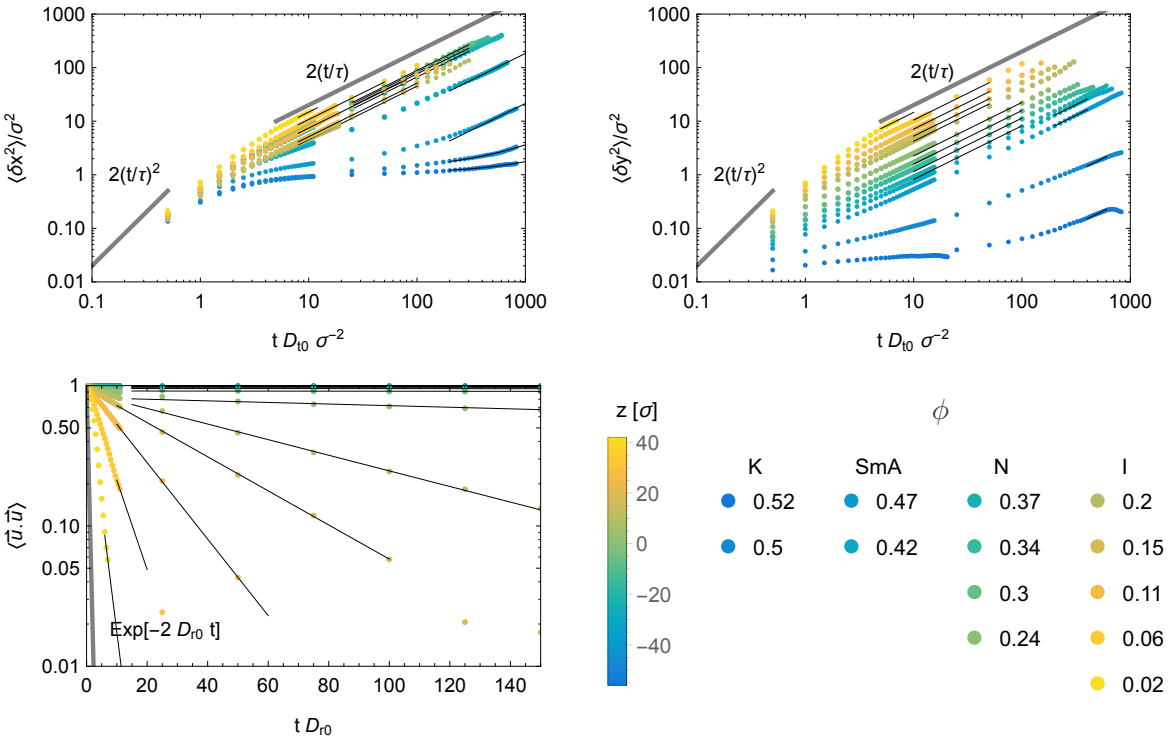


Figure 5.6: Fitting of the orientation correlation function ($\langle\vec{u}.\vec{u}\rangle$–bottom left), the MSD along the nematic director ($\langle\delta_x^2\rangle$ – top left) and the MSD perpendicular to the nematic director ($\langle\delta_y^2\rangle$ – top right). Each color correspond to a given height(z)/volume fraction (ϕ).

in the crystalline phase, where the parallel MSD was fitted by an affine function ($y = ax + b$). All orientation correlation functions were fitted by $\ln(y) = b - ax$ in the long-time limit, to extract the long-time rotational diffusion coefficient $D_r = a/2$.

In the left panel of figure 5.7, we plot the long-time diffusion coefficients as a function of the particle volume fraction. Let us first describe the translational diffusion.

In the *infinite dilution limit*, we expect to find $D_t = D_{t0}$. However, the trajectories in the dilute regime are too short to measure the diffusion coefficient. This is mostly due to the sedimentation-diffusion method inducing an exponential drop of the concentration, with the height z, at the top of the sediment.

In the whole *isotropic* regime, the translational diffusion coefficients along x- and y-directions are equal to each other and drop monotonically to a minimum value of $D_t/D_{t0} \approx 0.22$.

In the *nematic* phase, the diffusion coefficients parallel (●) and perpendicular (■) to the nematic director split up. The transition from isotropic to nematic results in an increase of the diffusion along the nematic director. Moreover a non-monotonic behavior is observed, within the nematic phase, with a peak around $\phi = 30\%$. On the other hand, the diffusion perpendicular to the nematic director keeps decreasing monotonically. However, we note a jump from $D_{t\perp} \approx 0.2 D_{t0}$

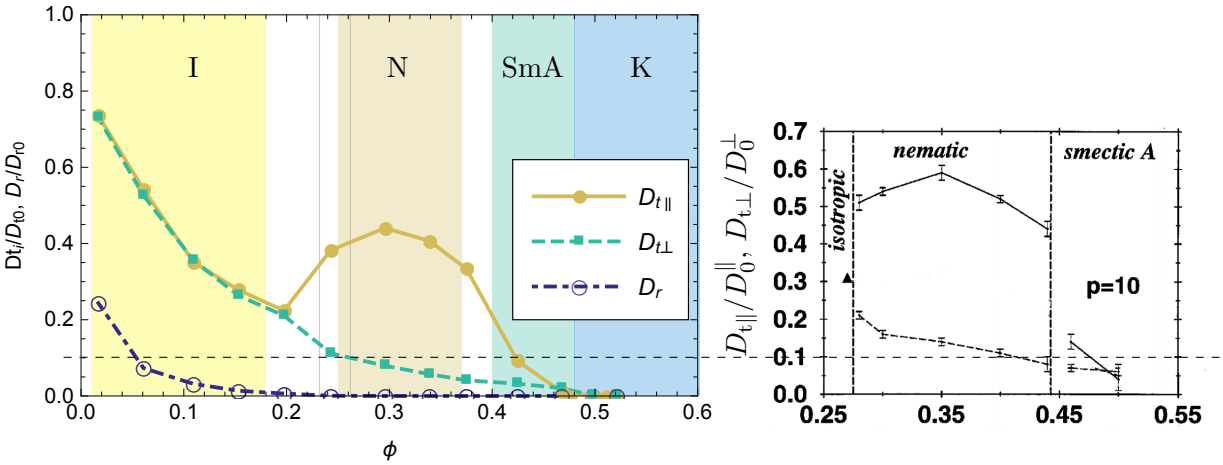


Figure 5.7: Normalized translational diffusion coefficient along ($D_{t\parallel}$-solid lines) and perpendicular ($D_{t\perp}$-dashed lines) to the nematic director for our simulation (left) and reproduced from [147] (right). The vertical lines indicate the bulk I-N coexistence found by DFT [70].

to $0.1D_{t0}$ at the $I-N$ transition.

In the *smectic* phase, we equally observe anisotropic behavior. The diffusion perpendicular to the nematic director keeps decreasing slowly, whereas the diffusion parallel drops quickly from $D_{t\parallel} \approx 0.3D_{t0}$ to $0.1D_{t0}$, keeps decreasing, and reaches a value smaller than $D_{t\perp}$ around $\phi \approx 0.45\%$.

In the *crystal* phase particles are mostly immobile: the diffusion perpendicular to the nematic director drops to zero.

In the right panel of figure 5.7, we reproduce Brownian dynamics simulation results on *spherocylinders* with an aspect ratio $p = 10$ [147]. All our observations are in qualitative agreement with these zero g bulk simulations. However, there are some quantitative disagreements. All our diffusion coefficients are shifted down. Furthermore, the maximum of $D_{t\parallel}$ in the nematic phase and the crossover between $D_{t\parallel}$ and $D_{t\perp}$ in the smectic phase are shifted to lower concentrations: $\phi = 30\%$ and $\phi = 45\%$ instead of $\phi = 35\%$ and $\phi = 50\%$.

The shift in the diffusion coefficients is likely to be due to the choice of D_{r0}/D_{t0}, $D_0^{\parallel}/D_{t0}$ and $D_0^{\perp}/D_{t0}$ that here were arbitrarily set to: σ^{-2}, 1 and 1. Lowën used the motivated values[2]: $0.058\sigma^{-2}$, 0.81 and 1.12.

It is interesting to see that our translational diffusion coefficients are both lower than in [147]. In particular, we observed that $D_{t\perp}/D_0^{\perp}$ is about twice smaller. This may be due to correlations between the diffusion coefficients. Translational and rotational motion are measured separately. However, signs of correlations have been reported [147, 161, 167–169]. One can imagine that,

[2]These values are determined from the hydrodynamic interactions with the solvent.

for example, fast rotating rods have many more collisions than slowly rotating ones, and would therefore have an increased effective translational friction reducing $D_{t\perp}$ and $D_{t\parallel}$. We may then expect that a part of the discrepancy with the simulations performed by Löwen is due to our choice of D_{r0}[3]. Furthermore, the difference of particle shape, here a chain of beads, might also play a role.
The shift in concentration may be related to the shape of the rods. A simple correction, where the rod volume is replaced by the one of its bounding cylinder, would increase the volume fraction by about 10%, and better agreement would be found, in particular, for the crossover between $D_{t\parallel}$ and $D_{t\perp}$.

The normalized rotational diffusion coefficient D_r/D_{r0} is found to decrease much more than in the zero g simulations performed by Löwen [152]. We find whilst approaching the I-N coexistence that $D_r = 0.0064 D_{r0}$ instead of $D_r = 0.19 D_{r0}$. Here, the discrepancy must certainly come from our choice of D_{r0} which is about 17 times larger than the value used by Lowën. Interestingly, the *absolute* rotation diffusion D_r, approaching the I-N transition, is comparable to the bulk simulation performed by Lowën: we find $D_r = 0.0064\tau^{-1}$, whereas he found $D_r = 0.0110\tau^{-1}$. Although, we have set D_{r0} about 15 times larger than Löwen, we find a smaller rotational diffusion coefficient at the I-N interface, which suggest that D_r is mostly independent of D_{r0} in the dense isotropic phase. This is a sign of the strong coupling between translations and rotations. In the dense isotropic regime, for long rods, translation perpendicular to the particle long axis and rotations are largely hindered by neighboring rods. The tube theory [30, 161] predicts that both long-time rotational and translational diffusion are directly correlated to the diffusion along the rod long axis ($D_0^{\parallel}$), but largely independent of $D_0^{\perp}$ and D_{r0}. The behavior observed here, in the dense isotropic, is then in qualitative agreement with the tube theory despite the rod's fairly small aspect ratio ($p = 10$).

In figure 5.8, we fit the translational and rotational diffusion coefficients in the isotropic phase. To do so, we use equations 5.3, which is derived by the tube theory [160, 161] assuming long rods, and where γ and β are fitting parameters. We find the best agreement with theory for $\gamma = 410$ and $\beta = 5$. The rotational diffusion, and so the value of β, is highly impacted by our arbitrary choice of D_{r0}. Hence, we comment on the translational diffusion. Apart from the lowest concentration ($\phi \approx 1.5\%$), where our method is inaccurate, we find that the tube model

[3]This could be tested by decreasing D_{r0} and restarting the simulation. However, I did not have the opportunity to discuss this with my colleague Maxime.

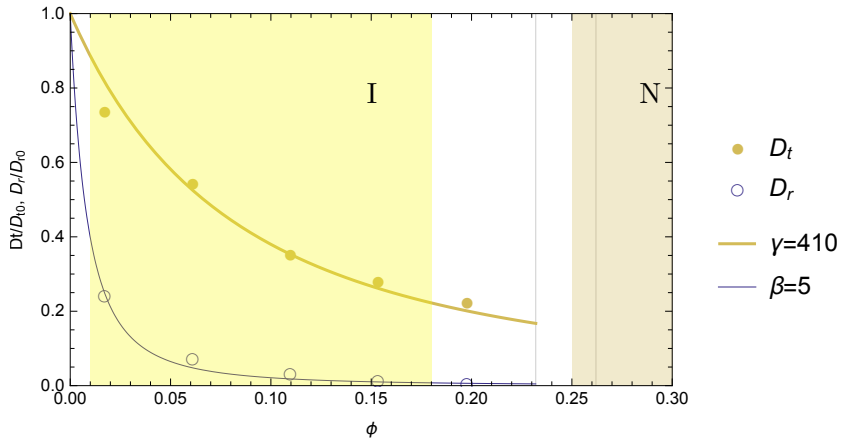


Figure 5.8: Comparison of the diffusion coefficients in the isotropic phase with the tube theory [160,161], β and γ are fitting parameters, the corresponding functions are provided in equation 5.3. The yellow and brown backgrounds correspond to measured nematic order parameters $S_2 < 0.2$ and $S_2 > 0.7$.

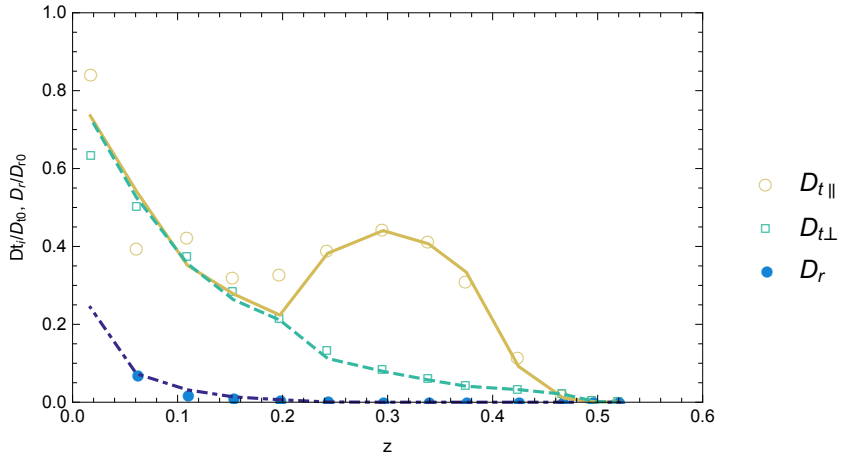


Figure 5.9: Comparison of the diffusion coefficients obtained when cutting trajectories (solid lines) and keeping them whole (symbols).

reproduces the data well. This agreement may be surprising in regards of the rod's finite aspect ratio ($p = 10$).

In section 5.3.2, we presented our method that consists of cutting trajectories when the particles diffuse too far in the z-direction. In figure 5.9, we present results where the method was not applied, but instead the trajectories were left intact. This had the effect of introducing biased data, as particles were able to diffuse in a wide range of concentrations. As a consequence, we observed large discrepancies, in particular, in the isotropic phase, where particles explore a wide range of concentrations, and at the different interfaces, where the diffusion coefficients change abruptly.

This show the importance of preventing trajectories from exploring wide ranges of concentrations, even though it reduces statistics at long times. Note that the same effect would be

expected for experimental data captured in 3D and similar precautions should be taken. For data captured in 2D snapshots, the effect would be less important, since trajectories end when particles diffuse out of focus, which limits the length of the trajectories. In this thesis, we captured 2D snapshots in the x-y plane and in the x-z plane. We will focus on the x-y plane data. Following particles in the x-y plane automatically prevents trajectories to explore wide range of concentrations as when a rod diffuses in the z-direction, it goes out of focus and therefore, it can not be tracked.

5.4 Experiments

5.4.1 Experimental methods

The diffusion of silica rods was measured for most experiments introduced in chapter 3. However, we will largely focus on the experiment 'Exp0441'. In this experiment, the rod sediment was imaged, from $z = 0$ to $z = 54\,\mu\text{m}$, by acquiring x-y snapshots separated by a distance $dz = 1.06\,\mu\text{m} \approx 2\sigma$. The image resolution and dimensions were $r = 0.19\,\mu\text{m pixel}^{-1}$ and 512×512 pixels^2. The maximum imaging speed was 30.3 frame per second.

We captured two data-sets of 51000 frames sampling 1000 times and 51 z-positions. The delay between frames were $dt = 0.1$ s and $dt = 1.78$ s, which compares well with the translational and rotational characteristic times in our system: $\tau \equiv \sigma^2/D_{\text{t0}} \approx 0.4$ s and $\tau_r \equiv 1/D_{r0} \approx 9$ s. The largest delay was long enough to capture z-stacks. In principle, z-stacks can be use to precisely detect particle orientations and positions in 3 dimensions [91]. However, this requires very high spatial and temporal resolutions, whereas here we are mostly interested in the long-time regime. Furthermore, as discussed in the simulation method we want to prevent trajectories to explore different z-dimensions fully. In experiments, this can simply be done by detecting rods in the x-y snapshots. Therefore, the experimental diffusion coefficients are measured from two dimensional snapshots.

The rod system is a dispersion of unlabeled rods 'LC017', hosting fluorescent particles 'LC010' used as tracers. The diffusion coefficients are measured from fluorescent particle trajectories, but the phase behavior is dictated by the rods 'LC017'. In an ideal case the labeled and non-labeled rods would be identical. In our experiments they have the same radius, however,

	L [µm]	(L-σ)/σ	(L-σ)/σ_{eff}	σ [µm]	$D_0^{\parallel}$ $[\sigma^2\,\mathrm{s}^{-1}]$	$D_0^{\perp}$ $[\sigma^2\,\mathrm{s}^{-1}]$	D_{t0} $[\sigma^2\,\mathrm{s}^{-1}]$	D_{r0} $[\mathrm{rad}^2\,\mathrm{s}^{-1}]$
LC010	4.1	9.8	8.1	0.38	2.69	1.93	2.18	0.11
LC017	5.26	12.6	10.4	0.39	2.17	1.52	1.74	0.06
Simulation	11σ	10	10	σ	$1\tau^{-1}$	$1\tau^{-1}$	$1\tau^{-1}$	$1\tau^{-1}$

Table 5.1: Rod properties: end-to-end length, aspect ratio, effective aspect ratio, diameter and diffusion coefficients at infinite dilution.

the rods 'LC010' have a length about 20% smaller than the rods 'LC017'. In table 5.1, we recall the rods properties, and we also provide their translational and rotational diffusion coefficients in DMF at infinite dilution from equations 2.25 and 2.29. Note that the translational diffusion coefficients (scaling with L^{-1}) are comparable for the two types of rods. However, the rotational diffusion coefficient (scaling with L^{-3}) is twice larger for the rods $LC010$.

Nota bene: $D^{\parallel}$ and $D^{\perp}$ are the diffusion coefficients parallel and perpendicular to the rod's *long axis*. They should not be confused with $D_{\parallel}$ and $D_{\perp}$, which are the diffusion coefficients parallel and perpendicular to the *nematic director*.

The most important parameters are:

- $p_{eff} = 10.4$, the effective aspect ratio of the bulk particles (LC017) that fixes the phase behavior.
- $D_{\mathrm{t0}} = 2.18\sigma^2\ \mathrm{s}^{-1}$ and $D_{r0} = 0.11\ \mathrm{rad}^2\,\mathrm{s}^{-1}$ the diffusion coefficient of the tracer rods (LC010) that we expect to measure at infinite dilution.

In figure 5.10, we give an overview of the phase behavior: (a) shows a reconstructed side view (x-z) of the sedimentation-diffusion equilibrium, (b) the nematic and smectic order parameters measured as a function of z, and (c) the number of dyed particle/intensity of back-scattered light measured as a function of z. We use background colors to indicate the locations of the different liquid crystal phases. The volume fraction could not be measured. However, as discussed in chapter 3, we expect the effective volume fraction to linearly drop from the beginning of the smectic phase (located at $z \approx 4\,\mu\mathrm{m}$) to $\phi = 1\%$ (estimated at $z \approx 54\,\mu\mathrm{m}$ from figure 5.10 (d)). The effective volume fraction at the smectic-crystal transition was approximated equal to 60%, the value expected for hard rods [46].

Each z-position was processed independently. The particle positions and orientations at each height were tracked over time. Rods were allowed to diffusive out of focus for $3 - 20$ s

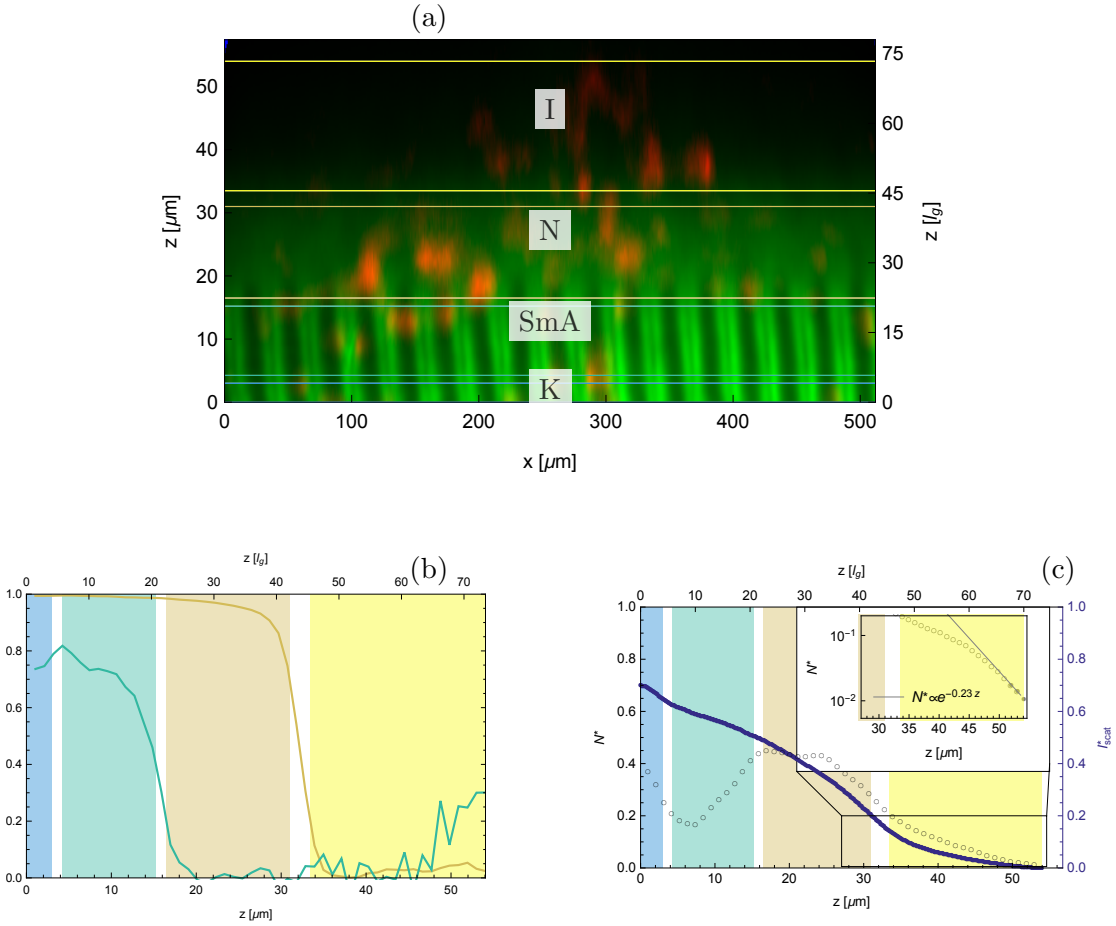


Figure 5.10: (a) Reconstructed side view of the x-z plane. (b) Order parameters as a function of z. (c) Number of dyed particles and intensity of scattered light as a function of z.

and return, i.e. disappear and reappear close by. The advantage of the method is that it increases the statistics at long times, but the drawback is that particles explore a wider range of concentrations, which could affect the precision of the method. However, the effect was too small to noticeably affect our results, validating the method.

The rotational diffusion was estimated by measuring the correlation function of the angle θ, which is the projection of the rod orientation in the x-z plane. We will show in the next section that, in the dilute isotropic and at long time (typically $P_2 < 0.5$), $P_2 = \langle 2\cos^2(\theta) - 1 \rangle = \exp(-6D_{r0}t)$. We assume that this holds at any concentration.

5.4.2 How to measure 3D rotation with 2D snapshots

There are two methods to measure the rotational diffusion coefficient: measuring either the mean square angular displacements [91,159] (MSDA) or an orientation correlation function [152]

(OCF). The OCF method is easier to implement and it is independent of the time resolution, whereas the MSDA method requires a high time resolution.

We will show that the projection of a rod in a 2D snapshot almost has the whole 3D information. Let us define the rod orientation by a three dimensional vector $\hat{u} = (u_x, u_y, u_z)$ and set the plane of observation as x-y. The orientation of the projection provides the magnitudes and signs of two components (u_x and u_y), and the length of the projection gives the magnitude of the third one (u_z). The rods nearly in plane ($u_z << 1$) will have long projections that can be measured accurately. By selecting these rods, the authors of [159] managed to measure the MSDA of rods with aspect ratios down to 2 µm from 2D video-microscopy. However, the inconvenience of the method is that rods rotating perpendicular to the plane cannot be accurately measured. This greatly reduces the long-time statistics as eventually all rods will rotate out of the plane. This is an issue for us, because we aim to measure the long-time limit. Furthermore, their method independently requires a very good time resolution, which is hardly compatible with long-time measurements. Here, we present an empirical method, which is only based on the orientations of the rods' projections θ.

The method is tested on a set of 10^4 trajectories generated to simulate random walks on the surface of a sphere. Each trajectory is composed of a list of 10^3 elements $\{t_i, \hat{u}_i\}$ describing the time evolution of a rod orientation $\hat{u_i} = (u_x, u_y, u_z)$. The first 200 elements of one trajectory are shown in figure 5.11 (top row). Note that we used dots to highlight the last 20 points of the trajectory. The rotational diffusion coefficient, related to the elementary displacements by equation 2.10 was set as $D_{r0} \approx 0.04t^{-1}$, where t is the elementary time step. The projection of u in the x-y plane is obtained by setting $u_z = 0$ and normalizing the vector: $\hat{u}'_1 = (u'_x, u'_y, 0)$. The dot product of two projected orientations $\hat{u}'_i$ is simply related to the orientations of the projections θ_i: $\hat{u}'_1.\hat{u}'_2 = \cos(\theta_1 - \theta_2)$, with θ_i defined with reference to the x-axis.

We consider three ways to analyses the rotational diffusion. They are summed up in figure 5.11. For each case, we calculate the OCFs $\Theta(t)$ and $P_2(t)$ that can take different forms in 2D and 3D (see figure 5.11). For each OCF, we look at two regimes: the 'short-time' regime defined by $\Theta(t) > 0.8$ (or $P_2(t) > 0.6$) and the 'long-time' regime where $\Theta(t) < 0.4$ (or $P_2(t) < 0.3$).

(i) The first case is the reference case. The correlation function is obtained in a standard way from the 3D orientations using all the data (e.g. see [152]) and is found to be in very good

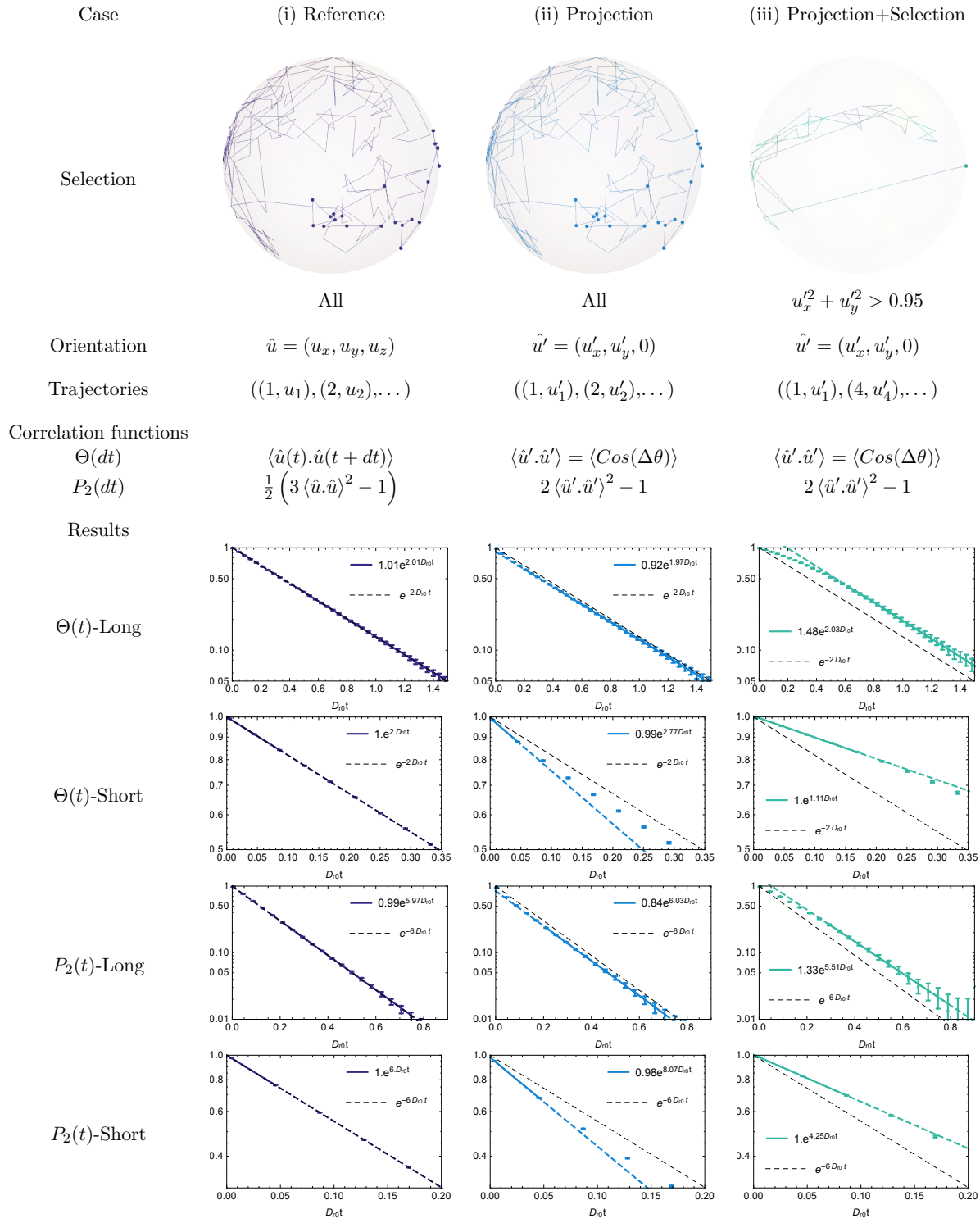


Figure 5.11: Calculation of the correlation functions using 3D orientations and their projections in the x-y plane. Graphs are compared to each other in figure 5.12.

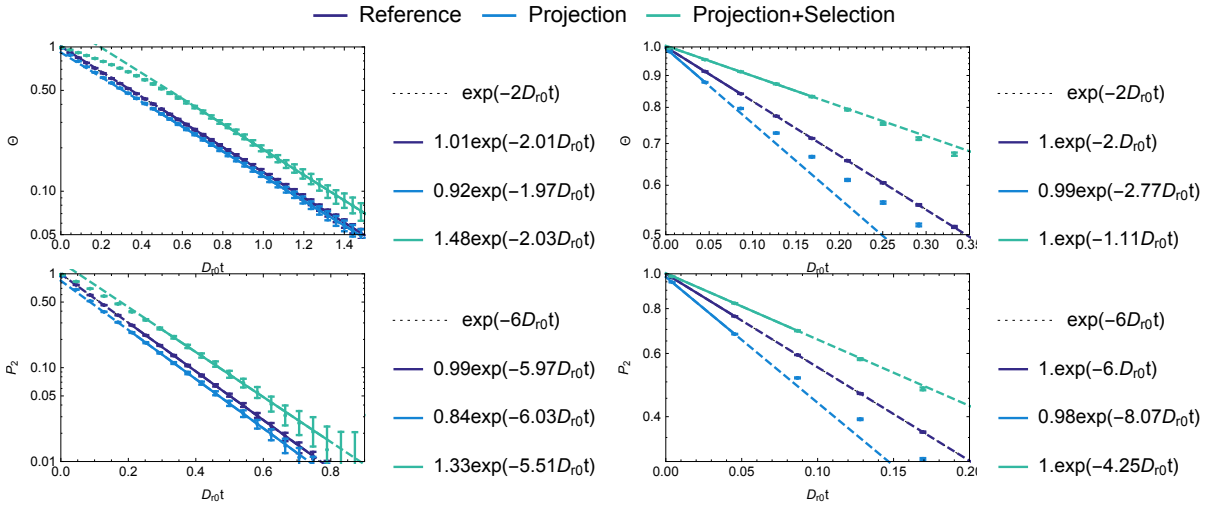


Figure 5.12: Orientation correlation functions Θ (top) and P_2 (bottom) at long times (left) and short times (right) calculated from 3D orientations (dark blue) and from 2D projections of the orientations (lighter curves).

agreement with theory: the orientation correlation function Θ decays as $\exp(-2D_{r0}t)$ at all time and the OCF P_2 decays as $\exp(-6D_{r0}t)$.

(ii) In the second case, the correlation function is obtained from the projected angles $\hat{u}'_i = (u'_x, u'_y)$ and we use the 2D form of the correlation function. At short times, the correlation function decays faster. However, at long times the decay is similar to the one obtained in the reference case.

(iii) The third case is identical to the second except that only the long projections are selected ($u'^2_x + u'^2_y > 0.95$). As a result some trajectories have missing points, however, rods are allowed to rotate out of the plane and come back. In this way we conserve good statistics at long times. At short times the correlation function is found to decay close to the behavior expected in purely 2D rotational diffusion ($\Theta \propto \exp(-D_{r0}t)$ and $P_2 \propto \exp(-4D_{r0}t)$). However, at long times the decay becomes similar to the reference case (i.e. 3D).

This empirically demonstrates[4] that, independently of whether or not rods are selected, the long-time 3D diffusion coefficient can be estimated from the (2D) orientation correlation function of the rod projections. The precision of the method will clearly depend on the definition of the long-time limit. In figure 5.12, we reproduced the results from above in order to compare the three methods more easily. On the left we fitted the OCFs for $\Theta(t) < 0.4$ and $P_2(t) < 0.3$, which was our guessed definition of long times. With these parameters, the largest error of 8% was

[4]My colleague Adam Stones, drafted a mathematical demonstration supporting this result.

found when selecting rod (case (iii) projection+selection), whereas without selection (case (ii) projection) the largest error is smaller than 2%. It is likely that even better agreement would be obtained at longer times. However, at long times the statistics worsen and eventually statistical errors become larger than the method errors. A compromise has to be made between these two types of errors.
To analyse experimental data, we will select all rod projections (case (ii) projection) and define the long times when $P_2(t) < 0.5$. We choose this slightly higher value, because we expect larger statistical errors in experiments due to the smaller amount of data. The OCF P_2 is convenient to use in experiments as it does not make the difference between $\hat{u}$ and $-\hat{u}$. On the contrary, in order to use Θ one should know which side of the rod is which, bringing unnecessary complications.

Note that this empirical method is meant to be employed to measure the long-time 3D diffusion coefficient of rods imaged in 2D. The short-time diffusion, if different from the long-time, should be measured with a different method, for example see [159]. The main advantage of our method is that it does not require high time or spatial resolutions. In that sense, it could be particularly relevant for fd-virus [87,166] and similar systems, which are even faster and smaller than our silica rods.

5.4.3 Experimental Results

We present results corresponding to the experiment 'Exp0441'. In figure 5.13, we show log-log plots of mean square displacements representative of the isotropic (a), nematic (b) and smectic (c-d) phases. The MSD is measured for two sets of data with time resolution $dt = 0.1$ s and $dt = 1.8$ s. We differentiate the directions parallel ($\bullet$) and perpendicular ($\circ$) to the nematic director that correspond to the x- and y-axes.
At long times $t > 20\,\sigma^2 D_{\mathrm{t0}}^{-1}$, we observe similar behavior to our simulation (figure 5.5): in the isotropic phase (a) the MSDs parallel and perpendicular to the nematic director overlap, in the nematic phase (b) they split, and in the dense smectic phase (d) we observe a crossover where the MSD perpendicular becomes larger than the MSD parallel.

In contrast with our simulation, here the MSDs are not linear with time. This is more easily observed at shorter times, where it is clear that the MSDs are not parallel to the black line $\langle \delta^2 \rangle = 2D_{\mathrm{t}}t = 2\,\sigma^2\,t/\tau$ indicating the diffusive behavior. In experiments, detection errors

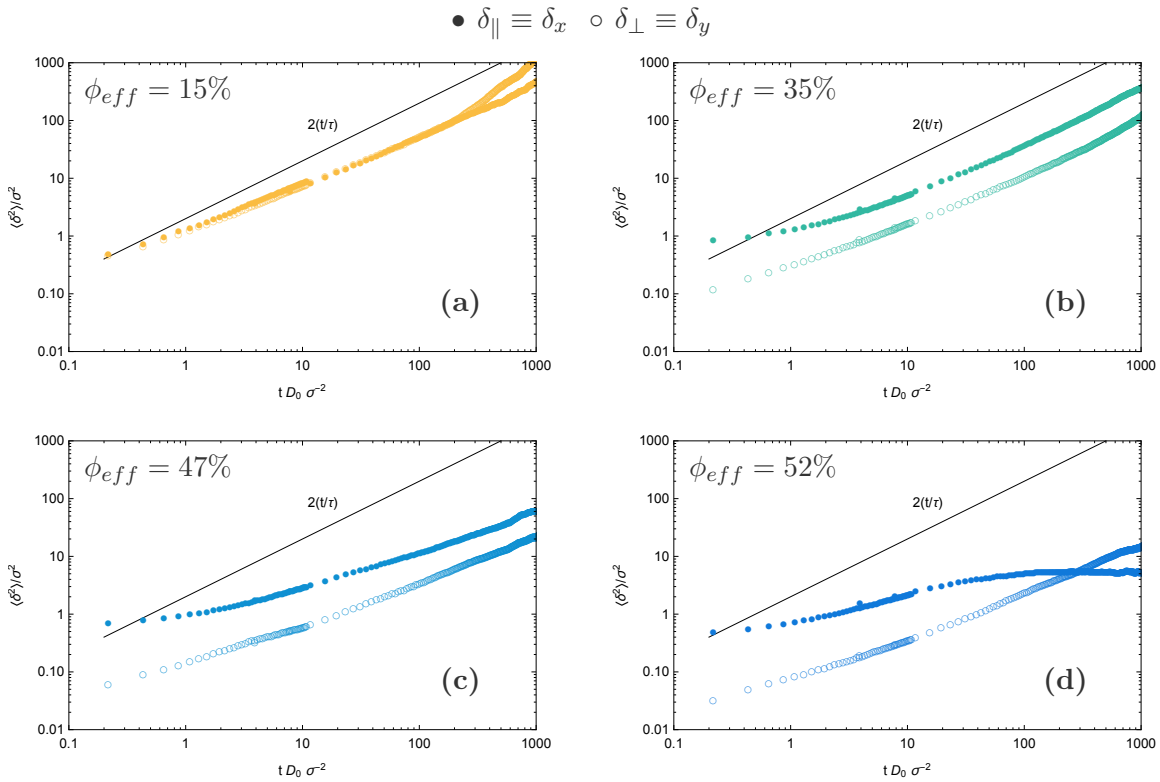


Figure 5.13: Representative examples of MSDs in the isotropic (a), nematic (b) and smectic phase (c-d). The dots (•) and circles (∘) correspond to displacements parallel and perpendicular to the nematic director, i.e. along $\hat{x}$ and $\hat{y}$.

on the particle positions induce a non-zero y-intercept: $\langle \delta^2 \rangle = 2D_{t0} + \epsilon^2$. In a log-log plot, the y-intercept leads to a plateau when $t << \epsilon^2 D_{t0}^{-1}$ but has vanishing effect when $t >> \epsilon^2 D_{t0}^{-1}$. Detection errors explain why at the shortest time we find $\langle \delta^2 \rangle > 2D_{t0}t$. However, the MSDs are equally sub-diffusive.

Identifying the long-time limit Sub-diffusivity is expected in a dense suspension at the transition between short-time and long-time self-diffusion. The characteristic time associated to this transition τ_I is defined by the time required for a particle to explore the free energy landscape emerging from interactions with other particles. It may strongly vary with the colloid concentration and structure.

We locate the transition by plotting the time evolution of the Non-Gaussian Parameter (NGP) α_2 (equation 5.1). We expect α_2 to present a peak at the transition, i.e. $t \approx \tau_I$. The long-time diffusion coefficient should then be measured for $t >> \tau_I$. In figure 5.14, we show the NGP for all concentrations. We will first comment on the position of the peak. The magnitude, which is related to the difference between long-time and short-time diffusion coefficients, will be treated

later on.

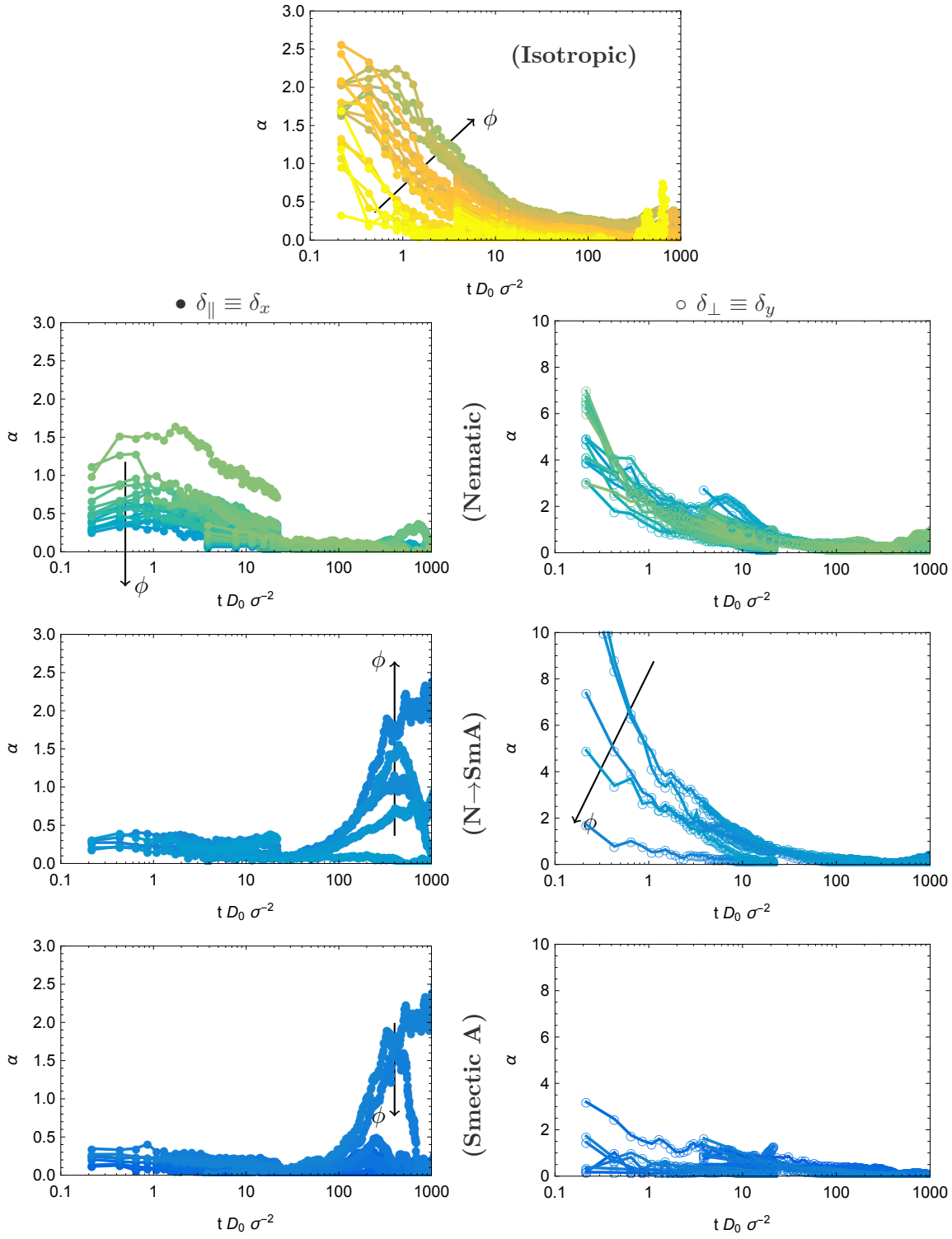


Figure 5.14: Non-Gaussian parameter α as a function of time in the I, N and SmA phases. Same legend as figure 5.15.

In the isotropic phase, there is no difference between the diffusion along the x- and y-axes. Then, we average the NGPs measured in the x- and y-directions and plot them in figure 5.14

(top graph). We overlay results from low to high concentrations ($\phi_{eff} \approx 2\%$ to $\phi_{eff} \approx 25\%$) using a color gradient from bright yellow to darker green. For low concentrations (bright yellow), only the right part of the peak can be observed. However, at the highest concentrations, the middle of the peak is observed around $t \approx 0.5 - 1\tau$. *We infer that the characteristic interaction time τ_I increases with concentration in the isotropic phase. This trend is expected as, at high concentration, the particle interaction are more important and the diffusion is slower.*

For the nematic and smectic phases, we make a distinction between diffusion parallel and perpendicular to the nematic director. The corresponding NGPs are plotted in figure 5.14 in the left and right columns.

In the nematic phase (second row), α_2 shows a peak around $t = 1 - 2\tau$ for the direction parallel to $\vec{n}$, whereas in the direction perpendicular the peak is located at time $t < 0.2\tau$. *In the nematic phase, particles are highly aligned. The typical lateral inter-particle distance is smaller than the longitudinal one. Frontal shock between particles are then more frequent in the lateral direction, which explains why we expect τ_I to be smaller. The long tail of α_2, in the perpendicular direction, may be related to some coupling with diffusion in the parallel direction.*

At the nematic-smectic transition and in the smectic phase (3rd and 4th row) we observe two peaks: one at $t \approx 1\tau$, that has mostly disappeared, and a second at $t \approx 300 - 1000\tau$. This second peak is due to particles diffusing through the static energy landscape created by the smectic layers. We only really observe the left part of the peak which means that we will not be able to precisely measure the long-time diffusion coefficient. In the perpendicular direction, the peak is located at $t < 0.2\tau$.

The long-time diffusion coefficients will be fitted for times $t > 10 - 30\tau$ in the semi-dilute isotropic. For the dense isotropic phase, the nematic phase and the perpendicular component of the smectic phase, we will use times $t > 30\tau$. For the parallel component of the smectic phase and the crystal phase, we will use times $t > 100\tau$ and $t > 300\tau$. We expect these times to capture the long-time self-diffusion well, apart for the translation parallel to the nematic director in the smectic phase where the long-time limit is not reached, and will therefore be overestimated.

The MSDs parallel and perpendicular to the nematic director are plotted and fitted in figure 5.15 for concentrations ranging from $\phi_{eff} = 2\%$ (semi-dilute isotropic) to $\phi_{eff} = 63\%$ (crystal phase). We use a color gradient to indicate the different concentrations, which are estimated from the z-positions in the sedimentation-diffusion equilibrium, see chapter 3. The

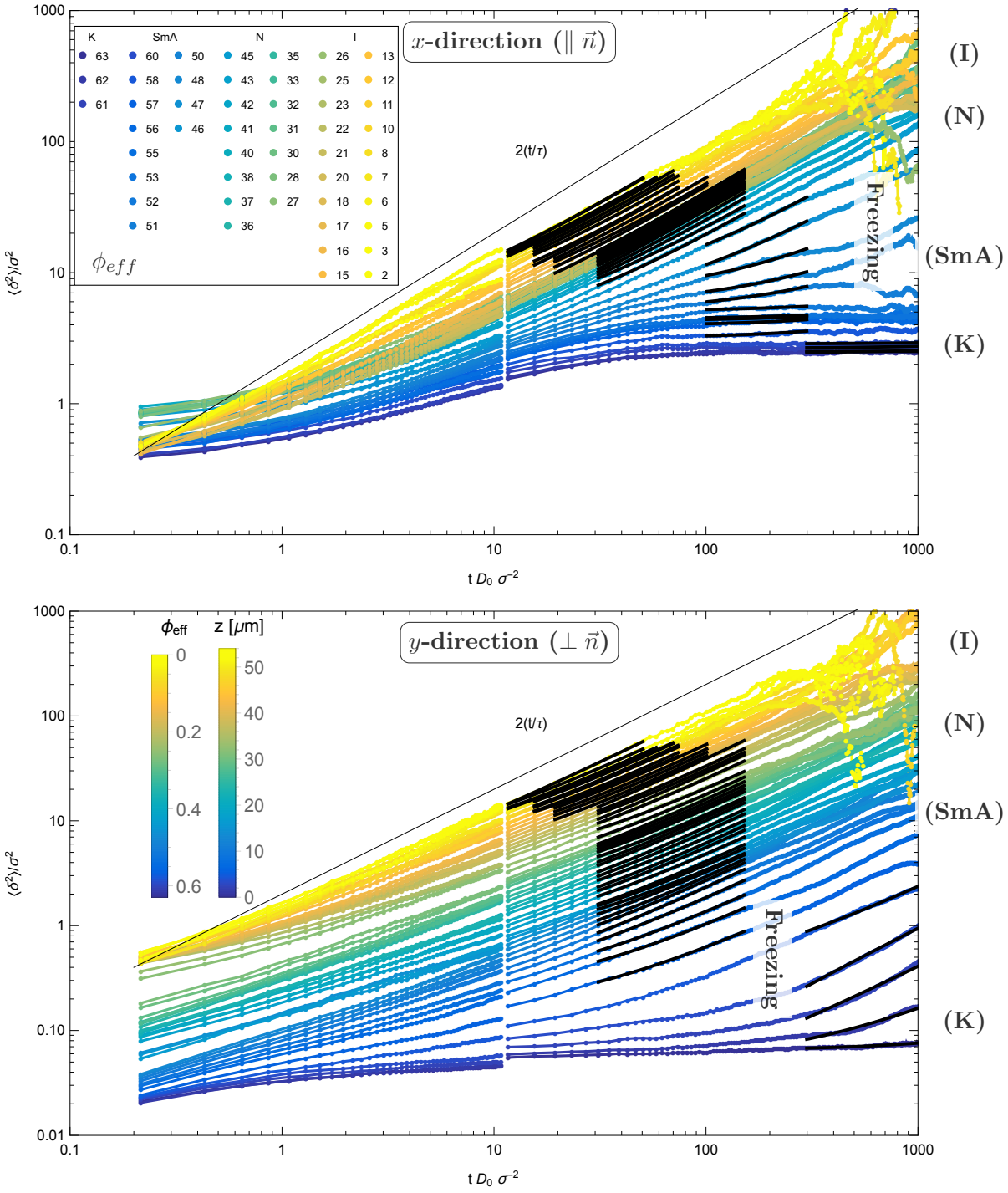


Figure 5.15: Fitting of the MSD along the nematic director ($\langle \delta_x^2 \rangle$) and the MSD perpendicular to the nematic director ($\langle \delta_y^2 \rangle$). Each color correspond to a given height(z), or equivalently effective volume fraction (ϕ_{eff}).

legends are shared between the two figures.

The MSDs are fitted over time ranges spreading typically half a decade. The fits are plotted with thick black lines. We indicate the MSD expected at infinite dilution with the thin black line labeled $2t/\tau$.

These graphs hold many pieces of information. The MSDs perpendicular to the nematic director (bottom graph) are nicely stacked on the top of each other due to the monotonic increase of the diffusion coefficient $D_{t\perp}$ with concentration. We measure the lowest MSD for the highest concentrations (—) and the largest one at the lowest concentration (—). In the parallel direction, we observe some overlap between the isotropic and nematic phases at long times, whereas at short times the MSDs are higher in the nematic phase. We expect larger detection errors in the nematic phase, which largely explain the behavior observe at short times.
The most interesting feature in these plots is the transition between impaired diffusion to frozen particle, in the sense that they only wiggle around their average position, like in a crystal. These 'freezing' transitions are characterized by a large drop of the MSDs which here means that the curves are spaced out. When increasing concentration, we clearly see that the dynamics freeze first in the parallel direction (smectic phase), and second in the perpendicular one (smectic to crystal transition).

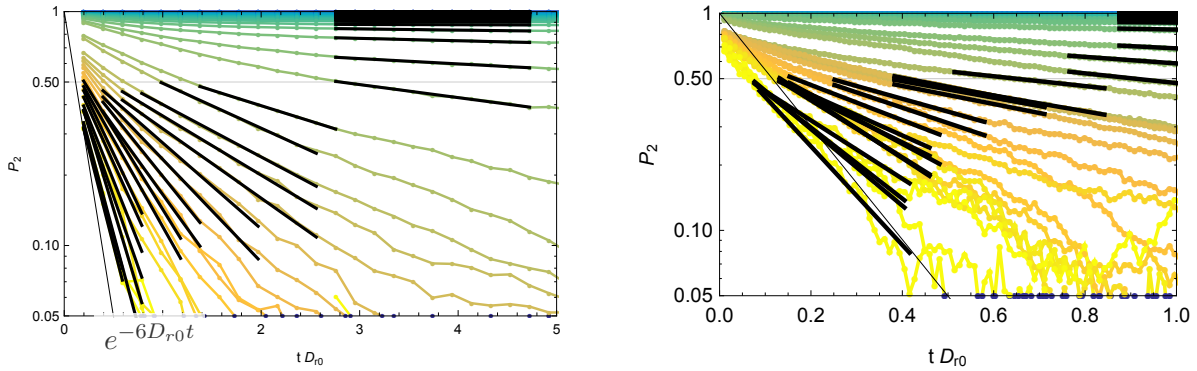


Figure 5.16: Fitting of the orientation correlation function P_2 of the rod projections. Measured for the 'long' times ($dt = 1.78s$) and 'short' times ($dt = 0.1s$) sets of data (left and right). Same legend as figure 5.15.

The orientation correlation functions of rod projections are plotted in figure 5.16 for the two sets of data. The time resolution is better in the right panel. However, the long-time statistic is better in the left panel, which will be used to calculate the rotational diffusion coefficients. The OCFs are fitted for values of $P_2 < 0.5$ following the method presented in section 5.4.2. From the MSDs and OCFs, we extract the translational and rotational diffusion coefficients and compare them to the simulations performed by Löwen [147] in figure 5.17. Note that Löwen normalized the translational diffusion coefficients by $D_0^{\parallel} \approx 1.2D_{t0}$ and $D_0^{\perp} \approx 0.9D_{t0}$, whereas we normalized them by D_{t0}.

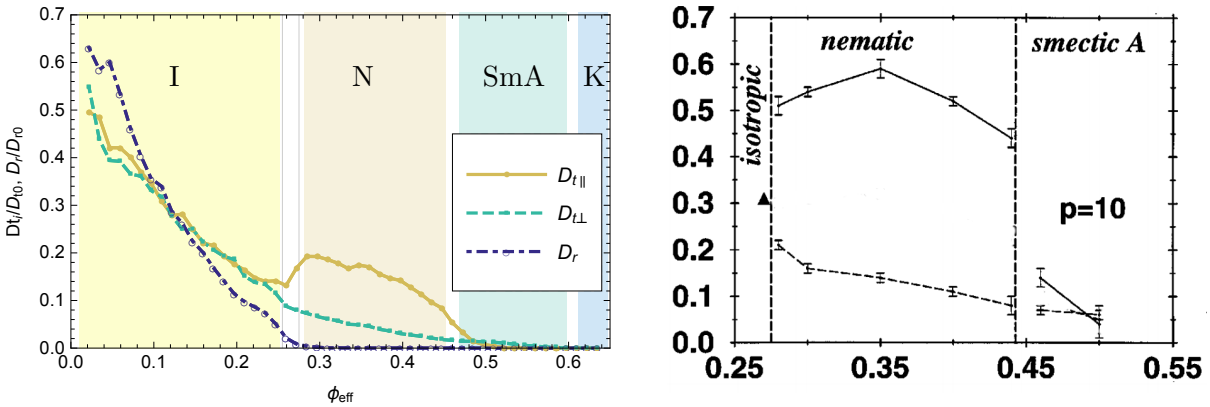


Figure 5.17: Normalized translational diffusion coefficient along ($D_{t\parallel}$-solid lines) and perpendicular ($D_{t\perp}$-dashed lines) to the nematic director for our simulation (left) and reproduced from [147] (right). The vertical lines indicate the bulk I-N coexistence found by DFT [70].

Long time diffusion coefficient The diffusion coefficients are plotted as a function of the effective volume fraction in figure 5.17. Overall, the trend introduced in section 5.3.3 is reproduced. We will consider each phases separately. But let us recall first that the effective volume fraction ϕ_{eff} has not been directly measured but estimated. The uncertainty on ϕ_{eff} could be relatively large, in particular at small values, and should be considered as indicative.

In the isotropic phase, the translational diffusion coefficients in the x- and y-directions are, within experimental precision, equal. Volume fractions smaller than $\phi = 2\%$, correspond to z-positions higher than $z = 53\,\mu m$ and were not experimentally measured.

In figure 5.18, we plot the translational (averaged over x and y) and rotational diffusion coefficients as a function of concentration focusing on the isotropic phase. The data are fitted with the expressions predicted by the tube theory (equation 5.3).

For the translational coefficient, the fit describes the data well for volume fraction $\phi > 5\%$, similar as with the simulation results in figure 5.8. Note that, in the semi-dilute isotropic regime, the diffusion coefficient drops quickly with z: it is halved on the length-scale of the particle. We then expect a strong interplay between different concentrations when $\phi < 5\%$. Therefore, the sedimentation-diffusion equilibrium method is not well suited to study the semi-dilute isotropic regime. However, as the concentration increases, rod dynamics evolve more slowly with z, so this effect will be less important.

The rotational diffusion does not seem to follow the trend predicted by the tube theory, particularly for $\phi > 15\%$. Note that, *a piori*, we do not expect the tube theory to work for short aspect ratios.

Approaching the nematic phase, at $\phi_{eff} \approx 24\%$, the diffusion parallel and perpendicular to the nematic director starts to split up and the rotational diffusion quickly drops to 0. At $\phi_{eff} = 24\%$ (the last isotropic point), we measure

$$D_{\mathrm{t}} = 0.14 D_{\mathrm{t0}} = 0.0025 L^2 \ \mathrm{s}^{-1} \qquad \text{and} \qquad D_r = 0.07 D_{r0} = 0.008 \ \mathrm{rad}^2 \mathrm{s}^{-1}.$$

Where, for a similar aspect ratio ($p = 10$) and concentration ($\phi \approx 27\%$) Löwen found:

$$D_t = 0.3 D_{\mathrm{t0}} = 0.003 L^2 \ \mathrm{s}^{-1} \qquad \text{and} \qquad D_r = 0.19 D_{\mathrm{t0}} = 0.011 \ \mathrm{rad}^2 \mathrm{s}^{-1}.$$

Relative to the infinitely dilute regime, the diffusion coefficients approaching the nematic phase are then 2 to 3 times lower in experiments than in simulations or than predicted by the tube theory for long rods ($D_{\mathrm{t}} = 1/3 D_{\mathrm{t0}}$ and $D_r \approx 0.3 D_{r0}$).
However, these values contain a striking similarity. In the dense isotropic, the rods are expected to only translate along their long axis. In order to rotate, a rod must escape from its 'tube', i.e. translate by a fraction of L. The ratio $\frac{D_{\mathrm{t}}}{L^2 D_r}$ only depends on the dimensions of the tube, i.e. on the structural properties. The values of $\frac{D_{\mathrm{t}}}{L^2 D_r}$ are 0.31 for us and 0.30 for Löwen. In our simulation we found $\frac{D_{\mathrm{t}}}{L^2 D_r} = 0.34$ and the tube theory predicts $\frac{D_{\mathrm{t}}}{L^2 D_r} = 0.2$.
This results confirms that the tube theory may be use to characterize rods with an aspect ratio of 10 in the dense isotropic phase, as observed in [152]. However, a correction for a finite aspect ratio is necessary to obtain quantitative agreement. Experimentally, the dimensions of the tube are found to be in very good agreement with simulations of hard rods [147, 152]. This is further evidence that our system of rods reproduces the structural properties of hard rods. If the difference in diffusion coefficients is not structural it may thus be due to hydrodynamic interactions.

In the nematic phase, the diffusion coefficients parallel and perpendicular to the nematic director are both at least half as large as in simulations. The largest difference is found close to the smectic phase, where they are measured to be about four times smaller.
In simulations, we observed a maximum in the diffusion parallel to $\vec{n}$ around the middle of the nematic phase. This non-monotonic behavior, within the nematic phase, is not observed here. Nevertheless, we equally found that the nematic order parameter was increasing much faster than in simulations (see chapter 3). Yet, it has been suggested that the increase in $D_{\mathrm{t}\parallel}$ is linked to the alignment of the rods [147]. The maximum of $D_{\mathrm{t}\parallel}$ found by Löwen corresponds to a value

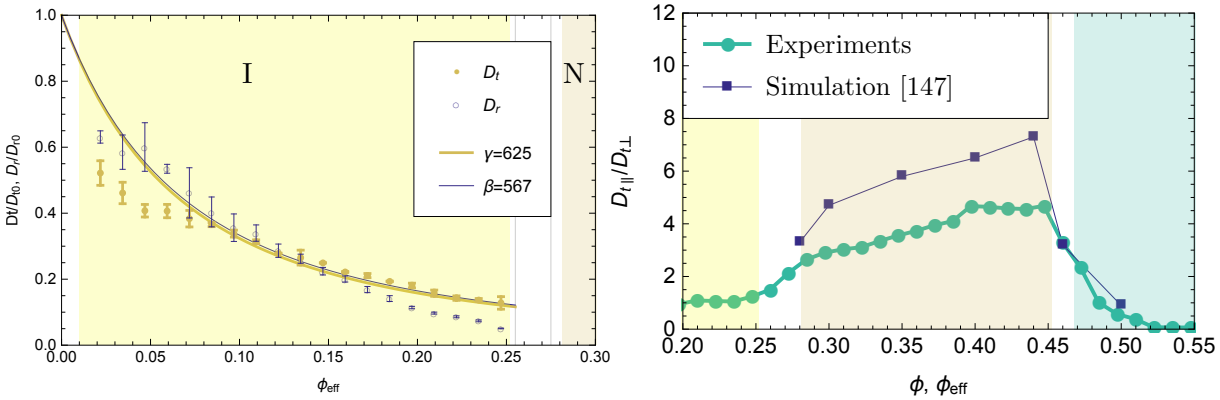


Figure 5.18: (left) Comparison of the diffusion coefficients in the isotropic phase with the tube theory [160, 161]. The fitting functions are provide in equation 5.3. The yellow and brown backgrounds correspond to measured nematic order parameters $S_2 < 0.2$ and $S_2 > 0.7$. (right) Ratio between diffusion parallel and perpendicular to the nematic director.

of $S_2 = 0.9$, which in our experiment is reached around $\phi = 30\%(z \approx 30\,\mu\text{m})$, very close to the I-N interface, see figure 5.10 (b). It is then likely that the fast increase of S_2 in experiments is shifting the maximum of $D_{t\|}$ to smaller concentrations.

In figure 5.18, we plot the ratio between the long-time diffusion coefficients along and perpendicular to the nematic director $\frac{D_{t\|}}{D_{t\perp}}$. The experimental data is compared to the simulations performed by Löwen [147]. The trend is found to be in very good agreement. However, we observe that the diffusion anisotropy is shifted down in our experiments. So compared to simulations, the diffusion is slowed down relatively more in the parallel direction than in the perpendicular one.

In the smectic phase, the diffusion coefficient parallel to the nematic director drops quickly to zero, whereas $D_{t\perp}$ keeps decreasing with concentration at about the same pace. The crossover between the two curves is found at $\phi = 48\%$ and $D_t = 0.014 D_{t0}$, which correspond to similar concentration than Löwen but again much lower diffusion coefficient value.

At the smectic crystal transition, $D_{t_\perp}$ drops quickly to 0.

In sum, we find a good qualitative agreement with simulations of hard rods [147, 152]. In particular structural similarities were established between experiments and simulations. However, we find smaller diffusion coefficients across the whole phase diagram, by typically a factor of 2 to 4.

In the nematic phase, similar quantitative disagreements were found between simulation and experiments on elongated viruses [148]. The authors showed that the discrepancy was at least

partly due to hydrodynamic interactions [148]. In Löwen's simulations, HI between particles were neglected, which may partly explain disagreements with our experiments.

Short time diffusion coefficient The short-time diffusion is expected for times

$$10^{-8}\mathrm{s} \approx \tau_D << t << \tau_I \tag{5.8}$$

By locating peaks in α_2 (figure 5.14), we have been able to find, for all phases, a transition between two diffusive regimes. In the smectic phase, parallel to the nematic director, we even found two transitions around $t \approx \tau$ and $t \approx 300 - 1000^{+}\tau$. This means that, if the structure presents multiple characteristic length-scales, intermediate diffusive regimes can be observed between the short and long-time regimes.
In the isotropic and nematic phases we only found one transition for $t \leq \tau$. We will assume this is *the* short-time to long-time transition. We will infer from the magnitude of α_2 information about the short-time diffusion.

The transition between short and long-time was found at times $t \leq \tau$, which are comparable to our time resolution $t = 0.2\tau$. Consequently, the short-time diffusion coefficient cannot be directly measured. However, the value of alpha is related to the difference between short-time and long-time diffusion coefficients (D^s and D^l). We can thus extract information about the short-time diffusion coefficient from the evolution of α_2. When the concentration increases, we have shown that the long-time diffusion coefficient decreases (figure 5.17). If the short-time diffusion is constant we then expect α_2 to increase, whereas α_2 should decrease if D^s decreases faster than D^l.
In the isotropic phase, the general trend is that α_2 increases with concentration. This means that particle interactions are slowing down the long-time diffusion but not as much the short-time diffusion. However, for $\phi > 20\%$, the NGP starts decreasing, and therefore, the short-time diffusion is now the most strongly impacted by the concentration increase. This may be due to HI.
In the nematic phase, along the nematic director, α_2 decreases. This is again an evidence of a slowing down of the short-time dynamics. Perpendicular to $\vec{n}$, the trend is not very clear. However, it shoots up approaching the N-Sm transition, which could be expected as $D^l \equiv D_{\mathrm{t}\perp}$ quickly drops by about 50%.

At the nematic-smectic interface, parallel to $\vec{n}$, the NGP increases as $D_{t\parallel}$ quickly decreases to 0 but goes back to 0 when $D_{t\parallel} = 0$ is reached. The behavior perpendicular to $\vec{n}$ is more interesting. Whereas the long-time diffusion is mostly unaffected by the nematic-smectic transition, α_2 decreases dramatically. It is unclear whether the peak is simply shifted to smaller times or if the short-time diffusion is actually slowed down. However, at the N-S transition, the NGP perpendicular to the nematic director is clearly connected to the diffusion *parallel* to the nematic director, which demonstrates the existence of a coupling between translation parallel and perpendicular to the nematic director around the N-S transition concentrations $\phi_{eff} \approx 40 - 50\%$. Strongly sub-diffusive diffusion perpendicular to the nematic director was also observe for viral rods, at similar concentration [155]. A rod in between two layers can potentially interact with twice more particle than a rod staying inside the layer. Therefore, one can imagine that the diffusion perpendicular will depend on whether or not the rods are able to diffuse in the third dimension.

In sum, we found at least two instances where, upon concentration increase, we measure a slow down of the short-time translational diffusion, i.e. a decrease of α_2: in the isotropic phase, approaching the nematic concentrations ($20\% < \phi_{eff} < 25\%$), and in the nematic phase, for the diffusion parallel to the nematic director. This implies that, if we were able to measure D_s, we would find $D_s < 2D_{tt0}t$. Reduced short-time diffusion coefficients were found in a system of quasi-two-dimensional colloidal hard sphere fluid and attributed to hydrodynamic interactions [150].
The highest values of α_2, i.e. the strongest sub-diffusive behavior is observed in the direction perpendicular to the nematic director. In particular, in the nematic phase and at the N-SmA transition. The peak in α_2 is found for times $t < 0.2\tau$. Interestingly, this was not observed in simulations [151].

Addition of salt The results presented above were obtained for rods dispersed in pure DMF. This did not allow a proper control of the Debye length κ^{-1}. In figure 5.19, we compare previous results with the experiment 'Exp0602' where 0.5mM of LiCl was added fixing the Debye length $\kappa^{-1} = 9.2\,\text{nm}$.
Apart from the salt concentration, all experimental parameters were kept constant. We do not observe significant differences between the two experiments, neither on the phase behavior, nor on the diffusion. Note that, for higher salt concentrations ($I = 5 - 10$ mM) no result is provided

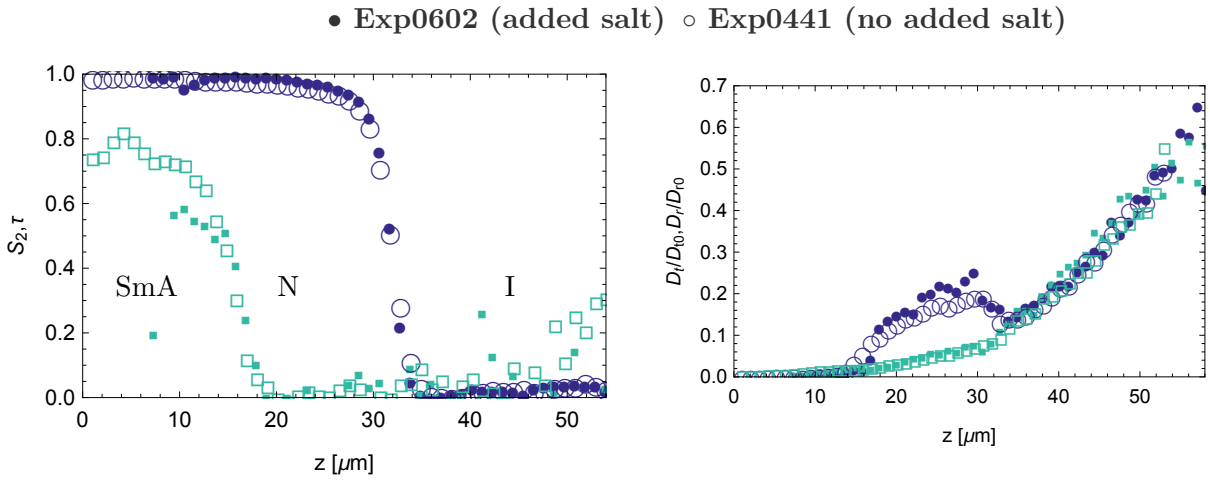


Figure 5.19: Behaviour of silica rods with (•) and without (○) added salt. (left) Nematic and smectic order parameters. (right) Diffusion coefficients along and perpendicular to the nematic director.

as the rods were starting to form aggregate. The results obtained above are then reproduced for a well controlled Debye length $\kappa^{-1} = 9.2\,\text{nm}$.

This independence of the phase behavior and diffusion with salt concentration (for $I \leq 1$ mM) is at first sight surprising. However, we note that similar behavior was observe on the rotational diffusion of silica sphere in DMSO-DMF mixture for ionic strength $I < 10$ mM, whereas clear dependence with salt concentration was found for $I = 100 - 500$mM (ref [170], FIG 3A). The authors mentioned the possible effect of charge regulation, which describes the strong coupling between electrostatics and chemical dissociation equilibrium at the surface [171].

5.5 Conclusion

In this chapter, we have exploited the sedimentation-diffusion equilibrium of rod-like particles to conveniently measure their dynamical properties across the whole phase diagram. We have performed simulations of chains of beads with an aspect ratio of 10 and experiments on silica rods with an effective aspect ratio $p_{eff} \approx 10.4$.

We first employed a molecular dynamic simulation in order to test the method. We showed that trajectories exploring a wide concentration range were affecting the long-time diffusion coefficient, particularly in the isotropic phase. However, the problem could be avoided by dividing trajectories. The method was not found to dramatically affect the long-time statistics. We were then able to measure the long-time diffusion coefficient across the whole phase diagram in

effectively a single simulation.

We then presented experimental results. By using relatively large rods, we achieved resolutions suitable for particle tracking for a time range of 4 decades. This enabled the identification of transitions between diffusive regimes. In the isotropic phase, the transition time was found to increase from $\tau_I < 0.2\, D_{t0}^{-1}\sigma^2$, for low concentrations, to $\tau_I \approx 1\, D_{t0}^{-1}\sigma^2$ for $\phi_{eff} > 17\%$. In the nematic and smectic phases, typical transition times were $\tau_I \approx D_{t0}^{-1}\sigma^2$ in the direction parallel to the nematic director and $\tau_I < 0.2\, D_{t0}^{-1}\sigma^2$ in the direction perpendicular.
Unfortunately, our time resolution was not good enough to precisely measure the short-time diffusion coefficients. Nevertheless, the analysis of the non-Gaussian parameter α_2 suggested that the 'short-time' diffusion was significantly slowed down as a function of concentration, which appeared particularly clearly in the dense isotropic ($\phi > 20\%$) and nematic phases.

We have subsequently measured the long-time diffusion coefficients from the semi-dilute isotropic to the crystalline phase. The results were found to be in good qualitative agreement with bulk simulations of hard rods [147]. In particular, dynamical insights on the structural features were found in very good agreement.
Approaching the nematic phase, we found the ratios $\frac{D_t}{L^2 D_r}$ in close agreement with simulations. This shows that, at this concentration, the rods motion is well captured by the tube theory and that the dimensions of the tube, i.e. the structural properties of the phase, are similar in simulations and experiments.
In the smectic phase, we found the crossover between $D_{\parallel}$ and $D_{\perp}$ predicted in the simulations performed by Löwen [147] with close quantitative agreement. This crossover is expected to be mostly driven by structural changes, i.e. reduction of the inter-particle distance within layer.
Our experiments confirm that both the volume fraction and aspect ratio can dramatically affect the diffusion anisotropy in the smectic phase [147], with a general trend where $D_{\parallel}$ is enhanced by low volume fraction and large aspect ratio. The opposite behavior observed between short silica rods [90] ($D_{\perp} > D_{\parallel}$) and long viruses [155]($D_{\perp} < D_{\parallel}$) can be simply explained by the difference between aspect ratios. The same behavior would be expected for hard rods.

Quantitatively we found large differences between our experiments and Löwen simulations: typically a factor of 2 or more in the dense phases. This could be explained by HI, that are expected to increase drag forces in dense suspension of rods [148]. However, note that even when accounting for HI, gaps were found between simulations and experiments on model viral particles

in the nematic phase [148]. Therefore, our work confirms the idea that current simulations and theories are not able to quantitatively capture the behavior of model experimental systems. We hope that our straight rods with shorter aspect ratio, that are easier to simulate, will motivate further work in that direction.

Outlooks could take different directions. Starting with further analysis, the correlations between rotation and translations could be directly measured by studying the angular root mean square displacement. This could be achieved without need of further data in the dense isotropic phase but equally in the nematic and smectic phases.
Variations of the method could of course include different particles, but also the application of an(other) external field. Silica rods are known to align with electric fields [139]. A simple electric field would then allow to measure the diffusion (and phase behavior) of perfectly aligned rods, which surely would be easier to model theoretically.

Acknowledgments

Again I would like to express my gratitude to Maxime Tortora who simulated the MD simulation, which was very helpful to check the experimental method.
I also would like to give my thanks to Pavlik Lettinga and Roel Dullens for providing me with feedback on this chapter, with particular appreciations to Pavlik who hosted me in Jülich and pushed me to image my sample from the bottom.
I finally would like to acknowledge helpful exchanges with Eric Grelet and Taiki Yanagishima.

Chapter 6

Confinement of colloidal liquid crystals

Abstract

We report on the confinement of colloidal liquid crystals in three dimensional chambers with a tailored footprint. To this end, we use colloidal silica rods 'LC017' and exploit their relatively large density difference with respect to the dispersing solvent to study isotropic, nematic and smectic phases confined into a single chamber. Combining laser scanning confocal microscopy and soft-lithography techniques enables us to characterize the configurations down to the single particle level. We focus on the smectic phase confined into squares, lozenges and annuli. In *squares* we find occurrences of the uniform and the smectic bridge states in agreement with theoretical expectations and simulations. We also find a meta-stable diagonal state. This diagonal state is found to be stabilized against the bridge state by *lozenges* with nose angle $\gamma < 60°$. Confinement in *annuli* reveals three well defined structures. In particular, we observe a transition from smectic bridge, for small inclusions, to the circular state, for large inclusions. The third state, made of three domains separated by three disclination lines radially oriented, seems to be stabilized by final size effects as it is only formed for a small range of annuli sizes around $r_{out} \approx 5L$.

The transitions observed in annuli and lozenges are explained in light of phenomenological models. This allows us to extract the relative energy between a disclination line of length λ ($\delta\lambda$), an edge dislocation (u_{ed}) and the bending energy (β) in our system. We find $\delta\lambda \approx \beta \approx 2u_{ed}$.

6.1 Introduction

The interest in confining colloidal liquid crystals arises from the interplay between "simple" packing problems satisfying local boundary conditions, competing elasticities and defects. Advances in lithography techniques mean that confining length-scales for *molecular* Liquid Crystals (LCs) become of the order of the extrapolation length ξ [172–174], which is set by the ratio between the elasticity K and the anchoring strength ω; for colloidal LCs the confinement may even reach the particle length L. Further advances in *colloidal* model systems, imaging techniques, and image analysis explain why experiments are now catching up with predictions made by theory and simulations, which have benefited from a steady increase in computational power.

Instances of extremely confined colloidal liquid crystals are found in biological systems, such as actin filament in cells [27] or DNA in viruses [28,175], but also in industrial applications like inklet printing [176] and fiber spinning [177] of giant graphene oxyde [178], or printing of semiconductor nanomaterials [179]. Confinement is know to affect the phase behavior of colloidal [180] and thermotropic [181, 182] liquid crystals. We would like to introduce the way confinement impacts the phase behavior of colloidal liquid crystal.

Most work has focused on the slit-pore geometry [180]. In the vicinity of the wall, many isotropic configurations that overlap with the wall are forbidden. This locally forces rod alignment to the wall and, for pore sizes comparable to a few particle lengths, lowers the isotropic to nematic phase transition concentration [180]. This phenomenon, studied by many authors in recent years [183–191], is referred to as *capillary nematization*. We note the very recent nature of the first experimental observations of this phenomenon [190, 191].
The effect of confinement on the nematic to smectic phase transition is more complex. *Smectization* has been studied in the slit-pore geometry, showing that the phase transition concentration can be either lowered or raised depending on the ratio between the pore size and the particle length [57,58]. Note that this valuable theoretical work considered homeotropic anchoring, which is generally not expected for hard rods confined between two hard walls. For planar anchoring, the case of aligned hard rods has been studied in cylindrical confinement [192]. The authors have predicted absorption of the particles on the wall and an increase of the N-S transition concentration. Absorption of hard rod-like particles on confining walls have been predicted by simulation [67] and theory [192] for the dense isotropic, nematic and smectic phases, but has

not been observed experimentally.

When the confinement becomes larger, its main effect is to impose the system's boundary conditions. For colloidal liquid crystals, degenerate strong planar anchoring imposes the nematic director (i.e. the orientation of the rods) to be parallel to the walls [183]. Then the interplay between boundary conditions, elastic deformations and defects leads to a host of possible structures.

Among the different liquid crystal phases, the *nematic* phase has received the most attention. Suspensions of elongated viruses [193–195] and actin filaments [196] have been observed in squares, circles, wedges and annuli. Further experiments on granular vibrated rods, where the physics is also governed by hard body interactions, showed interesting similarities with their Brownian counterpart [197, 198]. To a large extent the structures observed were qualitatively captured within the Oseen-Frank framework, see [194] for recent work on this. However, when the confinement chambers approach the size of the particles, simulations and experiments showed that the continuum theory breaks down [195]. To our knowledge, only density functional theories (DFTs) are then able to account for such commensurate effects [199–201].

The *smectic* phase has received less attention. Studying the smectic phase is computationally more intensive for both theory and simulations. On the theoretical side, DFTs are able to account for the smectic positional order. To reduce computational costs a restricted orientation approximation (Zwanzig model) has recently been used to explore the behavior of 2D hard rectangular particles in square chambers [200]. On the simulation side, smectic structures in confinement were mainly explored in one study [202], although smectic-like structures were found in publications focusing on the nematic phase [195, 203, 204]. Overall, confinement of the smectic phase is not well understood, in particular for large confinement chambers. Experimental work, which is not restricted by computational power, may greatly contribute. However, none is presently available.

In this chapter, we first illustrate a model experimental set-up where we may study isotropic, nematic and smectic phases at coexistence in a single confining chamber and down to the single particle level. We then focus our attention on confinement of the smectic phase. In section 6.4, we experimentally demonstrate the richness of the smectic structures confined in squares and rectangles and compare them to recent theories and simulations. In the following sections 6.5 and 6.6, we explore for the first time the shape of lozenges and annuli. We show

how the observed structures can be controlled by varying shape parameters. Furthermore, the energies of the discovered states are compared to each other by introducing simple models from which we extract two energy ratios: layer bending over disclination line and edge dislocation over disclination line. Finally, conclusions are drawn in section 6.7.

6.2 Experimental technique

The particles used for this chapter are the rods 'LC017'. They have a mean end-to-end length $L = 5.26\,\mu m$ and a mean aspect ratio $p = 12.6$. The rods are either dispersed in pure water or in a 1mM NaCl water solution. In the latter case they have an effective aspect ratio $p^{eff} = 10.4$, i.e. they behave like hard rods with an aspect ratio of 10.4. Experiments were performed with the cell schematically shown in figure 6.1. It is composed of two parts: first, a cover-slip on which a layer of UV-glue, containing micrometric cavities, was covalently bonded; secondly, a Teflon tube was added to form the reservoir. The cell's fabrication is detailed further in section 2.2.2. The most important part of the cell is the UV-glue layer, in which the cavities have been molded. For clarity, only one cavity is drawn in figure 6.1. However, since the actual size of cavities is smaller than $400\,\mu m$, a large number of cavities can be contained in one cell. The size and the shape of the cavities can be chosen at will. The minimal lateral size is about $5\,\mu m$, and the height can range from 1 to at least $100\,\mu m$. In this chapter, we use heights of 10 to $20\,\mu m$. However, note that the cavities are not directly sealed, but instead were covered by several mm of water from the reservoir. So, in principle, all cavities are connected. Therefore, at a given height, the same chemical potential is expected in all cavities. However, a small tilt of the cell can bias this equilibrium. Efforts were made to have cells as flat as possible. Nevertheless, an effective volume fraction difference of $5 - 10\%$ is to be expected.

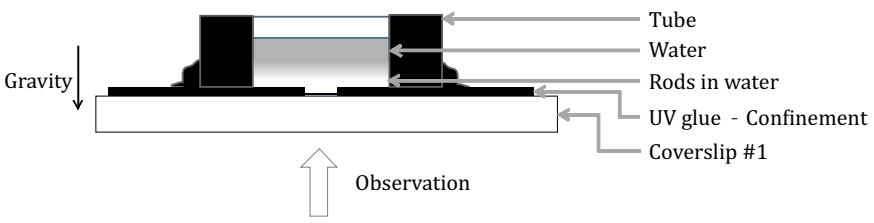
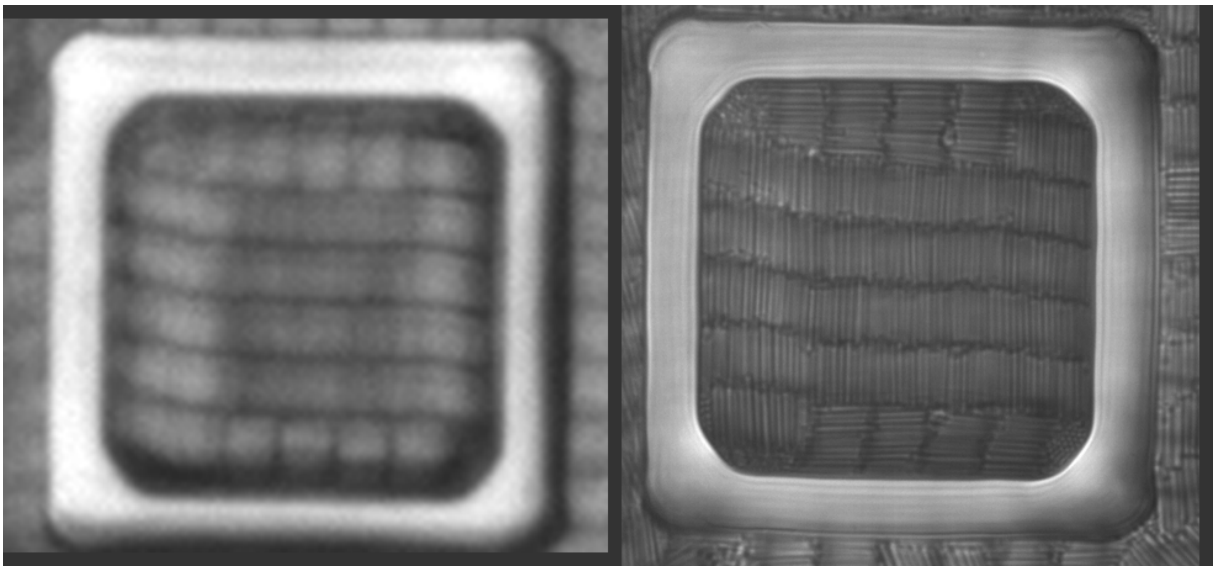


Figure 6.1: Experimental cell.

In this experiment, we are unable to directly measure the volume fraction of rods. We introduce instead an effective volume fraction that qualitatively matched our system concentration on the phase diagram of hard rods. The effective volume fraction at the bottom is estimated by the thickness of the smectic phase. At the nematic-smectic interface we assumed that $\phi_{eff} \approx 40\%$ and, based on the results from chapter 3, $9-11\,\mu m$ below the interface we expect the crystal phase, i.e. $\phi_{eff} = 60\%$. In between, we approximate the concentration via a linear relation.

In order to fill the sample cell, we followed the procedure below. First, the cell was plasma cleaned for 1 min, in order to make the UV-glue hydrophilic, and to avoid trapping of air bubbles in the cavities. Then, the cell was filled with water and left open. Rods were then added to the top. Because of their small gravitational length compared to the size of the cell, they sedimented in the cavities. Thus, by gradually adding rods to the cell isotropic, nematic and smectic phases can subsequently be formed and stabilized simultaneously in the cavities.

We used two different microscopy techniques, either simple bright field microscopy or laser scanning confocal microscopy. LSCM was used to observe structures in three dimensions. We exploited the refractive index mismatch between water and silica, to observe the rods without the need for dye. An alternative approach was followed in [91], which allows for both visualize *and* track all rods, but typically leads to heavier rods with a lower aspect ratio, which reduces



(10x) (60x)

Figure 6.2: Bright field microscopy of silica rods confined in square cavities. Comparison between 10x and 60x magnification objectives.

the nematic region. An example of a captured 3D volume is described in the next section. Bright field microscopy with 10x and 60x magnification objectives was used to capture 2D snapshots. In figure 6.2, we compare images from both objectives. The apochromat 60x objective offers sufficient resolution to identify most of the individual particles at the bottom wall. We can even see particles standing up in the corners. The 10x objective, with significantly lower numerical aperture, only allows to resolve the layers.

6.3 Applicability of the method

6.3.1 Sedimentation-diffusion equilibrium in confinement

Figure 6.3 illustrates the feasibility of our experimental approach. We show typical snapshots for a system with $W \approx 15L$, and a height $H \approx 4L$. After filling the sample cell with the colloidal suspension, the rods sediment under gravity, fill the chamber and different LC phases emerge.

Starting near the top of the chamber, at a distance from the bottom $z \approx 16\,\mu m$, we observe the isotropic phase characterized by random positions and orientations of the rods, figure 6.3 (I). Since the rods are dispersed in water the refractive index mismatch means that the images are somewhat noisy. We are detecting the scattered laser light and image the sample through the denser LC phases. In principle, this can be overcome by matching the refractive index of the rods and the solvent; however, the isotropic phase is not the focus of the current work.

Going down in the cell, the rod density smoothly increases and at a height of $z \approx 11\,\mu m$, we clearly see the hallmarks of the nematic phase, figure 6.3 (N). Rods show orientational order. Matching the planar anchoring conditions leads in this particular case to a deformation, which has defects in all 4 corners and of equal charge and two defects in the central part of the chamber. This particular nematic director seems to match the underlying smectic orientational order, as will be discussed later. The thickness of the nematic phase is estimated by trained eyes to be approximately $W_N = 6\text{-}8\,\mu m$. This is lower than without confinement, where we found $W_N = 13\text{-}14\,\mu m$. This implies that the square confinement is either enhancing the smectic phase, destabilizing the nematic phase, or both.

Going further down in the cell, the nematic-smectic transition occurs at a height $z = 6\text{-}8\,\mu m$, with a clear smectic phase at the bottom of the cell, figure 6.3 (Sm). Having the 3 phases

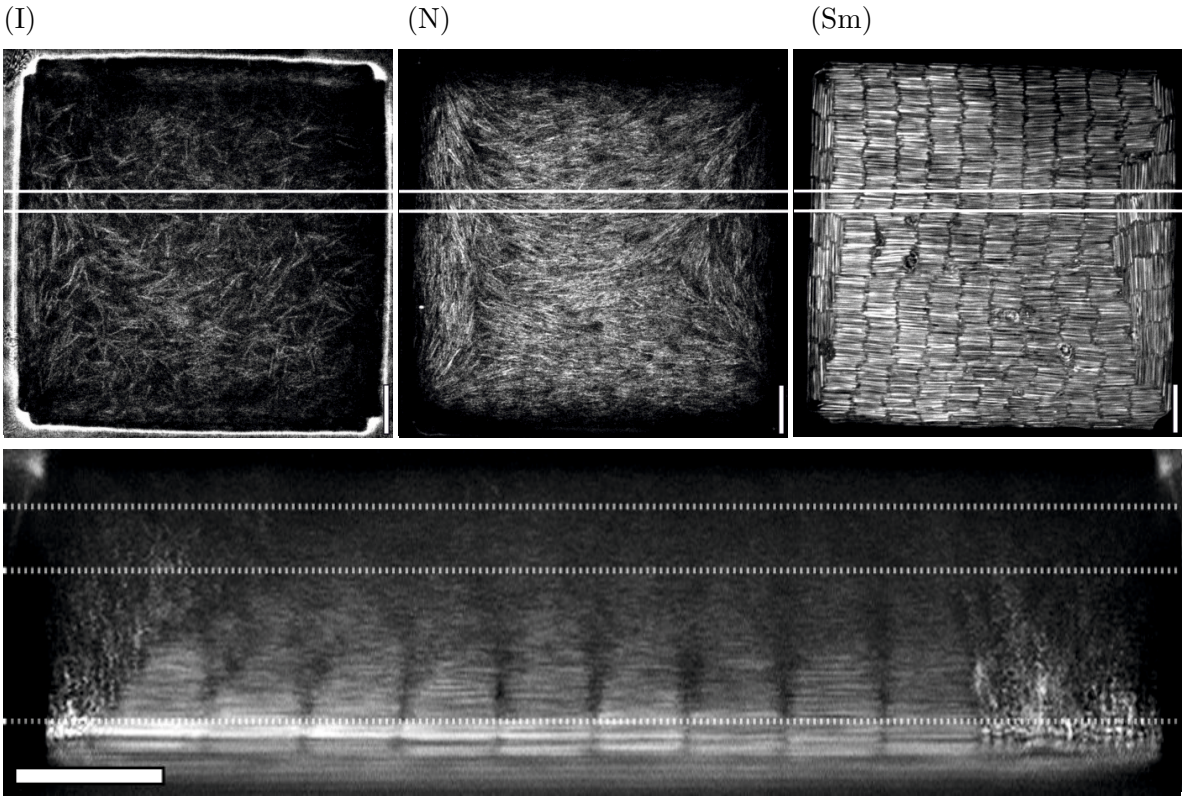


Figure 6.3: The top row shows LSCM images (scattered light) of coexisting isotropic (I), nematic (N) and smectic (Sm) phases confined in a $W \approx 15L$ cavity. The bottom row shows a side view (SW) reconstructed from the location indicated by the double solid lines *and* for z ranging from $z = -4\,\mu\text{m}$ to $z = 21\,\mu\text{m}$ with respect to the cell bottom. The dotted lines indicate the height where the top row snapshots were taken; from the bottom to the top (Sm): $z \approx 1\,\mu\text{m}$, (N): $z \approx 11\,\mu\text{m}$, (I): $z \approx 16\,\mu\text{m}$. All scale bars denote $10\,\mu\text{m}$. See the supplementary movie for a z-stack corresponding to the set of images.

at coexistence in a single chamber has the advantage that it becomes possible to take z-stacks by means of confocal microscopy and directly observe the three phases in a single image, see figure 6.3 (SW). The smectic layers can be clearly observed including the smectic regions where the domains lie perpendicular to the field of view.

The setup also offers the possibility to see the I-N and N-Sm interfaces and to study the interplay between the nematic and the smectic phases. In particular, we wonder how the smectic structure influence the nematic structure and *vice versa*. Returning to the nematic phase, although the side walls have degenerate planar anchoring conditions, this is not the case for the bottom "wall"; indeed, the nematic phase lies on top of the smectic phase. The N-Sm interface will impose its direction on the nematic phase. This effectively changes the anchoring conditions, a result which so far has not been explored in theory or simulation. We might be observing such an effect here. We find a configuration similar to the $U_1^\star$-like configuration

reported in [194] (figure 6.3 (N)), matching the underlying smectic orientation (figure 6.3 (Sm)), instead of the predicted diagonal state (figure 6.6 (a)).

Finally, note that by adding a tracer amount of fluorescent rods we are able to image single particle diffusion in dense phases [205].

6.3.2 Dynamics and stability

The coexistence of liquid crystal phases observed in figure 6.3 is the result of a two-step equilibration process. Firstly, rods sediment for one to two hours. During this step, the concentration of rods gradually increases at the bottom of the cell. This leaves time for the rods to self organize. The isotropic configuration first turns into a nematic and finally smectic, as illustrated in figure 6.4. Initially, the smectic phase will match the previously established nematic. However, as a second step the smectic configuration will rearrange to lower its energy. Depending on the experimental conditions, this second step can occurs during and/or after the establishment of the sedimentation-diffusion equilibrium. An example where a smectic rearrangement occurred days after the initial sedimentation is shown in figure 6.5. However, such events were rare, even more so for crystalline sediment where structures were found to be stable over at least three days. In sum, most of the structuring happens within a few hours. After this, the majority of

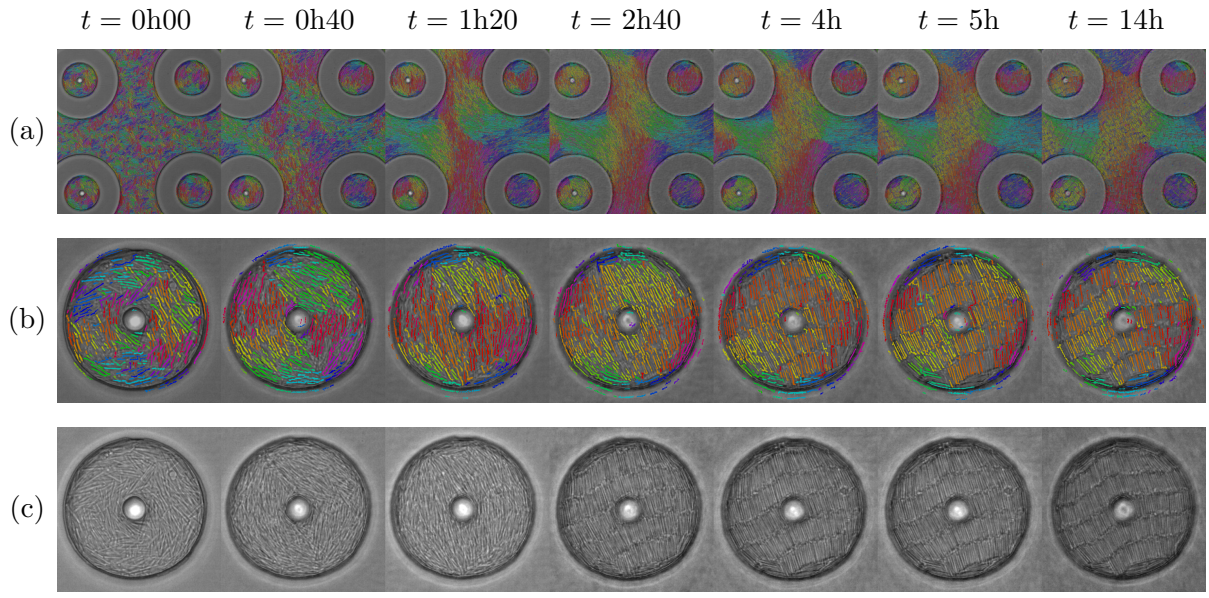
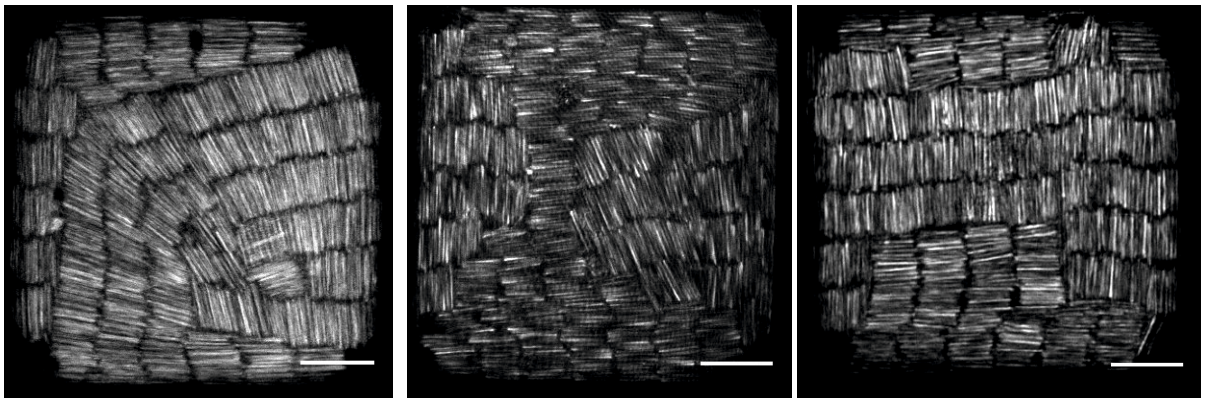


Figure 6.4: Sedimentation of silica rods into cavities with radius $r_{out} \approx 3.5L$. (a) Bright field snapshots with an 60x objective, particles are colored as a function of their absolute orientation. (b) Zoom in the top left corner. (c) Zoomed unprocessed image.



(a) (b) (c)

Figure 6.5: LSCM images (scattered light) of smectic configurations after filling $t \approx 1\,\mathrm{h}$ (a), at $t \approx 2\,\mathrm{d}$ (b) and at $t \approx 5\,\mathrm{d}$ (c). The square has a side size $W \approx 10L$. The scale bars represent 10 µm.

the structures remains stable for days.

Finally, we would like to highlight the quasi 2D nature of the setup that may play a role in equilibration. The system is inherently 3D, but the rods are confined by gravity to mainly lie along the bottom glass wall. Only occasionally do we find rods standing up along gravity.

6.4 Squares and rectangles

Previous work on confinement of the *nematic* phase in square cavities showed that the interplay between boundary conditions and elastic deformations leads to a host of possible structures [27, 194, 200, 202, 204, 206]. These can to a large extent be qualitatively captured within the Oseen-Frank framework. Taking the splay and bend elasticities (characterized by the elastic constants K_1 and K_3) into account, assuming Dirichlet boundary conditions and minimizing the elastic free energy, leads to a set of Euler-Langrange equations, see [194] for recent work on this. Within the one constant approximation ($K_1 = K_3$) minimizing the elastic free energy amounts to solving the Laplace equation for the orientation of the director. Recent work [194] has shown that the predicted structures are in good agreement with a colloidal model system, where both semi-flexible wild type *fd* virus (with $K_1 \approx K_3$) and the stiff mutant virus Y21M (with $K_1 > K_3$) were studied. Some of the predicted structures are reproduced here by numerically solving the Laplace equation using Mathematica, see figure 6.6 (a) and (b). The diagonal state (a), with opposing corners of the same defect strength ± 1, was found to be of lower energy with respect to the bend state (b), where opposing corners have opposite strength.

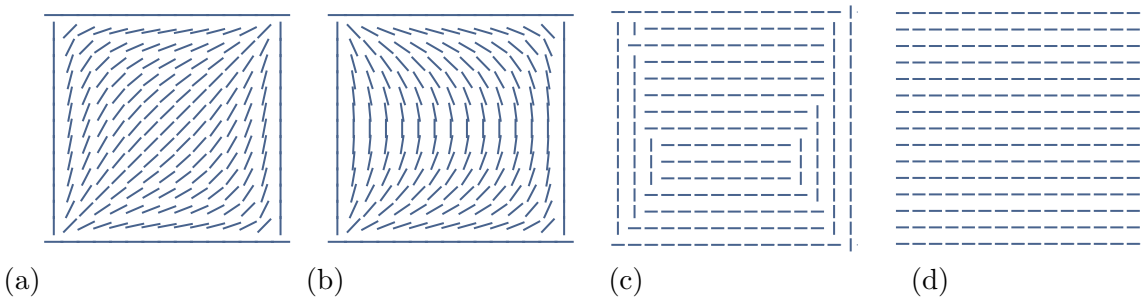


Figure 6.6: Local average orientation of lyotropic LCs in square confinement. Figures (a) and (b) display the equilibrium nematic orientation for diagonal and bend configurations. Figures (c) and (d) are sketches of a smectic bridge configuration and of a uniform smectic state.

Concerning the smectic phase, a recent theoretical study using the restricted orientation approximation (Zwanzig model) explored the behavior of 2D hard rectangular particles with aspect ratios ranging from 1 to 6 and confinement between 5 and $10L$ [200]. Notably, a "bridge" smectic configuration was found, which is characterized by 3 smectic domains, see the sketch in figure 6.6 (c). Two small domains assure planar anchoring on two opposite sides, and a large domain connects the two other sides. In contrast, a recent MC simulation of hard spherocylinders with aspect ratios 10-38 in quasi-2D confinement with the length of the wall $W \approx 3L$ shows a single smectic domain, although the focus of that paper was on the nematic phase [204]. Another very recent MC study of hard rectangles in 2D with an aspect ratio 20 and W = 3-$10L$ did show the bridge smectic, in agreement with the theoretical predictions, although the different domains are less well defined spatially. The authors of [202] raise the question whether the occurrence of the bridge state depends on the detailed particle shape, i.e. rectangular vs. spherocylindrical. In our experimental system, however, one end of the rod has a spherocylindrical cap, whereas the other end has a flat cap.

In this section, we will study the effect of confinement on the smectic phase into squares and rectangles for $\phi_{eff} \approx 50\%$ (middle of the smectic concentration region) and $\phi_{eff} \approx 60\%$ (almost the smectic-crystal transition). We will compare our experimental observations to the results from theory and simulations.

6.4.1 Qualitative observations

Figure 6.7 shows the smectic phase in square confinement ranging from $W \approx 5L$ to $W \approx 40L$, with a constant height $h \approx 4L \approx 20\,\mu m$ and an effective concentration estimated to be

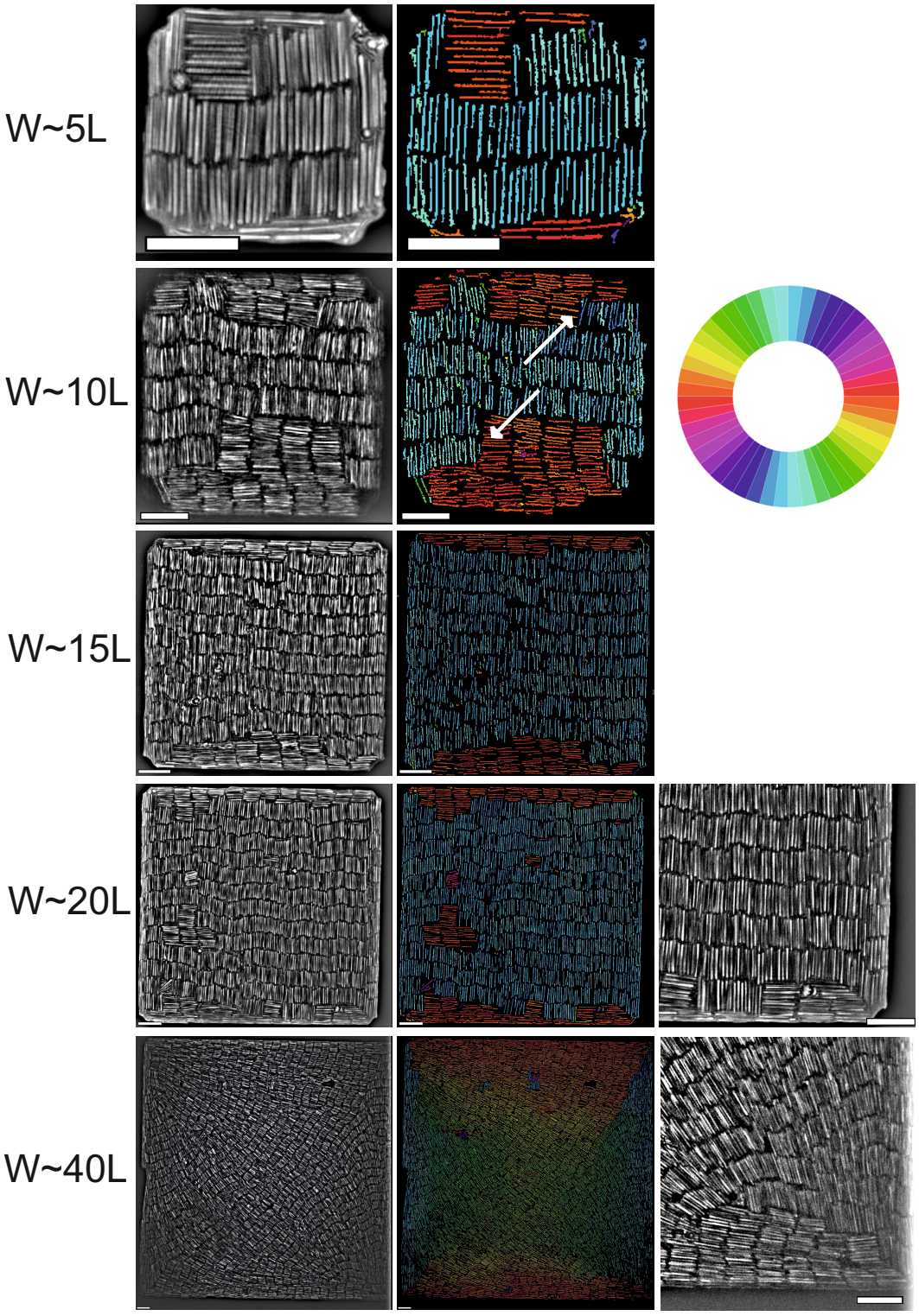


Figure 6.7: The left hand side column shows bandpass filtered LSCM images (scattered light) of smectic configurations in different square sizes, from top to bottom $W \approx 5L$, $W \approx 10L$, $W \approx 15L$, $W \approx 20L$ and $W \approx 40L$. The second column shows processed images. Rods are coloured as a function of their orientation. Arrows indicate commensurate jumps in the smectic layers at the domain boundary. The third column shows a zoom in of the bottom right hand side of snapshots of the first column. The scale bars represent 10 µm and the colour associated to each orientation is indicated by the coloured wheel.

$\phi_{eff} = 50\%$. The left hand panels display LSCM images after a bandpass filter (1-40 pixels) has been applied; for the second column we have used built-in Mathematica functions to detect the rods (Functions used were: LocalAdaptativeBinarize and MorphologicalComponents). Not all rods are correctly identified but the method is suitable for our purpose. By colouring the rods depending on their orientation it becomes clear that the planar boundary conditions are satisfied locally.

For the smallest squares, up to $W \approx 10L$, the system chooses to split into 3 smectic domains, with 2 small domains covering the width of two opposite walls, and a large domain bridging the two other square sides. For the square with $W \approx 20L$, we see a similar behavior, although a small domain trapped in the large domain can be observed. However, for the larger square $W \approx 40L$, the structure is different; this will be discussed later.

The typical spacing between the smectic layers can either be measured manually (in real space) or by Fourier transforming the images (a method that did not work for the two smallest squares). The two techniques give similar results within the margins of measurement error. We find for all squares a layer spacing between $6.2\,\mu\text{m} < \lambda < 7.2\,\mu\text{m}$, which corresponds to $1.2 < \lambda/L < 1.4$. This is a bit larger than theoretical predictions [207, 208]. However, we have underestimated the rod length for the smectic phase: we observe fractionation of the rods with on average longer rods in the smectic phase, particularly at the bottom, where the layer spacing is measured.

A closer inspection of the images shows that the small domains can be as thin as 2 or 3 particles diameters, possibly stabilised by the small roughness of the walls of the confining chambers, but wherever the small domains venture out into the bulk system they typically jump by once or twice the smectic layer spacing. This is indicated by arrows in figure 6.7. Such a commensurate jump may be expected.

As mentioned above we see the bridge state even for the smallest square $W \approx 5L$. This may be related to the exact value of the confinement: $W = 4.7L \approx 3.5\lambda$. This incommensurability may suppress the possibility of a uniform state. Furthermore, the non-sharp edges and especially corners or possibly even the exact shape of the particle may play a role. To investigate this further, rods where confined in rectangles with side W and length L_r. The box dimensions are expressed in terms of layer spacing $\lambda \approx 6.7\,\mu\text{m}$. The box size is gradually varied from $1\lambda \times 2.5\lambda$ to $2.5\lambda \times 4.5\lambda$. We identified three states shown in figure 6.8 (a), the predicted uniform and

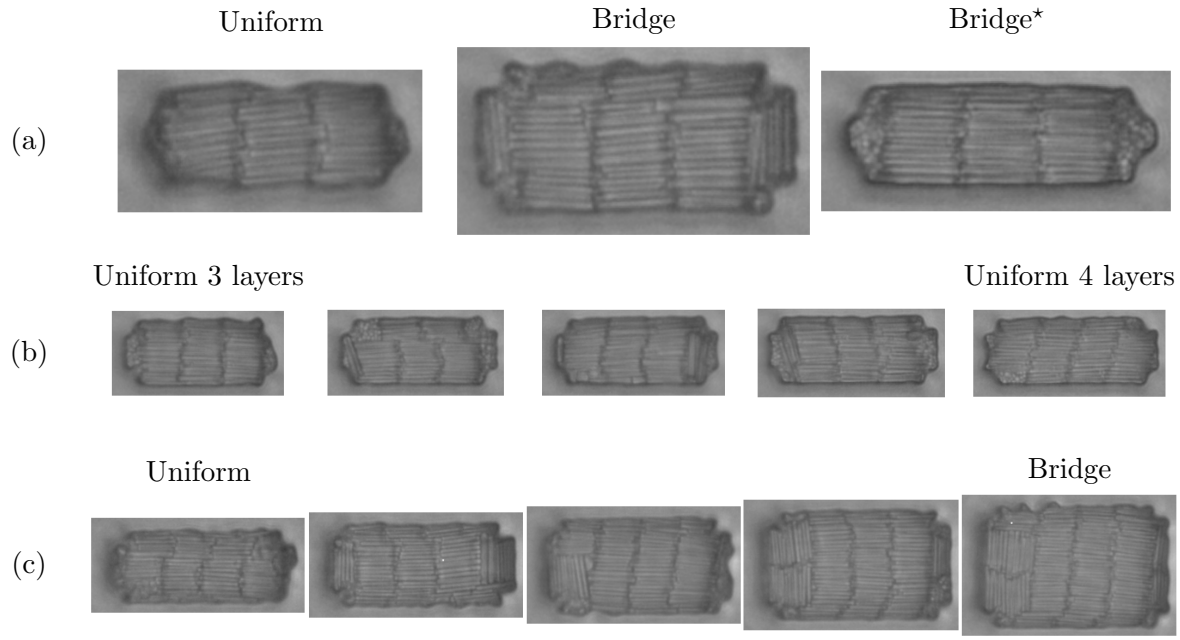


Figure 6.8: Confinement of smectic layers into small rectangles. (a) Variety of states, (b) transitions from the uniform with three to four layers and (c) transition from uniform to Bridge (bottom).

smectic bridge states, but also an alternative smectic bridge where the side domains are made of particles standing up. We also find two phenomenological transitions for increasing length and width. In figure 6.8 (b), for increasing length, we observe a double transition from a 3-layer-uniform to bridge, and then from bridge to 4-layer-uniform. This demonstrates that the uniform state is only stable for a commensurate size of the box. The second transition is found for increasing box width. In figure 6.8 (c), we show the transition from the uniform state to the bridge state with domains made of first 1 layer and then 2 layers. This result might depend on the detailed shape of the rods or the box. However, we observe no uniform states for $W > 2\lambda$. We conclude that the uniform state can only be stabilized by small boxes *and* commensurability between layer spacing and box length.

Returning to the largest square of figure 6.7, we observe that the system still satisfies planar anchoring conditions everywhere in the cell, but away from the corners smectic layers bend from one wall to another neighbouring wall. Closer to the corners this is no longer possible and the rod orientation changes abruptly by 90°. The bending of layers between adjacent sides of the squares was also observed for a smaller square, but this eventually disappeared. The example in figure 6.5 shows how the smectic structure in a square of size $W \approx 10L$ reorganizes as a function of time. We might therefore expect such a reorganization to eventually happen for the largest square as well. This will be investigated further in the next section.

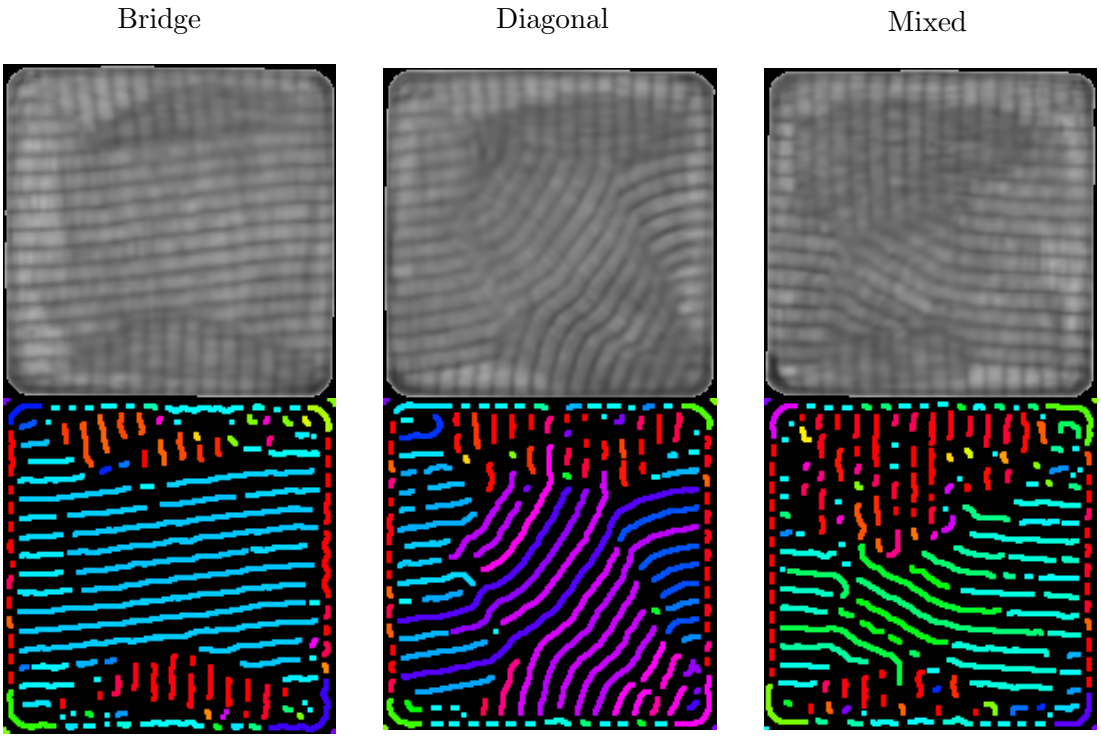


Figure 6.9: (Top) Bright field images (10x magnification) of silica rods confined in square cavities of width $W \approx 17\lambda \approx 40\,\mu\text{m}$. (Bottom) Layers are detected and colored by orientation.

6.4.2 Statistical analysis into squares

In the previous section, we observed the smectic phase ($\phi_{eff} = 50\%$) confined into squares with sizes ranging from $5L$ to $40L$, i.e. 3.5λ to 30λ. We found that for most squares the smectic layers were organized into the bridge configuration. However, for the larger square a diagonal state was observed. In order to check the reproducibility of this result we performed a statistical analysis.

We consider seven square sizes ranging from $W = 7\lambda$ to $W = 71\lambda$. Each square size is studied in 4 to 16 copies. The volume fraction of the rods was slightly increased to $\phi_{eff} = 60\%$. The chambers were imaged, with a 10x objective, on three consecutive days but no further evolution was detected after one day.

Three states were observed: the bridge state, the diagonal state and a mixed intermediate state. Examples of these states are shown in figure 6.9, for squares with sides $W \approx 17\lambda$. The layers were automatically detected and colored by orientation to assist visualization. We define

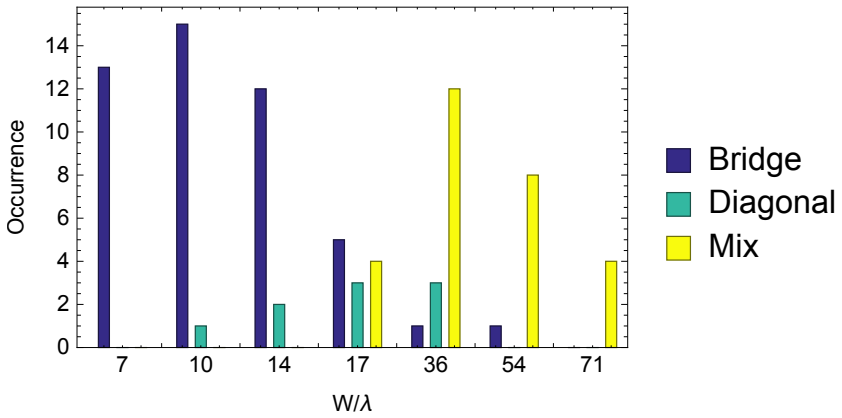


Figure 6.10: Occurrence of bridge, diagonal and mixed states as a function of the square side size W.

the bridge state as having layers bridging two opposite sides, whereas the diagonal state layers are bridging two adjacent sides. In the mixed state a part of the layers connects adjacent sides and the other part opposite sides.

In figure 6.10, we use a bar chart to represent the number of occurrences of each state as a function of the size of the box. For the smallest size $W \approx 7\lambda$, we only observed the bridge state. For increasing square sizes, the diagonal state becomes more frequent, but remains less probable than the bridge state for sides $W < 36\lambda$. However, for $W > 36\lambda$ the dominant state is the mixed state. We speculate the mixed state is the higher energy state as it has more deformations and defects than the other two states. We thus expect that equilibrium is not reached for large squares. We focus on the smallest squares. From the growing fraction of diagonal states, we conclude that the energy difference between the smectic bridge and the diagonal state is decreasing as the size of the square is increased. However, it remains uncertain which one of the smectic bridge and the diagonal states is the most stable for large squares.

Finally, we would like to compare the findings from this section, where $\phi_{eff} \approx 60\%$, to the previous section, where $\phi_{eff} \approx 50\%$. We find largely similar results. The smectic bridge is found to dominate for boxes of sides $W \leq 15\lambda(20L)$ in both cases. For $W \geq 20\lambda$, we find the bridge state to be slightly more frequent at $\phi_{eff} = 50\%$ than 60%. However, this could be explained by a slowing down of the dynamics that is expected in dense solutions.

In the next section, we will show that the diagonal state can be stabilized by reshaping the squares into lozenges. We will also introduce a simple model to characterize the transition.

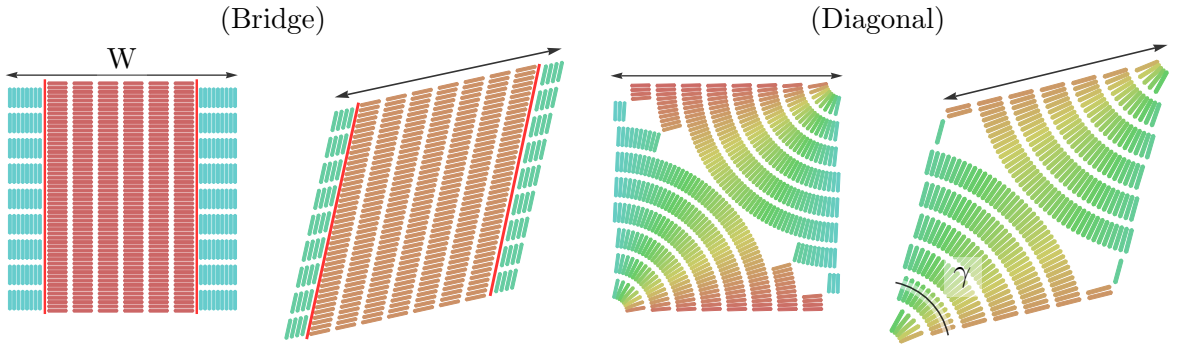


Figure 6.11: Models of bridge and diagonal configurations in squares and lozenges of side W. The red lines indicate disclination line defect.

6.5 Lozenges

In the previous section, we established that for confining square cavities (with $W > 3\lambda$) smectic layers could self organize into two well defined states: the bridge state, that was clearly the most stable for box sides $20\lambda > W > 3\lambda$, and the meta-stable diagonal state. In this section, we will first present a simple theoretical model predicting that the diagonal state may be stabilized by diamond-shaped cavities. The energy of the diagonal state will be related to layer bending, and the energy of the bridge state will be estimated by the length of the disclination lines. The transition from the bridge to the diagonal state will then be observed experimentally by gradually varying the chamber geometries from squares to thin lozenges. Finally, by combining the theoretical model and the experimental results we will estimate the ratio between bending and disclination line energies.

6.5.1 Model

To model the excess energy of the two states, we will only consider the main distortions or defects. We will further consider the problem in two dimensions. In figure 6.11, we represent the two configurations in squares and lozenges. The two shapes are defined by a side length W. An additional angular parameter, the lozenge nose angle $0 < \gamma \leq \pi/2$, is used to describe the lozenges. For $\gamma = \pi/2$ lozenges and squares are equivalent. The main defects of the bridge state are the two line disclinations represented by red lines. For the diagonal, the main excess energy come from bending the layer.

We approximate the excess of energy in the bridge state by the disclination line energy per

unit length δ multiplied by the length of the defects: $2W$.

$$\Delta U_B = 2W\delta \tag{6.1}$$

The energy of a bent layer is proportional to its curvature and its length [12]. Within our simple model, the curvature is $1/r$ and the length of each layer is γr, where r is the distance between the layer and the nearest nose corner. The energy of a full layer is then independent of r: $u_l = \gamma\beta$, where β is the bending constant energy. The total energy is then

$$\Delta U_D = \beta\gamma N_{layer} \approx \beta\gamma \frac{2W}{\lambda} \cos\left(\frac{\gamma}{2}\right), \tag{6.2}$$

where the number of layers N_{layer} is approximated by the length of the diagonal divided by the layer spacing λ. Note that for colloidal rods $\lambda \approx 1 - 1.3L$.

Within this simple model, for a square ($\gamma = \pi/2$), both the bridge and the diagonal configurations are directly proportional to the square sides W. In other words, in squares, the difference of energy between the two states does no depend on W. Consequently, one state is expected to be stable for all W. We know from experiment that the smectic bridge is clearly stable for $W < 20\lambda$, so within this model the smectic bridge is expected to be stable for any square side W.

Let us now change the shape by decreasing the lozenge nose angle. The bridge state keeps its energy constant, because the length of the disclination lines remains equal to $2W$. However, the energy of the diagonal state goes to zero in the limit where $\gamma \to 0$. We then expect a crossover between the energy of the diagonal state and the bridge state, which is independent of W. We establish the following relationship between the crossover nose angle γ_c, the bending energy β and the dislocation line energy per unit length δ:

$$\frac{\delta\lambda}{\beta} = \gamma_c \cos\left(\frac{\gamma_c}{2}\right). \tag{6.3}$$

We would like to highlight some limitations of the model. Firstly, for both states, we neglect the presence of defects located in the four corners. In particular, in the diagonal state we neglect the two disclination lines formed in the top left and bottom right corners, see figure 6.11 (diagonal). Secondly, the energy of the diagonal state is estimated from the number of smectic

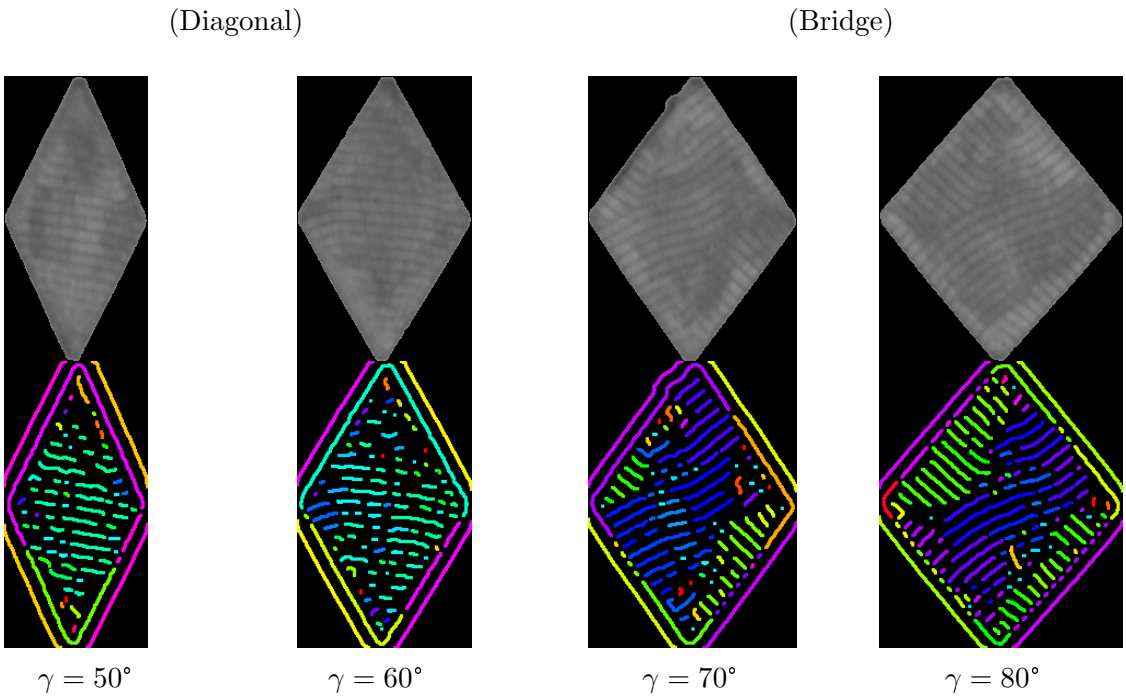


Figure 6.12: (Top) Bright field images (10x magnification) of silica rods confined in lozenges cavities of width $W \approx 15\lambda \approx 90\,\mu\text{m}$. (Bottom) Layers are detected and colored by orientation.

layers going from one nose to another. As a result, we do not account for the energy of the top-left and bottom-right areas of the squares. Thirdly, the bridge configuration in lozenges is characterized by a noticeable tilt of the particles. Indeed, the rods are not perpendicular to the layers. This increase of energy is not accounted for. We also completely ignore finite size effects. A more detailed model would certainly predict slightly different behavior, with a possible complex dependency on W. However, we expect the general transition from bridge to diagonal state to be well captured by our phenomenological model.

6.5.2 Method

The rods were confined in lozenges with diagonal nose-to-nose length $l_d = 2W\cos\left(\frac{\gamma}{2}\right)$ varying from 4λ to 80λ, and nose angles γ going from 10° to 90° with steps of 10°. The wall height was $h \approx 20\,\mu\text{m}$ and the effective volume fraction estimated to be $\phi_{eff} \approx 60\%$. Note that some of the chambers were damaged during the fabrication process, and so for them, no data can be provided. The configurations were observed after one and two days by means of BF microscopy with a 10x magnification objective, but no variation was observed.

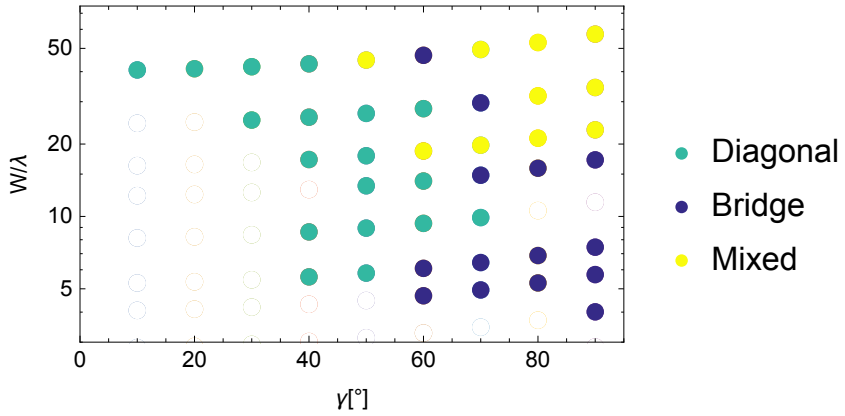


Figure 6.13: Smectic organization as a function of the side size of the lozenge W and the angle of it nose γ, $\gamma = 90$°correspond to a square.

6.5.3 Results

In figure 6.12, we show images of smectic layers confined into lozenges of side $W \approx 15\lambda$ and nose angles of 50°, 60°, 70° and 80°. For the smallest angles the diagonal state is found. However, for $\gamma > 65°$ we find the smectic bridge. This result mostly applies to larger and smaller chambers shown in figure 6.14 and figure 6.15.

In figure 6.13, we make a graphic representation of the states obtained as a function of the lozenge side length W and nose angle γ. The bridge states (●), are only found for $\gamma \geq 60°$. The diagonal states (●) are mostly found for $\gamma \leq 60°$. For large sizes, as observed in the squares, we found unequilibrated mixed states (●).

Our data clearly identifies a transition from the diagonal to the bridge state for increasing nose angle, as predicted by our model. The transition threshold γ_c varies from 50°to 70°. This variation might be caused by meta-stable states and or fine dependency of γ_c with W. Overall, the crossover angle is found to be mostly independent of the confinement size, as predicted. We estimate $\gamma_c \approx 60°$ and calculate the energy ratio between a disclination line of length λ and the bending energy constant

$$\frac{\delta\lambda}{\beta} = \gamma_c \cos\left(\frac{\gamma_c}{2}\right) \approx 1 \ . \tag{6.4}$$

In the next section we will extend these simple energy arguments to a more complex confining structure: the annulus.

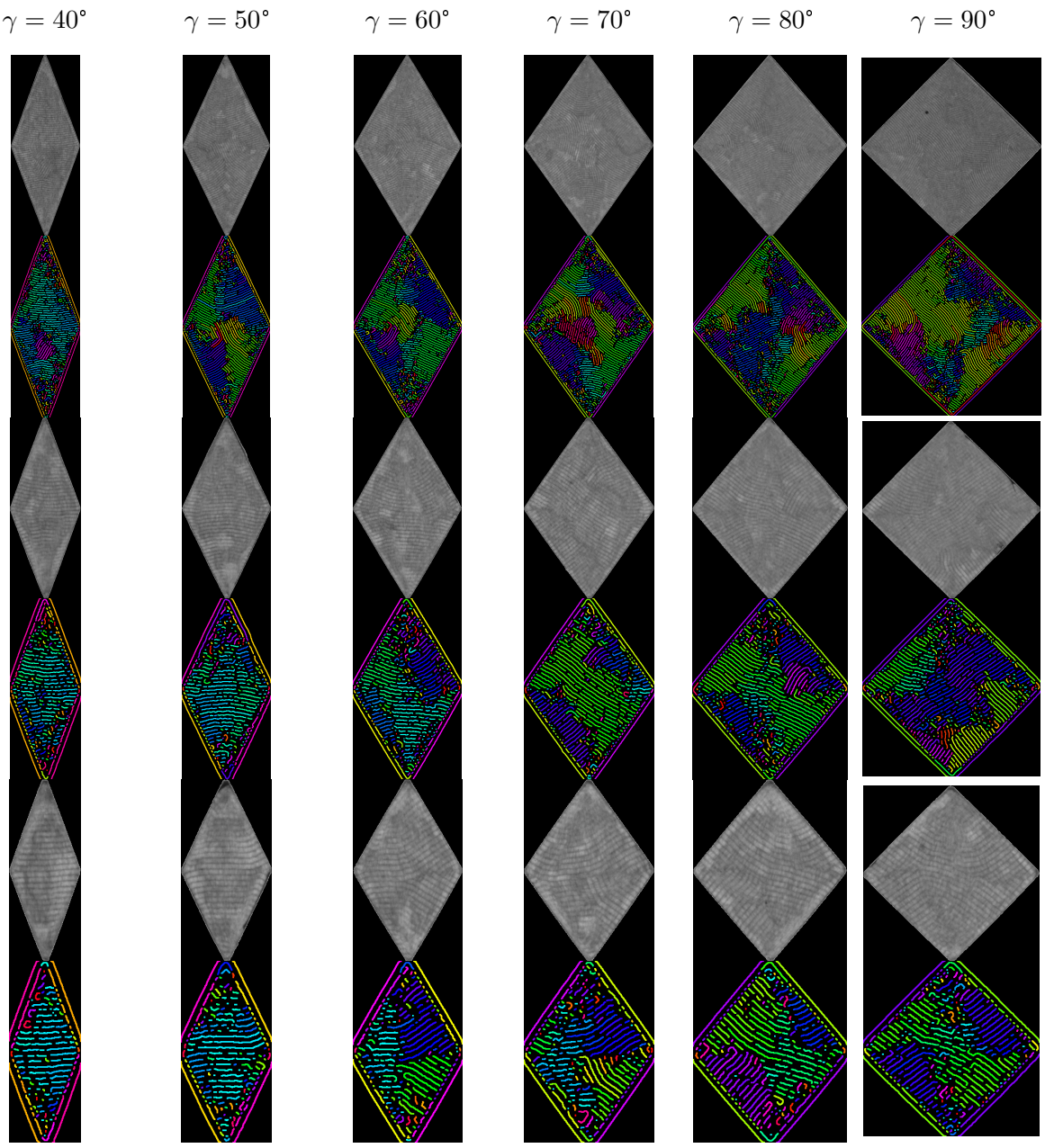


Figure 6.14: Smectic organization in large lozenge with increasing nose angle (left to right) and size (bottom to top).

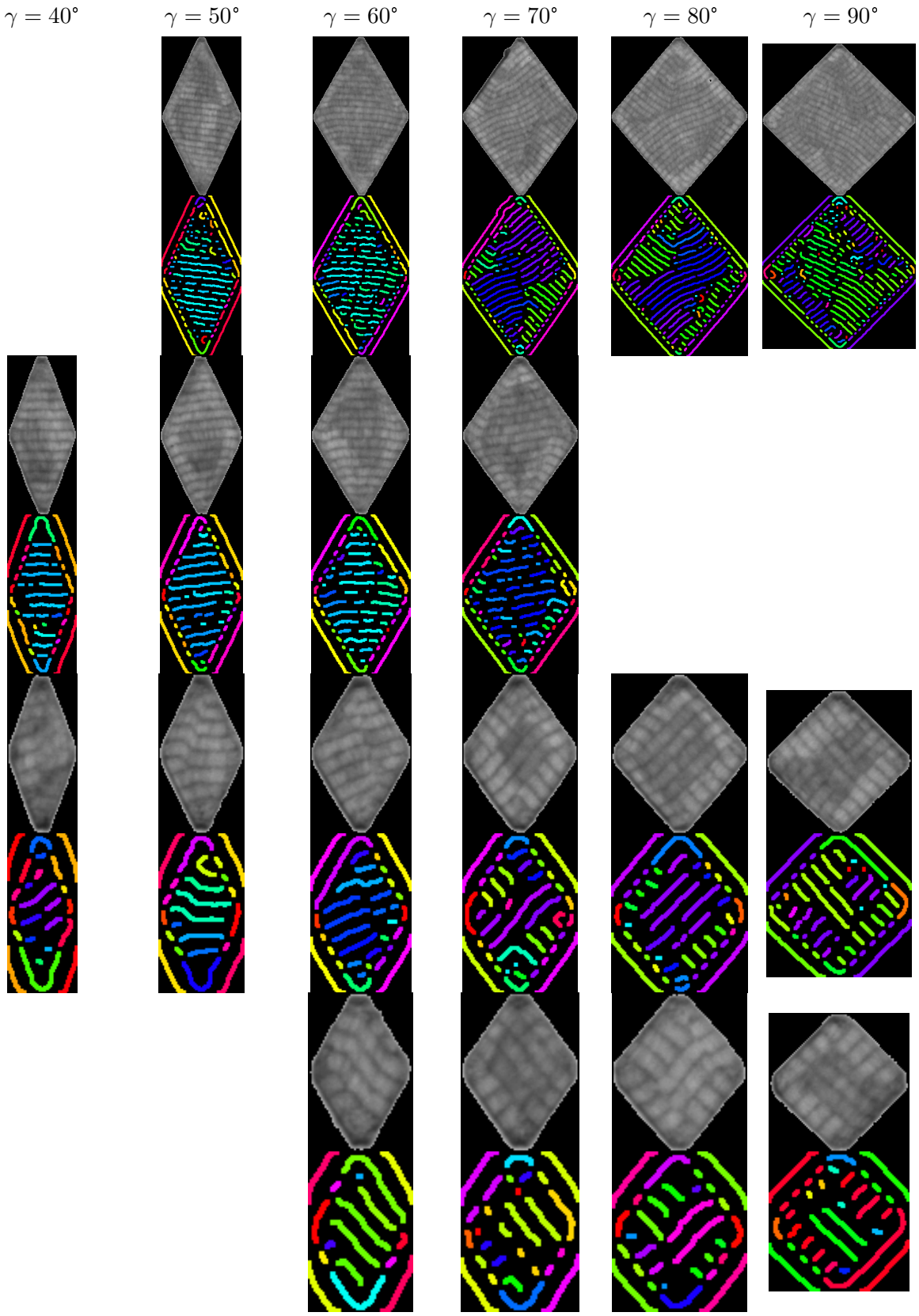


Figure 6.15: Smectic organization in small lozenge with increasing nose angle (left to right) and size (bottom to top).

6.6 Annuli

Configurations of colloidal smectic layers in annular confinement are largely unknown. However, experiments [195,198,209], simulations [195,203] and theories [198,206,209,210] have investigated the behavior of the nematic phase of CLCs in two dimensional disks and annuli. In figure 6.16, we represent a selection of possible configurations for confined nematics.

Within the Oseen-Frank framework, in two dimensions, the nematic director configuration will depend on: the annulus aspect ratio $b = \frac{r_{in}}{r_{out}}$, the elastic constants (K_1, K_3), and the anchoring strength ω.

For *disks*, the authors of [209], studied the relative stability of the states (a), (b) and (c) within the one constant approximation $K = K_1 = K_3$. They found that the configuration mostly depends on the extrapolation length $\xi = \frac{K}{\omega}$. Transitions from state (a) to (b) and then to (c) are expected as ξ becomes larger. The states (b) and (d) were observed in simulations of 2D rods with an aspect ratio $p = 40$ and box-radius $r_{out} = 7.5L$ [203]. The state (b) corresponding to the smallest correlation length was found for the lowest volume fraction ($\phi = 0.18$), whereas the state (d) was observed for $\phi = 0.40$. Interestingly, they also found a state with three defects, judged meta-stable, for $\phi = 0.20$ (similar to N_3 but without the inclusion).

For *annuli*, assuming a large correlation length, the author of [209] predicted the following sequence of states for increasing annulus aspect ratio b: $N_3 \to N_2 \to N_1 \to N_0$, where the existence of N_3 is conditional to the defects energy. The one constant approximation is convenient. However, it does not quantitatively capture the behavior of hard rods. For example, for $p = 10$, at $\phi = 35\%$, $K_1 \approx \frac{1}{15}K_3$ [77]. A theoretical treatment that accounts for the elastic constant anisotropy $\delta = 1 - \frac{K_1}{K_3}$ has recently become available [210] for nematics confined in annuli. It was predicted that an elastic constant anisotropy larger than 0.6 could qualitatively change the sequence of states for increasing b to $N_1 \to N_2 \to N_0$. The state N_3 was not considered in this study. However, the N_3 state was observed in experiments and simulations on strongly confined rods [204], which predicted for increasing b the sequence: $N_2 \to N_3 \to (N_4) \to N_0$. Note that they equally found experimental occurrences of the state N_1. The N_4 state was only found in simulations.

Finally, the confinement of hard rods in a annulus has been investigated by density func-

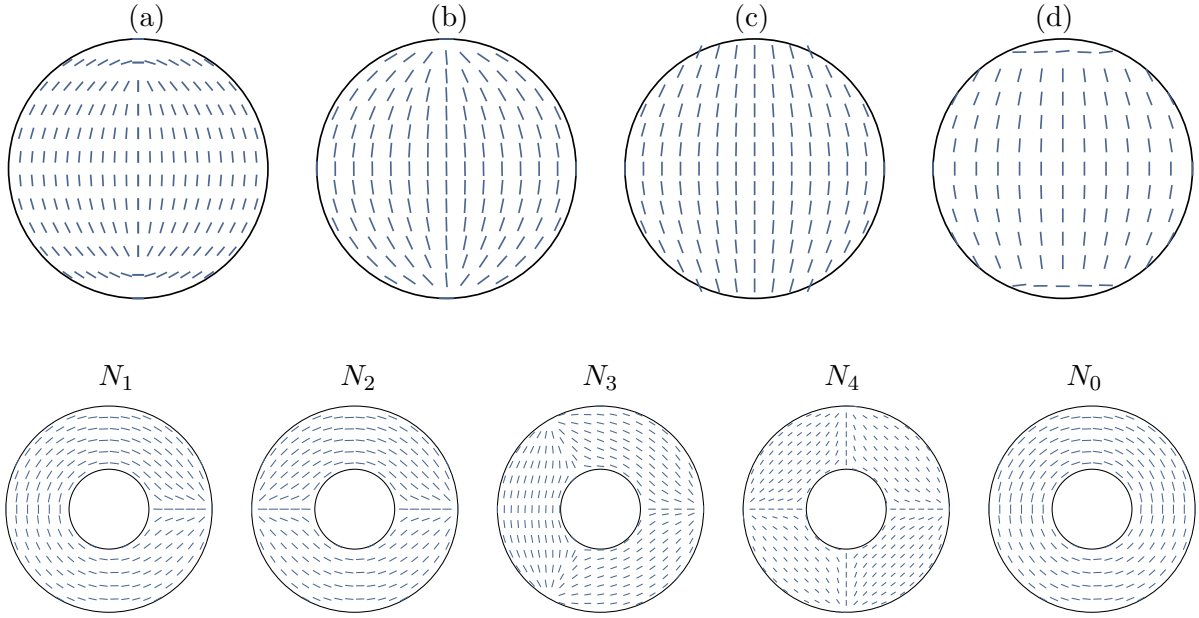


Figure 6.16: Example nematic configurations into disks and annuli.

tional theory [206]. In principle, DFT should allow to determine, for a given aspect ratio and concentration, the conformation of the nematic director without any fitting parameter. However, only exploratory work has been devoted to this problem.

In this section, we first study the behavior of the smectic phase into annuli. Then we introduce a model in order to quantify the difference of energy between the three states found. In particular, this enables a comparison between the energy of a disclination line of length λ and of an edge dislocation. Finally, we consider the structure of the nematic phase present on the top of the smectic phase.

6.6.1 Method

The rods were confined into chambers with walls height $h = 10\,\mu\text{m}$. The shape-space of the annulus was explored by varying its outer radius r_{out} and aspect ratio $b = \frac{r_{in}}{r_{out}}$, where r_{in} is the annulus inner radius. We varied b from 0 to 0.8 and r_{out} from $2L$ to $16L$. For each confining chamber, a snapshot was captured at the bottom ($h = 0$) and around the middle of the chamber at a height $h \approx 5{-}7\,\mu\text{m}$. For the larger chambers ($r_{out} > 3L$), the nematic phase was found at this height. For the smaller chambers, however, it was found a few microns higher. From this, we estimated an effective volume fraction at the bottom of $\phi_{eff} \approx 45\%$.

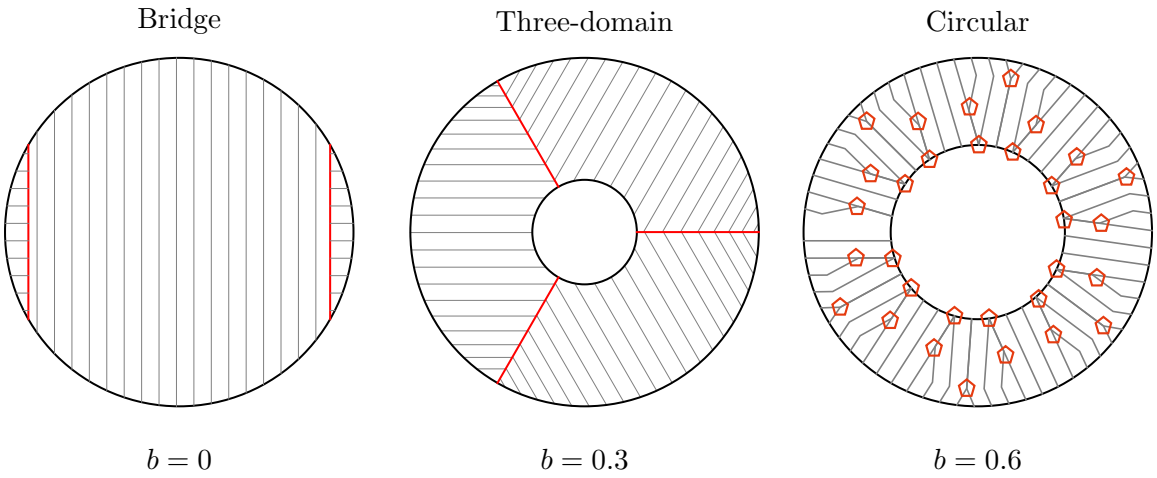


Figure 6.17: Representation of typical smectic configurations.

The configurations were imaged with a 60x objective in order to resolve single particle details. The sample was left for fifteen hours to equilibrate before capturing the images.

To identify the configurations more easily we proceeded as follows. First, we binarized the images and found the components' positions and orientations. Then the measured absolute orientations were transformed into orientations relative to the closest wall. Finally, elements were colored as a function of their orientation relative to the wall. Processed images are shown for example in figure 6.18 (c) and (d).

6.6.2 Results

By confining the smectic phase into annuli we unveiled two type of defects: disclination lines and edge dislocations, which are illustrated in figure 6.17 by red lines and pentagons. On one hand, the disclination lines prevent splay of the nematic director by creating boundaries between smectic domains with different orientations. And on the other hand, the edge dislocations are the natural answer to accommodate bending of the nematic director. We differentiate two kinds of line disclinations: the one parallel and the one perpendicular to the wall. In figure 6.17, we present three well defined smectic states that correspond to each kind of defect: the *bridge* state characterized by two line disclinations parallel to the walls, the *three-domains* state that has three line disclinations perpendicular to the wall, and the *circular* state which present many edge dislocations. These three structures were found experimentally. We show in figure 6.18 (a) representative data corresponding to relatively small boxes compared to the particle length:

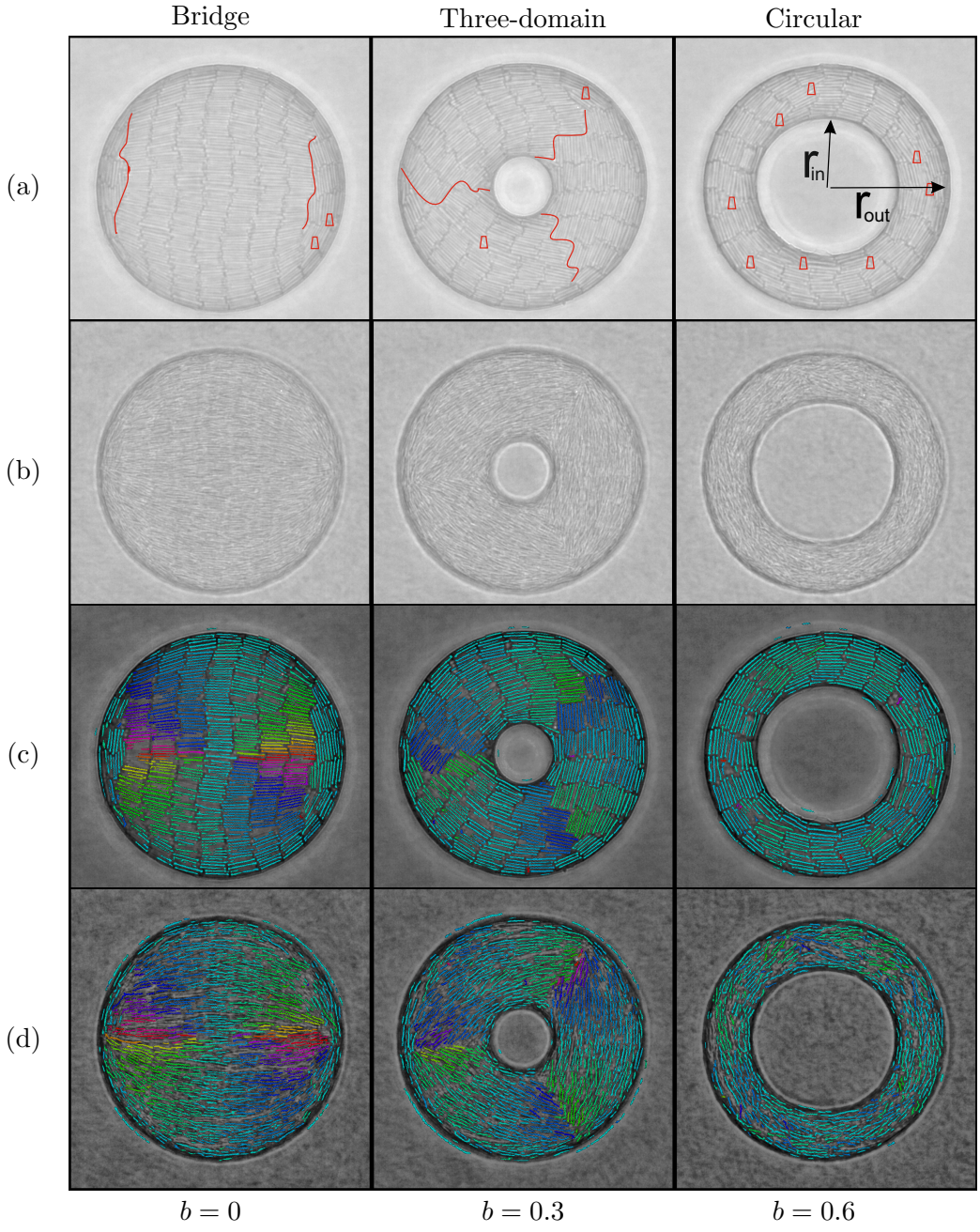


Figure 6.18: Colloidal liquid crystal confined into annular shapes with outer radius $r_{out} = 30\,\mu\text{m} \approx 5.7L$ and various inner/outer radius ratios b. (a) BF images of the smectic phase, we manually highlight in red disclination lines and edges dislocations (trapeze). (b) BF image of the overlying nematic phase. (c) Processed images of the smectic phase, rods are colored as a function of their orientation relative to the closest wall. (d) Processed images of the nematic phase.

$r_{out} = 5.7L$. The equilibrium state was found to depend on the annulus aspect ratio $b = \frac{r_{in}}{r_{out}}$: for $b = 0$, we observed the smectic bridge state, for $b \approx 0.3$, the three-domain state, and for $b = 0.6$ the circular state.

We also found many states with a mix of the two kinds of disclination and/or a non

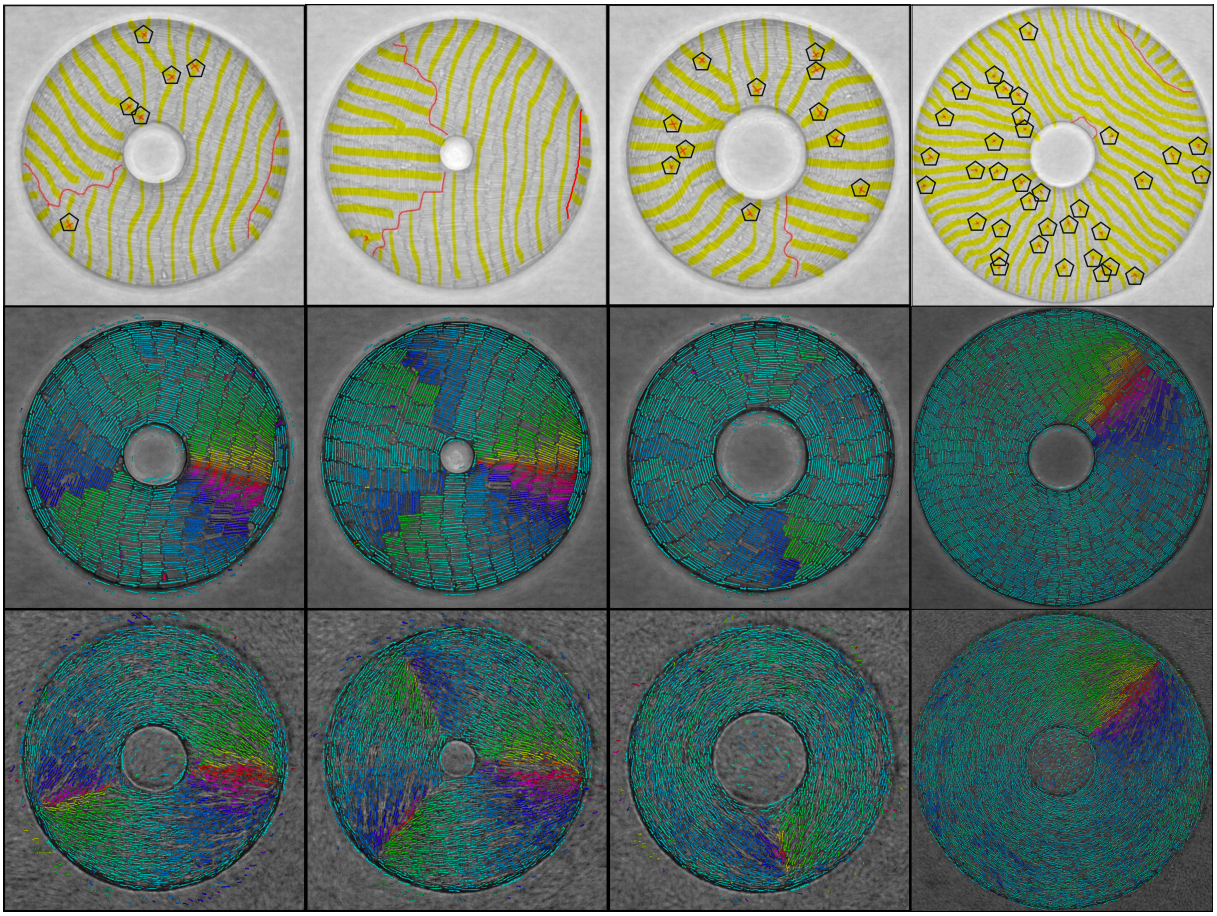


Figure 6.19: Examples of mixed states, from left to right: mix of three states, mix of bridge and 3-domain, mix of 3-domain and circular, mix of bridge and circular. (Top) Smectic, we highlight layers in yellow, the disclinations with red lines and the edge dislocations with black pentagons. (Middle) Processed smectic. (Bottom) Processed nematic.

negligible amount of dislocations. In figure 6.19, we show four combinations of defects; we highlight the disclinations with red lines, the edge dislocations with black pentagons and the layer positions in yellow.

We found that the states were easily identified when coloring the rods as a function of their orientation relative to the closest wall. Post-processing, the disclination lines parallel to the wall appear like a rainbow, the disclinations lines perpendicular to the wall appear greenish, and the edge dislocations blend into the background as they do not impact the particles' orientation. The typical color patterns for the bridge, three-domain and circular state are shown in 6.18 (c). They can be easily distinguished from the mixed states patterns shown in figure 6.19 (second row).

For each chamber we determine the configuration as bridge, three-domain, circular or mixed and we plot a state diagram as a function of the annulus aspect ratio ($b = \frac{r_{in}}{r_{out}}$) and the

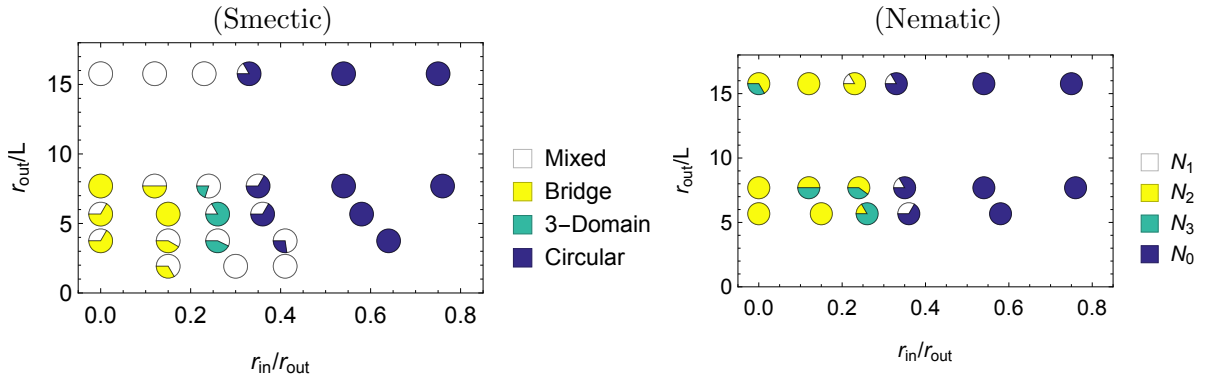


Figure 6.20: States occurrence probability as a function of the confinement chamber size r_{out}/L and the relative size of the inner radius r_{in}/r_{out}, for the smectic and nematic phases.

size of the chamber (r_{out}). We use a statistical approach to study the problem. Every state point combines the results from 3 to 12 chambers with the same dimensions. The state diagram obtained is presented in figure 6.20 (smectic).

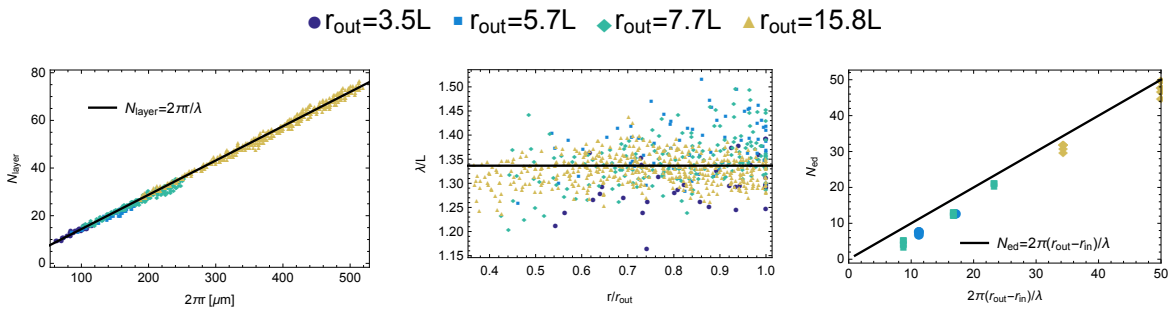
For the large cavities ($r_{out} > 15L$) and small inner radius, the states were not very well defined (○). But the remaining data confirms that the bridge state (●) dominates at low inner radius and that the circular state (●) dominates at large inner radius.

We note that the three-domain state (●) is only observed for an intermediate value of $b \approx 0.3$ and of $r_{out} \approx 3 - 6L$. For larger or smaller cavity sizes, mixed states are observed instead. In the next section, we will introduce a simple model quantifying the excess energy of this states. We will then consider the states in the nematic phase that is lying on the top of the smectic phase and highlight the interplay between the two phases.

6.6.3 A phenomenological model for the smectic states

We introduce models to approximate the excess energy due to defects in the bridge, three-domain and circular states shown in figure 6.17. The excess energy in the smectic bridge is approximated by two disclination lines of length r_{out}:

$$\Delta U_B = 2\delta r_{out}, \tag{6.5}$$



(a) (b) (c)

Figure 6.21: Analysis of edge dislocations in the circular states. (a)-(b) Number of layers and layer spacing as a function of the distance to the annulus center. (c) Test of the approximation $N_{ed} = 2\pi\frac{r_{out}-r_{in}}{\lambda}$.

where δ is the disclination line energy per unit of distance introduced in section 6.5. The excess of energy of the three-domain state is estimated by three disclination lines of length $r_{out} - r_{in}$:

$$\Delta U_{3-d} = 3(r_{out} - r_{in})\delta = 3(1-b)r_{out}\delta \ . \tag{6.6}$$

And finally, the excess of energy in the circular state is estimated by the number of edge dislocations:

$$\Delta U_c = N_{ed}u_{ed} = \frac{2\pi\,(r_{out} - r_{in})}{\lambda}u_{ed} = \frac{2\pi\,(1-b)}{\lambda}r_{out}u_{ed}, \tag{6.7}$$

where N_{ed} is the number of edge dislocations and u_{ed} the energy of one edge dislocation. For each circular state, we have located the position of the beginning of each layer. A fraction of the layers starts in contact with the inner radius perimeter, and the remaining are created by edge dislocations. In figure 6.21 (a), we show that the number of layers is proportional to the distance r from the center of the annulus: $N_{layers} = 2\pi\frac{r}{\lambda}$, with $\lambda = 1.3L \approx 6.9\,\mu\text{m}$. The number of edge dislocations in the circular state was approximated by $N_{ed} = \frac{2\pi(r_{out}-r_{in})}{\lambda}$. Figure 6.21 (c) shows that this slightly overestimates the number of edge dislocations actually found, in particular for small values of $r_{out} - r_{in}$. This is expected because our estimate of N_{ed} neglects the diameter of the rods and the curved nature of the wall. For simplicity we will stick to this model.

We know from experiments that for $r_{in} = 0$, the lowest energy state is the bridge state. For increasing annulus aspect ratio b, the energy of the bridge state remains constant. However, the energies of the two other states tend towards 0 when b tends towards 1. We then expect a transition. The three-domain state and the circular state are both directly proportional to

$(1-b)r_{out}$. Therefore, the model predicts that only one of the two states can be stable. We have either a transition from bridge to three-domain state if $3\delta < 2\pi\frac{u_{ed}}{\lambda}$ or from bridge to circular state in the opposite case.

Let us consider first the case where the three domain state has a lower energy than the circular state. In this scenario, the transition from two to three line disclinations is based on a purely geometrical argument and is predicted to happen for:

$$b = \frac{1}{3} \approx 0.33 \ . \tag{6.8}$$

If the circular state has a lower energy than the three-domain state, the model predicts a bridge to circular transition when:

$$b = 1 - \frac{\delta\lambda}{\pi u_{ed}}. \tag{6.9}$$

Looking back at the state diagram figure 6.20 (smectic), it appears clearly that, for small b the bridge state dominates and for large b the circular state dominates, but we also observe significant amount of three-domain state for $b \approx 0.25$ and $r_{out} \approx 3 - 5L$. This observation is in disagreement with our model that predicts only two stable states. Besides, we note that the value of b at the bridge to three-domain transition ($b \approx 0.25 - 0.3$) is found to be close but below the predicted value of $1/3$. It is likely that these disagreements are due to the simplicity of our model. In particular, two contributions are suspected to play an important role: distortions in the smectic phase, and a possible interplay with the nematic phase coexisting at the top of the smectic phase.

Whether the three domain state is stable or meta-stable does not affect the fact that we observe a clear transition from the bridge to the circular state in between $b = 0.2$ and $b = 0.4$. Therefore, we can estimate the ratio between a disclination line of length λ and an edge dislocation to be:

$$u_{ed} = \frac{\delta\lambda}{\pi\,(1-b)} \approx 0.4 - 0.5\delta\lambda \tag{6.10}$$

In the next section, we will observe the nematic structures present on the top of the smectic. In particular, we will show that the mixed states, that we speculate to be meta-stable, coexist

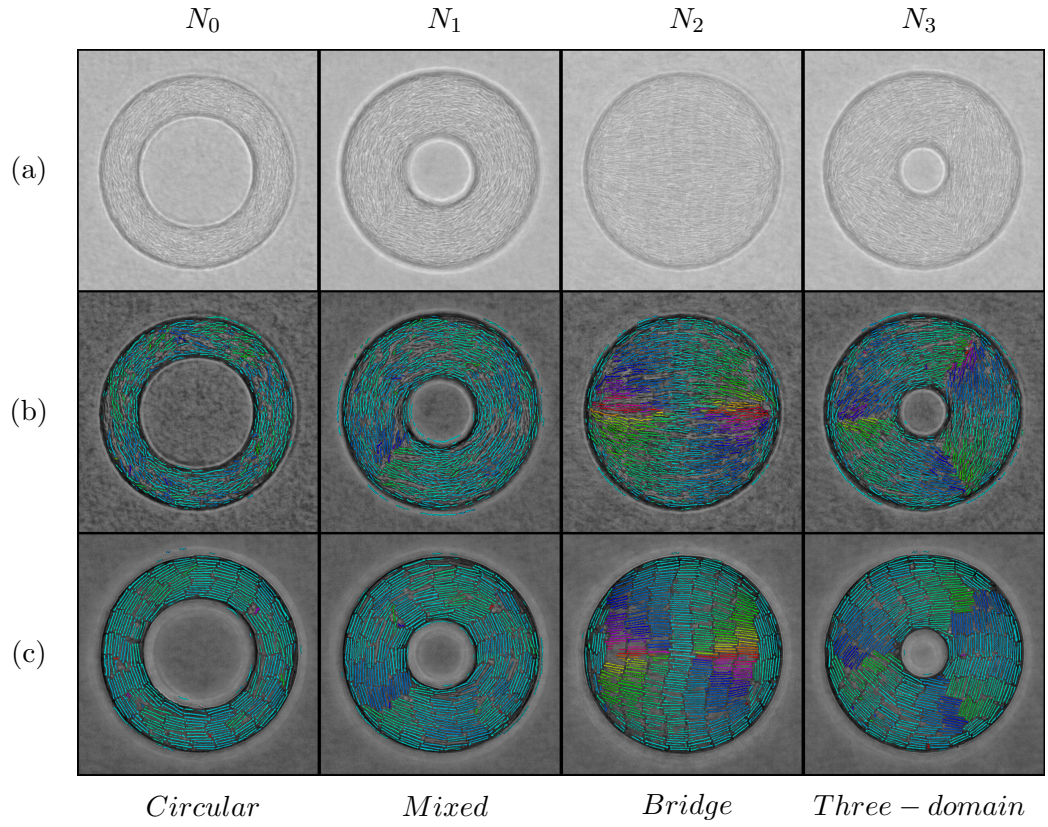


Figure 6.22: Confinement into annulus with outer radius $r_{out} = 30\,\mu\text{m} \approx 5.7L$. (a) BF images of the nematic phase. (b) Processed images of the nematic phase, rods are colored as a function of their orientation relative to the closest wall. (d) Processed images of the underlying smectic phase.

with well defined nematic states.

6.6.4 Coexisting nematic structures

The nematic states are only reported for $r_{out} > 5L$. They were found to be directly related to the number of line disclinations in the underlying smectic states: no line disclination corresponds to the state N_0 with no defect, one line disclination to the state N_1 with one pair of defects, etc. Consequently, all the bridge states turn into N_2, the three-domain into N_3 and the circular into N_0. In figure 6.22, we show instances of the nematic configuration N_0, N_1, N_2 and N_3 with the corresponding underlying smectic configurations.

The nematic state diagram is plotted alongside the smectic one in figure 6.20. The only difference between the two diagrams come from the smectic mixed states that turns into N_1, N_2 or N_3. For example, the mixed smectic states from figure 6.19 correspond to nematic states N_2, N_3, N_1 and N_1.

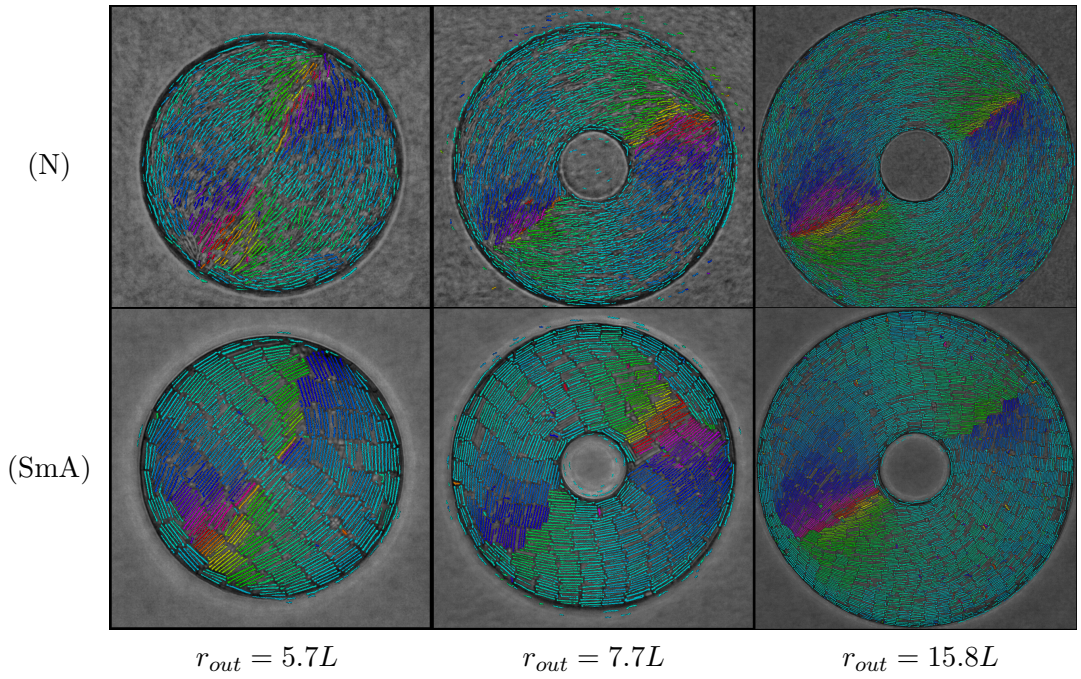


Figure 6.23: Asymmetric nematic N_2 states (top) lying on smectic states made of two disclinations lines, one parallel and one perpendicular to the wall (bottom).

We thus have a strong correlation between the nematic and the smectic states. To support this further we compare in figure 6.23, smectic and nematic states. We consider the asymmetric smectic mixed state, made of a disclination parallel to the wall and one perpendicular. Three chambers sizes are shown. We observe a close agreement between the particle orientation in the nematic and the smectic phase. The nematic director in the nematic phase is adapting close to the defects where the distortion is maximum. However, further away the nematic director seems to follow the configuration of the smectic phase and does not recover the symmetric form that would be expected. This indicates that the nematic phase is too thin (about a rod length) or equivalently the twist elastic constant is too large to allow reorientation of the nematic director.

When confined into squares, we observed that the smectic bridge state was forcing the nematic phase away from its lower energy state, the diagonal state. We expect this behavior to generalize to any shape, we expect the energy of the smectic structure to always be the dominant factor. However, if the difference of energy between multiple smectic structures is small we can then expect the nematic phase to play a role. That might be part of the reason why the three-domain state is only observed for a small island of the phase diagram in figure 6.20. Indeed, the three-domain smectic state coexists with the N_3 nematic state, and the N_3 nematic state

is predicted to be stable only in a small region of the phase diagram, stabilized by finite size effects [195, 209]. However, this is very speculative as we did not show that the N_3 state is actually stable in this region for our system. Moreover, we do not know how differences of energy between nematic states compares with the differences of energy between smectic states.

6.7 Conclusion

In this chapter, we have first presented an experimental method that allows to confine colloidal liquid crystals in cavities with tailored shapes and sizes. The chambers, were filled with particles by sedimentation, exploiting the small gravitational length of the rods. We have shown coexistence of isotropic, nematic and smectic phases in confinement, which is in qualitative agreement with the bulk experiments presented in chapter 3. However, when confined into square of side $W \approx 15L$, the nematic phase was found to be thinner than in bulk. This provided an example on how complex confinement may affect the phase behavior.

Then, the focus was shifted to how smectic structures, with characteristic elasticities and defects, respond to boundary conditions imposed by confinement. By combining large colloidal rods, with an effective aspect ratio $p_{eff} \approx 10$, and soft lithography techniques, we have confined particles in cavities with typical sizes ranging from 2 to 70 layer spacing ($\lambda \approx 1.3L$). In particular this was exploited to clarify the effect of square cavities.

For *square* confinement, we reproduced the two structures reported in literature: the uniform state found in a simulation with a square side $W \approx 3\lambda$ [204] and the smectic bridge found for $2.5\lambda < W < 8\lambda$ [202]. By gradually changing box dimensions, we showed that the uniform state could only be formed for small boxes ($W \leq 2\lambda$) *and* commensurability between λ and W. The particular value of 2λ may depend on specific rod and square shapes as suggested by [202]. However, we do not expect it to be larger than $3 - 4\lambda$. For $2\lambda < W < 15\lambda$ we mostly found the smectic bridge state, in agreement with simulation [202] and theory [200]. However, for $W \geq 15\lambda$, we observed the emergence of a meta-stable diagonal state that might become stable at larger W. This could not be verified experimentally due to the dominant nature of unequilibrated states for sides $W > 30\lambda$. Nevertheless, the diagonal state could be stabilized by turning squares into lozenges.

Smectic structures into *lozenges* were studied here for the first time. The side W of the lozenges

was varied from 2λ to 50λ, and the nose angle γ from 10° (thin lozenge) to 90° (square). For $5\lambda < W < 30\lambda$, we found a transition from the smectic bridge (large γ) to the diagonal state (small γ). This transition was found to be mostly independent of W and was located around $\gamma_c = 60°$. This results was supported by a phenomenological model accounting for the bending energy of the diagonal state and the line disclination energy of the bridge state. By combining our model and experiments we estimated the energy ratio between a disclination line of length λ and the bending energy constant β:

$$\frac{\delta\lambda}{\beta} = \gamma_c \cos\left(\frac{\gamma_c}{2}\right) \approx 1 \ , \tag{6.11}$$

where β is simply related to the product of the elastic modulus C and the squared penetration length λ_p^2 (see equation 2.62 page 30). A similar method was then employed to study the smectic structures into annuli.
The *annulus* aspect ratio $\left(b = \frac{r_{out}}{r_{in}}\right)$ was varied from 0 to 1 and the outer radius r_{out} from 1.5λ to 12λ. For $2\lambda < r_{out} < 10\lambda$, we identified a transition from the bridge ($b < 0.2$) to the circular state ($b > 0.4$) that is largely independent of r_{out}. The state energies were estimated from the length of the disclination lines (bridge) and the number of edge dislocations (circular). By combining this model and our experimental finding, we estimated the energy ratio between a disclination line of length λ and an edge dislocation to be:

$$\frac{\delta\lambda}{u_{ed}} = \pi\,(1-b) \approx 2 - 2.5. \tag{6.12}$$

We equally, observed occurrences of the three-domain state, composed of three disclination lines perpendicular to the walls. This state was found to be experimentally dominant for a small island in the state diagram: $2.5\lambda < r_{out} < 5\lambda$ and $0.2 < b < 0.4$. However, this could not be understood in light of our phenomenological model, that neglects distortions and a possible interplay with the nematic phase.

Our experiments equally showed a close match between the coexisting nematic and smectic structures, in both squares and annuli. In squares with $W \approx 10\lambda$, we found that the smectic phase was dictating the equilibrium structure by imposing boundary conditions to the thin nematic phase. This implies that, for $W \approx 10\lambda$, the energies involved in the smectic phase are somehow larger than in the nematic phase. Whether or not this can be generalized to large squares ($W > 30\lambda$) is unclear however.

In this chapter we aimed to provide an overview of the behavior of smectic colloidal liquid crystals in confinement, with a focus on the interplay between boundary conditions, deformations and defects. A step forward, would be to broaden this results to different aspect ratios and colloid concentrations. Preliminary results seemed to show little dependency with concentration. However, the problem was not investigated in detail. Equally, a more quantitative approach to describe the energy of nematic and smectic states would certainly help to understand the interplay between the nematic and the smectic phase. An ongoing collaboration with René Wittmann and Hartmut Löwen is aiming to address these points by means of DFT.

Acknowledgments

I would like to thank Kira Klop for briefing me on the soft lithography techniques and acknowledge the coauthors of my publication on the confinement of rods in square geometry [211] Roel and Yongxiang.

Summary

In this thesis, we investigated on the phase behaviour, self-diffusion and confinement of colloidal liquid crystals in sedimentation-diffusion equilibrium. Our aim was twofold: (i) deepen our understanding of these actively researched problems and (ii) provide test experiments for emerging simulation techniques and theoretical works.

In chapter 2, we presented the theoretical background and experimental methods. In particular, we introduced the gravitational length, and the two main silica rod systems used across the thesis.

In chapter 3, we compared our experimental results to the sedimentation-diffusion equilibrium predicted for hard rods. *Theoretically,* the density profiles of hard rods, with aspect ratio ranging from 5 to 20, were obtained within the local density approximation. We considered the case where isotropic (I), nematic (N), smectic (Sm) and crystal phases (K) are coexisting in a semi-infinite space. We focused our attention on the upper part of the sediment – isotropic, nematic and smectic phases, and found it to be largely independent of the rod aspect ratio: $W_{I+N+S} \approx 32 l_g$. *A molecular dynamic (MD) simulation* was performed by my colleague Maxime Tortora to test the validity of our theoretical prediction. The interfaces, between various liquid crystal phases, were localized by measuring the nematic, smectic and ψ_6 order parameters. Despite minor discrepancies, the thickness of the upper sediment was found to be in close agreement with our theoretical prediction. *Experimentally*, the nematic and smectic order parameters were obtained from real space tracking of tracer particles. The top of the sediment, defined at the height where $\phi = 1\%$, was estimated from the number of dyed particles as a function of height. At equilibrium, the upper sediment was equally found to be independent of the initial concentration of rods. However, we found that: (i) the smectic phase was relatively thin, and (ii) the upper sediment was inflated up to a factor of two. This first

effect was attributed to rod polydispersity. However, the inflation could only be understood in light of the the Donnan effect, which was explained in the next chapter.

In chapter 4, we generalized our method to predict the density profile of charged rods. We considered the double layer repulsion between rods – by introducing effective particle dimensions – and the osmotic pressure of ions – by including the Donnan effect (zero-field limit). We showed that only the Donnan effect could explain the inflation of the upper sediment, whereas the effective dimensions of the rods mainly impacted the thickness of the crystalline part of the sediment. In a 1mM water solution, the experimental trend was qualitatively reproduced for a particle surface charge $|\sigma_{Don}| = 1260\, e\, \mu m^{-2}$ and an effective diameter $D_{eff} \approx D{+}80nm \approx 1.2D$. To corroborate this result, we independently estimated the surface charge of silica rods based on the silanol group dissociation constants and by measuring the particles' zeta potential. Both approaches led to a surface charge $|\sigma_-| > 20000\, e\, \mu m^{-2}$. Qualitatively, such discrepancy with our treatment of the Donnan effect was expected because this treatment, using the zero-field approximation, does not account for ions trapped within the double layer. A quantitative comparison between σ_{Don} and σ_- may give a new perspective to study charge effects in dense colloidal suspensions, which are particularly complex.

In chapter 5, we studied the self-diffusion of colloidal liquid crystals at sedimentation-diffusion equilibrium. We first used the molecular dynamic simulation to show that the long-time diffusion coefficient of colloidal rods can be measured at sedimentation-diffusion equilibrium. We then analyzed the diffusion of silica rods, with an effective aspect ratio $p_{eff} = 10.4$ ($p = 12.6$), across the entire phase diagram, i.e. for effective volume fractions ranging from 2 to 63%.
In order to identify the long-time regime, we first measured the Non-Gaussian Parameter α_2 as a function of time. Each peak of α_2 was interpreted as a transition between two diffusive regimes. In the isotropic, nematic and smectic phases, at least one peak could be identified; two were found in the smectic phase – in the direction perpendicular to the nematic director. In all cases, the long-time regime was found to be well captured within our experimental time-range, apart from in the smectic phase – in the direction parallel to the nematic director. We further measured typical interactions times: in the isotropic phase we found $\tau_I < 0.2\tau = 0.2\sigma^2 D_{t0}^{-1} = 0.1s$ at low concentration, and $\tau_I \approx \tau$ for $20\% < \phi_{eff} < 25\%$; in the nematic phase, we measured $\tau_I \approx \tau$ in the direction parallel to the nematic director, and $\tau_I < 0.2\tau$ in the direction perpendicular.
The long-time rotational and translational diffusion coefficients were compared to existing sim-

ulations of hard rods with aspect ratio $p = 10$. A good qualitative agreement was found: in particular, striking structural similarities were identified in the isotropic and smectic phases. However, experimental diffusion coefficients were found to be typically 2-4 times smaller than in simulations, which confirms that present theories and simulations are unable to quantitatively predict the dynamics of model experimental systems.

In chapter 6, we presented an experimental method to confine dense colloidal liquid crystals in chambers with various shapes and sizes. The focus was placed on the response of smectic structures to boundary conditions imposed by confinement. Firstly, we revisited confinement in squares. The smectic bridge state, characterized by two line disclinations, was the most commonly found. However, we showed that a uniform state could be stabilized in small chambers. We equally found instances of the diagonal state, characterized by bent smectic layers, in the largest squares. We then showed that this diagonal state could be stabilized by progressively transforming squares into thin lozenges. By simply modeling the transition, we extracted the ratio between the energy of a disclination line of length $\lambda \approx L$ and the bending energy of smectic layers β: $\delta\lambda \approx \beta$. We finally studied disks, which predominantly induced the formation of the smectic bridge state. The disks were transformed into thin annuli to originate a transition from the smectic bridge to the circular state, characterized by the formation of edge dislocations. We equally modeled this transition and extracted energy ratio between an edge dislocation and a disclination line $\delta\lambda \approx 2u_{ed}$.

Bibliography

[1] Gustavo V Barbosa-Cánovas, Jozef L Kokini, Li Ma, and Albert Ibarz. The rheology of semiliquid foods. In *Advances in Food and Nutrition Research*, volume 39, pages 1–69. Academic Press, 1996.

[2] Norman Wagner and Eric D Wetzel. Advanced body armor utilizing shear thickening fluids, March 3 2009. US Patent 7,498,276.

[3] Ankita Srivastava, Abhijit Majumdar, and B S Butola. Improving the impact resistance of textile structures by using shear thickening fluids: a review. *Critical Reviews in Solid State and Materials Sciences*, 37(2):115–129, 2012.

[4] Omathanu Pillai and Ramesh Panchagnula. Polymers in drug delivery. *Current opinion in chemical biology*, 5(4):447–451, 2001.

[5] Scott J Woltman, Gregory D Jay, and Gregory P Crawford. Liquid-crystal materials find a new order in biomedical applications. *Nature materials*, 6(12):929, 2007.

[6] David Dunmur and Tim Sluckin. *Soap, science, and flat-screen TVs: a history of liquid crystals*. Oxford University Press, 2011.

[7] Daniela Cupelli, Fiore Pasquale Nicoletta, Sabrina Manfredi, Marco Vivacqua, Patrizia Formoso, Giovanni de Filpo, and Giuseppe Chidichimo. Self-adjusting smart windows based on polymer-dispersed liquid crystals. *Solar Energy Materials and Solar Cells*, 93(11):2008–2012, 2009.

[8] Clemens Bechinger, Roberto Di Leonardo, Hartmut Löwen, Charles Reichhardt, Giorgio Volpe, and Giovanni Volpe. Active particles in complex and crowded environments. *Reviews of Modern Physics*, 88(4):045006, 2016.

[9] Lars Onsager. The effects of shape on the interaction of colloidal particles. *Annals of the New York Academy of Sciences*, 51(4):627–659, 1949.

[10] P-G de Gennes. *Scaling concepts in polymer physics*. Cornell university press, 1979.

[11] Pierre-Gilles de Gennes. Wetting: statics and dynamics. *Reviews of modern physics*, 57(3):827, 1985.

[12] P-G de Gennes, J Prost, and R Pelcovits. *The physics of liquid crystals*. Oxford University Press, 1995.

[13] Luis Mederos, Enrique Velasco, and Yuri Martínez-Ratón. Hard-body models of bulk liquid crystals. *Journal of Physics: Condensed Matter*, 26(46):463101, 2014.

[14] Mahsa Siavashpouri, Christian H Wachauf, Mark J Zakhary, Florian Praetorius, Hendrik Dietz, and Zvonimir Dogic. Molecular engineering of chiral colloidal liquid crystals using dna origami. *Nature materials*, 16(8):849, 2017.

[15] F C Bawden, N W Pirie, J D Bernal, and I Fankuchen. Liquid crystalline substances from virus-infected plants. *Nature*, 138(3503):1051, 1936.

[16] Kimberly L Weirich, Shiladitya Banerjee, Kinjal Dasbiswas, Thomas A Witten, Suriyanarayanan Vaikuntanathan, and Margaret L Gardel. Liquid behavior of cross-linked actin bundles. *Proceedings of the National Academy of Sciences*, page 201616133, 2017.

[17] Marie M Giraud-Guille, Gervaise Mosser, and Emmanuel Belamie. Liquid crystallinity in collagen systems in vitro and in vivo. *Current Opinion in Colloid & Interface Science*, 13(4):303–313, 2008.

[18] M Zhao, F Ansari, M Takeuchi, M Shimizu, T Saito, L A Berglund, and A Isogai. Nematic structuring of transparent and multifunctional nanocellulose papers. *Nanoscale Horizons*, 3(1):28–34, 2018.

[19] M G Northolt and D J Sikkema. Lyotropic main chain liquid crystal polymers. In *Liquid Crystal Polymers: From Structures to Applications*, volume 1. Springer, 1992.

[20] Fritz Vollrath and David P Knight. Liquid crystalline spinning of spider silk. *Nature*, 410(6828):541, 2001.

[21] Krzysztof Koziol, Juan Vilatela, Anna Moisala, Marcelo Motta, Philip Cunniff, Michael Sennett, and Alan Windle. High-performance carbon nanotube fiber. *Science*, 318(5858):1892–1895, 2007.

[22] Youssef Habibi, Lucian A Lucia, and Orlando J Rojas. Cellulose nanocrystals: Chemistry, self-assembly, and applications. *Chemical Reviews*, 110(6):3479–3500, 2010.

[23] H N W Lekkerkerker and G J Vroege. Liquid crystal phase transitions in suspensions of mineral colloids: new life from old roots. *Philosophical Transactions of the Royal Society A: Mathematical, Physical and Engineering Sciences*, 371(1988), 2013.

[24] David S. Hecht, Liangbing Hu, and Glen Irvin. Emerging transparent electrodes based on thin films of carbon nanotubes, graphene, and metallic nanostructures. *Advanced Materials*, 23(13):1482–1513, 2011.

[25] Salvatore Torquato. *Random Heterogeneous Materials*. Springer, 2002.

[26] Shari P Finner, Mihail I Kotsev, Mark A Miller, and Paul van der Schoot. Continuum percolation of polydisperse rods in quadrupole fields: Theory and simulations. *The Journal of Chemical Physics*, 148(3):034903, 2018.

[27] Marina Soares e Silva, José Alvarado, Jeanette Nguyen, Nefeli Georgoulia, Bela M. Mulder, and Gijsje H. Koenderink. Self-organized patterns of actin filaments in cell-sized confinement. *Soft Matter*, 7:10631–10641, 2011.

[28] C. Earnshaw "William and R. Casjens" Sherwood. "dna packaging by the double-stranded dna bacteriophages". *"Cell"*, "21"("2"):"319 – 331", "1980".

[29] Timothée Vignaud, Laurent Blanchoin, and Manuel Théry. Directed cytoskeleton self-organization. *Trends in cell biology*, 22(12):671–682, 2012.

[30] M Doi. Rotational relaxation time of rigid rod-like macromolecule in concentrated solution. *Journal de Physique*, 36(7-8):607–611, 1975.

[31] Masao Doi and Sam F Edwards. Dynamics of rod-like macromolecules in concentrated solution. part 2. *Journal of the Chemical Society, Faraday Transactions 2: Molecular and Chemical Physics*, 74:918–932, 1978.

[32] Satoru Fujime, M Takasaki-Ohsita, and T Maeda. Dynamic light scattering from semidilute suspensions of fd virus. *Macromolecules*, 20(6):1292–1295, 1987.

[33] Dirk G. A. L. Aarts, Matthias Schmidt, and Henk N. W. Lekkerkerker. Direct visual observation of thermal capillary waves. *Science*, 304(5672):847–850, 2004.

[34] S Wolfsheimer, C Tanase, K Shundyak, R van Roij, and T Schilling. Isotropic-nematic interface in suspensions of hard rods: Mean-field properties and capillary waves. *Physical Review E*, 73(6):061703, 2006.

[35] Ronald H J Otten and Paul van der Schoot. Capillary rise of an isotropic-nematic fluid interface: Surface tension and anchoring versus elasticity. *Langmuir*, 25(4):2427–2436, 2009.

[36] Frederick G Donnan. The theory of membrane equilibria. *Chemical Reviews*, 1(1):73–90, 1924.

[37] Anke Kuijk, Alfons van Blaaderen, and Arnout Imhof. Synthesis of monodisperse, rod-like silica colloids with tunable aspect ratio. *Journal of the American Chemical Society*, 133(8):2346–2349, 2011.

[38] Jean Perrin. Mouvement brownien et réalité moléculaire. 18:5–104, 1909.

[39] Joseph Delsaulx. Thermo-dynamic origin of the brownian motions. *The Monthly Microscopical Journal*, 18(1):1–7, 1877.

[40] Carbonnelle. *Revue des Questions scientifiques*, 1880.

[41] Gouy. *Journal de Physique*, 1888.

[42] Gouy. *Comptes rendus*, 1889.

[43] Gouy. *Revue générale des sciences*, 1895.

[44] Albert Einstein. Über die von der molekularkinetischen theorie der wärme geforderte bewegung von in ruhenden flüssigkeiten suspendierten teilchen. *Annalen der physik*, 322(8):549–560, 1905.

[45] José García de la Torre and Victor A Bloomfield. Hydrodynamic properties of complex, rigid, biological macromolecules: theory and applications. *Quarterly Reviews of Biophysics*, 14(1):81–139, 1981.

[46] Peter Bolhuis and Daan Frenkel. Tracing the phase boundaries of hard spherocylinders. *The Journal of chemical physics*, 106(2):666–687, 1997.

[47] Wendell M Stanley et al. Isolation of a crystalline protein possessing the properties of tobacco-mosaic virus. *Science*, 81(2113):644–645, 1935.

[48] Wilhelm Maier and Alfred Saupe. Eine einfache molekular-statistische theorie der nematischen kristallinflüssigen phase. teil l1. *Zeitschrift für Naturforschung A*, 14(10):882–889, 1959.

[49] H N W Lekkerkerker, P Coulon, R van der Haegen, and R Deblieck. On the isotropic-liquid crystal phase separation in a solution of rodlike particles of different lengths. *The Journal of Chemical Physics*, 80(7):3427–3433, 1984.

[50] A Stroobants, H N W Lekkerkerker, and T Odijk. Effect of electrostatic interaction on the liquid crystal phase transition in solutions of rodlike polyelectrolytes. *Macromolecules*, 19(8):2232–2238, 1986.

[51] Szabolcs Varga, Péter Gurin, Julio C Armas-Pérez, and Jacqueline Quintana-H. Nematic and smectic ordering in a system of two-dimensional hard zigzag particles. *The Journal of Chemical Physics*, 131(18):184901, 2009.

[52] J A Martínez-González, S Varga, P Gurin, and J Quintana-H. Spontaneously bended nematic and antiferroelectric smectic structures of banana-shaped hard particles in two dimensions. *EPL (Europhysics Letters)*, 97(2):26004, 2012.

[53] T M Birshtein, B I Kolegov, and V A Pryamitsyn. Theory of athermal lyotropic liquid crystal systems. *Polymer Science U.S.S.R.*, 30(2):316 – 324, 1988.

[54] A Ferrarini. The theory of elastic constants. *Liquid Crystals*, 37(6-7):811–823, 2010.

[55] Masao Doi and Nobu Kuzuu. Structure of the interface between the nematic phase and the isotropic phase in the rodlike molecules. In *J. Appl. Polym. Sci.: Appl. Polym. Symp*, volume 41, pages 65–68, 1985.

[56] Michael P Allen. Molecular simulation and theory of the isotropic–nematic interface. *The Journal of Chemical Physics*, 112(12):5447–5453, 2000.

[57] D de las Heras, E Velasco, and L Mederos. Capillary smectization and layering in a confined liquid crystal. *Physical review letters*, 94(1):017801, 2005.

[58] D de las Heras, E Velasco, and L Mederos. Capillary effects in a confined smectic phase of hard spherocylinders: Influence of particle elongation. *Physical Review E*, 74(1):011709, 2006.

[59] J D Parsons. Nematic ordering in a system of rods. *Physical Review A*, 19(3):1225, 1979.

[60] Sin-Doo Lee. A numerical investigation of nematic ordering based on a simple hard-rod model. *The Journal of chemical physics*, 87(8):4972–4974, 1987.

[61] Simon C McGrother, Dave C Williamson, and George Jackson. A re-examination of the phase diagram of hard spherocylinders. *The Journal of Chemical Physics*, 104(17):6755–6771, 1996.

[62] H Zocher and K Jacobsohn. Über taktosole. *Kolloidchemische Beihefte*, 28(6):167–206, 1929.

[63] J-C P Gabriel and P Davidson. New trends in colloidal liquid crystals based on mineral moieties. *Advanced Materials*, 12(1):9–20, 2000.

[64] Gerald Oster. Two-phase formation in solutions of tobacco mosaic virus and the problem of long-range forces. *The Journal of general physiology*, 33(5):445–473, 1950.

[65] M Wadati and A Isihara. Theory of liquid crystals. *Molecular Crystals and Liquid Crystals*, 17(2):95–108, 1972.

[66] Masahito Hosino, Huzio Nakano, and Hatsuo Kimura. Effect of orientational fluctuation on nematic-smectic a transition in the system of hard rod molecules. *Journal of the Physical Society of Japan*, 47(3):740–745, 1979.

[67] Paul E Brumby, Henricus H Wensink, Andrew J Haslam, and George Jackson. Structure and interfacial tension of a hard-rod fluid in planar confinement. *Langmuir*, 33(42):11754–11770, 2017. PMID: 28885848.

[68] James M Polson and Daan Frenkel. First-order nematic-smectic phase transition for hard spherocylinders in the limit of infinite aspect ratio. *Phys. Rev. E*, 56:R6260–R6263, Dec 1997.

[69] Julia M Yeomans. *Statistical mechanics of phase transitions*. Clarendon Press, 1992.

[70] Maxime M C Tortora and Jonathan P K Doye. "personal communication".

[71] B I Halperin and D R Nelson. Theory of two-dimensional melting. *Phys. Rev. Lett.*, 41:121–124, Jul 1978.

[72] H Weber, D Marx, and K Binder. Melting transition in two dimensions: A finite-size scaling analysis of bond-orientational order in hard disks. *Phys. Rev. B*, 51:14636–14651, May 1995.

[73] B V Deraguin and L Landau. Theory of the stability of strongly charged lyophobic sols and of the adhesion of strongly charged particles in solution of electrolytes. *Acta Physicochim: USSR*, 14:633–662, 1941.

[74] E J W Verwey. Theory of the stability of lyophobic colloids. *The Journal of Physical and Colloid Chemistry*, 51(3):631–636, 1947.

[75] M J Sparnaay. *Recl Trav. chim. Pays-Bas*, 78:680, 1959.

[76] Jacob N Israelachvili. *Intermolecular and surface forces*. Academic press, 2011.

[77] Maxime M C Tortora and Jonathan P K Doye. Perturbative density functional methods for cholesteric liquid crystals. *The Journal of Chemical Physics*, 146(18):184504, 2017.

[78] K R Spring, T J Fellers, and M W Davidson. Resolution and contrast in confocal microscopy.

[79] T J Sluckin. Polydispersity in liquid crystal systems. *Liquid Crystals*, 6(1):111–131, 1989.

[80] Anne M Bohle, Robert Hołyst, and Thomas Vilgis. Polydispersity and ordered phases in solutions of rodlike macromolecules. *Phys. Rev. Lett.*, 76:1396–1399, Feb 1996.

[81] Martin A Bates and Daan Frenkel. Influence of polydispersity on the phase behavior of colloidal liquid crystals: A monte carlo simulation study. *The Journal of Chemical Physics*, 109(14):6193–6199, 1998.

[82] Yuri Martínez-Ratón and José A Cuesta. Smectic and columnar ordering in length-polydisperse fluids of parallel hard cylinders. *Molecular Physics*, 107(4-6):415–422, 2009.

[83] Hideatsu Maeda and Yoshiko Maeda. Liquid crystal formation in suspensions of hard rodlike colloidal particles: Direct observation of particle arrangement and self-ordering behavior. *Phys. Rev. Lett.*, 90:018303, 2003.

[84] K M Keville, E I Franses, and J M Caruthers. "preparation and characterization of monodisperse polymer microspheroids". *"Journal of Colloid and Interface Science"*, "144"("1"):"103 – 126", "1991".

[85] Ali Mohraz and Michael J Solomon. Direct visualization of colloidal rod assembly by confocal microscopy. *Langmuir*, 21(12):5298–5306, 2005.

[86] Carla Fernández-Rico, Taiki Yanagishima, Arran Curran, Dirk G A L Aarts, and Roel P A Dullens. Synthesis of colloidal su-8 polymer rods using sonication. *Advanced Materials*, 0(0):1807514, 2019.

[87] J Lapointe and D A Marvin. Filamentous bacterial viruses viii. liquid crystals of fd. *Molecular Crystals and Liquid Crystals*, 19(3-4):269–278, 1973.

[88] Seymour S Cohen and Wendell M Stanley. The molecular size and shape of the nucleic acid of tobacco mosaic virus. *Journal of Biological Chemistry*, 144(3):589–598, 1942.

[89] Anke Kuijk, Arnout Imhof, Margriet H W Verkuijlen, Thijs H Besseling, Ernst R H van Eck, and Alfons van Blaaderen. Colloidal silica rods: Material properties and fluorescent labeling. *Particle & Particle Systems Characterization*, 31(6):706–713, 2014.

[90] Anke Kuijk, Dmytro V Byelov, Andrei V Petukhov, Alfons van Blaaderen, and Arnout Imhof. Phase behavior of colloidal silica rods. *Faraday discussions*, 159(1):181–199, 2012.

[91] T H Besseling, M Hermes, A Kuijk, B de Nijs, T-S Deng, M Dijkstra, A Imhof, and A van Blaaderen. Determination of the positions and orientations of concentrated rod-like colloids from 3d microscopy data. *Journal of Physics: Condensed Matter*, 27(19):194109, 2015.

[92] S V Savenko and M Dijkstra. Sedimentation and multiphase equilibria in suspensions of colloidal hard rods. *Physical Review E*, 70(5):051401, 2004.

[93] Simone Dussi. *When shape is enough: from colloidal spheres to twisted polyhedra, from icosahedral to chiral order*. PhD thesis, Utrecht University, 2016.

[94] Denis Bartolo and Dirk G A L Aarts. Microfluidics and soft matter: small is useful. *Soft Matter*, 8(41):10530–10535, 2012.

[95] Microchem. Su-8 2000 processing guidelines, http://microchem.com.

[96] Oliver J Dammone. *Confinement of colloidal liquid crystal*. PhD thesis, University of Oxford, 2013.

[97] M Abramowitz and Davidson M W. Numerical aperture and resolution.

[98] Alice L Thorneywork, Joshua L Abbott, Dirk G A L Aarts, and Roel P A Dullens. Two-dimensional melting of colloidal hard spheres. *Phys. Rev. Lett.*, 118:158001, Apr 2017.

[99] Etienne P Bernard and Werner Krauth. Two-step melting in two dimensions: First-order liquid-hexatic transition. *Phys. Rev. Lett.*, 107:155704, Oct 2011.

[100] Roberto Piazza. Settled and unsettled issues in particle settling. *Reports on Progress in Physics*, 77(5):056602, 2014.

[101] René van Roij. Defying gravity with entropy and electrostatics: sedimentation of charged colloids. *Journal of Physics: Condensed Matter*, 15(48):S3569, 2003.

[102] Eric Grelet. Hard-rod behavior in dense mesophases of semiflexible and rigid charged viruses. *Physical Review X*, 4(2):021053, 2014.

[103] Joshua A Anderson and Sharon C Glotzer. The development and expansion of hoomd-blue through six years of gpu proliferation. *arXiv preprint arXiv:1308.5587*, 2013.

[104] Jens Glaser, Trung Dac Nguyen, Joshua A Anderson, Pak Lui, Filippo Spiga, Jaime A Millan, David C Morse, and Sharon C Glotzer. Strong scaling of general-purpose molecular dynamics simulations on gpus. *Computer Physics Communications*, 192:97–107, 2015.

[105] Trung Dac Nguyen, Carolyn L Phillips, Joshua A Anderson, and Sharon C Glotzer. Rigid body constraints realized in massively-parallel molecular dynamics on graphics processing units. *Computer Physics Communications*, 182(11):2307–2313, 2011.

[106] Bart de Braaf, Mariana Oshima Menegon, Stefan Paquay, and Paul van der Schoot. Self-organisation of semi-flexible rod-like particles. *The Journal of Chemical Physics*, 147(24):244901, 2017.

[107] H N W Lekkerkerker, P Coulon, R van der Haegen, and R Deblieck. On the isotropic-liquid crystal phase separation in a solution of rodlike particles of different lengths. *The Journal of chemical physics*, 80(7):3427–3433, 1984.

[108] Theo Odijk and Henk N W Lekkerkerker. Theory of the isotropic-liquid crystal phase separation for a solution of bidisperse rodlike macromolecules. *The Journal of Physical Chemistry*, 89(10):2090–2096, 1985.

[109] Alessandro Speranza and Peter Sollich. Simplified onsager theory for isotropic–nematic phase equilibria of length polydisperse hard rods. *The Journal of chemical physics*, 117(11):5421–5436, 2002.

[110] Alessandro Speranza and Peter Sollich. Isotropic-nematic phase equilibria of polydisperse hard rods: the effect of fat tails in the length distribution. *The Journal of chemical physics*, 118(11):5213–5223, 2003.

[111] Yuri Martínez-Ratón and José A. Cuesta. Smectic and columnar ordering in length-polydisperse fluids of parallel hard cylinders. *Molecular Physics*, 107(4-6):415–422, 2009.

[112] Kirstin R Purdy, Szabolcs Varga, Amparo Galindo, George Jackson, and Seth Fraden. Nematic phase transitions in mixtures of thin and thick colloidal rods. *Physical review letters*, 94(5):057801, 2005.

[113] Gert J Vroege, Dominique M E Thies-Weesie, Andrei V Petukhov, Bruno J Lemaire, and Patrick Davidson. Smectic liquid-crystalline order in suspensions of highly polydisperse goethite nanorods. *Advanced Materials*, 18(19):2565–2568, 2006.

[114] D V Byelov, M C D Mourad, I Snigireva, A Snigirev, A V Petukhov, and H N W Lekkerkerker. Experimental observation of fractionated crystallization in polydisperse platelike colloids. *Langmuir*, 26(10):6898–6901, 2010.

[115] L Bellier-Castella and H Xu. Sedimentation profiles of polydisperse fluids. *Journal of Physics: Condensed Matter*, 15(32):5417, 2003.

[116] Anne M Bohle, Robert Hołyst, and Thomas Vilgis. Polydispersity and ordered phases in solutions of rodlike macromolecules. *Physical review letters*, 76(8):1396, 1996.

[117] C P Royall, R van Roij, and Alfons van Blaaderen. Extended sedimentation profiles in charged colloids: the gravitational length, entropy, and electrostatics. *Journal of Physics: Condensed Matter*, 17(15):2315, 2005.

[118] Roberto Piazza, Tommaso Bellini, and Vittorio Degiorgio. Equilibrium sedimentation profiles of screened charged colloids: A test of the hard-sphere equation of state. *Physical review letters*, 71(25):4267, 1993.

[119] Albert P Philipse and Gijsberta H Koenderink. Sedimentation-diffusion profiles and layered sedimentation of charged colloids at low ionic strength. *Advances in colloid and interface science*, 100:613–639, 2003.

[120] Mircea Raşa and Albert P Philipse. Evidence for a macroscopic electric field in the sedimentation profiles of charged colloids. *Nature*, 429(6994):857, 2004.

[121] M Rasa, BH Erné, B Zoetekouw, R van Roij, and A P Philipse. Macroscopic electric field and osmotic pressure in ultracentrifugal sedimentation–diffusion equilibria of charged colloids. *Journal of Physics: Condensed Matter*, 17(15):2293, 2005.

[122] T Biben and J-P Hansen. Sedimentation equilibrium in concentrated charge-stabilized colloidal suspensions. *Journal of Physics: Condensed Matter*, 6(23A):A345, 1994.

[123] A Philipse and A Vrij. The Donnan equilibrium: I. On the thermodynamic foundation of the Donnan equation of state. *Journal of Physics: Condensed Matter*, 23(19):194106, 2011.

[124] Luc Belloni. Yes, pair correlations alone do determine sedimentation profiles of highly charged colloids. *The Journal of chemical physics*, 123(20):204705, 2005.

[125] Aldemar Torres, Alejandro Cuetos, Marjolein Dijkstra, and René van Roij. Sedimentation of charged colloids: The primitive model and the effective one-component approach. *Physical Review E*, 75(4):041405, 2007.

[126] A Stroobants, H N W Lekkerkerker, and T Odijk. Effect of electrostatic interaction on the liquid crystal phase transition in solutions of rodlike polyelectrolytes. *Macromolecules*, 19(8):2232–2238, 1986.

[127] Thijs Besseling. *Self-assembly of colloidal spheres and rods in external fields*. PhD thesis, Utrecht University, 2014.

[128] David van der Beek and Henk N W Lekkerkerker. Liquid crystal phases of charged colloidal platelets. *Langmuir*, 20(20):8582–8586, 2004.

[129] Gerald S Manning. Counterion condensation on charged spheres, cylinders, and planes. *The Journal of Physical Chemistry B*, 111(29):8554–8559, 2007.

[130] Sven H Behrens and David G Grier. The charge of glass and silica surfaces. *The Journal of Chemical Physics*, 115(14):6716–6721, 2001.

[131] Robert J Hunter. *Zeta potential in colloid science: principles and applications*, volume 2. Academic press, 1988.

[132] T Hiemstra, W H van Riemsdijk, and G H Bolt. Multisite proton adsorption modeling at the solid/solution interface of (hydr) oxides: A new approach: I. model description and evaluation of intrinsic reaction constants. *Journal of colloid and interface science*, 133(1):91–104, 1989.

[133] Michael L Hair. Hydroxyl groups on silica surface. *Journal of Non-Crystalline Solids*, 19:299–309, 1975.

[134] Taiki Yanagishima, Lorenzo Di Michele, Jurij Kotar, and Erika Eiser. Diffusive behaviour of pll–peg coated colloids on λ-dna brushes–tuning hydrophobicity. *Soft Matter*, 8(25):6792–6798, 2012.

[135] Arthur Adamson. *A Textbook of physical chemistry*. London: Academic Press inc., 1973.

[136] Hiroyuki Ohshima. Henry's function for electrophoresis of a cylindrical colloidal particle. *Journal of colloid and interface science*, 180(1):299–301, 1996.

[137] Hiroyuki Ohshima. Approximate analytic expression for the electrophoretic mobility of moderately charged cylindrical colloidal particles. *Langmuir*, 31(51):13633–13638, 2015.

[138] Henriëtte E Bakker, Thijs H Besseling, Judith E G J Wijnhoven, Peter H Helfferich, Alfons van Blaaderen, and Arnout Imhof. Microelectrophoresis of silica rods using confocal microscopy. *Langmuir*, 33(4):881–890, 2017.

[139] Anke Kuijk, Thomas Troppenz, Laura Filion, Arnout Imhof, René van Roij, Marjolein Dijkstra, and Alfons van Blaaderen. Effect of external electric fields on the phase behavior of colloidal silica rods. *Soft Matter*, 10(33):6249–6255, 2014.

[140] L Belloni, M Drifford, and P Turq. Counterion diffusion in polyelectrolyte solutions. *Chem. Phys.*, 83:147, 1984.

[141] S Alexander, P M Chaikin, P Grant, G J Morales, and P Pincus. Charge renormalization, osmotic pressure, and bulk modulus of colloidal crystals: Theory. *J. Chem. Phys.*, 80:5776, 1984.

[142] G V Ramanathan. Counterion condensation in micellar and colloidal solutions. *J. Chem. Phys.*, 88:3887, 1988.

[143] L Belloni. Ionic condensation and charge renormalization in colloidal suspensions. *Colloids Surf., A*, 140:227, 1998.

[144] Emmanuel Trizac, Miguel Aubouy, and Lydéric Bocquet. Analytical estimation of effective charges at saturation in poisson boltzmann cell models. *Journal of Physics: Condensed Matter*, 15(1):S291–S296, dec 2002.

[145] Niels Boon, Guillermo Ivan Guerrero-García, René van Roij, and Monica Olvera de la Cruz. Effective charges and virial pressure of concentrated macroion solutions. *Proceedings of the National Academy of Sciences*, 112(30):9242–9246, 2015.

[146] Guillaume Bareigts and Christophe Labbez. Effective pair potential between charged nanoparticles at high volume fractions. *Physical Chemistry Chemical Physics*, 19(6):4787–4792, 2017.

[147] Hartmut Löwen. Anisotropic self-diffusion in colloidal nematic phases. *Physical Review E*, 59(2):1989, 1999.

[148] M P Lettinga, J K G Dhont, Z Zhang, S Messlinger, and G Gompper. Hydrodynamic interactions in rod suspensions with orientational ordering. *Soft Matter*, 6(18):4556–4562, 2010.

[149] Jan K G Dhont. *An introduction to dynamics of colloids*, volume 2. Elsevier, 1996.

[150] Alice L Thorneywork, Roberto E Rozas, Roel P A Dullens, and Jürgen Horbach. Effect of hydrodynamic interactions on self-diffusion of quasi-two-dimensional colloidal hard spheres. *Physical review letters*, 115(26):268301, 2015.

[151] Alessandro Patti, Djamel El Masri, René van Roij, and Marjolein Dijkstra. Collective diffusion of colloidal hard rods in smectic liquid crystals: Effect of particle anisotropy. *The Journal of chemical physics*, 132(22):224907, 2010.

[152] Hartmut Löwen. Brownian dynamics of hard spherocylinders. *Physical Review E*, 50(2):1232, 1994.

[153] M P B van Bruggen, H N W Lekkerkerker, and J K G Dhont. Long-time translational self-diffusion in isotropic dispersions of colloidal rods. *Physical Review E*, 56(4):4394, 1997.

[154] M P B van Bruggen, H N W Lekkerkerker, G Maret, and J K G Dhont. Long-time translational self-diffusion in isotropic and nematic dispersions of colloidal rods. *Physical Review E*, 58(6):7668, 1998.

[155] Eric Grelet, M Paul Lettinga, Markus Bier, René van Roij, and Paul van der Schoot. Dynamical and structural insights into the smectic phase of rod-like particles. *Journal of Physics: Condensed Matter*, 20(49):494213, 2008.

[156] Laura Alvarez, M Paul Lettinga, and Eric Grelet. Fast diffusion of long guest rods in a lamellar phase of short host particles. *Physical review letters*, 118(17):178002, 2017.

[157] Jay Newman, Harry L Swinney, and Loren A Day. Hydrodynamic properties and structure of fd virus. *Journal of molecular biology*, 116(3):593–603, 1977.

[158] J K Phalakornkul, A P Gast, and R Pecora. Rotational and translational dynamics of rodlike polymers: a combined transient electric birefringence and dynamic light scattering study. *Macromolecules*, 32(9):3122–3135, 1999.

[159] R Colin, M Yan, L Chevry, J-F Berret, and B Abou. 3d rotational diffusion of micrometric wires using 2d video microscopy. *EPL (Europhysics Letters)*, 97(3):30008, 2012.

[160] Iwao Teraoka and Reinosuke Hayakawa. Theory of dynamics of entangled rod-like polymers by use of a mean-field green function formulation. i. transverse diffusion. *The Journal of Chemical Physics*, 89(11):6989–6995, 1988.

[161] Iwao Teraoka and Reinosuke Hayakawa. Theory of dynamics of entangled rod-like polymers by use of a mean-field green function formulation. ii. rotational diffusion. *The Journal of chemical physics*, 91(4):2643–2648, 1989.

[162] Masao Doi, Izumi Yamamoto, and Fumiaki Kano. Monte carlo simulation of the dynamics of thin rodlike polymers in concentrated solution. *Journal of the Physical Society of Japan*, 53(9):3000–3003, 1984.

[163] Siegfried Hess, Daan Frenkel, and Michael P Allen. On the anisotropy of diffusion in nematic liquid crystals: test of a modified affine transformation model via molecular dynamics. *Molecular physics*, 74(4):765–774, 1991.

[164] Shuang Tang and Glenn T Evans. Self-diffusion in isotropic and nematic phases of highly elongated hard particles. *The Journal of chemical physics*, 98(9):7281–7288, 1993.

[165] Michael P Allen. Diffusion coefficient increases with density in hard ellipsoid liquid crystals. *Physical review letters*, 65(23):2881, 1990.

[166] M Paul Lettinga, Edward Barry, and Zvonimir Dogic. Self-diffusion of rod-like viruses in the nematic phase. *EPL (Europhysics Letters)*, 71(4):692, 2005.

[167] Y Han, A M Alsayed, M Nobili, J Zhang, T C Lubensky, and A G Yodh. Brownian motion of an ellipsoid. *Science*, 314(5799):626–630, 2006.

[168] Claire Ribrault, Antoine Triller, and Ken Sekimoto. Diffusion trajectory of an asymmetric object: information overlooked by the mean square displacement. *Physical Review E*, 75(2):021112, 2007.

[169] Zhongyu Zheng and Yilong Han. Self-diffusion in two-dimensional hard ellipsoid suspensions. *The Journal of chemical physics*, 133(12):124509, 2010.

[170] Gijsberta H. Koenderink, M. Pavlik Lettinga, and Albert P. Philipse. Rotational dynamics of charged colloidal spheres: Role of particle interactions. *The Journal of Chemical Physics*, 117(16):7751–7764, 2002.

[171] Jean-Pierre Hansen and Hartmut Löwen. Effective interactions between electric double layers. *Annual Review of Physical Chemistry*, 51(1):209–242, 2000.

[172] C Tsakonas, A J Davidson, C V Brown, and N J Mottram. Multistable alignment states in nematic liquid crystal filled wells. *Applied Physics Letters*, 90:111913, 2007.

[173] T Lopez-Leon, V Koning, K B S Devaiah, V Vitelli, and A Fernandez-Nieves. Frustrated nematic order in spherical geometries. *Nature Physics*, 7:391–394, 2011.

[174] Mykola Tasinkevych, Michael G Campbell, and Ivan I Smalyukh. Splitting, linking, knotting, and solitonic escape of topological defects in nematic drops with handles. *Proceedings of the National Academy of Sciences*, 111:16268–16273, 2014.

[175] Jeffrey A Speir and John E Johnson. Nucleic acid packaging in viruses. *Current opinion in structural biology*, 22(1):65–71, 2012.

[176] Pei He and Brian Derby. Inkjet printing ultra-large graphene oxide flakes. *2D Materials*, 4(2):021021, 2017.

[177] Zhen Xu, Haiyan Sun, Xiaoli Zhao, and Chao Gao. Ultrastrong fibers assembled from giant graphene oxide sheets. *Advanced materials*, 25(2):188–193, 2013.

[178] Budhadipta Dan, Natnael Behabtu, Angel Martinez, Julian S Evans, Dmitry V Kosynkin, James M Tour, Matteo Pasquali, and Ivan I Smalyukh. Liquid crystals of aqueous, giant graphene oxide flakes. *Soft Matter*, 7(23):11154–11159, 2011.

[179] Jong-Hyun Ahn, Hoon-Sik Kim, Keon J Lee, Seokwoo Jeon, Seong Jun Kang, Yugang Sun, Ralph G Nuzzo, and John A Rogers. Heterogeneous three-dimensional electronics by use of printed semiconductor nanomaterials. *science*, 314(5806):1754–1757, 2006.

[180] A B G M Leferink op Reinink, E van den Pol, A V Petukhov, G J Vroege, and H N W Lekkerkerker. Phase behaviour of lyotropic liquid crystals in external fields and confinement. *The European Physical Journal Special Topics*, 222(11):3053–3069, 2013.

[181] Leo Radzihovsky and John Toner. Smectic liquid crystals in random environments. *Physical Review B*, 60(1):206, 1999.

[182] Germano S Iannacchione and Daniele Finotello. Calorimetric study of phase transitions in confined liquid crystals. *Physical review letters*, 69(14):2094, 1992.

[183] Y Mao, P Bladon, H N W Lekkerkerker, and M E Cates. Density profiles and thermodynamics of rod-like particles between parallel walls. *Molecular Physics*, 92:151–159, 1997.

[184] R van Roij, M Dijkstra, and R Evans. Orientational wetting and capillary nematization of hard-rod fluids. *EPL (Europhysics Letters)*, 49(3):350, 2000.

[185] René van Roij, Marjolein Dijkstra, and Robert Evans. Interfaces, wetting, and capillary nematization of a hard-rod fluid: Theory for the zwanzig model. *The Journal of Chemical Physics*, 113(17):7689–7701, 2000.

[186] Marjolein Dijkstra, René van Roij, and Robert Evans. Wetting and capillary nematization of a hard-rod fluid: A simulation study. *Physical review E*, 63(5):051703, 2001.

[187] D de las Heras, E Velasco, and L Mederos. Effects of wetting and anchoring on capillary phenomena in a confined liquid crystal. *The Journal of chemical physics*, 120(10):4949–4957, 2004.

[188] Hendrik Reich and Matthias Schmidt. Capillary nematization of hard colloidal platelets confined between two parallel hard walls. *Journal of Physics: Condensed Matter*, 19(32):326103, 2007.

[189] Alexandr Malijevskỳ and Szabolcs Varga. Phase behaviour of parallel hard rods in confinement: an onsager theory study. *Journal of Physics: Condensed Matter*, 22(17):175002, 2010.

[190] Sergei Egorov, Andrey Milchev, and Kurt Binder. Semiflexible polymers in the bulk and confined by planar walls. *Polymers*, 8(8):296, 2016.

[191] Kira E Klop, Roel P A Dullens, M Paul Lettinga, Sergei A Egorov, and Dirk G A L Aarts. Capillary nematisation of colloidal rods in confinement. *Molecular Physics*, 116(21-22):2864–2871, 2018.

[192] Szabolcs Varga, Yuri Martínez-Ratón, and Enrique Velasco. Hard rods in a cylindrical pore: the nematic-to-smectic phase transition. *Journal of Physics: Condensed Matter*, 26(7):075104, 2014.

[193] Oliver J Dammone, Ioannis Zacharoudiou, Roel P A Dullens, Julia M Yeomans, M Paul Lettinga, and Dirk G A L Aarts. Confinement induced splay-to-bend transition of colloidal rods. *Physical review letters*, 109(10):108303, 2012.

[194] Alexander H Lewis, Ioana Garlea, José Alvarado, Oliver J Dammone, Peter D Howell, Apala Majumdar, Bela M Mulder, M Paul Lettinga, Gijsje H Koenderink, and Dirk G A L Aarts. Colloidal liquid crystals in rectangular confinement: theory and experiment. *Soft Matter*, 10(39):7865–7873, 2014.

[195] Ioana C Gârlea, Pieter Mulder, José Alvarado, Oliver J Dammone, Dirk G A L Aarts, M Pavlik Lettinga, Gijsje H Koenderink, and Bela M Mulder. Finite particle size drives defect-mediated domain structures in strongly confined colloidal liquid crystals. *Nature communications*, 7:12112, 2016.

[196] Marina Soares e Silva, José Alvarado, Jeanette Nguyen, Nefeli Georgoulia, Bela M Mulder, and Gijsje H Koenderink. Self-organized patterns of actin filaments in cell-sized confinement. *Soft Matter*, 7(22):10631–10641, 2011.

[197] Jennifer Galanis, Daniel Harries, Dan L Sackett, Wolfgang Losert, and Ralph Nossal. Spontaneous patterning of confined granular rods. *Physical review letters*, 96(2):028002, 2006.

[198] Jennifer Galanis, Ralph Nossal, Wolfgang Losert, and Daniel Harries. Nematic order in small systems: measuring the elastic and wall-anchoring constants in vibrofluidized granular rods. *Physical review letters*, 105(16):168001, 2010.

[199] Hartmut Löwen. A phase-field-crystal model for liquid crystals. *Journal of Physics: Condensed Matter*, 22(36):364105, 2010.

[200] Miguel González-Pinto, Yuri Martínez-Ratón, and Enrique Velasco. Liquid-crystal patterns of rectangular particles in a square nanocavity. *Physical Review E*, 88(3):032506, 2013.

[201] René Wittmann, Matthieu Marechal, and Klaus Mecke. Fundamental measure theory for smectic phases: scaling behavior and higher order terms. *The Journal of Chemical Physics*, 141(6):064103, 2014.

[202] Thomas Geigenfeind, Sebastian Rosenzweig, Matthias Schmidt, and Daniel de las Heras. Confinement of two-dimensional rods in slit pores and square cavities. *The Journal of chemical physics*, 142(17):174701, 2015.

[203] Daniel de las Heras and Enrique Velasco. Domain walls in two-dimensional nematics confined in a small circular cavity. *Soft Matter*, 10(11):1758–1766, 2014.

[204] Ioana C Gârlea and Bela M Mulder. Defect structures mediate the isotropic–nematic transition in strongly confined liquid crystals. *Soft Matter*, 11(3):608–614, 2015.

[205] M Paul Lettinga and Eric Grelet. Self-diffusion of rodlike viruses through smectic layers. *Phys. Rev. Lett.*, 99:197802, 2007.

[206] Jeff Z Y Chen. Structure of two-dimensional rods confined by a line boundary. *Soft Matter*, 9(45):10921–10930, 2013.

[207] Glenn T Evans. Hard body model for chiral nematic liquid crystals. *Molecular Physics*, 77:969–981, 1992.

[208] Marc Esposito and Glenn T Evans. Isotropic, nematic and smectic a phases in fluids of hard spherocylinders. *Molecular Physics*, 83:835–845, 1994.

[209] O V Manyuhina, K B Lawlor, M C Marchetti, and M J Bowick. Viral nematics in confined geometries. *Soft matter*, 11(30):6099–6105, 2015.

[210] A H Lewis, D G A L Aarts, P D Howell, and Apala Majumdar. Nematic equilibria on a two-dimensional annulus. *Studies in Applied Mathematics*, 138(4):438–466, 2017.

[211] Louis B G Cortes, Yongxiang Gao, Roel P A Dullens, and Dirk G A L Aarts. Colloidal liquid crystals in square confinement: isotropic, nematic and smectic phases. *Journal of Physics: Condensed Matter*, 29(6):064003, dec 2016.

List of Publications

Louis B G Cortes, Yongxiang Gao, Roel P A Dullens and Dirk G A L Aarts. *Colloidal liquid crystals in square confinement: isotropic, nematic and smectic phases.* Journal of Physics: Condensed Matter, 29(6), 2016. (Chapters 6).

Louis B G Cortes, René Wittmann, Roel P A Dullens, Hartmut Löwen and Dirk G A L Aarts. *Confinement of smectic colloidal liquid crystals into annuli: theory and experiments.* In preparation. (Chapters 6).

Louis B G Cortes, Clément O Robert, Maxime M C Tortora, Roel P A Dullens, Jonathan P K Doye and Dirk G A L Aarts. *Sedimentation-diffusion equilibrium of charged rods.* In preparation. (Chapters 3 and 4).

Louis B G Cortes, Roel P A Dullens, M Paul Lettinga and Dirk G A L Aarts. *Self-diffusion of colloidal rods in sedimentation-diffusion equilibrium: isotropic, nematic and smectic phases.* In preparation. (Chapters 5).

Acknowledgement of Funding

This project has received funding from the European Union's Horizon 2020 research and innovation programme under the Marie Skłodowska-Curie Grant Agreement No 641839.

Acknowledgements

I would like to express my deep and sincere gratitude to my research supervisor, Dirk for his guidance and support, but also for introducing me to a wonderful groups of people both within Oxford Colloid Group (OCG) and DiStruc, the innovative training network founding my positon. I am extremely grateful to Dirk and Irini, the administrator of DiStruc, for their friendliness and joviality that, despite the weather, made my transition to Oxford such a good experience. I would also like to thank Roel, for co-leading the OCG with enthusiasm, organizing annual barbecue and taking responsibility for the legendary PTCL Christmas party, but also for following my work and for his open door policy. More generally, I am grateful to Roel and Dirk for making a priority of cultivating a friendly atmosphere within the group.

I would like to express my thanks to the master students I had the chance to supervise – Balkis, Clément and Han Sol – for their quality exploratory work on the phase and flow behavior of silica rods. They are now PhD students in the University of Oxford, Saint-Gobain Research Paris and the Max Plank Institute.

I would like to acknowledge our collaborators in the context of this thesis and beyond: Roel Dullens, Maxime Tortora and Jon Doye, Pavlik Lettinga, Yongxiang Gao, René Wittmann and Hartmut Löwen.

I am grateful to the Oxford Colloid Group members for pleasant scientific discussions and trainings. My special thanks go to Marjolein, Kira and Yongxiang for teaching me experimental techniques. I also would like to thank the group members for the good time I had outside the lab, in particular: the pub Friday aficionados, the market people, the runners – with or without hairy legs, the tennis and squash players, the skilled punters, etc. Special thanks for Siyu, with whom I had a synchronized DPhil experience and shared a lot of memories.

I am extremely grateful to the DiStruc's supervisory board that spent a lot of time and efforts to provide us with the best possible training and was always very cheerful and friendly. I wish they have the opportunity to take in charge a second generation of young and brilliant scientists, even though we will always remain their favorites. More seriously, I am extremely grateful to the DiStruc fellows, that became like a second family, and with whom I had incredible times in Heraklion, Eindhoven, Oxford, Bordeaux and Julich. I would like to thank particularly Roland and Krassimir for hosting my secondment at Unilever, and Pavlik for hosting my sec-

ondment in Julich. My thanks equally go to Eric, for supervising my master thesis and opening my mind to colloidal liquid crystal but also the DiStruc job opportunities. My special thanks go for Max, with whom I used to share accommodation during DiStruc events and had very good fun preparing the talks (no stress with $T\iota\tau\alpha\kappa\eta\sigma$).

I would like to thank my college, Christ Church, and my college adviser, Jason, for their help and support. I am particularly thankful for the squash courts, punts and nice dinners, but also for financial support and affordable accommodation. It was a great pleasure to hang out with Christ Church graduates studying various subjects. I would like to thank my consecutive housemates for enduring me, in particular Matt – the future of energy distribution, and Sam – arguably a brilliant Italian opera singer. My thanks also go to Jack my brewing companion, with whom I may or may not have flooded a historic room with 5 gallons of beer.

I am grateful to Joe, Sam and Jack for proofreading parts of my thesis, I shall liquefy this dept.

My final thanks go to my friends and family that came to visit me in Oxford and/or supported me during my time abroad. I would like to thank my parents – Ines and Bernard, brothers – Arthur and Charles – and cousins that filled my agenda with weddings and visits, and my phone with baby pictures. I also would like to thank my grandparents–Mémé, Pipo and Mijo, aunts and uncles, in particular Mathieu that helped me with my cover letter. I am very grateful to Mathieu, Romain, Julien, Hugo, Alex and Bastien – a group of friends that I am delighted to find when I come back to my hometown or when we decide to explore the world together. I would also like to thank Jimmy and Sylvain for our annual mojito-raclette fun-party. Finally, I would like to thank other friends I wish I could see more often.

Remerciements. Enfin, je voudrais adresser mes remerciements à ma famille et à mes amis qui sont venus me voir à Oxford, et/ou m'ont soutenu pendant mon séjour au Royaume-Uni. En particulier, je voudrais remercier mes parents – Inès et Bernard, mes frères – Arthur et Charles, et mes cousins qui ont agrémenté mon calendrier de visites et mariages, et qui ont rempli mon téléphone de photos de bébés. Je voudrais aussi remercier mes grand-parents—Mémé, Pipo et Mijo, mes oncles et mes tantes, en particulier Mathieu qui m'a aidé à rédiger ma lettre de motivation. Je tiens à remercier mes amis de longue date – Mathieu, Romain, Julien, Hugo, Alex et Bastien – que je suis ravi de retrouver lorsque je rentre au pays ou part en vadrouille. Je voudrais aussi remercier Jimmy et Sylvain avec qui chaque retrouvaille est un festival de rire. Pour terminer je voudrais adresser une pensée à tous mes autres amis que je n'ai pas pu voir autant que je l'aurais voulu.